Alma Mater Studiorum – Università di Bologna

DOTTORATO DI RICERCA IN

CHIMICA

Ciclo 35

Settore Concorsuale: 03/C2 - CHIMICA INDUSTRIALE

Settore Scientifico Disciplinare: CHIM/04 - CHIMICA INDUSTRIALE

Synthesis and Catalytic Activity of New Cu-based Catalytic Systems for the Enhanced Electrochemical CO_2 Reduction

Presentata da: Martina Serafini

Coordinatore Dottorato

Chiar.mo Prof. Luca Prodi

Supervisore

Chiar.mo Prof. Francesco Basile

Co-supervisore

Chiar.ma Prof.ssa Domenica Tonelli

Esame finale anno 2023

If we knew what we were doing,

it would not be called research,

would it?

(Albert Einstein)

To my family,

Elisa, Marco, and Chiara

ABSTRACT

This Ph.D. thesis concerns the synthesis of nanostructured Cu-containing materials to be used as electrode modifiers for the CO_2 electroreduction in aqueous phase and the evaluation of their catalytic performances. Inspired by the fascinating concept of the artificial photosynthesis-oriented systems, several catalytic layers were electrochemically loaded on carbonaceous gas diffusion membranes, *i.e.*, 3D structures that allow the design of eco-friendly materials for applications in green carbon recycling processes. In particular, early studies on Cu^{I-II}-Cu^0 nanostructured materials were carried out to produce films on 4 cm^2 sized supports by means of a fast and low-cost electrochemical procedure. Besides, through a screening of potentials, it was possible to find out a selective value for the CH_3COOH production at -0.4 V *vs* RHE with a maximum productivity (1h reaction), ensured by the presence of the Cu^+/Cu^0 active redox couple (0.31 mmol g_{cat}^{-1} h^{-1}). On the basis of these results, further optimisations of the electrocatalyst chemical composition were carried out with the aim of (i) facilitating the interaction with CO_2, (ii) increasing the dispersion of the catalytic active phase, and (iii) enhancing the CH_3COOH productivity. To this aim, novel electrocatalysts based on layered double hydroxides (LDHs) were optimised, having as a final goal the formation of a new Cu_2O-Cu^0 based electrocatalyst derived from electrochemically achieved CuMgAl LDHs, subjected to calcination and reduction processes. The as-obtained electrocatalysts were tested for the selective production of CH_3COOH and unprecedented results were obtained with the pristine CuMgAl LDH (2.0 mmol g_{cat}^{-1} h^{-1}). Additional characterisations of such an electrocatalyst have highlighted the possibility to achieve a ternary LDH in intimate contact with Cu_2O-Cu^0 species starting from the electrochemical deposition. The presence of these species, along with an alkaline environment on the electrode surface, were essential to preserve the selectivity towards the desired product, as confirmed by further *operando* studies.

TABLE OF CONTENT

CHAPTER 1

General Introduction

1.1 Climate Change

In history, the climate of the Earth has undergone frequent alterations, switching among natural cycles of glacial and interglacial ages. There were times when most of the planet was covered by ice followed by warmer periods, a cyclical pattern driven by natural factors, and the temperatures used to slowly fluctuate. Contrarily, the climate change that we are witnessing today is different and strongly correlated to the anthropologic development. According to the Milankovitch's theories [1,2], the climate variations during the last millions of years occurred with variable periodicity of 100,000 – 41,000 years, in correspondence to orbital motions, with big changes in temperatures. However, from 10,000 BC, our planet has entered in a geological epoch named as Holocene, in which the average of the temperatures was stunningly stable, marking the end of the Ice Age era [3]. During this period, humans have had a great evolution, starting from the huge development of the agriculture until the birth of the modern societies, covering years between the prehistory and our day's history. Interestingly, around 5,000 BC, a long-term cooling trend has started. However, what might have been the beginning of a new natural cycle unfortunately ended around the middle of the XVIII century. During that period, another type of age was about to start with the name of Industrial Era. Such era marked the surge of the global temperatures that rose from near the coldest to the warmest levels of the Holocene in just 100 years [4]. Although the large temperature variations have been caused by many factors including volcanic eruptions, changes in the sun or the Earth's orbital motions, the main factor that has most contributed to the current climatic alteration is the uncontrolled emissions of the greenhouse gases (GHGs) [5].

Such compounds, including water vapour, carbon dioxide, methane, fluorinated gases, and nitrous oxide are natural or artificial gases capable of trapping the heat generated from the solar radiation.

Once the sun rays have hit the surface of our planet, the energy is converted into heat that is partly thrown back into space and the rest is absorbed by the atmospheric gases and released back to Earth. In fact, thanks to these gases, our planet is able to maintain a stable energetic balance from which all living beings benefit. However, the uncontrolled increase of GHGs is destroying this energetic balance, causing the climate change that we are experiencing nowadays.

Carbon dioxide is the second most abundant greenhouse gas in the atmosphere, second only to the water vapor [6], and it represents the largest contributor to the climate change, although being not the most powerful one. Indeed, sulphur hexafluoride is considered as the most dangerous GHG, as 1 ton of SF_6 is equivalent to 23,500 tons of CO_2, but its current contribution to the global warming is estimated around 0.2% due to the very low concentration in the atmosphere and thus it cannot be included among the mainly responsible compounds [7].

In 2013, the Intergovernmental Panel on Climate Change (IPCC) [8] released a report where the importance of the carbon dioxide as greenhouse gas compared to the other compounds was demonstrated. By measuring the abundance of GHGs in (i) polar ice cores, (ii) atmosphere, and (iii) from other climate factors between 1750 and 2011, they achieved the "radiative forcing" value (RF) for each climate driver. Such indicator, measured as W m^{-2}, gives an idea of the influence of each target GHG on the energetic balance between the incoming and outgoing energy from the atmosphere. A positive value mean that the related compound contributes in a "positive way" to the earth's surface warming, thus raising it up. The RF values for the main responsible GHGs are summarised in Table 1.1.

Table 1.1. Summary of the estimates of Radiative Forcing (with uncertainties) in 2011 relative to 1750. Data reported from 2013 IPCC report [8]

Drivers of climate change	*Radiative Forcing estimates (W m^{-2})*
CO_2	1.68 ± 0.35
CH_4	0.97 ± 0.23
N_2O	0.17 ± 0.04
Halocarbons (O_3, CFCs, HCFCs)	0.18 ± 0.17
CO	0.23 ± 0.07
Solar irradiance	0.05 ± 0.05

Among them, the carbon dioxide reported the highest value. Moreover, considering all the carbon-containing gases, the RF value for CO_2 increases to 1.82 W m^{-2}, confirming its main contribution to the climate change and thus explaining the importance of monitoring its emissions.

In particular, the collected data, gained from the polar ice core samples, revealed that the CO_2 concentrations recorded today are 50% higher than those registered at the starting point of the industrial revolution (1760) and higher than any point over the past 800,000 years. Such a trend is shown in the technical report of Keramidas *et al.* [9] (Figure 1.1) and originally taken from the *National Oceanic and Atmospheric Administration* [10].

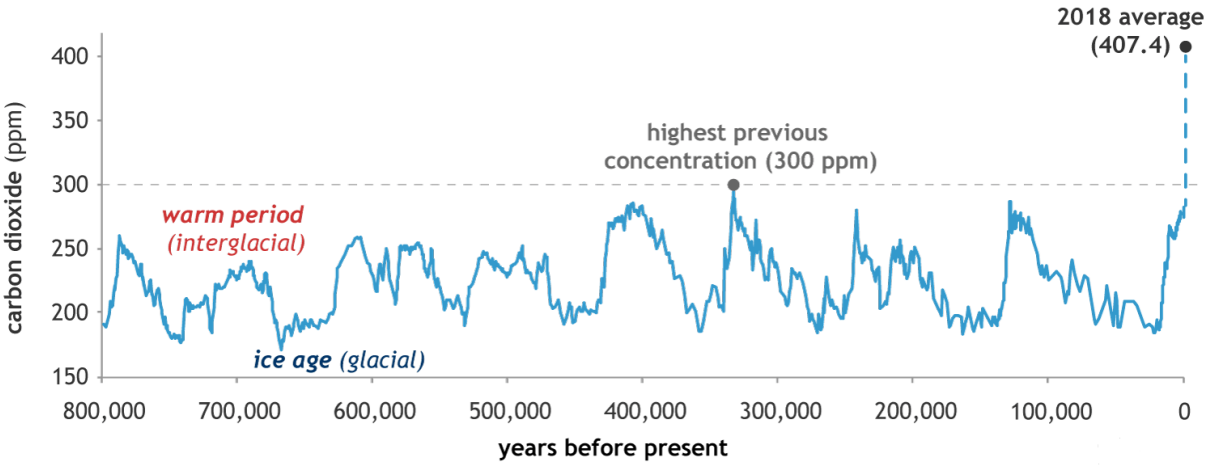

Figure 1.1. Atmospheric CO_2 concentrations for the past 800,000 years. Reproduced with permission from Keramidas *et al.* [9], © European Union, 2020

Here, a trend of the anthropogenic carbon dioxide emissions is showed and it clearly highlights the alarming evidence. Although the CO_2 concentration has varied during the ancient epochs, fluctuating between 190 and 290 ppm in correspondence of the glacial and interglacial cycles, an increase of about 120 ppm within a single century has been recorded.

In 2014, a second report of the IPCC [11] stated that between 1750 and 2011 the total anthropogenic emissions of carbon dioxide were 2,040 ± 310 $GtCO_2$, whose 60% was removed from the atmosphere and stored in lands and oceans, causing their acidification, and it is estimated that half of them have occurred in the last 40 years. In particular, between 1970 and 2000, the total GHGs emissions are increased by 1.3% $GtCO_2$-eq/yr (equivalent per year) while between 2000 and 2010 it has reached the 2.2% $GtCO_2$-eq/yr.

More recently, Friedlingstein *et al.* [12], reported that the cumulative manmade CO_2 emissions from 1850 to 2020 was almost 2,420 ± 240 $GtCO_2$, including more than 30% (726 $GtCO_2$) occurred since 2000.

On average, starting from 2011 to 2020, the total emission per year was stable around 39.7 ± 0.8 $GtCO_2$, with an atmospheric CO_2 growth of 5.1 ± 0.02 GtC/year (47% of the total emissions).

Therefore, starting from a CO_2 concentration of 277 ppm in 1750 [13], the several increases registered during the years led to a recorded concentration in 2020 of 412.4 ± 0.1 ppm [14]. Currently, the CO_2 levels are above 410 ppm, as shown in Figure 1.2, and, in May 2022, the Global Monitoring Laboratory of the National Oceanic and Atmospheric Administration (NOAA) and the Scripps Institution of Oceanography [15] reported an average value of 421 ppm registered at NOAA's Mauna Loa Atmospheric Baseline Observatory. This value is comparable to the Pliocene Climatic Optimum epoch (4.1 – 4.5 million years ago) when the sea level was proved to be 23.5 meters above the present one [16].

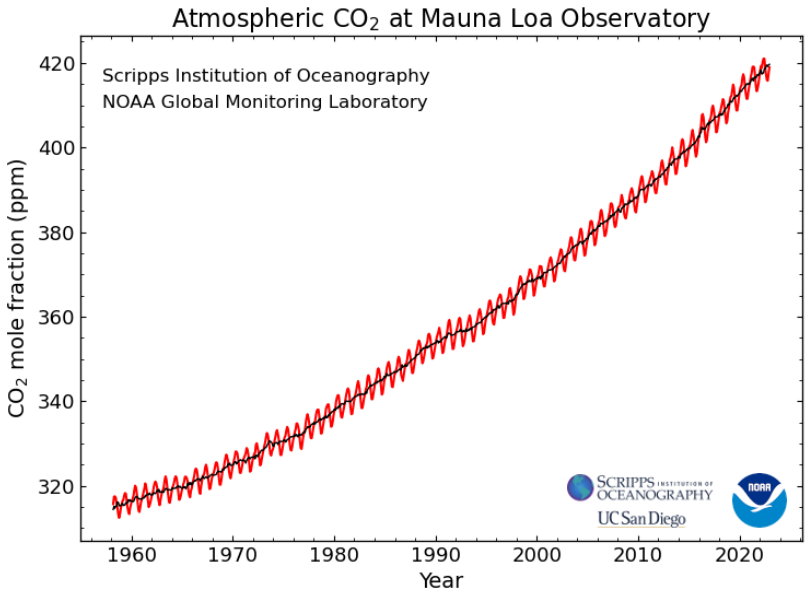

Figure 1.2. Monthly mean CO_2 measured at Mauna Loa Observatory, centred on the middle of each month. Reproduced with permission from Tans and Keeling [15]

Therefore, the main difference between the ancient climate changes and the one occurring today is the time-scale.

Indeed, in two centuries and a half, a percentage increase in the carbon dioxide concentration of 52% has occurred, while the planet is significantly warming, reaching an average temperature of +1.15 K above the 1850-1900 levels. Those alarming data highlight the destroying human influence on the earth's climate system that sees in the uncontrolled combustion of fossil fuels and the huge deforestations the principal causes [17].

Therefore, nowadays there are real fears that the global warming will have a dramatic impact on the habitats for terrestrial and marine ecosystems, irreversibly modifying their compositions [18–22].

According to NOAA scientists, since 1981 Earth's temperature has risen by 0.18 K per decade and in 2021 the average temperature across global surfaces was 0.84 K above the 20th century average. Indeed, the hottest 7 years started from 2015 to 2021.

Between 2014 and 2017, a dramatic decrease of the ice extent of the Arctic Ocean sea occurred dropping from 12.73 to 10.70 million km^2, similarly to the mean decrease of the Arctic ice registered over the entire 41 years (1981 – 2022) [23]. In 2021, the snow coverage over the Northern Hemisphere averaged 24.3 million km^2, 0.6 million km^2 less than the 1991-2020 average [24].

From the 2022 IPCC Report [25], in Europe it is expected that the number of deaths will double or triple for a rise in temperature of +3 K, when heat and drought will lead to substantial losses in terms of agricultural productions and floods will be more frequent. Moreover, between 1900 and 2000, the level of the Mediterranean Sea increased by 1.4 mm per year, accelerating during the end of the century, and values potentially close to the meter in 2100 are estimated in the worst scenario.

The EEA scientists [26] also reported that the ocean pH decreased from 8.11 to below 8.06 between 1980 and 2016, corresponding to a 30% increase of acidity.

Such reduction measured in surface mixed-layer depths is consistent with that estimated from atmospheric CO_2 concentrations, assuming the thermodynamic equilibrium between the ocean surface, and air.

Therefore, the predictions for our future are very alarming and different ecosystems will not be able to adapt themselves to such a sudden change over the short run.

For these reasons, the problem of the climate change cannot be solved by a single or a group of states. The whole world has to deal with the consequences and the effects of such climate crisis, and so mitigation policies and global civil liability are urgently needed.

1.1.1 Overview of the Mitigation Policies

The issue of the climate change emerged at global level in the mid-1970s [27]. At that time, the World Meteorological Organization (WMO) started to express some concern about the human activities, notably the CO_2 emissions, and in 1979 the First World Climate Conference was held in Geneva [28]. Although it did not attract the attention of many policy makers, scientists of various disciplines agreed about the problem and arranged several working groups with the aim to collect climate data about its variability and effects on the planet. By increasing the number of scientific data, and with the discovery in 1985 of the decrease in the stratospheric column density over Antartica (known today as the *ozone hole*) [29], the human attention on the climate crisis began to rapidly increase.

Although the response of the governmental officials to the Farman's article was again initially cool [30], such event triggered off a series of political and scientific conferences including those in Villach (1985), Hamburg (1987), and Toronto (1988).

On that last occasion, the Intergovernmental Panel on Climate Change (IPCC) [31] suggested to identify the measures for the mitigations of the GHGs emissions and to raise awareness on the public information and education, setting the stage for the climate change negotiations. Hence, although the climate crisis had already been declared at least 20 years earlier, only in the 1990s it changed from a scientific to a political issue and politicians finally recognised its dangerous potential. Although in the first IPCC assessment report there were no specific national or international targets to limit the GHGs productions, it was a key step for future climate change debates and negotiations [32] that culminated with the conclusion of the Kyoto Protocol in December 1997 [33]. The goal of this international deal, entered into force in 2005 after the Russia's ratification, was to set the targets to reduce the GHGs emissions, in the period 2008 – 2012, by at least 5.2% compared to the levels registered in 1990. To do so, the Kyoto Protocol was based on three market-based "flexible mechanisms", described in the following scheme:

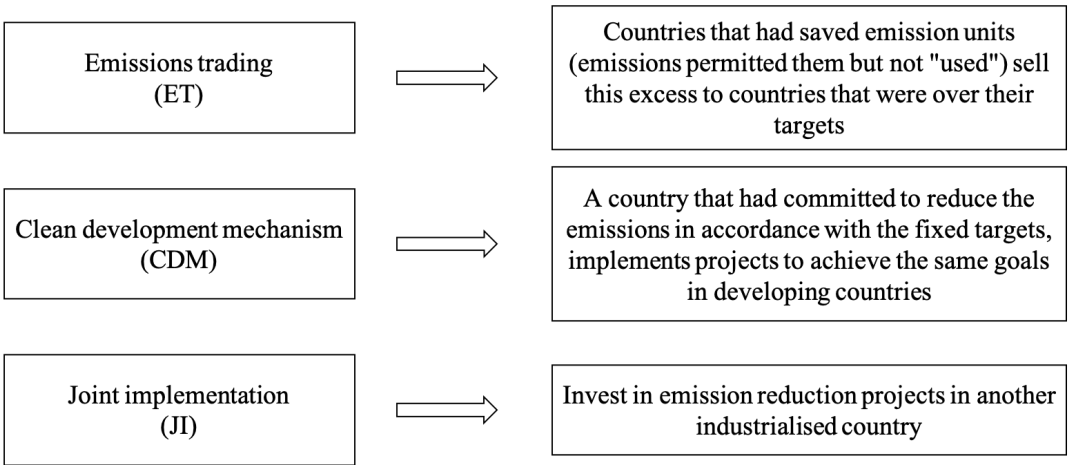

Figure 1.3. The Kyoto Protocol market-based mechanisms [34]

Moreover, in 2012 a second commitment period was established during the 18th Conferences of the Parties in Doha, known as the "Doha Amendment". This new phase of the Kyoto protocol extended the life of such deal 8 years further (2012-2020). The real change between the first and the second Kyoto period concerned the targets of the emissions reduction, moving from 5.2% to 18% [35].

Despite several studies indicate that the CO_2 emissions decreased during the Protocol period [36,37], the overall effectiveness of the restrictions was scarce and the main reason was due to the lack of worldwide support, *i.e.*, United States did not adhere to the protocol obligations and Canada went out in 2011 [38].

Indeed, the Kyoto countries emitted about 7% less than those who did not ratify the deal [39], and the developing countries India and China, which were excluded from the protocol restrictions, contribute nowadays for 27% and 6.6% to the global GHGs emissions, respectively, outpacing together the United States set at 11% [40]. Therefore, the emissions of GHGs and in particular those of carbon dioxide never stopped growing.

The last main deal written to reinforce the global response to climate change entered into force in November 2016 and it is known as the Paris Agreement. The goals over long run were set to limit the global warming to no more than +2 K, preferably +1.5 K, compared to pre-industrial levels. According to this treaty, starting from 2020, over 140 countries have been committed to achieve net zero CO_2 emissions, estimating that global GHGs emission levels, which were at 52.7 $GtCO_2$-eq in 2014, should be cut down to 48 $GtCO_2$-eq by 2025, and to 42 $GtCO_2$-eq in 2030 [41]. Therefore, over the years the whole humanity has become increasingly aware about the climate crisis trying to limit the anthropological impact. However, the human awareness and responsibility towards the climate change often encountered economic and political obstacles that, on the one hand, have limited the effectiveness of the mitigation policies, while, on the other hand, have pushed the scientific community to put great efforts in developing new strategies in order to guarantee a sustainable future for our society.

1.2 Strategies to Reduce CO_2: From a Threat to an Opportunity

Despite three decades of political efforts, global carbon dioxide emissions have never stopped to increase. Hundreds of formal decisions, action plans, and work programs should have led to a change in the slope of the emissions curve, but this is not how it was (see Figure 1.2). The challenges are "recognised" and "internalised", but the existing power structures remain unchallenged, giving only promises that are carefully translated in elaborate models [42].

The scientific community is not indifferent to the crisis that all of us are experiencing, but dealing with carbon dioxide at global scale requires systematic approaches. To this purpose, there is a lot of technological solutions that may have the potential to face the problem, including the emissions reduction, the removal and the storage of the already released CO_2, and finally its conversion.

1.2.1 Natural Climate Solutions

An important role in the mitigation process of the atmospheric carbon dioxide could be attributed to the forests. In particular, the tropical, temperate, and boreal ones are the three main forest biomes representing the 31% of the coverage of the global land [43].

To date, the existing forests store about 45% of the organic carbon on land and they can absorb about 2 GtC/year, which is however a very little amount compared to the total anthropogenic carbon released so far (~ 600 GtC) [44].

Moreover, the forest coverage is not homogeneous all over the world as it ranges from a peak of 0% in dry desert to 100% in the equatorial forest, with fewer intermediate values.

Theoretically, in order to reach the goal of the Paris Agreement, an equally spread reforestation of about 1 billion hectares would be necessary [45], that would be able to absorb more than 205 GtC/year, according to the estimates of the group of Bastin *et al.* [46].

However, such calculations did not consider the availability of suitable lands, the water resources, the future climate conditions, and the time required to mature a newly born forest.

Veldman *et al.* [47] criticised the estimation of Bastin, proposing a more concrete view and suggesting that such potential carbon sequestration was overestimated by 5 times. Indeed, Veldman reported that the actual potential was limited to 45 GtC/year, which represents only the 7.5% of the total anthropogenic carbon amount.

Moreover, it is also worth noting that planting trees in some different ecosystems can somehow increase the carbon emissions. As an example, in polar zones the native vegetation is often covered by the snow that helps to reflect the sun rays and avoids the absorption of more solar energy. Besides, planting trees in dry lands such as savannahs may increase the risk of fire thus achieving an increase in carbon releases in the atmosphere.

Contrarily, a reforestation process in tropical regions is expected to be most effective in mitigating the CO_2 levels, providing a forest-based climate mitigation [44]. On the other hand, by converting all the existent forests for agricultural purposes, by the 2100 the carbon dioxide concentration would increase by 130-290 ppm [48]. While, if the carbon released in the same time frame was absorbed by the actual forests, there would be a decrease of 17-31 ppm. Therefore, the presence of forests is essential to avoid the increase of the CO_2 concentration over the years, despite the scarce contribution to its reduction. Moreover, it is important to protect the forest biomes through ecological and sociological liability with the aim to preserve ecosystems that otherwise will go towards extinction.

Together with the forest biomes, oceans play another key role to fight the climate change. Similarly to the terrestrial ecosystems, the marine ecosystems can store a substantial amount of carbon. Recent studies have reported the potential of the coastal vegetation, known as “blue carbon” ecosystems, performing estimations over the possible carbon removal accessible with

their maintenance [49]. Therefore, it is important to ensure healthy oceans as they can absorb CO_2 from the atmosphere at rates up to four times higher than the terrestrial ecosystems [50].

For the decade 2011-2020, the percentage of CO_2 absorbed by the ocean was around 26% of the total emissions, approximately 2.8 ± 0.4 GtC/year, with a preliminary estimate of 3 GtC/year for the 2021 [12].

Moreover, from ideal Earth system models [51,52], by enhancing the weathering and the ocean alkalinity, it would be possible to dissolve a higher amount of CO_2 in the sea water. As an example, Mg-rich minerals (*i.e.*, Mg_2SiO_4) can be naturally added to the water thus enhancing the CO_2 absorption. In fact, every 1.5 Gt of Mg_2SiO_4-rich rocks may absorb 1 $GtCO_2$ [53].

Therefore, Natural Climate Solutions (NCS) have a fundamental role in fighting the climate change. As an example, Graves *et al.* [54] reported the contribution of the NCS activities on GHGs (including CO_2) emissions reduction in Oregon (Figure 1.4), expressed as million metric tons of CO_2 equivalents (MMT CO_2e). 1 MMT is equal to 1 ton.

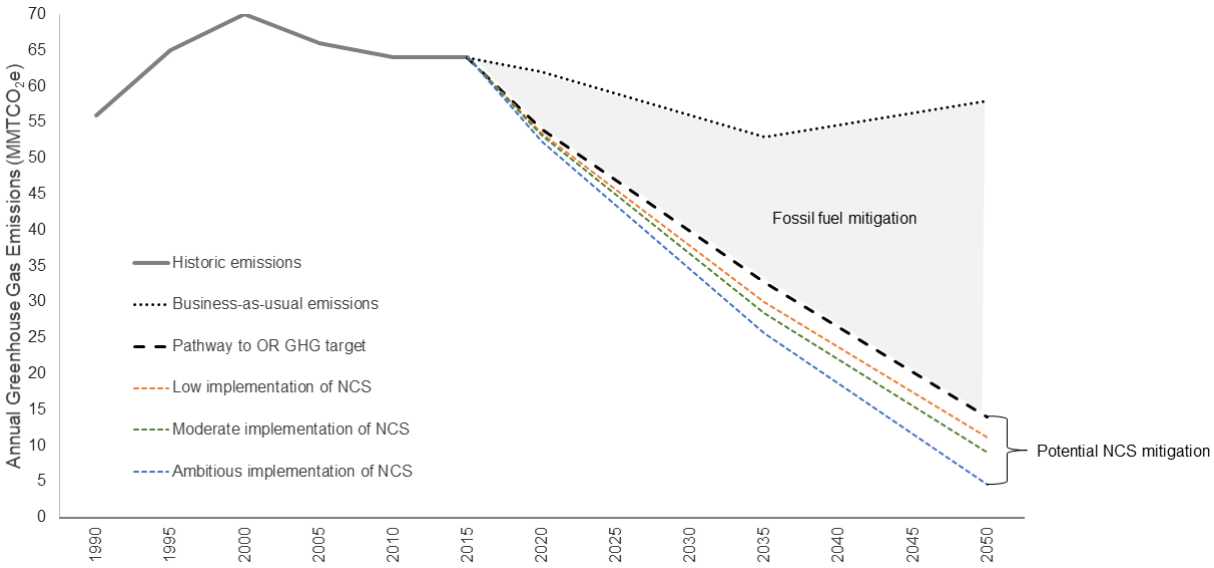

Figure 1.4. Trend of the CO_2 emissions with NCS activities to Oregon's CO_2 reduction goals in different scenarios. Reproduced with permission from Graves *et al.* [54], © 2020, published by PLOS

Here, assuming a substantial fossil fuel mitigation which could led to a decrease of GHGs emissions of 14 MMT CO_2e by 2050, the NCS activities have the potential to contribute from 20% to 70% of the additional reduction required to reach zero emissions by that time.

Moreover, they can provide many benefits such as the conservation of biodiversity, the preservation of ecosystems, the habitats improvements or the oceans protection.

Human well-being, food and water security, and the effective decrease of the risk of natural disasters are some of the positive aspects for human beings that can be achieved from the natural solutions but they require ecological and sociological liability. However, the actual levels of CO_2 are frighteningly high and, along with the imperative to move to the NCS opportunities, it is equally imperative to move to faster actions.

1.2.2 Anthropological Climate Solutions

In analogy with the natural CO_2 sinks, there are manmade confinement processes that can provide higher reductions of the carbon dioxide emissions coming from industries. Such technologies, known as Carbon Capture and Storage (CCS), are mostly known as anthropological actions that essentially prevent the CO_2 from reaching the atmosphere [55]. Indeed, along with the natural absorption of CO_2 carried out by trees or oceans, technologically advanced platforms or plants can be designed to improve the decarbonisation process.

The CCS technologies include three main steps: the CO_2 capture and separation, transportation and storage. The first step can be achieved by a series of different capture systems, as stated by Irons *et al.* [56] : (i) pre-combustion, (ii) post-combustion, and (iii) oxy-fuel combustion. Such technologies aim to remove the carbonaceous component inside the fuels with the aim of avoiding its release in the atmosphere in favour of carbon-less energies.

In the pre-combustion capture system, also known as gasification or reforming process, it is possible to isolate the carbon dioxide prior to the fuel combustion [57]. First, the fuel reacts with steam (steam reforming) or O_2 (partial oxidation) developing a gaseous mixture of CO and H_2, according with the following reactions, respectively:

$$CxHy + xH_2O \leftrightharpoons xCO + (x + \frac{y}{2})\, H_2 \qquad \Delta H°(CH_4) = 206\ kJ\ mol^{-1} \qquad (1)$$

$$CxHy + \frac{x}{2} O_2 \leftrightharpoons xCO + \frac{y}{2} H_2 \qquad \Delta H°(CH_4) = -36\ kJ\ mol^{-1} \qquad (2)$$

Then the mixture is fluxed into a shift converter reactor, where the water gas shift reaction (WGS) takes place (reaction 3) and the CO reacts with water vapour to give CO_2 and additional H_2:

$$CO + H_2O \leftrightharpoons CO_2 + H_2 \qquad \Delta H° = -41\ kJ\ mol^{-1} \qquad (3)$$

The obtained gases are then separated by physical or chemical absorption processes. The main methods consist of three physical separations: one carried out by a glycol or methanol-based solvent, known as Selexol or Rectisol process, respectively [58], the second one by means of membranes [59–61], and the last one by means of solid adsorbing materials like zeolites or activated carbon used at high pressure, known as pressure swing adsorption [62].

The aim of the pre-combustion approach is to convert a C-based energy into a H_2-based energy prior to use, avoiding the release of carbon dioxide during the further combustion processes. It provides higher CO_2 concentration and pressure obtained in the output flux that can facilitate the separation process with lower energy penalties for refrigeration [63].

The main disadvantages of the pre-combustion capture system are the high amount of energy needed for the air separation and for the reforming/gasification reactions and the losses of energy recovery during syngas temperature swing [57].

The post-combustion process involves the separation of CO_2 from the gases developed during the fossil fuel combustion. It is designed to be placed after the purification of the exhaust gases, a mixture of CO_2, SO_2, NO_2, and O_2 (namely flue gases), to remove particulate and to capture NO_x and SO_x species. Due to the low concentration of the CO_2 in the flue gases around 13-15%, the driving force for the separation is very low but, like the pre-combustion capture systems, the post-combustion technologies can be implemented to the majority of coal-fired plants. Such technologies include membrane separation [64,65], cryogenic fractionation [66], and Ca-looping technologies [67]. However, the most widely used method in the coal-fired power plants is the chemical absorption and, according to Basile *et al.* [68], the most common one is the amine-based absorption carried out in aqueous monoethanolamine (MEA) solution, whose stronger chemical reaction is capable to achieve more than 90% of CO_2 from the flue gas. However, the main disadvantage for this process consists in the solvent degradation that requires high cost of energy to be regenerated [63].

The last procedure used for the CO_2 capture is the oxy-fuel combustion, which is actually a modified post combustion process. Here, the fuel is burnt with nearly pure oxygen (about 98%) to guarantee the presence of carbon dioxide and water in the output gas, with traces amount of other compounds. In this way, contrarily to the composition of the flue gas released during the post combustion process, the CO_2 concentration is greater than 80%, facilitating the separation processes without the need of any reagent and/or solvents which represents the main advantage

of this approach. On the other side, the main disadvantage relies on the O_2 separation from air which is usually carried out cryogenically.

Such procedure is expensive in terms of energy consumption and capital cost [68] and for this reason it is still under investigation due to the prohibitive costs for the oxygen production. Hence, it has only been demonstrated in pilot plants or by means of simulations [69]. For the sake of clarity, Figure 1.5 schematically shows the three CO_2 capture technologies applied to the energy field.

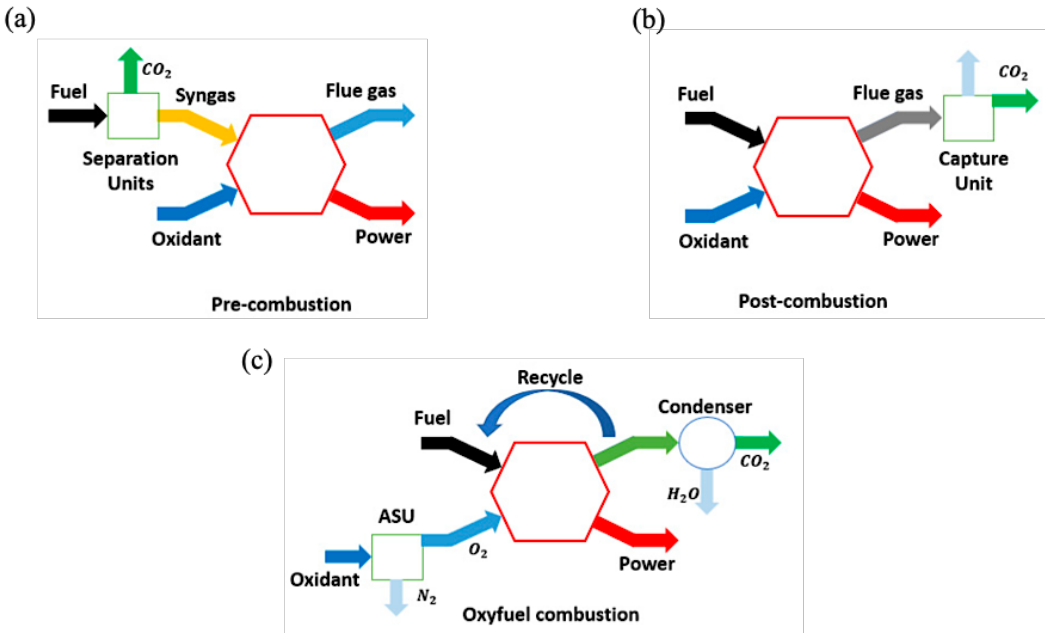

Figure 1.5. Summary of the principal CO_2 capture systems: (a) pre-combustion; (b) post-combustion; (c) oxyfuel combustion. Adapted with permission from Cannone *et al.* [70], © 2021 by the authors. Licensee MDPI, Basel, Switzerland

Once the CO_2 has been captured and isolated from the rest of the other gaseous compounds, it has to be transported to the storage area [55]. Before the moving, the impurities such as water vapour, nitrogen, methane or other hydrocarbons are removed and the CO_2 is compressed into the supercritical state (80-150 bar), reaching a density of 900 kg m^{-3} [71]. Commonly, the CO_2 is stored far from where it is captured and, depending on the distance, it could be achieved by ship, pipeline or truck.

Although shipping is not widely used for the CO_2 transportation, the main advantage relies on the possibility to become the most cost-effective for transporting the carbon dioxide over long distances by virtue of its mature technology [72]. Tankers that are usually employed for the liquefied petroleum gas (LGP) could be repurposed for CO_2. However, the temperature and pressure monitoring during the journey requires high costs and thus this method needs further improvements. Indeed, with the aim of alleviating these critical issues, efforts are devoted to build tankers specifically designed for the carbon dioxide, decreasing the capital cost and enhancing the maximum capacity, as stated by Orchard *et al.* [73].

Differently, the transportation towards pipelines is the primary way to transport CO_2 as it represents the most cost-effective approach. Such mature technology dates back to the 1970s and in 2015 it exceeded 8,000 km, most of them in the United States. Moreover, thanks to the Paris Agreement in 2016, the demand for CO_2 pipeline construction started to increase and it is estimated that it will take over 200,000 km in order to transport 10 billion tons CO_2 [74].

Like the CH_4 pipelines, those engaged on CO_2 have the same characteristics except for some features. In case of leaking, the CO_2 diffuses slower than the natural gas but its transportation state is affected by pressure, temperature and impurities. In particular, the water vapour content needs to be reduced to a lower percentage to avoid the reaction between CO_2 and acidic compounds to form acids [55,75]. Moreover, the materials of the pipes have higher requirements due to the decompression waves and low temperature. Indeed, although the transportation volume is large and the operating costs are low, the initial investment is the highest among all the transportation strategies [74].

The last strategy consists of trains or trucks transportation, which is, however, economically affordable only for short distances and small amounts of CO_2.

Such approach is expected to become important in the small-scale transportation during the expansion of the carbon capture systems [72].

Indeed, by using trains or trucks there are no specific facilities that need to be built.

However, on the one hand, the main disadvantage for the trains is that the CO_2 source and destination places need to be close to the railways. On the other hand, nowadays the fuel needed for the trucks is very expensive, due to the problems deriving from the Russia-Ukraine war and the Covid pandemic, and they are exposed to weather and traffic conditions.

A comprehensive summary of the main CO_2 transport technologies, including the key issues for each system (Table 1.2), was obtained from Baroudi *et al.*. [76]

Table 1.2. Summary of the CO_2 transportation methods. Adapted with permission from Baroudi *et al.* [76], © 2021 The Author(s). Published by Elsevier Ltd.

Method	*Conditions (T and p)*	*Phase*	*Capacity (Mt CO_2 yr^{-1})*	*Features*
Pipelines	283 – 307 K 4.8 – 20 Mpa	Vapour, dense phase	~100	• Higher capital costs, lower operating costs • Low-pressure pipeline system is 20% more expensive than dense phase transmission • Well-established for EOR USE
Ships	221 – 283 K 0.65 – 4.5 Mpa	Liquid	> 70	• Higher operating costs, lower capital costs • Currently applied in food and brewery industry for smaller quantities and different conditions • Enhanced sink-source matching
Motor carriers	243 – 253 K 1.7 – 2 Mpa	Liquid	> 1	• 2–30 tonnes per batch • Not economical for large-scale CCUS projects • Boil-off gas emitted 10% of the load
Railway	223 – 253 K 0.65 – 2.6 Mpa	Liquid	> 3	• No large-scale systems in place • Loading/unloading and storage infrastructure required • Only feasible with existing rail line • More advantageous over medium and long distances

Finally, regardless of how the carbon dioxide is transported, it must be stored. In 2018, the IPCC report [45], according with the goals of the Paris agreement, stated that the negative emission technologies have to remove tens of $GtCO_2$ already released, together with the emissions reduction and its capture from the early sources. Indeed, by 2100, about 125 $GtCO_2$ must be removed towards the CCS technologies [77]. To permanently store the carbon dioxide and reduce the overall contribution in the atmosphere, the storage must be safe, verifiable, environmental-friendly, and the risk of catastrophic events must be minimised.

According with the IPCC report written in 2005 [78], the storage options can be divided in: (i) geological reservoirs, (ii) ocean sinks, and (iii) mineral carbonation.

The principal locations for the geological storage are rocks and the main ones consist of sedimentary basins, including oil or gas wells and saline aquifers. Such sinks need to be at least 1 km thick in order to facilitate the injection and trapping of CO_2. Here, although the temperatures are above the critical value (304 K), the pressures are high enough to ensure densities of about 500 kg m^{-3} [79]. Among all the options, the saline aquifers are the best choice by virtue of their enormous storage capacity and high capture capability. Moreover, their saline nature makes them unsuitable for agricultural or human activities [80].

The injection process could be carried out by means of already developed technologies, usually employed for the gas injection into the oil well, in order to enhance its extraction or by exploiting the know-how derived by the natural gas storage [81]. Sedimentary basins worldwide can store up to 8,200 $GtCO_2$, if conservatively estimated, and between 20,000 and 35,000 $GtCO_2$, if highly estimated. Most of these potential geological reservoirs are located in Asia (~2,974 $GtCO_2$), Northern (2,600–21,770 $GtCO_2$) and Southern America (~2,030 $GtCO_2$) [77].

However, there is no real way to fully prevent rare but catastrophic accidents, nor there is any way to ensure that each site is gas-tight. To this purpose, numerical simulations and field observations must be achieved prior the injection to ensure the ability of the geological site to safely store the carbon dioxide. Hence, strategies to minimise the risks including engineering and site evaluation studies must be considered [81].

The second place in which CO_2 can be stored is the ocean. The ocean storage represents both a natural climate solutions (NCS), as already mentioned, and a possible CO_2 reservoir by creating artificial pools at the ocean floor. In the latter case, the carbon dioxide is injected at great depths, below 1 km from the surface. Here, the water has a lower density and the carbon dioxide dissolves or forms hydrates, that are dispersed in the water body [80,81].
Several techniques were tested to achieve the CO_2 transfer to the ocean: (i) vertical injection; (ii) inclined pipe; (iii) pipe towed by ship, and (iv) dry ice [55]. However, the main disadvantage linked to the increase of CO_2 concentration in the ocean is the consequences in marine ecosystems. Indeed, it is not possible to control the site in which the carbon dioxide has been stored due to the sea currents thus likely causing prohibitive acidification. For these reasons, such technologies are still under investigation.

The last approach for the CO_2 storage is the mineral sequestration. Such method, already discussed for the ocean alkalization process, includes the reaction between CO_2 and minerals containing alkaline-earth oxides like magnesium or calcium. In particular, serpentine – $Mg_3Si_2O_5(OH)_4$, olivine – Mg_2SiO_4, and wollastonite – $CaSiO_3$ minerals are the most suitable for the CO_2 absorption [82], resulting in the following reactions, respectively:

$$Mg_3Si_2O_5(OH)_4 + 3CO_2 \longrightarrow 3MgCO_3 + 2SiO_2 + 2H_2O \quad (4)$$

$$Mg_2SiO_4 + 2CO_2 \longrightarrow 2MgCO_3 + SiO_2 \quad (5)$$

$$CaSiO_3 + CO_2 \longrightarrow CaCO_3 + SiO_2 \quad (6)$$

However, such reactions take very long time and need to be accelerated to become industrially affordable. Moreover, the mineralisation approach needs to be divided in two categories: *in situ* and *ex situ* mineralisation. In the *in situ* route, the CO_2 sequestration reaction occurs directly at the site of the mineral deposit where the gas is stored underground. At the beginning, the carbon dioxide spontaneously dissolved inside the rain, producing H_2CO_3. Then, the carbonic acid dissociated into H^+ and HCO_3^- or CO_3^{2-}, and its acidic component started to degrade minerals, releasing Ca^{2+} and Mg^{2+} that can bind bicarbonate to form solid carbonates [83]. Annually, it is estimated that about 300 Mt of CO_2 is removed from the atmosphere through the *in situ* mineralisation [84]. However, due to the slow reaction between the bicarbonate and the minerals, such approach is unlikely to be adopted by industries.

On the other hand, by applying the *ex situ* approach, the reactions are accelerated by using chemical reagents and harsh operative conditions (high T and p), exploiting industrial processes. However, this approach inevitably leads to higher costs. Indeed, it is estimated that to remove 1 ton CO_2, the amount of olivine and wollastonite required is about 1.6 tons and 2.6 tons, respectively [83].

In summary, the CCS technologies have a great potential to reduce the concentration of carbon dioxide in the atmosphere by virtue of their ability to capture the gas directly from the sources and permanently store it into natural reservoirs. Indeed, the storage of the carbon dioxide is essential for the industrial decarbonization as it represents a cost-effective and a realistic way to meet the target of the Paris agreement.

However, there are not enough regulatory drivers to incentivise or require the use of the CCS technology in the worldwide industry field and, for this reason, the cost of the equipment and the materials are very high. Moreover, Dooley *et al.* [85] estimates that only few countries will have the possibility to store the carbon dioxide and thus implement the carbon capture technologies, making the evaluation of the amount of CO_2 storage difficult to be carried out. Finally, an essential goal that needs to be addressed is the worldwide public awareness about the CCS. To date, when people know about what such technologies entail, in most cases, they have a positive perception until it comes to the CO_2 storage location. Indeed, they tend to reject large capture and storage projects near their homes as they are perceived risky to health and lifestyle [86]. Moreover, Wallquist *et al.* [87] carried out a conjoint study in order to evaluate the acceptance of the CCS technologies based on three different factors: CO_2 source, transport, and storage. Interestingly, they found out that the greater concerns were related to the pipelines and storage locations only if the CO_2 came from a gas-fired power plant. Indeed, if the CO_2 came from a biogas-fired power plant, there was no "Not in My Back Yard" effect, regardless of the fact that they could live near the storage site, while, if the CO_2 came from a gas-fired power plant, people rejected the idea. For such reasons, together with the incentives and the safety measures required for the CCS technology, it is also very important to avoid bad information and to raise the public awareness about all the CCS advantages and critical points.

Together with the CCS technologies, there is another process based on the use of the captured CO_2 as a possible feedstock to produce more valuable substances or to be used as it is. Differently from the CCS technologies, such promising strategy is also known as Carbon Capture and Utilisation (CCU), and differs from the previous approach that it does not aim to set a recycle, as show in Figure 1.6.

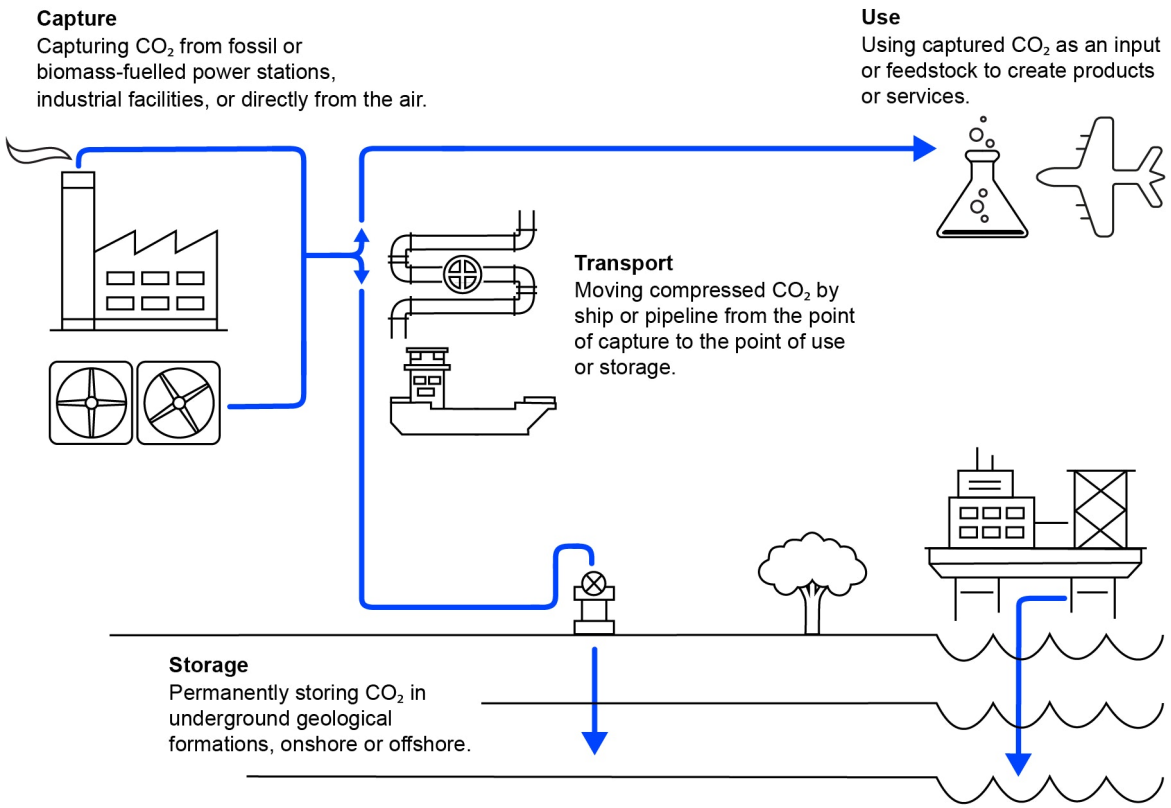

Figure 1.6. Schematic illustration of the CCS and CCU approaches from the International Energy Agency. Reproduced with permission from IEA, 2020 [88]

CO_2 is already used for commercial purpose. Indeed, in its pure form, it is notably employed to carbonate the beverages, as an extractant to make flavourings, or to accelerate the production of greenhouse tomatoes. Likewise, it can be used as solvent for the decaffeination process or to produce dry ice. CO_2 is also employed as fire extinguisher or to enhance the fuel recovery by pumping it under supercritical conditions into oil fields, where conventional recovery has become unpractical [89].

However, the further use of CO_2 as a starting material to be transformed into valuable products is becoming a concrete opportunity to successfully reduce the carbon dioxide emissions [90]. Indeed, carbon dioxide waste streams can have value as feedstocks for producing a wide range of products, subdivided in long-lived products such as cement, durable polymers or building insulations, and short-lived products which include fuels and chemicals [91].

The US National Academy of Sciences [89] has classified products as having a long shelf-life if they have the possibility to keep the CO_2 out of the atmosphere for at least 100 years, making the concept of the long-lived products similar to the geological storage. Indeed, the principal long-lived product coming from the CO_2 conversion is cement that is obtained by means of mineralisation processes, as mentioned before. Along with cements, CO_2 based polymers represent a sustainable and environmentally benign alternative to reduce the dependence of commodity plastics on fossil fuels [92]. By means of endothermic reactions, the CO_2 can be co-polymerised with a number of cyclic ethers to produce aliphatic and thermoplastic polycarbonates like poly (ethylene carbonate - PEC), poly (propylene carbonate - PPC), poly (butylene carbonate - PBC), and poly (cyclohexene carbonate - PCHC), that represent the major industrial CO_2 application potentials [93].

Although the long-lived products are capable to reduce CO_2 emissions over a long run, the possibility to develop new platforms capable to enhance the conversion towards fuels and chemicals is attracting growing scientific interest. Among these compounds, C_2 products represent the main building blocks for many chemical syntheses and they have the highest industrial values [94]. For these reasons, many efforts have been invested to obtain such commodities from the direct hydrogenation of CO_2 at ambient operative conditions, employing non-critical raw materials, paving the way to the development of a circular economy in which decarbonisation route takes place through a "green carbon recycling" [95,96]. However, due to the high thermodynamic stability of the CO_2 molecule, external energy must be introduced to drive its transformation to reduced products. In particular, the molecule of CO_2 owns a binding energy of the C=O double bond of 750 kJ mol^{-1}, a heat of formation of $\Delta G_f^0 = -394.4$ kJ mol^{-1}, and a formal electrochemical redox potential to obtain the initial radical species $CO_2^{\bullet-}$ of -1.85 V *vs* SHE at neutral pH [97–99].

The conversion of the carbon dioxide can be achieved through different approaches, which involve thermochemical [100], biochemical [101,102], radiochemical [103], photochemical [104,105], or electrochemical reactions [106,107]. Although the use of CO_2 will not be the ultimate answer, additional strategies such as minimisation of energy usage, shifting towards renewable energy sources, and developing innovative processes, the conversion could be a promising solution. In the following paragraphs, detailed understanding of the most promising routes will be discussed to give a comprehensive overview of the state of the art with regard to the usage of carbon dioxide.

1.2.2.1 Thermochemical CO_2 Conversion

The thermal catalytic route is the most mature pathway for CO_2 conversion as it is carried out by both homogeneous and heterogeneous catalytic processes, that combine the use of a catalyst with heat and pressure. For decades, huge efforts have been dedicated to this approach and technological innovations are also being developed every day [108]. Indeed, through the thermochemical reduction of carbon dioxide, a wide range of valuable products can be obtained via a direct CO_2 conversion or through integrated processes (indirect routes) [109], as schematically shows in Figure 1.7.

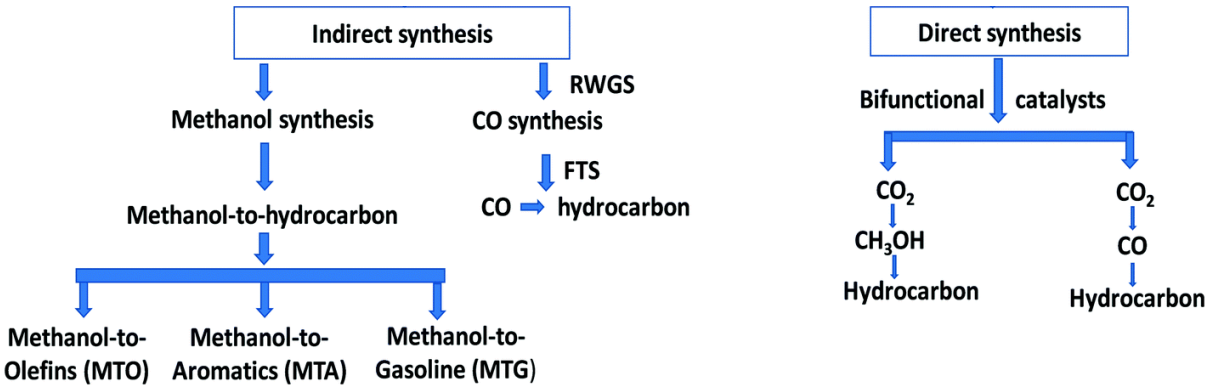

Figure 1.7. Overview of hydrocarbon synthesis. Adapted with permission from Xu *et al.* [108], © 2020 by the authors. Licensee MDPI, Basel, Switzerland

The main reaction that takes place in the thermal catalytic process is the CO_2 heat and pressure-driven hydrogenation to methanol, methane, lower olefins, or long-chain hydrocarbons [110].

The hydrogenation reaction has been identified as the most important discovery among all the CO_2 transformations as it cannot be spontaneously achieved. Indeed, it allows to form valuable compounds for energetic applications. Moreover, along with the possibility to gain H_2 directly from the renewables [111,112], avoiding processes like CH_4 steam reforming as it produces additional CO_2, it provides a great opportunity for sustainability in the energy and environment sectors.

The first industrially developed CO_2 hydrogenation reaction, known as the Sabatier process [113], dates back to the early 1900s, and led Paul Sabatier to win the Nobel Prize in 1912. Also known as CO_2 methanation, this discovery has been essential to understand the modern catalysis. Here, the carbon dioxide is combined with hydrogen by means of an exothermic reaction [114], carried out with Ni-based catalysts, according to:

$$CO_2 + 4H_2 \longrightarrow CH_4 + 2H_2O \qquad \Delta H° = -165\ kJ\ mol^{-1} \qquad (7)$$

Such a reaction (Figure 1.8) needs to be carried out at high temperatures (> 573 K) and pressures (approximately 30 bar) in order to avoid deactivation processes due to possible nickel oxidations or the formation of the toxic and volatile species $Ni(CO)_4$ [115].

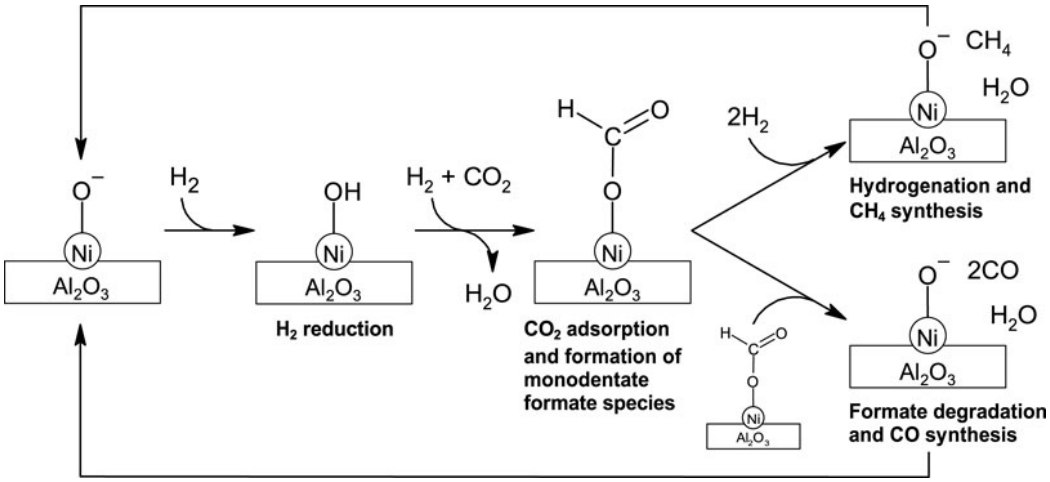

Figure 1.8. Reaction mechanism of the CO_2 methanation over Ni-based catalyst. Reproduced with permission from Tan *et al.* [116], © 2022 The Authors. Published by Frontiers, Lausanne, Switzerland

Interestingly, Müller *et al.* [117] investigated the catalytic activity of a NiO/silica catalyst towards the methanation of CO_2 coming from flue gases emitted by conventional power plants on the base of brown coal (lignite). The results were obtained in laboratory scale and reported a 100% selectivity towards methane with a conversion of CO_2 greater than 80%, thus demonstrating the high potential of such reaction in the long road towards the reduction of carbon dioxide, giving also an energetic continuity to the renewables as hydrogen can be converted to methane which is easier to storage. Although the Sabatier approach provides cost-effective catalyst alternatives to noble metals, the large consumption of H_2 and the difficult storage have lowered the industrial interest [118,119], especially after the development of the Fischer-Tropsch process towards the production of alkanes. However, the methanation process has been investigated and developed for more than 100 years. Indeed, the Sabatier reaction is now discussed as "Power-to-Gas" approach and in 2013 the world's first industrially operated plant, namely e-gas, for catalytic methanation of CO_2 was commissioned in Werlte (DE) by the Audi group for the production of sustainable synthetic natural gas. To date, the Sabatier process is mainly used to produce water during space exploration [115].

Another useful process to thermochemically reduce CO_2 is the reverse water gas shift reaction (RGWS), widely employed for the production of carbon monoxide.

$$CO_2 + H_2 \rightleftharpoons CO + H_2O \qquad \Delta H° = 41\ kJ\ mol^{-1} \qquad (8)$$

According to reaction 8, the formation of CO is an endothermic process that requires high temperatures (823 – 1023 K).

Since the reaction is very similar to that of Sabatier, there may be a competition between the achievable products. Indeed, Gorimbo *et al.* [120] investigated the ΔG values for both reactions while changing the operative temperature. As a result, they demonstrated that at temperatures below 868 K, ΔG values for the Sabatier reaction were negative, facilitating the formation of CH_4 instead of CO. Therefore, with the aim to achieve a 100% selectivity towards CO, thermodynamic limitations can be used (*i.e.*, work at higher temperatures), along with an efficient design of the catalyst.

Depending on the employed catalyst, the RWGS can be achieved through a redox mechanism or through decomposition of an intermediate, *i.e.*, formate, and it can be performed as a single process or as a middle reaction for further processes [100,121]. On the one hand, the redox mechanism preferentially takes place when Cu-based catalysts are employed, as Cu^0 is oxidised to Cu^I and favours the CO_2 reduction to CO [122]. On the opposite, the formate pathway requires a bifunctional catalyst, *i.e.*, noble metals supported on metal oxides [123]. Other materials that can be used are transition metal carbide (TMC)-based and reducible oxide supported catalysts [100]. The principal active phases are noble metals like Pt, Pd, Rh, Ru, and Au, but also Cu, Ni, and Fe exhibit substantial catalytic activities. In particular, Pt catalysts exhibited the highest overall CO_2 conversions while Cu and Fe displayed better selectivity towards CO [124].

However, due to their high hydrogenation activities, noble metals are more popular in this CO_2 conversion approach but their higher cost and low-availability makes their use prohibitive on large-scale industry applications. For this reason, Cu and Ni represent promising materials even though their oxides species suffer from the high temperatures needed [125].

Usually, the RWGS is coupled with the Fischer-Tropsch (FT) reaction to produce liquid synthetic fuels such as long chain hydrocarbons, according to the reaction below [126]:

$$nCO + (2n+1)H_2 \longrightarrow C_nH_{2n+2} + nH_2O \qquad \Delta H° = -152\ kJ\ mol^{-1} \tag{9}$$

The temperatures employed for this reaction vary from 473 to 648 K depending on the desired product: shorter alkanes chains required low temperatures while longer ones need more energy [127]. The main challenge relies on the catalyst choice, because it should be active for both reactions and, to this purpose, the principal used materials are Fe, Co, and Ru.

Another noteworthy compound, whose thermochemical conversion from CO_2 has a mature industrial application background is methanol. Methanol represents an important reaction intermediate to produce formaldehyde, acetic acid, dimethyl ether (DME), and methyl tertbuthyl ether (MTBE). Moreover, it can be used as a convenient energy-storage material, a feedstock to synthesise hydrocarbons, and a fuel. The latter last option is gaining a growing interest, thanks to the China's policy to the use of methanol as transportation fuel [128]. To date, the worldwide production is about 110 millions of metric tonnes spread over 90 plants [129]. Among them, the first commercially developed plant based on the production of renewable methanol is the "George Olah Renewable Methanol Plant", active in Iceland since 2011.

Such plant is capable to convert about 5,500 tons CO_2 which translates into a production capacity of 4,000 tons CH_3OH.

Predominantly, methanol is synthesised starting from an optimum mixture of syngas (CO, H_2, and CO_2), according to the following reactions:

$$CO_2 + H_2 \rightleftharpoons CO + H_2O \qquad \Delta H° = 41\ kJ\ mol^{-1} \qquad (8)$$

$$CO_2 + 3H_2 \longrightarrow CH_3OH + H_2O \qquad \Delta H° = -49.5\ kJ\ mol^{-1} \qquad (10)$$

$$CO + 2H_2 \longrightarrow CH_3OH \qquad \Delta H° = -90\ kJ\ mol^{-1} \qquad (11)$$

The overall process, known as Syngas to Methanol (STM), requires high pressures ranging from 50-100 bar and relatively low temperatures between 473-573 K [130,131].

The majority of the catalysts employed for those reactions are Cu-based materials for which the medium on which the active phase is dispersed or the amount of copper may vary [132–134]. At the core of this industrial catalysis, the CZA catalysts are the most extensively used [100] as they are made of $CuO/ZnO/Al_2O_3$ and display very high selectivity towards methanol (almost 100%) [135]. Selective catalysts are needed since the employed reactants are the same of those of the Sabatier reaction.

In general, new catalyst designs for thermochemical CO_2 conversions are being developed every day, building up new catalytic routes with the aim to improve the overall yields or to implement greener pathways. As an example, the group of Chueh *et al.* [136] successfully demonstrated the use of CeO_2 for the CO_2 splitting into CO by means of solar-driven thermochemical CO_2 conversion.

Here, the initial endothermic activation of the catalyst, driven by the sun-rays, generates oxygen vacancies which will be later replaced in the ceria lattice by an exothermic non-solar oxidation of the CeO_{2-X} into CeO_2, driven by the CO_2, along with the CO release.

To conclude, the development of further innovative processing and synthesis techniques to promote the thermochemical CO_2 conversion presents the potential to create industrially affordable pathways. However, nowadays, due to the harsh operative conditions needed, its chemical conversion and economical utilisation is still a scientific and technical challenge in view of a sustainable economy.

1.2.2.2 Biochemical CO_2 Conversion

The biochemical conversion of carbon dioxide simulates the process used in nature by living beings, such as plants and several groups of microorganisms, to fix the carbon dioxide with the aim to gain energy and nutrients. It is mainly carried out by two different routes: the microbial and the enzymatic conversion. Such systems, taken from natural sources, are used inside reactors in order to exploit their natural processes.

The microbial conversion can be achieved by a wide range of microbes, including non- and photosynthetic bacteria. Moreover, with the aim to enhance the capabilities of the microorganisms' CO_2 fixation, genetically modified microbes have also been investigated.

The non-photosynthetic bacteria are autotrophic bacteria belonging to several phyla including *Euryarchaeota*, *Crenarchaeota*, *Proteobacteria*, *Actinobacter*, *Aquificae*, *Chlorobi*, *Firmicutes*, and *Chloroflexi* that are studied most for industrial purposes [137,138]. Among them, the most promising performances were obtained by *Euryarchaeota* microbes. They consist of hydrogenotrophic methanogens *archaea*, characterised by their ability to biologically produce CH_4 by means of a process called biological methanogenesis production (BMP) [139].

The auto-catalytic reaction provides the parallel production of methane and biomass by using H_2 as energy source and CO_2 as both carbon and energy source. Depending on the different genus or the bioreactor design, the yield in CH_4 production can vary from 10 [140] to 534.5 mmol g^{-1} h^{-1} [141], with a selectivity of almost 100% . Table 1.3 highlights two of the main advantages of the BMP process compared to the Sabatier reaction [113].

Table 1.3. Comparison between the temperatures and the main catalysts employed for the BMP process and the Sabatier reaction

Method	*Range of temperature (K)*	*Catalyst*
Biological methanogenesis	268 - 395	Ni or Fe
Sabatier reaction	523 - 673	Ru or Ti

Another promising class of microbes, capable to convert carbon dioxide into valuable industrial products, are the acetogenic bacteria belonging to the *Firmicutes* phylum, a type of strictly anaerobic microorganisms capable to capture carbon dioxide and produce a wide range of valuable products. In particular, the *Clostridium* genus is able to fix the CO_2 towards the Wood-Ljungdahl pathway (Figure 1.9) discovered in 1986 [142,143].

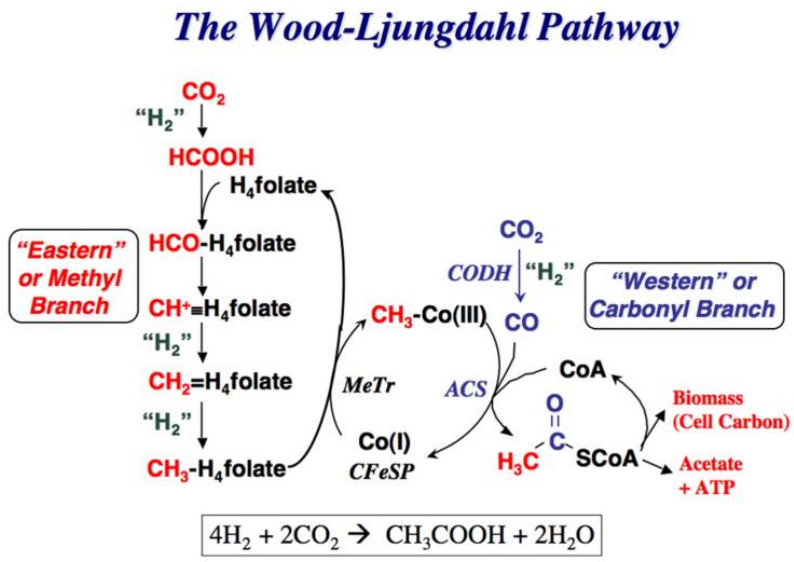

Figure 1.9. The Wood-Ljungdahl Pathway ("H_2" is used to define the requirement of two electrons and two protons in the reaction). Reproduced with permission from Ragsdale *et al.* [144], © 2008 Elsevier B.V. All rights reserved

Although this reaction pathway can be used both in the oxidative and the reductive directions, the CO_2 fixation process follows the reductive way and thus two molecules of CO_2 are reduced to acetyl-CoA and CO or H_2 [144]. Acetyl-CoA is then converted into acetate and adenosine triphosphate (ATP) which, however, is produced also by different mechanisms [145]. Moreover, the acetyl-CoA is not only the precursor for acetate production but, through further reaction steps involving NADH (the protonated form of the nicotinamide adenine dinucleotide) and ATP, is possible to obtain butanol, acetone, ethanol, isobutene, lactate, 2-3 butanediol, and isoprene [146].

Together with the non-photosynthetic bacteria, there are classes of microorganism capable to perform photosynthesis and it can be carried out by several pathways. These include the Calvin-Benson-Bassham (CBB) cycle [147], the reductive tricarboxylic acid (rTCA) cycle [148], the Wood-Ljungdahl pathway, the dicarboxylate/4-hydroxybutyrate (DC/HB) cycle [149], and the 3-hydroxypropionate/4-hydroxybutyrate cycle (HP/HB) [150].

Algae and cyanobacteria are of industrial interest by virtue of their very fast growth and the possibility to be grown on a large scale [138]. Among the products that can be achieved by using cyanobacteria, there are sucrose [151], ethanol or hydrocarbon fuels [152], and 2-3 butanediol [153].

In addition to the natural microorganisms, many attempts have been done to develop genetically modified bacteria with the aim to enhance the CO_2 fixation and thus its conversion yield. In particular, many research groups focused the attention on the modification of *Escherichia coli*, capable to synthesised sugar and other biomass compounds, and *S. Cerevisiae* which is widely employed for the production of ethanol [154]. Moreover, this latter bacterium has the possibility to produce glycine from formate feedstocks [155].
Although these hybrid systems are still in the early stage of the research, they are able to reduce the same amount of CO_2 as the natural bacteria, but exploiting less energy intake.

Differently from the microorganisms, the biochemical conversion can be also carried out by a single enzyme *in vitro*. Generally known as biological catalysts, the enzymes possess the capability to accelerate or favour a wide range of biochemical reactions in biological processes. However, only two classes of enzymes have shown selectivity to the production of chemicals and fuels directly from the carbon dioxide, namely oxidoreductases and lyases [101]. The first include the formate dehydrogenase (FateDH), the carbon monoxide dehydrogenases (CODHs), or nitrogenases. Lu *et al.* [156] reported a CO_2 conversion of 95.6% to formate by using the FateDH immobilised in an alginate gel at 310 K and neutral pH. Besides, inspired by the natural code O_2-sensitive $[Fe_4S_4Ni]$ [157], Shin *et al.* [158] demonstrated the possibility to obtain a CO_2 conversion to CO of 100% by applying -0.57 V *vs* NHE at nearly neutral pH conditions (pH = 6.3). Finally, the main product that can be obtained by the nitrogenases is methane, while minor products are CO and other hydrocarbons, *i.e.*, acetylene or propylene [138].

Yang *et al.* [159] found out that, under optimised conditions, 1 nmol of nitrogenase MoFe protein has the capacity to produce 21 nmol of CH_4 in 20'.

Unlike the oxidoreductases, the lyases stream are a group of enzymes capable to reduce the carbon dioxide by breaking chemical bonds instead of exploiting oxidative processes.

The most promising enzyme system belonging to the lyases group is the carbonic anhydrase (CA) that directly hydrates the CO_2 to HCO_3^- [101,138].

By virtue of its high capability to capture the carbon dioxide, the CA is capable to enhance the solvation of the gaseous CO_2 in water, producing the solvated form $CO_{2\,(aq)}$ followed by the hydrated species HCO_3^- and both species act as substrates for other microorganisms or enzymes to produce valuable chemicals [160]. The natural rate of the CO_2 hydration in water is about $3.58 \cdot 10^{-2}$ s^{-1} at 298 K [161] which, compared to the solvation or de-solvation rate ($k^1 = k^{-1} = 10^{10}$ s^{-1} at 25° [162]), is relatively low. For this reason, the latter process will always be more favoured with respect to the hydration. However, by adding a few amount of carbonic anhydrase, the rate of hydration of $CO_{2\,(aq)}$ to HCO_3^- is increased up to 10^6 s^{-1} [101], so enhancing the overall process of solvation and hydration and bringing a lot of benefits from an industrial point of view. Indeed, this enzyme can be produced with a cost-effective investment and it provides good kinetics, re-usability, and the possibility to work in mild operative conditions [163]. Furthermore, by employing multi-enzyme systems where the enzymes are immobilised on inorganic substrates, methanol with substantial yields was also obtained [164–166].

Therefore, the biochemical conversion carried out by microbial organisms or enzymes represents a natural alternative to the energetically intensive chemical CO_2 transformation, providing a significant effort to the construction of a sustainable carbon dioxide recycle. However, the low adsorption capacity and efficiency, as well as the low energy collecting system, are considered the main drawbacks of this approach.

1.2.2.3 Radiochemical CO_2 Conversion

Nuclear power has long been considered the net-zero CO_2 alternative to basic electricity and heat demand, currently met by fossil fuel contributions. Decades of developments have demonstrated that commercial civil nuclear power plants (NPPs) are the most reliable technology for the production of large-scale, carbon-free electricity [167].

Indeed, this type of energy produces a wide range of inherent, multicomponent radiation fields, otherwise wasted, *i.e.*, neutrons, fast electrons, heat, and γ-rays that can be exploit in further chemical transformations. In this way, it is possible to design binary systems composed of a first nuclear reaction pathway essential to generate an energetic product which will be used to produce added value chemicals or fuels by a second pathway. As an example, the "Generation IV" nuclear reactors [168] have an outlet temperature of 823 – 1123 K that generally is slowly dissipated. Instead, with the aim of recycling such precious source of energy, the heat can be exploited to carry out the endothermic reaction of the methane steam reforming, following a method known as "Adam-Eva" process (Figure 1.10) [169].

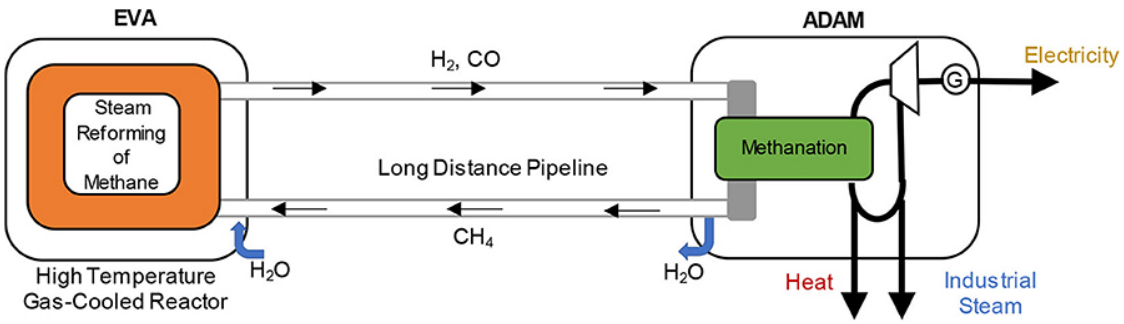

Figure 1.10. Adam-Eva process. Reproduced with permission from Ramirez-Corredores *et al.* [171], © 2020 The Authors. Published by Frontiers, Lausanne, Switzerland

Along with the heat, other wasted products can be exploited. As an example, a techno-economic analysis has been recently done by Schmeda-Lopez *et al.* [170] on the use of γ-rays to simplify the production of propylene through the radiolysis of propane.

Similarly to this procedure that includes the direct irradiation of a target reactant, several years ago it has been widely demonstrated the possibility to obtain different species from the CO_2 radiolysis [171], although the use of the energies coming from the NPPs remains limited.

Preliminary studies on the CO_2 radiolysis phenomena date back to the 1920s [172], with renewed interest after the second world war. During those years, it was discovered that under the presence of a radiation source, carbon monoxide could be obtained as primary product from the direct CO_2 radiolysis [173], together with a little amount of oxygen likely achieved by the formation of the CO_3 species, un unstable form deriving from the reaction between CO_2 and atomic oxygen [174]. Depending on the status of the carbon dioxide (solid or gaseous) or the additives added during the process, the CO_2 radiolysis may be more or less facilitated and also the selectivity can be finely tuned:

- The irradiation of solid CO_2 (dry ice) and water, under harsh temperature conditions (8-10 K) and an inert atmosphere (preferably noble gases), favoured the formation of CO and HOCO radical species [171,175].
- CO and ethane were observed if gaseous CO_2 was irradiated together with propane [176], while the irradiation of a CO_2/CH_4 mixture promoted the formation of a wax-like solid with formula CH_2O, recognised as a possible formaldehyde polymer [177].

More recently, radiations have been also employed to induce the CO_2 reduction mechanism. Several studies have been performed on the irradiation of a CO_2-saturated solution containing Fe or Cu ions [103,178]. The reactions, occurring in aqueous phase, led to the formation of mainly CO and H_2 with scarce yields for hydrocarbons, which were probably due to the low control on the γ-rays. To alleviate this critical issue, integrated systems offer great opportunities to enhance the overall reaction productivity. In these cases, the ionizing radiation is absorbed by a catalyst, *i.e.*, zeolites [179] or a metal oxide [180] that acts as absorber or radiation-induced electrocatalyst capable to transport the energy to the adsorbate.

Although the implementation of the nuclear energy to produce electricity has avoided the emission of about 63 $GtCO_2$ from 1971 to 2018 [181], to date, there are no industrial technologies based on the radiochemical CO_2 conversion. However, the main advantage of using such systems relies on the low or zero carbon emissions to obtain the energy needed for the overall process, even though they become cost-effective if applied on large plants.

1.2.2.4 Photochemical CO_2 Conversion

Inspired by the natural photosynthesis, the photochemical systems represent one of the most promising and sustainable alternatives for CO_2 transformation even though they are still in the early stages of the development. With the aim to activate the CO_2 molecule and break the C=O bonds, the photocatalyst takes advantage of radiations, in analogy with the radiolysis process, that are directly gained from the sun. However, contrarily to the γ-rays coming from the nuclear reactions, the sun-rays that reach the Earth (in particular, in the visible light range) do not have enough energy to directly promote the CO_2 splitting, as the maximum intensity of sunlight lies at about a wavelength of 500 nm (3-1.8 eV *vs* $>10^3$ eV for the γ-rays). For this reason, the studies that are conducted on the photochemical CO_2 reduction employ an auxiliary component capable to absorb the light necessary to start the CO_2 activation steps. One of the key challenges of the photocatalytical route is the low utilisation of solar power and thus great efforts have been done to engineer photocatalysts able to enhance the absorption of solar light, with particular regard for the visible light [182].

Starting from the work of Inoue *et al.* [183] that successfully obtained a photo-electrocatalytic CO_2 reduction to formic acid, formaldehyde, and methanol in a CO_2-saturated solution containing semiconductors powders (*e.g.*, TiO_2, ZnO, SiC) irradiated by a Xe lamp, the development of the photocatalytic processes increased.

Indeed, two main pathways can be chosen to perform the photocatalytic reaction: the homogeneous and the heterogeneous process.

The homogeneous photocatalysis is usually performed using light sensitive transition metal complexes or organometallic compounds [184]. On the one hand, CO_2 can be used as a source of C_1 with reactive molecules such as olefins and epoxides for the occurrence of polymerisation reactions or carboxylation of various substrates like organohalides or alkynes [185,186]. On the other hand, it can be photo-catalytically activated to produce CO, CH_4, and CH_3OH. In both cases, the materials mainly employed for the photocatalytic CO_2 reduction are Ru and Re complexes [185] but also studies with cost-effective catalysts such as Fe^0-tetraphenylporphyrin with substantial production of CO were performed [187]. Besides, Kaneco *et al.* [188] demonstrated the possibility to photo-catalytically obtain HCOOH, employing TiO_2 powders as homogeneous catalyst, continuously dispersed in supercritical CO_2.

Concerning the mechanism, the reaction consists of three different electron-transfer steps (Figure 1.11).

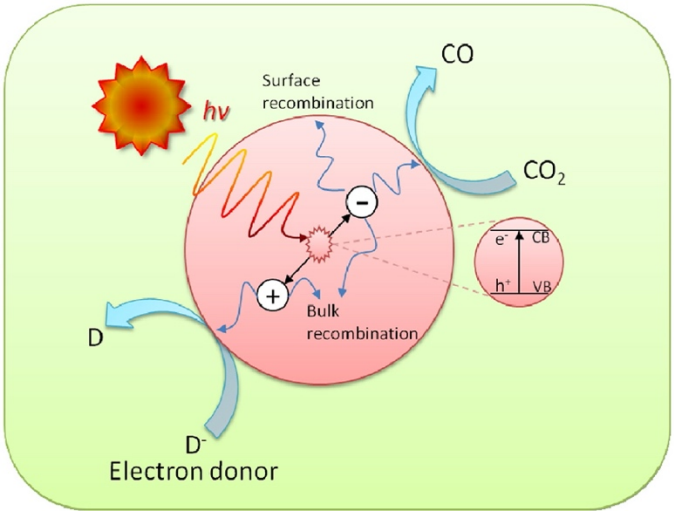

Figure 1.11. Simplified diagram of the photoexcitation and electron transfer process. Reproduced with permission from Li *et al.* [189], © 2014 The Authors. Published by Elsevier B.V.

The photon is first absorbed by the photosensitiser, generating the formation of light-excited electrons and holes [189]. Then photo-generated carriers can undergo different processes, like charge transfer to the catalyst surface, in-band transitions, or electron-hole recombination. Finally, the CO_2 is reduced to CO by the electrons or holes that reach the surface of the catalyst. However, the homogeneous photocatalysis suffers from the difficulties due to the necessity of separating the catalyst from the reaction outcomes, thus making prohibitive its recycle [182,187]. Moreover, future innovations towards the production of energy conversion devices will be difficult to achieve. For these reasons, the use of homogeneous photocatalysts is limited to the laboratory scale.

Nevertheless, such harsh downstream processes can be outpaced with the use of a heterogeneous catalyst.

Similarly to the thermochemical approach, the photo-induced CO_2 reduction occurs at the surface of the catalyst, forming either a solid-gas or a solid-liquid interface. While the thermochemical catalysts exploit high temperature to overcome the energetic barriers, heterogeneous photochemical catalysts take advantage of materials that show abilities to photo-activate the CO_2 like metal oxides or sulphide semiconductors, noble metals, transition metals, or semiconductors [182]. Among them, the visible-light photo-activated catalysts, capable to work in aqueous media, have acquired an increasing interest with the aim of imitating the natural photosynthesis. Indeed, using water has several advantages like the high availability of the reagent, the low-cost, and the higher simplicity of the systems [190].

The principal material employed for this purpose is TiO_2, where the carbon dioxide reacts with H_2O as source of protons. The titanium oxide can be used pure or modified with high-pressure densification [191], introducing oxygen vacancies [192], non-metal doping [193], or dye-sensitisation [104] in order to enhance the absorption of light. CO, CH_4, CH_3OH are the main obtainable products, even though with yields in the order of millimoles [182].

Among the sulphide catalysts, CdS is a visible-light photocatalyst that matches well with the solar spectrum and is capable to produce CH_2O, CH_3OH, $HCOO^-$, CH_3COO^-, and glyoxylate as the main products [194]. Other materials well known to be photochemically active towards the CO_2 reduction are layered, porous, and carbonaceous materials.

Among the other compounds, the most promising materials, already known for their photocatalytic properties in water splitting processes [195] are represented by the Layered Double Hydroxides (LDHs), which are anionic clays with molecular formula $[M(II)_{1-x}M(III)_x(OH)_2]^{x+}(A^{n-}_{x/n})\cdot mH_2O$, coming from the natural hydrotalcite $Mg_6Al_2(OH)_{16}(CO_3)\cdot 4H_2O$ [196–198] (Figure 1.12).

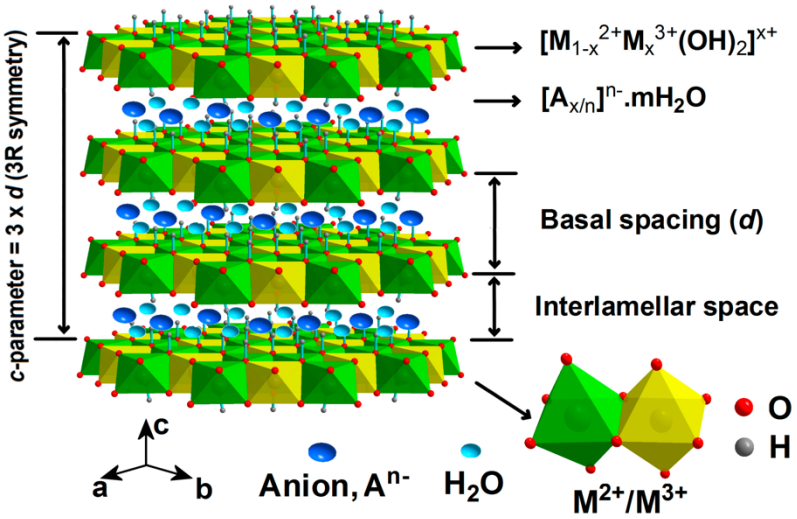

Figure 1.12. Layered Double Hydroxides structure. Reproduced with permission from Li *et al.* [199], © 2017 by the authors. Licensee MDPI, Basel, Switzerland

To date, only few products can be obtained, *i.e.*, CO, CH_4, CH_3OH, but the interest for this class of materials for CO_2 conversion applications keeps increasing [200].

Besides, Metal-Organic Frameworks are a family of porous materials that own an outstanding versatility by virtue of their 3D nature, as they may contain photosensitisers and catalytic centres in a single solid.

To date, depending on the compositions, the main product today achieved is formate [201,202], but emerging studies reported also a considerable formation of methanol [203].

Finally, thanks to their earth abundance and low-cost, carbonaceous materials have been widely employed in the photocatalysis field [204].

However, the carbonaceous material itself has a negligible catalytic activity towards the activation of the CO_2 molecule [99]. For this reason, a modification to improve the performances, thus enhancing the catalytic activities and selectivity of the material, is needed. Doping carbon materials with heteroatoms such as nitrogen, boron, or sulphur, which provide functional groups capable to convert CO_2 represents one of the possible strategies.

Of particular interest is the graphitic C_3N_4 because of its nontoxicity, good stability, and good absorption of light in the visible range. Such carbon nitride widely proved its ability to produce CO, CH_4, C_2H_6, HCOOH, and CH_3OH [201,205].

Overall, the photocatalytic approach allows to work with mild operative conditions, the protons are directly gained from water, and the solar-light is the only source of energy to promote the reduction. Moreover, this approach and the electrochemical route (paragraph 1.2.3.), where the renewable energies may be used for the production of the electricity, represent very promising green alternatives towards sustainable processes, which culminate in the concept of artificial photosynthesis [206–208].

Such a system takes advantage of photo-electrochemical reactions, where a photo-induced reaction is coupled with an electrochemical set-up, and they were primarily employed for

sustainable water splitting processes inside of technologically advanced devices known as photo-electrochemical cells (PECs) [209], shown in Figure 1.13.

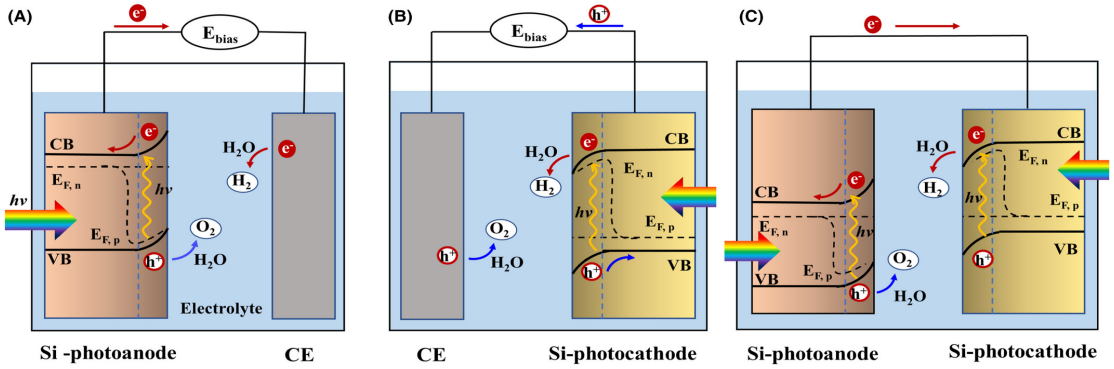

Figure 1.13. Different configurations of photo-electrochemical cells for water splitting (Si-based electrode): (a) photoanode for OER; (b) photocathode for HER; (c) dual photoelectrode for both OER and HER. Reproduced with permission from Cheng *et al.* [210], © 2022 The Authors. Energy Science & Engineering published by Society of Chemical Industry and John Wiley & Sons Ltd

Similarly to the water splitting process, the same cell configurations can be exploited for the reduction of CO_2. In presence of a photoanode, light is first absorbed by it to generate electricity and protons that are then used at the surface of a cathode (dark electrode) for the reduction of CO_2, thus ideally eliminating the need of any external power supply. On the other hand, in the presence of a photocathode, the light is directly absorbed by the catalyst where the CO_2 reduction takes place. Here, an electron is excited from the semiconductor's valence band (VB) to the conduction band (CB), and the minority charge carriers move from the inside of the semiconductor to the surface where they are consumed by the redox process of CO_2 reduction. This process is facilitated by an additional external power supply. As a result, biomimetic PEC, can achieve the thorough imitation of photosynthesis (Figure 1.14).

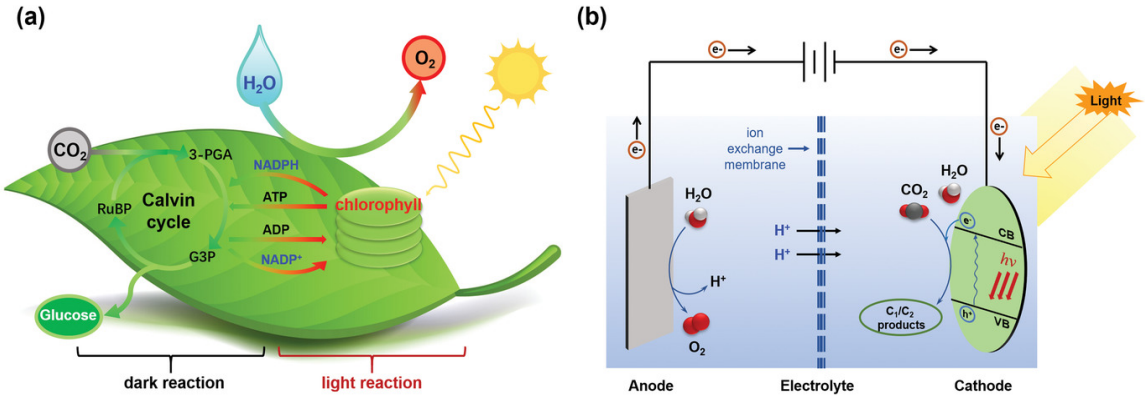

Figure 1.14. Reaction mechanism of (a) natural photosynthesis and (b) photo-electrochemical CO_2 reduction. Reproduced with permission from Xu *et al.* [211], © 2022 The Authors. Advanced Science published by Wiley-VCH GmbH

However, to date using photocatalysis to promote the CO_2 conversion towards chemicals or fuels is not suitable for industrial applications since the conversions are too sluggish to meet the right requirements for commercialisation and the photoreactor designing are complex. The solar energy is considered as an intermittent energy source [212], so resulting in a discontinuous supply of energy.

Other limitations of the photo-activated CO_2 reduction are related to a lack of solar sensitivity, the hydrogen evolution (HER) as side reaction, the fast back electrons transfer processes, and the recombination reactions. Moreover, nowadays the conversion yields are still very low and the product selectivity remains one of the main challenges.

Nevertheless, the photocatalytic route remains one of the greenest routes to close the anthropogenic carbon cycle and the mentioned limitations represent the starting and inspiring point for the continuous research and development of new materials that may be suitable for future industrial realities.

1.2.3 Electrochemical CO_2 Conversion

The electrochemical reduction of CO_2 into C_1, C_2, and, sometimes, C_3 valuable products provides a unique opportunity to develop a green CO_2 recycle, by virtue of its mild operative conditions, its easily customised reaction outcomes, and its great potential towards scale up [213–216]. While in the photo-induced CO_2 reduction the catalyst is directly activated from the photons arising from the sun or a solar-light simulator, the electrochemical CO_2 reduction (CO_2ER) occurs due to the absorption of artificial electric energy. However, even in the latter approach, the renewable energies may play a key role as the electrons required for the activation of the CO_2 molecule can be produced from such intermittent alternative energies (solar, wind-powered, geothermal, etc.). The solar-light, for example, can be used either as a direct energy supply for the *in situ* electricity generation at the photoanode, as mentioned before (paragraph 1.2.2.4.), or as a way to produce and store the electrical energy, exploiting, for instance, the solar panels. While in the former case the electrons are directly generated *in situ*, promoting the concept of the artificial photosynthesis [207], in the latter one, the solar light is first converted into electrical energy and stored as a source of electrons that will be later used as catalyst activators to initiate the reaction.

However, both cases ensure eco-friendly alternatives and set the scene towards the fascinating concept of the solar light-driven chemistry [107,217,218].

Moreover, as for the photocatalysis, one of the most straightforward strategy to promote a green CO_2 reduction alternative is to carry out the CO_2ER in aqueous media [219].
However, the solubility of the carbon dioxide in water is relatively low compared to the solubility in organic solvents such as acetonitrile (35 mM *vs* 280 mM, at 1 atm and 298 K) [220], thus decreasing the availability of reagent if the reaction is conducted in liquid phase.

In addition, another alternative to better dissolve CO_2 is the use of ionic liquids as supporting electrolytes [221,222]. Indeed, they can provide an environmentally benign medium with respect to the organic solvents and contribute to lower the energy supply for the molecule activation. Nevertheless, despite the beneficial effects of different electrolytes, the use of water as a continuous source of protons is always the best choice in view of a sustainable approach, by virtue of its accessibility, environmental compatibility, and cost-efficiency [223]. Indeed, the majority of the investigated reaction set-up usually employ different concentrations of inorganic salts solutions (mainly $KHCO_3$) at neutral or slightly acidic pHs (6.8-7), but the solvent is always water.

However, to seize all the benefits that the electrochemical approach can provide and to make it affordable from an industrial point of view [224], many challenges still need to be solved.

Unlike the thermochemical or radiochemical approaches, electrochemical systems offer the possibility to work at ambient pressure and temperature, but high overpotentials are usually required for the activation of the carbon dioxide molecule [225]. Generally, such reduction reaction suffers from a sluggish kinetics, multi-phase rate limiting steps and poor selectivity, as well as intermediates-sharing or multiple reaction pathways, whose mechanisms are still under debate. Moreover, experimental parameters such as catalyst properties, local pH, chemical nature of the electrolyte solution, and the applied potential dramatically affect the reaction and, consequently, the products distribution [226–228].

As for the photocatalysis, homogeneous and heterogeneous electrocatalysis can be performed, although available commercial systems do not exist today.

Between the methods, the less suitable for industrial applications is represented by the homogeneous electrocatalysis, that, however, has been widely studied by the scientific community for decades [229].

With regard to the conversion of the carbon dioxide, such technology aims to facilitate redox mediation in liquid phase, taking advantage of a homogeneous catalyst dispersed into the electrolytic bath and directly interposed as a redox shuttle between electrode and CO_2. Briefly, an initial electron transfer reaction occurs between the catalyst and the electrode, both dipped in a CO_2-saturated solution. Once the catalyst has been reduced, it interacts with the carbon dioxide present in solution and carries out the relevant redox reduction. The most widely investigated homogeneous electrocatalysts are the metal-organic compounds (Figure 1.15) designed to mimic the biochemical CO_2 conversion and capable to operate close to the thermodynamic potential of the reaction, if properly tuned with specific ligands [230,231].

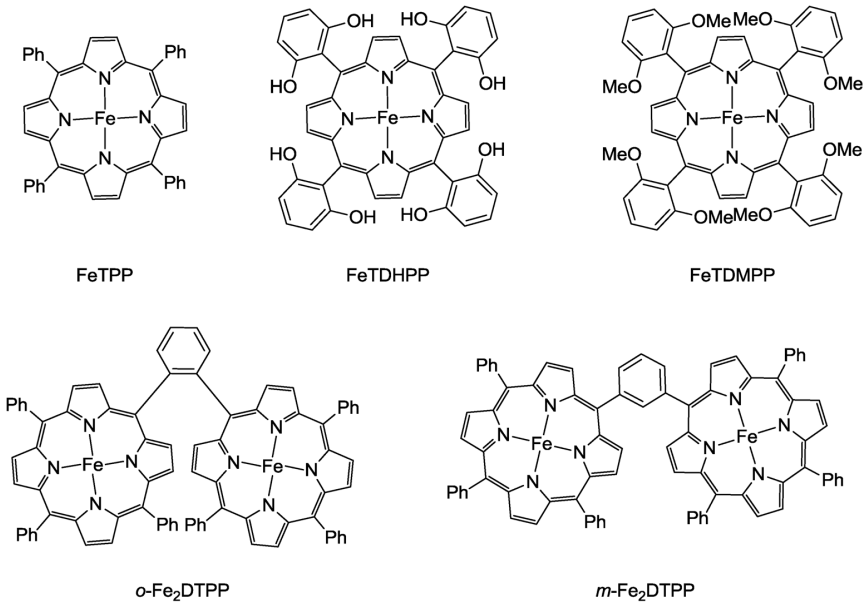

Figure 1.15. Examples of Fe^0 complex electrocatalysts. Reproduced with permission from Feng *et al.* [232], © 2017 by the authors. Licensee MDPI, Basel, Switzerland

Moreover, by virtue of their well-defined and controlled molecular structure, the optimisation of the selectivity is much easier in homogeneous electrocatalysis. However, this sub-category hides several drawbacks that significantly reduce its applicability in industry, exhibiting the most important challenging issues in the recovery of the catalyst and the separation of the products [229], similarly to the homogeneous photoreduction, previously discussed.

Despite the wide range of studies concerning the homogeneous CO_2 electroreduction [229,233,234], the most promising electrocatalytic route relies on the heterogeneous approach and a more in-depth discussion will be provided. As the name suggests, this second sub-category of electrocatalysis concerns reduction reactions that occur at the electrode-electrolyte interface [235].

Unlike the homogeneously catalysed reaction, the catalyst is directly attached on the surface of the electrode, forming a single system acting both as acceptor and donor of electrons, that can be exploited for reactions in both liquid and gaseous phase. Moreover, even the bulk electrode itself can be use as direct catalyst, without the need of further functionalisation (Figure 1.16).

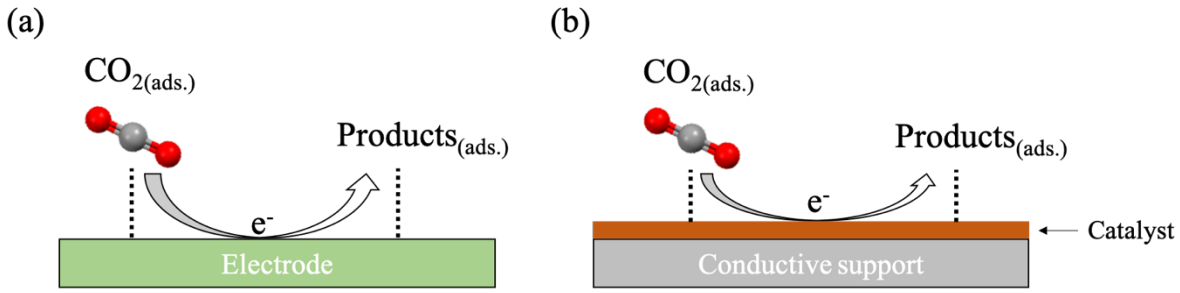

Figure 1.16. Mechanism of heterogeneous electrochemical CO_2 reduction: (a) bulk electrode and (b) active phase loaded on a conductive support

Theoretically, the first step of the reaction is the chemical adsorption of the carbon dioxide at the surface of the electrocatalyst followed by the formation of the intermediates through the cleavage of the C=O bond, carried out by electrons and protons. Once the intermediate is rearranged into the target product, it is desorbed from the electrode surface and dispersed into the bulk electrolyte [236]. In a typical H-cell for the CO_2 electroreduction, cathode and anode are placed in two different chambers separated with an ions-conducting membrane with the aim of avoiding further oxidation of the reduced products of reaction (Figure 1.17).

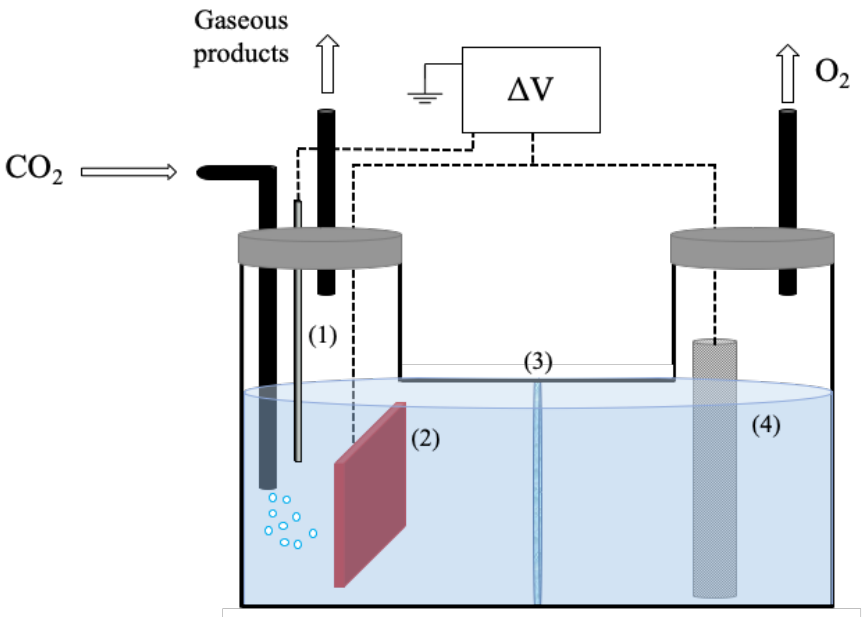

Figure 1.17. H-type cell configuration (liquid phase). (1) Reference electrode, (2) electrocatalyst; (3) ions-conducting membrane, and (4) counter electrode

Indeed, at the anode side, water is oxidised to molecular oxygen and protons are produced, while CO_2 is reduced to different carbonaceous species at the cathode side [107]. The choice of the membrane depends essentially on the pH of the electrolyte, but the mainly employed membranes are made of Nafion as they favour H^+ diffusion from the anode to the cathode side. The majority of the well-known applications of electrocatalysis like fuel cells, chlor-alkali electrolysers and water splitting process (hydrogen evolution reaction – HER) are examples of heterogeneous electrocatalysis.

The rate of all these reactions, and therefore also of the CO_2ER, depends on the electrochemical potential gradient at the electrode-electrolyte interface [237], on the activity of the electrocatalyst and the type of electrolyte. Since water has been recognised as the most useful source of protons to be implemented inside the electrocatalytic cells in view of sustainable and cost-effective systems, the type of electrocatalysts naturally becomes the key challenge.

Indeed, despite all the benefits that water can provide as source of protons, the rate of the CO_2 electroreduction reaction is significantly decreased by the low carbon dioxide concentration in aqueous solution, and suffers from diffusion limitations [220].

Moreover, by performing the CO_2ER in aqueous media, such reaction is inevitably accompanied by the hydrogen evolution as it occurs at similar potentials.

For the sake of clarity, the standard redox potentials for the hydrogen evolution reaction in comparison with the former two-electron transfer products, that can be obtained from the CO_2ER, are reported below [238]:

$$2H^+ + 2e^- \longrightarrow H_2 \qquad E^0 = -0.41\ V \tag{12}$$

$$CO_2 + 2H^+ + 2e^- \longrightarrow HCOOH \qquad E^0 = -0.61\ V \tag{13}$$

$$CO_2 + 2H^+ + 2e^- \longrightarrow CO + H_2O \qquad E^0 = -0.53\ V \tag{14}$$

Moreover, that undesired reaction is more kinetically favoured than the multi-electron transfer reactions of the CO_2 reduction [239], thus greatly affecting the proton availability and, consequently, the pH at the electrode-electrolyte interface. Therefore, much efforts have been put towards the study of novel electroactive materials with optimal binding energies capable of enhancing the CO_2 conversion, so improving the control over the selectivity and impeding the HER in aqueous media. Moreover, the understanding of the reaction mechanisms that affect the electrocatalytic performances, alongside the changes in the catalyst structure, is of particular interest.

The main products that can be obtained from the electrochemical CO_2 reduction, including the electrons required for their formation, are schematically shown below (Figure 1.18):

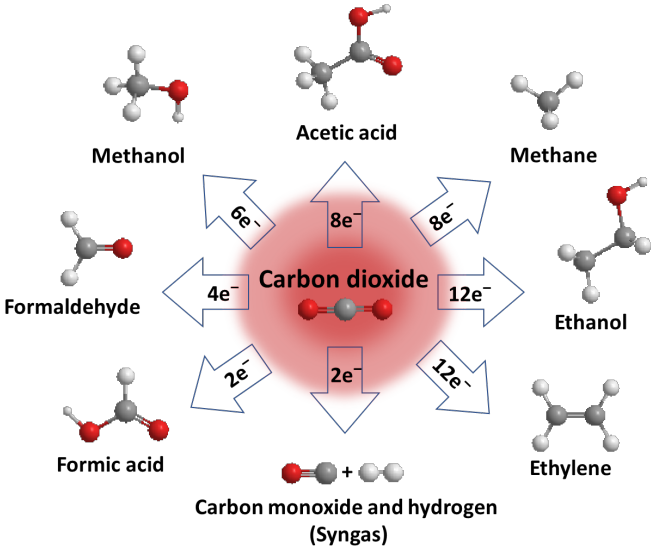

Figure 1.18. CO_2 electroreduction products of particular interest

In addition, CO_2 can be converted into other products such as n-propanol, allyl alcohol, acetaldehyde, propionaldehyde, ethylene glycol, glycolaldehyde, hydroxyacetone, and glyoxal [240,241].

In the CO_2ER scenario, there are some important indicators that need to be considered in order to classify the performances of the overall reaction set-up and thus its industrial applicability [242]. Since the process costs are not yet scheduled into standard protocols, the most common provided parameters are the Faradaic Efficiency (FE) and the Current Density (J).

Another important value that aims to give an indication of the energy required to overcome the energetic barrier for the activation of the CO_2 molecule is the overpotential (η). Given as an absolute value, this term symbolises the difference between the equilibrium potential for the relevant CO_2ER half reaction and the applied potential at which a target product is produced. The required overpotential is often an indicator of the efficacy of a catalyst to promote the reaction: the less overpotential is needed, the more active is the electrocatalyst.

The Faradaic Efficiency represents the selectivity of the overall reaction towards a given product, in terms of percentage of electrons that are transferred to the products. High selectivity, and thus high FE, for the target product is most advantageous to avoid losing energy in the production of unwanted compounds, and also to simplify products separation.

It can be expressed as a ratio between the theoretical charge needed for the production of a defined amount of product and the overall charge passed during the reaction, following the equation below:

$$FE\ (\%) = \frac{n \cdot z \cdot F}{Q} \cdot 100 \qquad (15)$$

where n are the number of moles obtained for a target product, z is the number of electrons exchanged during the reaction to get the product, F is the Faraday's constant (F = 96,485 C mol^{-1}), and Q represents the overall charge passed during the reaction.

The last important performance indicator is the current density (J). Commonly used in heterogeneous electrocatalysis to define the average activity of the catalyst, since active sites with different structures often coexist, it defines the rate of the electrochemical reaction [235]. Contrarily to the homogeneous electrocatalysis where the turnover frequency is mostly used to indicate the reaction rate [243], the current density is calculated by dividing the current developed as a result of a given cell potential by the geometrical or the electrochemical surface area of the electrode. Since the latter value is not always easy to determine, the geometrical area is the most used as it also gives an indirect indication of the size of the electrochemical cell, and thus of the overall necessary investment.

Hence, the following discussion will be focused on the evolution of the materials employed as heterogeneous electrocatalysts for the CO_2 conversion performed in aqueous media or in electrolyte-less systems that exploit water as source of protons at the anode side. Henceforth, the heterogeneous CO_2 electroreduction will be referred as the CO_2 electroreduction.

1.2.3.1 Traditional Electrocatalysts

The first studies on the electrochemical CO_2 reduction date back to the 1950s, when Teeter *et al.* [244] reported the formation of formic acid using a Hg-based cathode. However, the most relevant studies that include a total quantification of both gaseous and liquid products were performed by Hori and coworkers [245–248] and were mainly based on monometal bulk catalysts, especially the transition ones.

Starting from these researches, the monometallic electrodes were divided into categories, depending on the different binding affinity [228,249].

Based on the primary CO_2 reduction product, bulk metals electrodes can be divided in (i) CO, (ii) HCOOH, (iii) H_2 selective materials, and (iv) beyond CO.

Such classification was established after an exhaustive study carried out by Hori *et al.* [250] in 2008, where he showed different performances of each bulk metal electrode achieved during galvanostatic CO_2 electroreduction.

In those experiments, the current density was kept constant at 5.0 mA cm^{-2}, along with the pH that was fixed at 6.8, by using a 0.1 M $KHCO_3$ electrolyte, and stabilised under operating conditions.

The metal electrodes capable to produce CO includes noble metals like Au, Ag, Pt, and Pd [251], but also non-noble metals like Cu, Zn, Ga, and Ni [241]. Among them, Au and Ag provide the highest catalytic activity with a maximum FE of 87% for Au.

However, due to their low abundance on earth and high cost, up to now, they are not considered for large scale industrial applications [252]. Hence, since Zn^0 has demonstrated similar performances, it represents the most promising metal electrode for the selective production of CO.

The second class of bulk metal electrodes is represented by Pb, Hg, Tl, In, Sn, Cd, and Bi which produce HCOOH as the primary product. A noticeable FE in formic acid production was achieved with Pb and Hg (up to 99.5%) [241]. Differently from the CO, the production of formate/formic acid (depending on the operating pH), involves the use of protons and thus it follows a different pathway. Despite the mechanism is still under debate, the most accredited route includes the formation of the *OCHO intermediate [236]. To date, Sn and Bi have attracted a lot of interest for the large-scale use because of their relevant catalytic activity, the environmentally friendly nature, and the economical convenience [253].

The third class of monometal electrodes includes materials with very low activity for the CO_2 electroreduction but with substantial efficiency for the hydrogen evolution reaction. Indeed, bulk electrodes like Pt, Ni, Fe, and Ti displayed Faradaic efficiencies that reach up to 90%.

Finally, concerning the last group, Cu has been overall recognised as the gold standard among pure metal catalysts [228,245,254] due to its unique ability to catalyse CO_2ER beyond CO, *i.e.*, towards a number of hydrocarbons, aldehydes and alcohols requiring more than two electron transfers with substantial FE.

In particular, the main advantage of Cu electrodes relies on their capability to stabilise both the chemisorbed $CO_2^{\cdot-}$ radical anions and CO species, which are the key intermediates in the initial phase of the catalytic CO_2 conversion and in the subsequent process of hydrocarbons and alcohols formation, respectively.

In its bulk form, it was the only material capable to produce methane, ethylene, ethanol, propanol along with low amounts of carbon monoxide and formic acid [250]. For this reason, starting from those pioneering studies, nowadays copper is considered as the most promising material to be used in the electrochemical CO_2 reduction field.

To summarise, a schematic diagram (Figure 1.19) of the three classes of bulk electrodes that promote the reduction of carbon dioxide is reported from Zhang *et al.* [255], including the reaction mechanisms that led to the formation of the desired product.

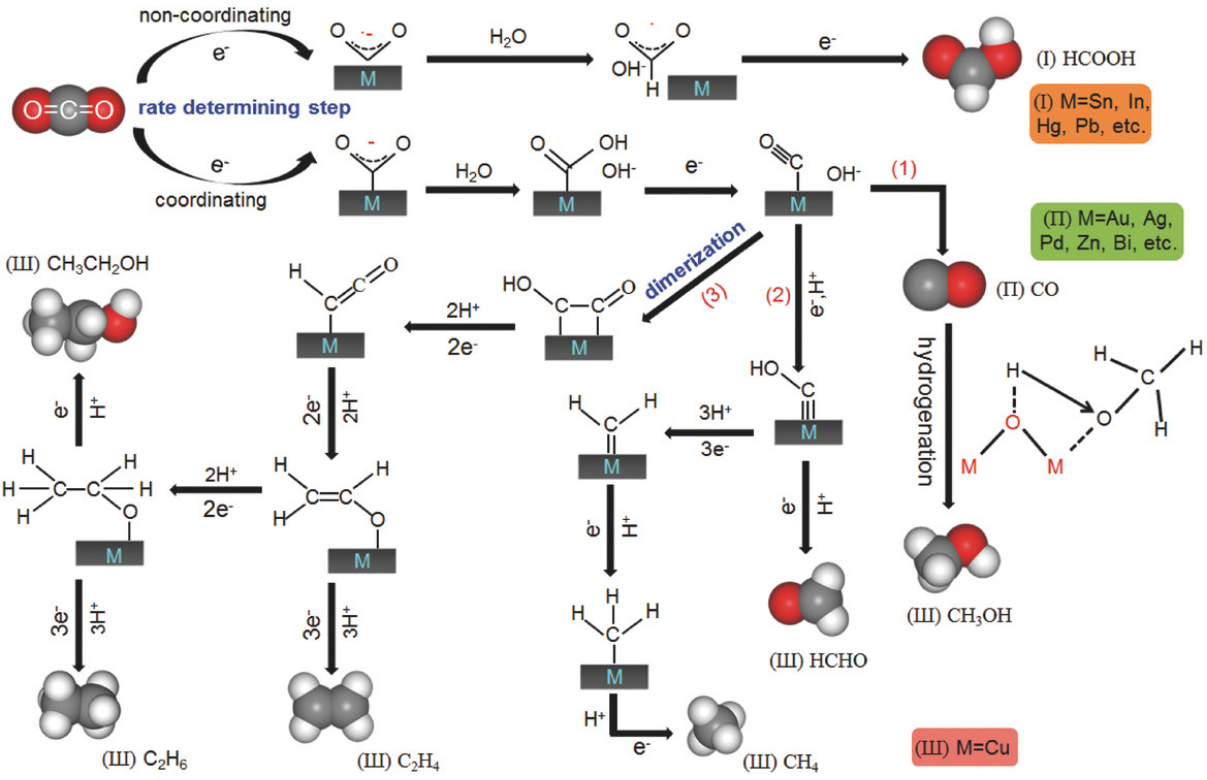

Figure 1.19. Possible CO_2 reduction mechanisms on different bulk metal electrodes.
Reproduced with permission from Zhang *et al.* [255], © 2017 The Authors. Published by WILEY-VCH Verlag GmbH & Co. KGaA, Weinheim

Along with the polycrystalline bulk metals, also single-crystal metals have been widely studied, finding out that a specific crystalline lattice rather than others can considerably enhance the overall production or tune the selectivity using the same metal electrode [256–259].

Moreover, it is worth mentioning that among the traditional broadly investigated electrocatalysts, the properties of the metal oxides materials are already well-known in the heterogeneous catalysis field and these compounds have been also widely used in CO_2ER.

On the one hand, their utilisation in the water gas shift reaction [260], the synthesis of methanol [261], and CO oxidation processes [262] represents one of the most common applications. Moreover, many metal oxides like TiO_2 or ZnO are widely employed as semiconductors for the photochemical CO_2 conversion (see paragraph 1.2.2.4.). On the other hand, the use of metal oxides as electrocatalysts for the activation of the CO_2 molecule have been proved to bring significant improvement in the overall performance, when compared with metal electrodes [263–266]. As an example, Deng *et al.* [267] showed that Bi-O systems can lower the energy barriers for the intermediate formation in the HCOOH production pathway, demonstrating the importance of oxygen-species in switching the rate-determining step. Recently, Gao *et al.* [268] verified how the presence of the metal-oxide interface during the CO_2ER can considerably enhance the gas adsorption at the surface of the catalyst. However, studies achieved by means of advanced *in situ* characterisation techniques have reported the instability of the metal oxides species under the CO_2 electroreduction conditions [269,270]. Such instability not only affects the oxidation state of the metal active phase but also its structure. Indeed, the thin oxide layers over the bulk electrode generally promote the formation of nanostructured interfaces, that will be discussed in the following paragraph. For these reasons, the origin of the higher catalytic activity of the metal oxides species compared to the bulk metal electrodes may result from various aspects and thus it is still under debate [271].

For this reason, great efforts are being carried out on the design of the electrocatalysts in order to achieve competitive performances and higher energetic efficiencies. To this purpose, a new generation of electrocatalysts is taking hold for the CO_2ER with advanced structures and new reactive sites that own attractive qualities over bare bulk electrodes.

Different materials in terms of size of the catalyst particles, oxidation state, porous hierarchical structure, doping, alloying, and defect engineering have been developed as novel selective and active electrocatalysts with the aim of outpacing the limitations of the CO_2ER in view of feasible and greener processes for future CO_2 electrolysers. Among them, nanostructured materials, nano- or micro-porous films, oxide-derived metals, or carbon-based materials are some examples of the more recent advanced systems that, to date, represent the leading electrocatalysts for the electrochemical CO_2 reduction in aqueous media.

1.2.3.2 New Generation of Electrocatalysts

The major parameters that significantly impact the final outcome of the CO_2ER are the electronic and geometrical structure and composition of the materials [235].

In particular, the required overpotential and the selectivity are mainly affected by the changes on the electronic structure, while the geometric structure is related to the catalytic sites density and thus influences the current density recorded during the reaction.

The size and morphology of the active catalyst play a very important role in the overall CO_2ER efficiency. In particular, it has been widely demonstrated that reducing the dimensions from macro- to nano-sized materials enhances the number of superficial active sites and thus the available electrochemical surface area of the catalyst [272]. To this aim, various methods have been developed including bottom up or top down approaches [273] and the principal characteristics that discriminate a nanostructured or nano-electrocatalyst from a bulk one are the increase of the catalyst surface per mass and the introduction of many edge/low-coordinated sites [238,274].

Notably, several studies have been carried out on nano-sized metal catalysts, including metal nanoparticles (metal NPs) [275–278], nanocubes [279,280], or nanostructured catalysts [107,189].

Creating nanostructures over the surface of a bulk electrode can substantially outpace the reaction performances of its bare polycrystalline counterpart. As an example, Wenlei Zhu *et al.* [281], Liu *et al.* [282], and Wenjin Zhu *et al.* [283] demonstrated that Au nanowires, Ag triangular nanoplates, and ultrathin Pd nanosheets, respectively, increased more the surface ratio of their edge sites than their spherical nanoparticles counterpart, so balancing the *COOH/*CO adsorption ratio with beneficial effect on the overall reaction performance.

Besides, an early study carried out by Li *et al.* [284] reported outstanding efficiency and selectivity towards the production of formate using a 3D hierarchical structure composed of mesoporous SnO_2 nanosheets with an average pore diameter of 4-5 nm. The active phase, supported on carbon cloth, exhibits an unprecedented current density of 50 mA cm^{-2} with a total FE of about 87%. Despite the reaction performance was comparable to the one achieved using the bulk Sn electrode, whose FE for formate was 88% [250], the possibility to obtain similar results using less loaded catalyst (0.34 mg cm^{-2}) and a flexible and sustainable support was demonstrated, thus avoiding the use of heavy bulk electrode.

Moreover, inside the group of nanostructured and porous materials, catalysts as Layered Double Hydroxides (Figure 1.12) or Metal-Organic frameworks, even if different from each other but usually employed for the preparation of photocatalytic reduction devices, are gaining increasing interest as they are suitable also for electroreduction applications. Such materials will be better described in the following chapters.

Among all the transition metals, the majority of the studies performed on the different morphology of the catalysts has been achieved by using Cu, which was found to be facet/shape-dependent [285–287]. Although the description of the reaction mechanism at the basis of the different undertaken pathways is still challenging, several researchers have demonstrated the possibility to tune the reaction selectivity by manipulating the copper's morphology and size.

A comparative study among electropolished, Cu NPs covered and sputtered copper surfaces was performed by Tang *et al.* [288].

The reactions were carried out in aqueous media, using $KClO_4$ as inorganic salt, applying a potential of -1.1 V *vs* reversible hydrogen electrode (RHE) and they clearly showed the outstanding performances of the nanoparticles covered surface, with respect to the others, which displayed the highest C_2H_4/CH_4 ratio highest. Such evidence clearly stands out the importance of the morphology of the employed copper, beyond the reaction conditions. Moreover, stressing on this feature, Suen *et al.* [289] have recently reported the tremendous shift of the reaction selectivity from C_2 to C_1 products by changing the morphology of copper from cube-like and hexarhombic docadehedron-like Cu single-crystals to octahedron-like Cu nano single-crystals.

However, several changes may sometimes cause undesired effects on the product selectivity towards hydrocarbons.

Reske *et al.* [290] was one of the first to evaluate the effect of different Cu particles sizes (2-15 nm), with respect to the bulk electrode. He demonstrated that particles with dimension below 5 nm exhibited a dramatic decrease in the catalytic activity towards hydrocarbons, so favouring the production of H_2 and CO. Moreover, although a higher selectivity for hydrocarbons was observed for the 5-15 nm particles, the FE in CH_4 and C_2H_4 obtained for Cu NPs of 5-15 nm dropped in respect to their bulk counterpart (10-15% *vs* almost 60% for CH_4, and 0-15% *vs* 20% for C_2H_4). Hence, if the purpose is the hydrocarbons production, the proper Cu nanoparticles dimension must be considered. Indeed, due to the well-known changes in the material's properties at the nano-scale dimension [291], other transition metals displayed size effects along with copper.

On the one hand, by decreasing the Pb nanoparticles size (2.4 – 3.7 nm) an increase in CO production was observed [275], while, on the other hand, a maximum CO FE was obtained employing middle size Au nanoparticles (8 nm) [292].

Besides, an alternative method to enhance the density of the active sites consists in an *in situ* reduction of the catalyst, starting from its oxidised form, where the final catalyst is referred as oxide-derived electrocatalyst. Such phenomenon is carried out through oxidation and reduction processes that lead to the formation of defects and roughened surfaces. As an example, in the case of Cu, it has been demonstrated that using oxide-derived copper species enhances the selectivity towards C_2 products [227].

Along with the morphology and size of the catalyst, another important parameter that contributes to selectively change the reaction outcome is the oxidation state of the active phase. Although higher oxidation states are unstable under the reductive reaction conditions, several experimental evidences have confirmed the increase in catalytic activity by modulating the oxidative state of a material. As an example, the addition of S to a Sn catalyst allowed to reach a current density of 55 mA cm^{-2} and a total FE for HCOOH of 93%.

In this case, the electronic properties of Sn significantly change due to the fact that the oxidation state was between 0 and +2, differing from the metal Sn [293].

Concerning the catalytic activity of copper, there are still many open questions regarding the stability of its oxidised forms during the CO_2ER and the possible role that they may have in the reaction pathways. However, several experimental evidences have highlighted the fundamental role of Cu^+ species towards the production of C_2 product [294].

Apart from the bulk metal electrodes that are generally employed as such, the new generations of catalysts, especially nanostructured or porous materials and metal-based nanoparticles need to be loaded on a conductive support.

Such systems can be considered as composite materials made either of different forms of the same materials (*e.g.*, bulk electrodes covered by a metal nanostructured layer) or of different materials (*e.g.*, metal NPs supported on carbon fibers). Since the electrochemical CO_2ER has been usually evaluated employing a traditional H-type cell [295] thanks to its simple configuration, the geometry and the nature of the conductive support, along with the nature of the active phase, are important features to be considered. The main problem that occurs when the reaction is performed in a H-type cell is the mass transfer limitation due to the low CO_2 solubility which directly limits the current density usually below 30 mA cm^{-2} [296]. The catalyst active phase can be supported either on planar or non-planar electrodes such as porous/3D materials. However, the use of planar electrodes contributes to lower the current density of the reaction cause of the slow CO_2 diffusion towards the surface of the conductive material [297,298].

To alleviate these limitations, porous/3D porous materials have been preferentially employed as they can act both as active phase support and as a material interface between the gaseous reactant and the catalyst layer. The most common materials are metal foams [299,300] or carbonaceous gas diffusion layers such as carbon fibers or carbon nanotubes [301,302].

Porous/3D electrodes are greatly desirable in energy conversion applications, since they not only possess large surface areas to increase the number of active sites and provide high degree of dispersion of the catalyst, but also decrease the contact resistance and, hence, facilitate electron transfer. Therefore, interconnecting macro or micro porous structures with nanostructured catalysts likely brings an optimal set-up to overcome the current density challenge and reduce the energy barriers for the CO_2 activation (overpotential-η).

Such systems, designed to interact with a gaseous phase, can be also employed in CO_2ER liquid phase as their hydrophobic nature might trap the CO_2 near the catalyst layer to locally form a solid–liquid–gas interfaces, which could improve the activity and selectivity for CO_2 reduction [295].

As for the photocatalytic applications, the carbonaceous materials, especially large area gas diffusion layers, are gaining an increasing interest also for electrochemical applications. Indeed, thanks to their large availability and eco-friendly nature, they embody the most sustainable alternatives for the preparation of cost-effective electrodes with promising performances towards the CO_2ER and easy scalability.

As an example, one of the latest devices which involves the use of carbonaceous gas diffusion layers and allows to further improve the reaction efficiency is the Gas Diffusion Electrode configuration (GDE) [303]. It facilitates the diffusion of the gaseous reactant towards the catalytic layers as the electrode is located between a continuous gaseous flow (the electrolyte-less compartment) and the supporting electrolyte connected to the anode side.

1.2.3.3 Benchmark Electrocatalysts

After entering the 21st century, the number of the investigated catalysts and the related research about the CO_2ER has exponentially increased [236]. Nowadays, the principally investigated catalysts are nanostructured/porous materials, composed of monometal or metal alloys, at different oxidation states depending on the desired product. The catalytic active phase is generally loaded on 3D conductive electrodes, mainly carbonaceous, that offer the possibility to be employed for CO_2ER both in liquid and gaseous phase.

Although the applicability of these systems is still under the standard levels for industrial applications that require very high current densities (200-300 mA cm^{-2}) alongside a selectivity of 90% and a CO_2 conversion of 50% [304], big efforts have been done from the scientific point of view, as stated in the previous discussions.

This paragraph aims to give a brief overview of the leader catalysts that have displayed outstanding performances in aqueous media for the CO_2 conversion towards the principal desired product. Wu *et al.* [305] reported an exhaustive list of the main electrocatalysts, which illustrates the recent strategies to enhance the FE with respect to the target products.

Concerning the 2-electron transfer products, in 2018, Liu *et al.* [306] carried out a CO_2ER with the aim to improve the conversion towards the production of CO by means of 5-fold twinned Ag nanowires supported on a glassy carbon electrode (GCE), with diameters less than (i) 25 nm (D-25) and (ii) 100 nm (D-100). As a result, the D-25 Ag NWs displayed the highest conversion to CO, up to 99.3%, and a current density of 2.2 mA cm^{-2} upon application of -0.956 V *vs* RHE in 0.1M $KHCO_3$.

Besides, an outstanding conversion from CO_2 to formate was reported by Zhang *et al.* [307], who was able to obtain a FE for HCOOH of ~ 91% at -0.9 V *vs* RHE using a pipet-like N-doped carbon nanotubes semi-filled with Bi nanorods (Bi-NRs@NCNTs) supported on a GCE. The reaction was performed in a H-type cell, employing 0.1 M $KHCO_3$ as supporting electrolyte, at ambient conditions.

Concerning the multi-electron transfer products, the most common compounds reported in literature are CH_3OH, CH_4, C_2H_4, CH_3CH_2OH, CH_3COOH, and $CH_3CH_2CH_2OH$ (n-propanol). Except for methane, all the catalysts employed to carry out the reaction include the presence of copper. Indeed, the highest FE in CH_4 was obtained with both Zn [308] and Cu [309] based electrocatalysts. In particular, by employing a catalyst based on Cu-based conductive metal-organic framework supported on carbonaceous GDL or on Zn atoms supported on microporous N-doped carbon (SA-Zn/MNC), Faradaic efficiencies of 80% and 85% were achieved, respectively.

Besides, the highest FEs for the three alcoholic species were obtained by using three Cu-based catalysts of different morphologies, according with the previously mentioned morphology-dependent selectivity towards C_2 or C_1 products. In particular, CH_3OH was gained with a copper selenide nanocatalysts supported over a 1 cm^2-sized carbon paper ($Cu_{1.63}Se(1/3)$) , with a FE of 77.6% [310], while a carbon-supported Cu catalyst - Cu_n (n = 3 and 4) cluster was used to obtain CH_3CH_2OH with a FE of 91% [311]. On the other hand, n-propanol, that requires both stabilisation of $*C_2$ intermediates and subsequent C_1–C_2 coupling, was preferentially achieved on a hexagonal double sulfur vacancy-rich CuS catalyst (CuS_x – DSV) with a FE of 15.1% [312]. Differently, as to the production of acetate until 2017, the highest Faradaic Efficiency (~ 72 %) was reported by Marepally *et al.* [313] by employing Cu^0 NPs on carbon nanotubes (Cu^0NPs@CNTs), upon application of -1.35 V *vs* RHE. However, such catalytic performance was outpaced during the studies carried out in this thesis and the obtained results will be discussed in the following chapters.

Finally, a comparison between the Faradaic Efficiencies of the most relevant reduced products obtained with the benchmark catalysts described above and the results achieved in the Hori's pioneering studies on bulk metal electrodes is reported in Table 1.4.

Table 1.4. Faradaic Efficiencies and current densities (J_{tot}) of the main CO_2 reduction products obtained with benchmark catalysts and the Hori's studies on bulk electrodes

				Pioneering Hori's studies [241]		
Product	*Benchmark catalyst*	*J_{tot} (mA cm^{-2})*	*FE (%)*	*Bulk catalyst*	*J_{tot} (mA cm^{-2})*	*FE (%)*
CO	5-fold twinned Ag NWs [306]	~2.2	99.3	Au	5.0	87.1
HCOOH	Bi-NRs@NCNTs [307]	6.0	~ 91	Hg	0.5	99.5
CH_4	SA-Zn/MNC [308]	31.8	85	Cu	5.0	33.3
CH_3OH	$Cu_{1.63}Se(1/3)$ [310]	41.4	77.6	nd	nd	nd
CH_3CH_2OH	Cu_n (n= 3 and 4) cluster [311]	~ 2.0	91	Cu	5.0	5.7
n-propanol	CuS_X – DSV [312]	9.9	15.4	Cu	5.0	3.0
CH_3COOH	Cu^0 NPs@CNTs [313]	~0.9	~71	nd	nd	nd

1.3 References

(1) Köppen, W. P.; Wegener, A. *Die Klimate Der Geologischen Vorzeit*; **1924**, 1–255.

(2) Milankovitch, M. *Kanon Der Erdbestrahlungen Und Seine Anwendung Auf Das Eiszeitenproblem*; **1941**; Vol. 133, 1–663.

(3) Shakun, J. D.; Clark, P. U.; He, F.; Marcott, S. A.; Mix, A. C.; Liu, Z.; Otto-Bliesner, B.; Schmittner, A.; Bard, E. Global Warming Preceded by Increasing Carbon Dioxide Concentrations during the Last Deglaciation. *Nature* **2012**, *484* (7392), 49–54.

(4) Marcott, S. A.; Shakun, J. D.; Clark, P. U.; Mix, A. C. A Reconstruction of Regional and Global Temperature for the Past 11,300 Years. *Science (80).* **2013**, *339* (6124), 1198–1201.

(5) EPA's Inventory of U.S. Greenhouse Gas Emissions and Sinks. *Overview of Greenhouse Gases*. Agency EPA - United States Environmental Protection. https://www.epa.gov/ghgemissions/overview-greenhouse-gases.

(6) Karl, T. R.; Trenberth, K. E. Modern Global Climate Change. *Science (80).* **2003**, *302* (5651), 1719–1723.

(7) Simmonds, P. G.; Rigby, M.; Manning, A. J.; Park, S.; Stanley, K. M.; McCulloch, A.; Henne, S.; Graziosi, F.; Maione, M.; Arduini, J.; Reimann, S.; Vollmer, M. K.; Mühle, J.; O'Doherty, S.; Young, D.; Krummel, P. B.; Fraser, P. J.; Weiss, R. F.; Salameh, P. K.; Harth, C. M.; Park, M.-K.; Park, H.; Arnold, T.; Rennick, C.; Steele, L. P.; Mitrevski, B.; Wang, R. H. J.; Prinn, R. G. The Increasing Atmospheric Burden of the Greenhouse Gas Sulfur Hexafluoride (SF6). *Atmos. Chem. Phys.* **2020**, *20* (12), 7271–7290.

(8) Stocker, T. F.; Qin, D.; Plattner, G.-K.; Tignor, M.; Allen, S. K.; Boschung, J.; Nauels, A.; Xia, Y.; Bex, V.; Midgley, P. M. *IPCC, 2013: Summary for Policymakers. In: Climate Change 2013: The Physical Science Basis. Contribution of Working Group I to the Fifth Assessment Report of the Intergovernmental Panel on Climate Change*; Cambridge, United Kingdom and New York, NY, USA, **2013**, 3–203.

(9) Keramidas, K.; Diaz Vazquez, A.; Weitzel, M.; Vandyck, T.; Tamba, M.; Tchung-Ming, S.; Soria Ramirez, A.; Krause, J.; Van Dingenen, R.; Chai, Q.; others. Global Energy and Climate Outlook 2019: Electrification for the Low-Carbon Transition. Publications Office of the European Union, **2020**, 1–148.

(10) *https://www.noaa.gov/*.

(11) Pachauri, R. K.; Meyer, L. A.; Core Writing Team. *IPCC, 2014: Climate Change 2014: Synthesis Report. Contribution of Working Groups I, II and III to the Fifth Assessment Report of the Intergovernmental Panel on Climate Change*; Geneva, Switzerland, **2014**, 1–169.

(12) Friedlingstein, P.; Jones, M. W.; O'Sullivan, M.; Andrew, R. M.; Bakker, D. C. E.; Hauck, J.; Le Quéré, C.; Peters, G. P.; Peters, W.; Pongratz, J.; Sitch, S.; Canadell, J. G.; Ciais, P.; Jackson, R. B.; Alin, S. R.; Anthoni, P.; Bates, N. R.; Becker, M.; Bellouin, N.; Bopp, L.; Chau, T. T. T.; Chevallier, F.; Chini, L. P.; Cronin, M.; Currie, K. I.; Decharme, B.; Djeutchouang, L. M.; Dou, X.; Evans, W.; Feely, R. A.; Feng, L.; Gasser, T.; Gilfillan, D.; Gkritzalis, T.; Grassi, G.; Gregor, L.; Gruber, N.; Gürses, Ö.; Harris, I.; Houghton, R. A.; Hurtt, G. C.; Iida, Y.; Ilyina, T.; Luijkx, I. T.; Jain, A.; Jones, S. D.; Kato, E.; Kennedy, D.; Klein Goldewijk, K.; Knauer, J.; Korsbakken, J. I.; Körtzinger, A.; Landschützer, P.; Lauvset, S. K.; Lefèvre, N.; Lienert, S.; Liu, J.; Marland, G.; McGuire, P. C.; Melton, J. R.; Munro, D. R.; Nabel, J. E. M. S.; Nakaoka, S.-I.; Niwa, Y.; Ono, T.; Pierrot, D.; Poulter, B.; Rehder, G.; Resplandy, L.; Robertson, E.; Rödenbeck, C.; Rosan, T. M.; Schwinger, J.; Schwingshackl, C.; Séférian, R.; Sutton, A. J.; Sweeney, C.; Tanhua, T.; Tans, P. P.; Tian, H.; Tilbrook, B.; Tubiello, F.; van der Werf, G. R.; Vuichard, N.; Wada, C.; Wanninkhof, R.; Watson, A. J.; Willis, D.; Wiltshire, A. J.; Yuan, W.; Yue, C.; Yue, X.; Zaehle, S.; Zeng, J. Global Carbon Budget 2021. *Earth Syst. Sci. Data* **2022**, *14* (4), 1917–2005.

(13) Joos, F.; Spahni, R. Rates of Change in Natural and Anthropogenic Radiative Forcing over the Past 20 000 Years. *Proc. Natl. Acad. Sci.* **2008**, *105* (5), 1425–1430.

(14) Dlugokencky, E.; Tans, P. *Trends in atmospheric carbon dioxide*. National Oceanic and Atmospheric Administration, Earth System Research Laboratory (NOAA/ESRL). www.esrl.noaa.gov/gmd/ccgg/trends/global.html.

(15) Tans, P. NOAA/GML (gml.noaa.gov/ccgg/trends/); Keeling, R. Scripps Institution of Oceanography (scrippsco2.ucsd.edu/)

(16) Dumitru, O. A.; Austermann, J.; Polyak, V. J.; Fornós, J. J.; Asmerom, Y.; Ginés, J.; Ginés, A.; Onac, B. P. Constraints on Global Mean Sea Level during Pliocene Warmth. *Nature* **2019**, *574* (7777), 233–236.

(17) Hirsch, T. Internationale Klimapolitik: Rückblick und künftige Herausforderungen Inhalt. *Fond. Friedrich Ebert, Accad. online* **2012**, 1–26.

(18) Lenoir, J.; Svenning, J.-C. Climate-Related Range Shifts - a Global Multidimensional Synthesis and New Research Directions. *Ecography (Cop.).* **2015**, *38* (1), 15–28.

(19) Nunez, S.; Arets, E.; Alkemade, R.; Verwer, C.; Leemans, R. Assessing the Impacts of Climate Change on Biodiversity: Is below 2 °C Enough? *Clim. Change* **2019**, *154* (3–4), 351–365.

(20) Román-Palacios, C.; Wiens, J. J. Recent Responses to Climate Change Reveal the Drivers of Species Extinction and Survival. *Proc. Natl. Acad. Sci.* **2020**, *117* (8), 4211–4217.

(21) Halsch, C. A.; Shapiro, A. M.; Fordyce, J. A.; Nice, C. C.; Thorne, J. H.; Waetjen, D. P.; Forister, M. L. Insects and Recent Climate Change. *Proc. Natl. Acad. Sci.* **2021**, *118* (2), 1–9.

(22) Wells, C. P.; Barbier, R.; Nelson, S.; Kanaziz, R.; Aubry, L. M. Life History Consequences of Climate Change in Hibernating Mammals: A Review. *Ecography (Cop.).* **2022**, *2022* (6), 1–19.

(23) Simmonds, I.; Li, M. Trends and Variability in Polar Sea Ice, Global Atmospheric Circulations, and Baroclinicity. *Ann. N. Y. Acad. Sci.* **2021**, *1504* (1), 167–186.

(24) Robinson, D. A. *Northern Hemisphere Continental Snow Cover Extent: 2021 Update*; **2021**, 1-4. http://climate.rutgers.edu/snowcover/files/Robinson_snowdata2021.pdf.

(25) Pörtner, H.-O.; Roberts, D. C.; Tignor, M.; Poloczanska, E. S.; Mintenbeck, K.; Alegría, A.; Craig, M.; Langsdorf, S.; Löschke, S.; Möller, V.; Okem, A.; Rama, B. *IPCC, 2022: Climate Change 2022: Impacts, Adaptation and Vulnerability. Contribution of Working Group II to the Sixth Assessment Report of the Intergovernmental Panel on Climate Change*; 2022.

(26) Eionet - European Environment Information and Observation. *Ocean acidification*. European Environment Agency. https://www.eea.europa.eu/ims/ocean-acidification.

(27) Haibach, H.; Schneider, K. The Politics of Climate Change: Review and Future Challenges. In *Climate Change: International Law and Global Governance*; Nomos Verlagsgesellschaft mbH, 2013; pp 357–374.

(28) Zillman, J. W. *A History of Climate Activities*; 2009, 141–150.

(29) Farman, J. C.; Gardiner, B. G.; Shanklin, J. D. Large Losses of Total Ozone in Antarctica Reveal Seasonal ClO_x/NO_x Interaction. *Nature* **1985**, *315* (6016), 207–210.

(30) Solomon, S. The Discovery of the Antarctic Ozone Hole. *Nature* **2019**, *575* (7781), 46–47.

(31) Houghton, J. T.; Jenkins, G. J.; Ephraums, J. J. *IPCC 1990, Climate Change. The IPCC Scientific Assessment*; Cambridge, Great Britain, New York, NY, USA and Melbourne, Australia, **1990**, 1–414.

(32) Gupta, J. A History of International Climate Change Policy. *WIREs Clim. Chang.* **2010**, *1* (5), 636–653.

(33) Aichele, R.; Felbermayr, G. The Effect of the Kyoto Protocol on Carbon Emissions. *J. Policy Anal. Manag.* **2013**, *32* (4), 731–757.

(34) EEA. *Report 18/2014 - Progress towards 2008-2012 Kyoto Targets in Europe*; Luxembourg (Luxembourg), **2014**, 1–58.

(35) Rosen, A. M. The Wrong Solution at the Right Time: The Failure of the Kyoto Protocol on Climate Change. *Polit. Policy* **2015**, *43* (1), 30–58.

(36) Kumazawa, R.; Callaghan, M. S. The Effect of the Kyoto Protocol on Carbon Dioxide Emissions. *J. Econ. Financ.* **2012**, *36* (1), 201–210.

(37) Almer, C.; Winkler, R. Analyzing the Effectiveness of International Environmental Policies: The Case of the Kyoto Protocol. *J. Environ. Econ. Manage.* **2017**, *82*, 125–151.

(38) Helm, D. The Kyoto Approach Has Failed. *Nature* **2012**, *491* (7426), 663–665.

(39) Grunewald, N.; Martinez-Zarzoso, I. Did the Kyoto Protocol Fail? An Evaluation of the Effect of the Kyoto Protocol on CO_2 Emissions. *Environ. Dev. Econ.* **2016**, *21* (1), 1–22.

(40) Larsen, K.; Pitt, H.; Grant, M.; Houser, T. *China's Greenhouse Gas Emissions Exceeded the Developed World for the First Time in 2019*. Rodhium Group. https://rhg.com/research/chinas-emissions-surpass-developed-countries/#_ftn1.

(41) Falkner, R. The Paris Agreement and the New Logic of International Climate Politics. *Int. Aff.* **2016**, *92* (5), 1107–1125.

(42) Stoddard, I.; Anderson, K.; Capstick, S.; Carton, W.; Depledge, J.; Facer, K.; Gough, C.; Hache, F.; Hoolohan, C.; Hultman, M.; Hällström, N.; Kartha, S.; Klinsky, S.; Kuchler, M.; Lövbrand, E.; Nasiritousi, N.; Newell, P.; Peters, G. P.; Sokona, Y.; Stirling, A.; Stilwell, M.; Spash, C. L.; Williams, M. Three Decades of Climate Mitigation: Why Haven't We Bent the Global Emissions Curve? *Annu. Rev. Environ. Resour.* **2021**, *46* (1), 653–689.

(43) FAO; UNEP. *The State of the World's Forests 2020. Forests, Biodiversity and People*; FAO and UNEP, **2020**, 1–214.

(44) Waring, B.; Neumann, M.; Prentice, I. C.; Adams, M.; Smith, P.; Siegert, M. Forests and Decarbonization – Roles of Natural and Planted Forests. *Front. For. Glob. Chang.* **2020**, *3*, 1–6.

(45) Masson-Delmotte, V.; Zhai, P.; Pörtner, H.-O.; Roberts, D.; Skea, J.; Shukla, P. R.; Pirani, A.; Moufouma-Okia, W.; Péan, C.; Pidcock, R.; Connors, S.; Matthews, J. B. R.; Chen, Y.; Zhou, X.; Gomis, M. I.; Lonnoy, E.; Maycock, T.; Tignor, M.; Waterfield, T. *IPCC, 2018: Global Warming of 1.5°C. An IPCC Special Report on the Impacts of Global Warming of 1.5°C above Pre-Industrial Levels and Related Global Greenhouse Gas Emission Pathways, in the Context of Strengthening the Global Response to the Threat of Cli*; **2018**, 1–630.

(46) Bastin, J.-F.; Finegold, Y.; Garcia, C.; Mollicone, D.; Rezende, M.; Routh, D.; Zohner, C. M.; Crowther, T. W. The Global Tree Restoration Potential. *Science (80-.).* **2019**, *365* (6448), 76–79.

(47) Veldman, J. W.; Aleman, J. C.; Alvarado, S. T.; Anderson, T. M.; Archibald, S.; Bond, W. J.; Boutton, T. W.; Buchmann, N.; Buisson, E.; Canadell, J. G.; Dechoum, M. de S.; Diaz-Toribio, M. H.; Durigan, G.; Ewel, J. J.; Fernandes, G. W.; Fidelis, A.; Fleischman, F.; Good, S. P.; Griffith, D. M.; Hermann, J.-M.; Hoffmann, W. A.; Le Stradic, S.; Lehmann, C. E. R.; Mahy, G.; Nerlekar, A. N.; Nippert, J. B.; Noss, R. F.; Osborne, C. P.; Overbeck, G. E.; Parr, C. L.; Pausas, J. G.; Pennington, R. T.; Perring, M. P.; Putz, F. E.; Ratnam, J.; Sankaran, M.; Schmidt, I. B.; Schmitt, C. B.; Silveira, F. A. O.; Staver, A. C.; Stevens, N.; Still, C. J.; Strömberg, C. A. E.; Temperton, V. M.; Varner, J. M.; Zaloumis, N. P. Comment on "The Global Tree Restoration Potential." *Science (80).* **2019**, *366* (6463), 1–4.

(48) House, J. I.; Colin Prentice, I.; Le Quéré, C. Maximum Impacts of Future Reforestation or Deforestation on Atmospheric CO_2. *Glob. Chang. Biol.* **2002**, *8* (11), 1047–1052.

(49) Gattuso, J.-P.; Williamson, P.; Duarte, C. M.; Magnan, A. K. The Potential for Ocean-Based Climate Action: Negative Emissions Technologies and Beyond. *Front. Clim.* **2021**, *2*, 1–8.

(50) Searles Jones, J. To solve climate change, remember the ocean. *Nature*, **2019**, 1–1.

(51) Feng, E. Y.; Koeve, W.; Keller, D. P.; Oschlies, A. Model-Based Assessment of the CO_2 Sequestration Potential of Coastal Ocean Alkalinization. *Earth's Futur.* **2017**, *5* (12), 1252–1266.

(52) Lenton, A.; Matear, R. J.; Keller, D. P.; Scott, V.; Vaughan, N. E. Assessing Carbon Dioxide Removal through Global and Regional Ocean Alkalinization under High and Low Emission Pathways. *Earth Syst. Dyn.* **2018**, *9* (2), 339–357.

(53) Bach, L. T.; Gill, S. J.; Rickaby, R. E. M.; Gore, S.; Renforth, P. CO_2 Removal With Enhanced Weathering and Ocean Alkalinity Enhancement: Potential Risks and Co-Benefits for Marine Pelagic Ecosystems. *Front. Clim.* **2019**, *1*, 1–21.

(54) Graves, R. A.; Haugo, R. D.; Holz, A.; Nielsen-Pincus, M.; Jones, A.; Kellogg, B.; Macdonald, C.; Popper, K.; Schindel, M. Potential Greenhouse Gas Reductions from Natural Climate Solutions in Oregon, USA. *PLoS One* **2020**, *15* (4), 1–30.

(55) Pires, J. C. M.; Martins, F. G.; Alvim-Ferraz, M. C. M.; Simões, M. Recent Developments on Carbon Capture and Storage: An Overview. *Chem. Eng. Res. Des.* **2011**, *89* (9), 1446–1460.

(56) Irons, R.; Sekkappan, G.; Panesar, R.; Gibbins, J.; Lucquiaud, M. *IEA Greenhouse Gas R & D Programme, "CO_2 Capture Ready Plants";* **2007**, 1–17.

(57) Jansen, D.; Gazzani, M.; Manzolini, G.; Dijk, E. van; Carbo, M. Pre-Combustion CO_2 Capture. *Int. J. Greenh. Gas Control* **2015**, *40*, 167–187.

(58) Mohammed, I. Y.; Samah, M.; Sabina, G.; Mohamed, A. Comparison of Selexol™ and Rectisol® Technologies in an Integrated Gasification Combined Cycle (IGCC) Plant for Clean Energy Production. *Int. J. Eng. Res.* **2014**, *3* (12), 742–744.

(59) Mendes, D.; Mendes, A.; Madeira, L. M.; Iulianelli, A.; Sousa, J. M.; Basile, A. The Water-Gas Shift Reaction: From Conventional Catalytic Systems to Pd-Based Membrane Reactors-a Review. *Asia-Pacific J. Chem. Eng.* **2010**, *5* (1), 111–137.

(60) Korelskiy, D.; Ye, P.; Fouladvand, S.; Karimi, S.; Sjöberg, E.; Hedlund, J. Efficient Ceramic Zeolite Membranes for CO_2 /H_2 Separation. *J. Mater. Chem. A* **2015**, *3* (23), 12500–12506.

(61) Rezaee, P.; Naeij, H. R. A New Approach to Separate Hydrogen from Carbon Dioxide Using Graphdiyne-like Membrane. *Sci. Rep.* **2020**, *10* (1), 1–13.

(62) Sircar, S.; Golden, T. C. Purification of Hydrogen by Pressure Swing Adsorption. *Sep. Sci. Technol.* **2000**, *35* (5), 667–687.

(63) Olajire, A. A. CO_2 Capture and Separation Technologies for End-of-Pipe Applications – A Review. *Energy* **2010**, *35* (6), 2610–2628.

(64) Zhao, L.; Riensche, E.; Menzer, R.; Blum, L.; Stolten, D. A Parametric Study of CO_2/N_2 Gas Separation Membrane Processes for Post-Combustion Capture. *J. Memb. Sci.* **2008**, *325* (1), 284–294.

(65) Chen, G.; Wang, T.; Zhang, G.; Liu, G.; Jin, W. Membrane Materials Targeting Carbon Capture and Utilization. *Adv. Membr.* **2022**, *2*, 1–14.

(66) Bi, Y.; Ju, Y. Review on Cryogenic Technologies for CO_2 Removal from Natural Gas. *Front. Energy* **2022**, *16* (5), 793–811.

(67) Medina-Carrasco, S.; Valverde, J. M. The Calcium Looping Process for Energy Storage: Insights from in Situ XRD Analysis. *Chem. Eng. J.* **2022**, *429*, 1–15.

(68) Basile, A.; Gugliuzza, A.; Iulianelli, A.; Morrone, P. Membrane Technology for Carbon Dioxide (CO_2) Capture in Power Plants. In *Advanced Membrane Science and Technology for Sustainable Energy and Environmental Applications*; Elsevier, **2011**, 113–159.

(69) Huang, X.; Ai, N.; Li, L.; Jiang, Q.; Wang, Q.; Ren, J.; Wang, J. Simulation of CO_2 Capture Process in Flue Gas from Oxy-Fuel Combustion Plant and Effects of Properties of Absorbent. *Separations* **2022**, *9* (4), 1–12.

(70) Cannone, S. F.; Lanzini, A.; Santarelli, M. A Review on CO_2 Capture Technologies with Focus on CO_2-Enhanced Methane Recovery from Hydrates. *Energies* **2021**, *14* (2), 1–32.

(71) Haugen, H. A.; Eldrup, N.; Bernstone, C.; Liljemark, S.; Pettersson, H.; Noer, M.; Holland, J.; Nilsson, P. A.; Hegerland, G.; Pande, J. O. Options for Transporting CO_2 from Coal Fired Power Plants Case Denmark. *Energy Procedia* **2009**, *1* (1), 1665–1672.

(72) Smith, E.; Morris, J.; Kheshgi, H.; Teletzke, G.; Herzog, H.; Paltsev, S. The Cost of CO_2 Transport and Storage in Global Integrated Assessment Modeling. *Int. J. Greenh. Gas Control* **2021**, *109*, 1–11.

(73) Orchard, K.; Hay, M.; Ombudstvedt, I.; Skagestad, R.; Joos, M.; Nysæter, G.; Sjøbris, C.; Gimnes Jarøy, A.; Durusut, E.; Craig, J. *The Status and Challenges of CO_2 Shipping Infrastructures*; **2021**, 1–10.

(74) Lu, H.; Ma, X.; Huang, K.; Fu, L.; Azimi, M. Carbon Dioxide Transport via Pipelines: A Systematic Review. *J. Clean. Prod.* **2020**, *266*, 1–17.

(75) Koornneef, J.; Spruijt, M.; Molag, M.; Ramírez, A.; Turkenburg, W.; Faaij, A. Quantitative Risk Assessment of CO_2 Transport by Pipelines—A Review of Uncertainties and Their Impacts. *J. Hazard. Mater.* **2010**, *177* (1–3), 12–27.

(76) Al Baroudi, H.; Awoyomi, A.; Patchigolla, K.; Jonnalagadda, K.; Anthony, E. J. A Review of Large-Scale CO_2 Shipping and Marine Emissions Management for Carbon Capture, Utilisation and Storage. *Appl. Energy* **2021**, *287*, 1–42.

(77) Kelemen, P.; Benson, S. M.; Pilorgé, H.; Psarras, P.; Wilcox, J. An Overview of the Status and Challenges of CO_2 Storage in Minerals and Geological Formations. *Front. Clim.* **2019**, *1*, 1–20.

(78) Metz, B.; Davidson, O.; de Coninck, H.; Loos, M.; Meyer, L. *IPCC, 2005: IPCC Special Report on Carbon Dioxide Capture and Storage. Prepared by Working Group III of the Intergovernmental Panel on Climate Change*; **2005**, 1–443.

(79) Gibbins, J.; Chalmers, H. Carbon Capture and Storage. *Energy Policy* **2008**, *36* (12), 4317–4322.

(80) Ajayi, T.; Gomes, J. S.; Bera, A. A Review of CO_2 Storage in Geological Formations Emphasizing Modeling, Monitoring and Capacity Estimation Approaches. *Pet. Sci.* **2019**, *16* (5), 1028–1063.

(81) Lackner, K. S.; Brennan, S. Envisioning Carbon Capture and Storage: Expanded Possibilities Due to Air Capture, Leakage Insurance, and C-14 Monitoring. *Clim. Change* **2009**, *96* (3), 357–378.

(82) Zevenhoven, R.; Fagerlund, J.; Songok, J. K. CO_2 Mineral Sequestration: Developments toward Large-Scale Application. *Greenh. Gases Sci. Technol.* **2011**, *1* (1), 48–57.

(83) Hills, C. D.; Tripathi, N.; Carey, P. J. Mineralization Technology for Carbon Capture, Utilization, and Storage. *Front. Energy Res.* **2020**, *8*, 1–14.

(84) Beaulieu, E.; Goddéris, Y.; Donnadieu, Y.; Labat, D.; Roelandt, C. High Sensitivity of the Continental-Weathering Carbon Dioxide Sink to Future Climate Change. *Nat. Clim. Chang.* **2012**, *2* (5), 346–349.

(85) Dooley, J. J.; Dahowski, R. T.; Davidson, C. L.; Wise, M. A.; Gupta, N.; Kim, S. H.; Malone, E. L. *Carbon Dioxide Capture and Geologic Storage: A Core Element of a Global Energy Technology Strategy to Address Climate Change*; College Park Maryland, **2006**, 1–37.

(86) L′Orange Seigo, S.; Dohle, S.; Siegrist, M. Public Perception of Carbon Capture and Storage (CCS): A Review. *Renew. Sustain. Energy Rev.* **2014**, *38*, 848–863.

(87) Wallquist, L.; Seigo, S. L.; Visschers, V. H. M.; Siegrist, M. Public Acceptance of CCS System Elements: A Conjoint Measurement. *Int. J. Greenh. Gas Control* **2012**, *6*, 77–83.

(88) IEA (2020). *CCUS in Clean Energy Transitions*. IEA, Paris. https://www.iea.org/reports/ccus-in-clean-energy-transitions.

(89) National Academies of Sciences Engineering and Medicine. *Gaseous Carbon Waste Streams Utilization*; National Academies Press: Washington, D.C., **2019**, 1–240.

(90) The Royal Society. *Dealing with Carbon Dioxide at Scale*; **2017**, 1–32.

(91) Morrow, D. R.; Thompson, M. S. *Reduce, Remove, Recycle: Clarifying the Overlap between Carbon Removal and CCUS*; Working Paper No. 2; Washington, DC, **2020**, 1–11.

(92) Muthuraj, R.; Mekonnen, T. Recent Progress in Carbon Dioxide (CO_2) as Feedstock for Sustainable Materials Development: Co-Polymers and Polymer Blends. *Polymer (Guildf).* **2018**, *145*, 348–373.

(93) Klaus, S.; Lehenmeier, M. W.; Anderson, C. E.; Rieger, B. Recent Advances in CO_2/Epoxide Copolymerization—New Strategies and Cooperative Mechanisms. *Coord. Chem. Rev.* **2011**, *255* (13–14), 1460–1479.

(94) Ruiz-López, E.; Gandara-Loe, J.; Baena-Moreno, F.; Reina, T. R.; Odriozola, J. A. Electrocatalytic CO_2 Conversion to C_2 Products: Catalysts Design, Market Perspectives and Techno-Economic Aspects. *Renew. Sustain. Energy Rev.* **2022**, *161*, 1–26.

(95) Ampelli, C.; Genovese, C.; Marepally, B. C.; Papanikolaou, G.; Perathoner, S.; Centi, G. Electrocatalytic Conversion of CO_2 to Produce Solar Fuels in Electrolyte or Electrolyte-Less Configurations of PEC Cells. *Faraday Discuss.* **2015**, *183*, 125–145.

(96) Wang, H.; Liu, Y.; Laaksonen, A.; Krook-Riekkola, A.; Yang, Z.; Lu, X.; Ji, X. Carbon Recycling – An Immense Resource and Key to a Smart Climate Engineering: A Survey of Technologies, Cost and Impurity Impact. *Renew. Sustain. Energy Rev.* **2020**, *131*, 1–21.

(97) Surdhar, P. S.; Mezyk, S. P.; Armstrong, D. A. Reduction Potential of the Carboxyl Radical Anion in Aqueous Solutions. *J. Phys. Chem.* **1989**, *93* (8), 3360–3363.

(98) White, J. L.; Baruch, M. F.; Pander, J. E.; Hu, Y.; Fortmeyer, I. C.; Park, J. E.; Zhang, T.; Liao, K.; Gu, J.; Yan, Y.; Shaw, T. W.; Abelev, E.; Bocarsly, A. B. Light-Driven Heterogeneous Reduction of Carbon Dioxide: Photocatalysts and Photoelectrodes. *Chem. Rev.* **2015**, *115* (23), 12888–12935.

(99) Yang, N.; Waldvogel, S. R.; Jiang, X. Electrochemistry of Carbon Dioxide on Carbon Electrodes. *ACS Appl. Mater. Interfaces* **2016**, *8* (42), 28357–28371.

(100) Roy, S.; Cherevotan, A.; Peter, S. C. Thermochemical CO_2 Hydrogenation to Single Carbon Products: Scientific and Technological Challenges. *ACS Energy Lett.* **2018**, *3* (8), 1938–1966.

(101) Shi, J.; Jiang, Y.; Jiang, Z.; Wang, X.; Wang, X.; Zhang, S.; Han, P.; Yang, C. Enzymatic Conversion of Carbon Dioxide. *Chem. Soc. Rev.* **2015**, *44* (17), 5981–6000.

(102) Sultana, S.; Chandra Sahoo, P.; Martha, S.; Parida, K. A Review of Harvesting Clean Fuels from Enzymatic CO_2 Reduction. *RSC Adv.* **2016**, *6* (50), 44170–44194.

(103) Grodkowski, J.; Neta, P. Copper-Catalyzed Radiolytic Reduction of CO_2 to CO in Aqueous Solutions. *J. Phys. Chem. B* **2001**, *105* (21), 4967–4972.

(104) Habisreutinger, S. N.; Schmidt-Mende, L.; Stolarczyk, J. K. Photocatalytic Reduction of CO_2 on TiO_2 and Other Semiconductors. *Angew. Chemie Int. Ed.* **2013**, *52* (29), 7372–7408.

(105) Rej, S.; Bisetto, M.; Naldoni, A.; Fornasiero, P. Well-Defined Cu_2O Photocatalysts for Solar Fuels and Chemicals. *J. Mater. Chem. A* **2021**, *9* (10), 5915–5951.

(106) Genovese, C.; Ampelli, C.; Perathoner, S.; Centi, G. Electrocatalytic Conversion of CO_2 to Liquid Fuels Using Nanocarbon-Based Electrodes. *J. Energy Chem.* **2013**, *22* (2), 202–213.

(107) Serafini, M.; Mariani, F.; Fasolini, A.; Scavetta, E.; Basile, F.; Tonelli, D. Nanostructured Copper-Based Electrodes Electrochemically Synthesized on a Carbonaceous Gas Diffusion Membrane with Catalytic Activity for the Electroreduction of CO_2. *ACS Appl. Mater. Interfaces* **2021**, *13* (48), 57451–57461.

(108) Xu, L.; Xiu, Y.; Liu, F.; Liang, Y.; Wang, S. Research Progress in Conversion of CO_2 to Valuable Fuels. *Molecules* **2020**, *25* (16), 1–23.

(109) Sharma, P.; Sebastian, J.; Ghosh, S.; Creaser, D.; Olsson, L. Recent Advances in Hydrogenation of CO_2 into Hydrocarbons via Methanol Intermediate over Heterogeneous Catalysts. *Catal. Sci. Technol.* **2021**, *11* (5), 1665–1697.

(110) Li, W.; Wang, H.; Jiang, X.; Zhu, J.; Liu, Z.; Guo, X.; Song, C. A Short Review of Recent Advances in CO_2 Hydrogenation to Hydrocarbons over Heterogeneous Catalysts. *RSC Adv.* **2018**, *8* (14), 7651–7669.

(111) Turner, J.; Sverdrup, G.; Mann, M. K.; Maness, P.-C.; Kroposki, B.; Ghirardi, M.; Evans, R. J.; Blake, D. Renewable Hydrogen Production. *Int. J. Energy Res.* **2008**, *32* (5), 379–407.

(112) Porosoff, M. D.; Yan, B.; Chen, J. G. Catalytic Reduction of CO_2 by H_2 for Synthesis of CO, Methanol and Hydrocarbons: Challenges and Opportunities. *Energy Environ. Sci.* **2016**, *9* (1), 62–73.

(113) Sabatier, P. New Synthesis of Methane. *Comptes Rendus* **1902**, *82* (134), 514–516.

(114) Schaaf, T.; Grünig, J.; Schuster, M. R.; Rothenfluh, T.; Orth, A. Methanation of CO_2 - Storage of Renewable Energy in a Gas Distribution System. *Energy. Sustain. Soc.* **2014**, *4* (1), 1–14.

(115) Vogt, C.; Monai, M.; Kramer, G. J.; Weckhuysen, B. M. The Renaissance of the Sabatier Reaction and Its Applications on Earth and in Space. *Nat. Catal.* **2019**, *2* (3), 188–197.

(116) Tan, C. H.; Nomanbhay, S.; Shamsuddin, A. H.; Park, Y.-K.; Hernández-Cocoletzi, H.; Show, P. L. Current Developments in Catalytic Methanation of Carbon Dioxide—A Review. *Front. Energy Res.* **2022**, *9*, 1–7.

(117) Müller, K.; Fleige, M.; Rachow, F.; Schmeißer, D. Sabatier Based CO_2-Methanation of Flue Gas Emitted by Conventional Power Plants. *Energy Procedia* **2013**, *40*, 240–248.

(118) Saeidi, S.; Amin, N. A. S.; Rahimpour, M. R. Hydrogenation of CO_2 to Value-Added Products—A Review and Potential Future Developments. *J. CO_2 Util.* **2014**, *5*, 66–81.

(119) Olah, G. A.; Mathew, T.; Prakash, G. K. S. Chemical Formation of Methanol and Hydrocarbon ("Organic") Derivatives from CO_2 and H_2 — Carbon Sources for Subsequent Biological Cell Evolution and Life's Origin. *J. Am. Chem. Soc.* **2017**, *139* (2), 566–570.

(120) Gorimbo, J.; Hildebrandt, D. Thermochemical Conversion of Carbon Dioxide to Carbon Monoxide by Reverse Water-Gas Shift Reaction over the Ceria-Based Catalyst. In *Conversion of Carbon Dioxide into Hydrocarbons Vol. 1 Catalysis*; **2020**, 43–61.

(121) González-Castaño, M.; Dorneanu, B.; Arellano-García, H. The Reverse Water Gas Shift Reaction: A Process Systems Engineering Perspective. *React. Chem. Eng.* **2021**, *6* (6), 954–976.

(122) Ginés, M. J. L.; Marchi, A. J.; Apesteguía, C. R. Kinetic Study of the Reverse Water-Gas Shift Reaction over $CuO/ZnO/Al_2O_3$ Catalysts. *Appl. Catal. A Gen.* **1997**, *154* (1–2), 155–171.

(123) Wang, X.; Shi, H.; Kwak, J. H.; Szanyi, J. Mechanism of CO_2 Hydrogenation on Pd/Al_2O_3 Catalysts: Kinetics and Transient DRIFTS-MS Studies. *ACS Catal.* **2015**, *5* (11), 6337–6349.

(124) Oshima, K.; Shinagawa, T.; Nogami, Y.; Manabe, R.; Ogo, S.; Sekine, Y. Low Temperature Catalytic Reverse Water Gas Shift Reaction Assisted by an Electric Field. *Catal. Today* **2014**, *232*, 27–32.

(125) Bown, R. M.; Joyce, M.; Zhang, Q.; Reina, T. R.; Duyar, M. S. Identifying Commercial Opportunities for the Reverse Water Gas Shift Reaction. *Energy Technol.* **2021**, *9* (11), 1–9.

(126) Kaiser, P.; Unde, R. B.; Kern, C.; Jess, A. Production of Liquid Hydrocarbons with CO_2 as Carbon Source Based on Reverse Water-Gas Shift and Fischer-Tropsch Synthesis. *Chemie Ing. Tech.* **2013**, *85* (4), 489–499.

(127) Pastor-Pérez, L.; Baibars, F.; Le Sache, E.; Arellano-García, H.; Gu, S.; Reina, T. R. CO_2 Valorisation via Reverse Water-Gas Shift Reaction Using Advanced Cs Doped Fe-Cu/Al_2O_3 Catalysts. *J. CO_2 Util.* **2017**, *21*, 423–428.

(128) Zhao, K. *A Brief Review of China's Methanol Vehicle Pilot and Policy*; **2019**, 1–10.

(129) Methanol Institute. *The Methanol Industry*. https://www.methanol.org/the-methanol-industry/.

(130) Bozzano, G.; Manenti, F. Efficient Methanol Synthesis: Perspectives, Technologies and Optimization Strategies. *Prog. Energy Combust. Sci.* **2016**, *56*, 71–105.

(131) Simon Araya, S.; Liso, V.; Cui, X.; Li, N.; Zhu, J.; Sahlin, S. L.; Jensen, S. H.; Nielsen, M. P.; Kær, S. K. A Review of The Methanol Economy: The Fuel Cell Route. *Energies* **2020**, *13* (3), 1–32.

(132) Joo, O.-S.; Jung, K.-D.; Moon, I.; Rozovskii, A. Y.; Lin, G. I.; Han, S.-H.; Uhm, S.-J. Carbon Dioxide Hydrogenation To Form Methanol via a Reverse-Water-Gas-Shift Reaction (the CAMERE Process). *Ind. Eng. Chem. Res.* **1999**, *38* (5), 1808–1812.

(133) Larmier, K.; Liao, W.-C.; Tada, S.; Lam, E.; Verel, R.; Bansode, A.; Urakawa, A.; Comas-Vives, A.; Copéret, C. CO_2-to-Methanol Hydrogenation on Zirconia-Supported Copper Nanoparticles: Reaction Intermediates and the Role of the Metal-Support Interface. *Angew. Chemie Int. Ed.* **2017**, *56* (9), 2318–2323.

(134) Jiang, X.; Koizumi, N.; Guo, X.; Song, C. Bimetallic Pd–Cu Catalysts for Selective CO_2 Hydrogenation to Methanol. *Appl. Catal. B Environ.* **2015**, *170–171*, 173–185.

(135) Sheldon, D. Methanol Production - A Technical History. *Johnson Matthey Technol. Rev.* **2017**, *61* (3), 172–182.

(136) Chueh, W. C.; Falter, C.; Abbott, M.; Scipio, D.; Furler, P.; Haile, S. M.; Steinfeld, A. High-Flux Solar-Driven Thermochemical Dissociation of CO_2 and H_2O Using Nonstoichiometric Ceria. *Science (80).* **2010**, *330* (6012), 1797–1801.

(137) Yaashikaa, P. R.; Senthil Kumar, P.; Varjani, S. J.; Saravanan, A. A Review on Photochemical, Biochemical and Electrochemical Transformation of CO_2 into Value-Added Products. *J. CO_2 Util.* **2019**, *33*, 131–147.

(138) Gupta, R.; Mishra, A.; Thirupathaiah, Y.; Chandel, A. K. Biochemical Conversion of CO_2 in Fuels and Chemicals: Status, Innovation, and Industrial Aspects. *Biomass Convers. Biorefinery* **2022**, 1–24.

(139) Rittmann, S.; Seifert, A.; Herwig, C. Essential Prerequisites for Successful Bioprocess Development of Biological CH_4 Production from CO_2 and H_2. *Crit. Rev. Biotechnol.* **2015**, *35* (2), 141–151.

(140) Morii, H.; Koga, Y.; Nagai, S. Energetic Analysis of the Growth of Methanobrevibacter Arboriphilus A2 in Hydrogen-Limited Continuous Cultures. *Biotechnol. Bioeng.* **1987**, *29* (3), 310–315.

(141) Peillex, J.-P.; Fardeau, M.-L.; Belaich, J.-P. Growth of Methanobacterium Thermoautotrophicum on H_2CO_2: High CH_4 Productivities in Continuous Culture. *Biomass* **1990**, *21* (4), 315–321.

(142) Wood, H. G.; Ragsdale, S. W.; Pezacka, E. The Acetyl-CoA Pathway of Autotrophic Growth. *FEMS Microbiol. Lett.* **1986**, *39* (4), 345–362.

(143) Ljungdhal, L. G. The Autotrophic Pathway of Acetate Synthesis in Acetogenic Bacteria. *Annu. Rev. Microbiol.* **1986**, *40* (1), 415–450.

(144) Ragsdale, S. W.; Pierce, E. Acetogenesis and the Wood–Ljungdahl Pathway of CO_2 Fixation. *Biochim. Biophys. Acta - Proteins Proteomics* **2008**, *1784* (12), 1873–1898.

(145) Müller, V. Energy Conservation in Acetogenic Bacteria. *Appl. Environ. Microbiol.* **2003**, *69* (11), 6345–6353.

(146) Katsyv, A.; Müller, V. Overcoming Energetic Barriers in Acetogenic C1 Conversion. *Front. Bioeng. Biotechnol.* **2020**, *8*, 1–23.

(147) Bassham, J. .; Calvin, M. The Way of CO_2 in Plant Photosynthesis. *Comp. Biochem. Physiol.* **1962**, *4* (2–4), 187–204.

(148) Buchanan, B. B.; Arnon, D. I. A Reverse KREBS Cycle in Photosynthesis: Consensus at Last. *Photosynth. Res.* **1990**, *24* (1), 47–53.

(149) Huber, H.; Gallenberger, M.; Jahn, U.; Eylert, E.; Berg, I. A.; Kockelkorn, D.; Eisenreich, W.; Fuchs, G. A Dicarboxylate/4-Hydroxybutyrate Autotrophic Carbon Assimilation Cycle in the Hyperthermophilic Archaeum Ignicoccus Hospitalis. *Proc. Natl. Acad. Sci.* **2008**, *105* (22), 7851–7856.

(150) Berg, I. A.; Kockelkorn, D.; Buckel, W.; Fuchs, G. A 3-Hydroxypropionate/4-Hydroxybutyrate Autotrophic Carbon Dioxide Assimilation Pathway in Archaea. *Science (80).* **2007**, *318* (5857), 1782–1786.

(151) Erb, T. J.; Zarzycki, J. Biochemical and Synthetic Biology Approaches to Improve Photosynthetic CO_2-Fixation. *Curr. Opin. Chem. Biol.* **2016**, *34*, 72–79.

(152) Weiss, T. L.; Young, E. J.; Ducat, D. C. A Synthetic, Light-Driven Consortium of Cyanobacteria and Heterotrophic Bacteria Enables Stable Polyhydroxybutyrate Production. *Metab. Eng.* **2017**, *44*, 236–245.

(153) Dürre, P.; Eikmanns, B. J. C1-Carbon Sources for Chemical and Fuel Production by Microbial Gas Fermentation. *Curr. Opin. Biotechnol.* **2015**, *35*, 63–72.

(154) Alper, H.; Moxley, J.; Nevoigt, E.; Fink, G. R.; Stephanopoulos, G. Engineering Yeast Transcription Machinery for Improved Ethanol Tolerance and Production. *Science (80).* **2006**, *314* (5805), 1565–1568.

(155) Liang, B.; Zhao, Y.; Yang, J. Recent Advances in Developing Artificial Autotrophic Microorganism for Reinforcing CO_2 Fixation. *Front. Microbiol.* **2020**, *11*, 1–16.

(156) Lu, Y.; Jiang, Z.; Xu, S.; Wu, H. Efficient Conversion of CO_2 to Formic Acid by Formate Dehydrogenase Immobilized in a Novel Alginate–Silica Hybrid Gel. *Catal. Today* **2006**, *115* (1–4), 263–268.

(157) Appel, A. M.; Bercaw, J. E.; Bocarsly, A. B.; Dobbek, H.; DuBois, D. L.; Dupuis, M.; Ferry, J. G.; Fujita, E.; Hille, R.; Kenis, P. J. A.; Kerfeld, C. A.; Morris, R. H.; Peden, C. H. F.; Portis, A. R.; Ragsdale, S. W.; Rauchfuss, T. B.; Reek, J. N. H.; Seefeldt, L. C.; Thauer, R. K.; Waldrop, G. L. Frontiers, Opportunities, and Challenges in Biochemical and Chemical Catalysis of CO_2 Fixation. *Chem. Rev.* **2013**, *113* (8), 6621–6658.

(158) Shin, W.; Lee, S. H.; Shin, J. W.; Lee, S. P.; Kim, Y. Highly Selective Electrocatalytic Conversion of CO_2 to CO at −0.57 V (NHE) by Carbon Monoxide Dehydrogenase from Moorella Thermoacetica. *J. Am. Chem. Soc.* **2003**, *125* (48), 14688–14689.

(159) Yang, Z.-Y.; Moure, V. R.; Dean, D. R.; Seefeldt, L. C. Carbon Dioxide Reduction to Methane and Coupling with Acetylene to Form Propylene Catalyzed by Remodeled Nitrogenase. *Proc. Natl. Acad. Sci.* **2012**, *109* (48), 19644–19648.

(160) Talekar, S.; Jo, B. H.; Dordick, J. S.; Kim, J. Carbonic Anhydrase for CO_2 Capture, Conversion and Utilization. *Curr. Opin. Biotechnol.* **2022**, *74*, 230–240.

(161) Ho, C.; Sturtevant, J. M. The Kinetics of the Hydration of Carbon Dioxide at 25°. *J. Biol. Chem.* **1963**, *238* (10), 3499–3501.

(162) Mitchell, M. J.; Jensen, O. E.; Cliffe, K. A.; Maroto-Valer, M. M. A Model of Carbon Dioxide Dissolution and Mineral Carbonation Kinetics. *Proc. R. Soc. A Math. Phys. Eng. Sci.* **2010**, *466* (2117), 1265–1290.

(163) González, J. M.; Fisher, S. Z. Carbonic Anhydrases in Industrial Applications. *Subcell. Biochem.* **2014**, *75*, 405–426.

(164) Obert, R.; Dave, B. C. Enzymatic Conversion of Carbon Dioxide to Methanol: Enhanced Methanol Production in Silica Sol−Gel Matrices. *J. Am. Chem. Soc.* **1999**, *121* (51), 12192–12193.

(165) Xu, S.; Lu, Y.; Li, J.; Jiang, Z.; Wu, H. Efficient Conversion of CO_2 to Methanol Catalyzed by Three Dehydrogenases Co-Encapsulated in an Alginate−Silica (ALG−SiO_2) Hybrid Gel. *Ind. Eng. Chem. Res.* **2006**, *45* (13), 4567–4573.

(166) Wang, X.; Li, Z.; Shi, J.; Wu, H.; Jiang, Z.; Zhang, W.; Song, X.; Ai, Q. Bioinspired Approach to Multienzyme Cascade System Construction for Efficient Carbon Dioxide Reduction. *ACS Catal.* **2014**, *4* (3), 962–972.

(167) Weisser, D. A Guide to Life-Cycle Greenhouse Gas (GHG) Emissions from Electric Supply Technologies. *Energy* **2007**, *32* (9), 1543–1559.

(168) Ramirez-Corredores, M. M.; Diaz, L. A.; Gaffney, A. M.; Zarzana, C. A. Identification of Opportunities for Integrating Chemical Processes for Carbon (Dioxide) Utilization to Nuclear Power Plants. *Renew. Sustain. Energy Rev.* **2021**, *150*, 1–15.

(169) Höhlein, B.; Menzer, R.; Range, J. High Temperature Methanation in the Long-Distance Nuclear Energy Transport System. *Appl. Catal.* **1981**, *1* (3–4), 125–139.

(170) Schmeda-Lopez, D.; McConnaughy, T. B.; McFarland, E. W. Radiation Enhanced Chemical Production: Improving the Value Proposition of Nuclear Power. *Energy* **2018**, *162*, 491–504.

(171) Ramirez-Corredores, M. M.; Gadikota, G.; Huang, E. E.; Gaffney, A. M. Radiation-Induced Chemistry of Carbon Dioxide: A Pathway to Close the Carbon Loop for a Circular Economy. *Front. Energy Res.* **2020**, *8*, 1–17.

(172) Lind, S. C.; Bardwell, D. C. The Chemical Action of Gaseous Ions Produced by Alpha Particles. VI. Reactions of the Oxides of Carbon. *J. Am. Chem. Soc.* **1925**, *47* (11), 2675–2697.

(173) Harteck, P.; Dondes, S. Decomposition of Carbon Dioxide by Ionizing Radiation. Part II. *J. Chem. Phys.* **1957**, *26* (6), 1727–1733.

(174) Anbar, M.; Perlstein, P. Mechanism of Radiolysis of Carbon Dioxide. *Trans. Faraday Soc.* **1966**, *62*, 1803–1811.

(175) Ryazantsev, S. V.; Feldman, V. I. Matrix-Isolation Studies on the Radiation-Induced Chemistry in H_2O/CO_2 Systems: Reactions of Oxygen Atoms and Formation of HOCO Radical. *J. Phys. Chem. A* **2015**, *119* (11), 2578–2586.

(176) Ikezoe, Y.; Sato, S. Radiation Chemical Reactions in Carbon Dioxide-Propane System Formation of Carbon Monoxide by Fission Fragments. *J. Nucl. Sci. Technol.* **1976**, *13* (9), 503–507.

(177) Lind, S. C.; Bardwell, D. C. The Chemical Action of Gaseous Ions Produced by Alpha Particles. IX. Saturated Hydrocarbons. *J. Am. Chem. Soc.* **1926**, *48* (9), 2335–2351.

(178) Fujita, N.; Morita, H.; Matsuura, C.; Hiroishi, D. Radiation Induced CO_2 Reduction in an Aqueous Medium Suspended with Iron Powder. *Radiat. Phys. Chem.* **1994**, *44* (4), 349–357.

(179) Garibov, A. A.; Velibekova, G. Z.; Agayev, T. N. Heterogeneous Radiolysis of CO_2 in the Presence of Zeolites. *Int. J. Radiat. Appl. Instrumentation. Part C. Radiat. Phys. Chem.* **1987**, *29* (1), 71–73.

(180) Shkrob, I. A.; Marin, T. W.; He, H.; Zapol, P. Photoredox Reactions and the Catalytic Cycle for Carbon Dioxide Fixation and Methanogenesis on Metal Oxides. *J. Phys. Chem. C* **2012**, *116* (17), 9450–9460.

(181) IEA. *IEA (2019), Global Energy & CO_2 Status Report 2019*; Paris, 2019. https://www.iea.org/reports/global-energy-co2-status-report-2019.

(182) Wang, C.; Sun, Z.; Zheng, Y.; Hu, Y. H. Recent Progress in Visible Light Photocatalytic Conversion of Carbon Dioxide. *J. Mater. Chem. A* **2019**, *7* (3), 865–887.

(183) Inoue, T.; Fujishima, A.; Konishi, S.; Honda, K. Photoelectrocatalytic Reduction of Carbon Dioxide in Aqueous Suspensions of Semiconductor Powders. *Nature* **1979**, *277* (5698), 637–638.

(184) Hennig, H. Homogeneous Photo Catalysis by Transition Metal Complexes. *Coord. Chem. Rev.* **1999**, *182* (1), 101–123.

(185) Cokoja, M.; Bruckmeier, C.; Rieger, B.; Herrmann, W. A.; Kühn, F. E. Transformation of Carbon Dioxide with Homogeneous Transition-Metal Catalysts: A Molecular Solution to a Global Challenge? *Angew. Chemie Int. Ed.* **2011**, *50* (37), 8510–8537.

(186) Huang, W.; Lin, J.; Deng, F.; Zhong, H. Photocatalytic Carboxylation with CO_2 : A Review of Recent Studies. *Asian J. Org. Chem.* **2022**, *11* (7), 1–15.

(187) Bonin, J.; Robert, M.; Routier, M. Selective and Efficient Photocatalytic CO_2 Reduction to CO Using Visible Light and an Iron-Based Homogeneous Catalyst. *J. Am. Chem. Soc.* **2014**, *136* (48), 16768–16771.

(188) Kaneco, S.; Kurimoto, H.; Shimizu, Y.; Ohta, K.; Mizuno, T. Photocatalytic Reduction of CO_2 Using TiO_2 Powders in Supercritical Fluid CO_2. *Energy* **1999**, *24* (1), 21–30.

(189) Li, K.; An, X.; Park, K. H.; Khraisheh, M.; Tang, J. A Critical Review of CO_2 Photoconversion: Catalysts and Reactors. *Catal. Today* **2014**, *224*, 3–12.

(190) Zhu, Z.; Liu, X.; Bao, C.; Zhang, K.; Song, C.; Xuan, Y. How Efficient Could Photocatalytic CO_2 Reduction with H_2O into Solar Fuels Be? *Energy Convers. Manag.* **2020**, *222*, 1–8.

(191) Carini Jr., G.; Parrino, F.; Palmisano, G.; Scandura, G.; Citro, I.; Calogero, G.; Bartolotta, A.; Di Marco, G. Nanostructured Anatase TiO_2 Densified at High Pressure as Advanced Visible Light Photocatalysts. *Photochem. Photobiol. Sci.* **2015**, *14* (9), 1685–1693.

(192) Hu, Y. H. A Highly Efficient Photocatalyst-Hydrogenated Black TiO_2 for the Photocatalytic Splitting of Water. *Angew. Chemie Int. Ed.* **2012**, *51* (50), 12410–12412.

(193) Dey, G. R. Chemical Reduction of CO_2 to Different Products during Photo Catalytic Reaction on TiO_2 under Diverse Conditions: An Overview. *J. Nat. Gas Chem.* **2007**, *16* (3), 217–226.

(194) Eggins, B. R.; Irvine, J. T. S.; Murphy, E. P.; Grimshaw, J. Formation of Two-Carbon Acids from Carbon Dioxide by Photoreduction on Cadmium Sulphide. *J. Chem. Soc. Chem. Commun.* **1988**, No. 16, 1123–1124.

(195) Sahoo, D. P.; Nayak, S.; Reddy, K. H.; Martha, S.; Parida, K. Fabrication of a $Co(OH)_2$/ZnCr LDH "p–n" Heterojunction Photocatalyst with Enhanced Separation of Charge Carriers for Efficient Visible-Light-Driven H_2 and O_2 Evolution. *Inorg. Chem.* **2018**, *57* (7), 3840–3854.

(196) Cavani, F.; Trifirò, F.; Vaccari, A. Hydrotalcite-Type Anionic Clays: Preparation, Properties and Applications. *Catal. Today* **1991**, *11* (2), 173–301.

(197) Forano, C.; Hibino, T.; Leroux, F.; Taviot-Guého, C. Chapter 13.1 Layered Double Hydroxides. *Dev. Clay Sci. Vol. 1* **2006**, *1*, 1021–1095.

(198) Tonelli, D.; Gualandi, I.; Musella, E.; Scavetta, E. Synthesis and Characterization of Layered Double Hydroxides as Materials for Electrocatalytic Applications. *Nanomaterials* **2021**, *11* (3), 1–20.

(199) Li, T.; Miras, H.; Song, Y.-F. Polyoxometalate (POM)-Layered Double Hydroxides (LDH) Composite Materials: Design and Catalytic Applications. *Catalysts* **2017**, *7* (9), 1–17.

(200) Razzaq, A.; Ali, S.; Asif, M.; In, S.-I. Layered Double Hydroxide (LDH) Based Photocatalysts: An Outstanding Strategy for Efficient Photocatalytic CO_2 Conversion. *Catalysts* **2020**, *10* (10), 1–43.

(201) Wu, J.; Huang, Y.; Ye, W.; Li, Y. CO_2 Reduction: From the Electrochemical to Photochemical Approach. *Adv. Sci.* **2017**, *4* (11), 1–29.

(202) Yu, Y.; Li, S.; Huang, L.; Yu, J.; Zhang, H.; Song, S.; Zeng, T. Solar-Driven CO_2 Conversion Promoted by MOF−on−MOF Homophase Junction. *Catal. Commun.* **2021**, *150*, 1–6.

(203) Ramyashree, M. .; Shanmuga Priya, S.; Freudenberg, N. C.; Sudhakar, K.; Tahir, M. Metal-Organic Framework-Based Photocatalysts for Carbon Dioxide Reduction to Methanol: A Review on Progress and Application. *J. CO_2 Util.* **2021**, *43*, 1–22.

(204) Kandy, M. M. Carbon-Based Photocatalysts for Enhanced Photocatalytic Reduction of CO_2 to Solar Fuels. *Sustain. Energy Fuels* **2020**, *4* (2), 469–484.

(205) Kuriki, R.; Sekizawa, K.; Ishitani, O.; Maeda, K. Visible-Light-Driven CO_2 Reduction with Carbon Nitride: Enhancing the Activity of Ruthenium Catalysts. *Angew. Chemie Int. Ed.* **2015**, *54* (8), 2406–2409.

(206) Amao, Y.; Shuto, N.; Furuno, K.; Obata, A.; Fuchino, Y.; Uemura, K.; Kajino, T.; Sekito, T.; Iwai, S.; Miyamoto, Y.; Matsuda, M. Artificial Leaf Device for Solar Fuel Production. *Faraday Discuss.* **2012**, *155*, 289–296.

(207) Bensaid, S.; Centi, G.; Garrone, E.; Perathoner, S.; Saracco, G. Towards Artificial Leaves for Solar Hydrogen and Fuels from Carbon Dioxide. *ChemSusChem* **2012**, *5* (3), 500–521.

(208) Zhang, G.; Liu, B.; Wang, T.; Gong, J. Arificial Leaves for Solar Fuels. *Chinese J. Chem.* **2021**, *39* (6), 1450–1458.

(209) Moon, C.; Shin, B. Review on Light Absorbing Materials for Unassisted Photoelectrochemical Water Splitting and Systematic Classifications of Device Architectures. *Discov. Mater.* **2022**, *2* (1), 1–16.

(210) Cheng, C.; Zhang, W.; Chen, X.; Peng, S.; Li, Y. Strategies for Improving Photoelectrochemical Water Splitting Performance of Si-based Electrodes. *Energy Sci. Eng.* **2022**, *10* (4), 1526–1543.

(211) Xu, S.; Shen, Q.; Zheng, J.; Wang, Z.; Pan, X.; Yang, N.; Zhao, G. Advances in Biomimetic Photoelectrocatalytic Reduction of Carbon Dioxide. *Adv. Sci.* **2022**, *9* (31), 1–24.

(212) Zhang, S.; Fan, Q.; Xia, R.; Meyer, T. J. CO_2 Reduction: From Homogeneous to Heterogeneous Electrocatalysis. *Acc. Chem. Res.* **2020**, *53* (1), 255–264.

(213) Agarwal, A. S.; Zhai, Y.; Hill, D.; Sridhar, N. Corrigendum: The Electrochemical Reduction of Carbon Dioxide to Formate/Formic Acid: Engineering and Economic Feasibility. *ChemSusChem* **2011**, *4* (12), 1705–1705.

(214) Bevilacqua, M.; Filippi, J.; Miller, H. A.; Vizza, F. Recent Technological Progress in CO_2 Electroreduction to Fuels and Energy Carriers in Aqueous Environments. *Energy Technol.* **2015**, *3* (3), 197–210.

(215) Li, L.; Huang, Y.; Li, Y. Carbonaceous Materials for Electrochemical CO_2 Reduction. *EnergyChem* **2020**, *2* (1), 1–63.

(216) Jin, S.; Hao, Z.; Zhang, K.; Yan, Z.; Chen, J. Advances and Challenges for the Electrochemical Reduction of CO_2 to CO: From Fundamentals to Industrialization. *Angew. Chemie Int. Ed.* **2021**, *60* (38), 20627–20648.

(217) Pawar, A. U.; Kim, C. W.; Nguyen-Le, M.-T.; Kang, Y. S. General Review on the Components and Parameters of Photoelectrochemical System for CO_2 Reduction with in Situ Analysis. *ACS Sustain. Chem. Eng.* **2019**, *7* (8), 7431–7455.

(218) Kumar, A.; Hasija, V.; Sudhaik, A.; Raizada, P.; Van Le, Q.; Singh, P.; Pham, T.-H.; Kim, T.; Ghotekar, S.; Nguyen, V.-H. Artificial Leaf for Light-Driven CO_2 Reduction: Basic Concepts, Advanced Structures and Selective Solar-to-Chemical Products. *Chem. Eng. J.* **2022**, *430*, 1–19.

(219) Long, C.; Li, X.; Guo, J.; Shi, Y.; Liu, S.; Tang, Z. Electrochemical Reduction of CO_2 over Heterogeneous Catalysts in Aqueous Solution: Recent Progress and Perspectives. *Small Methods* **2019**, *3* (3), 1–20.

(220) Rudnev, A. V.; Zhumaev, U. E.; Kuzume, A.; Vesztergom, S.; Furrer, J.; Broekmann, P.; Wandlowski, T. The Promoting Effect of Water on the Electroreduction of CO_2 in Acetonitrile. *Electrochim. Acta* **2016**, *189*, 38–44.

(221) Feng, J.; Zeng, S.; Feng, J.; Dong, H.; Zhang, X. CO_2 Electroreduction in Ionic Liquids: A Review. *Chinese J. Chem.* **2018**, *36* (10), 961–970.

(222) Blanchard, L. A.; Hancu, D.; Beckman, E. J.; Brennecke, J. F. Green Processing Using Ionic Liquids and CO_2. *Nature* **1999**, *399* (6731), 28–29.

(223) Costentin, C.; Robert, M.; Savéant, J.-M. Catalysis of the Electrochemical Reduction of Carbon Dioxide. *Chem. Soc. Rev.* **2013**, *42* (6), 2423–2436.

(224) Sánchez, O. G.; Birdja, Y. Y.; Bulut, M.; Vaes, J.; Breugelmans, T.; Pant, D. Recent Advances in Industrial CO_2 Electroreduction. *Curr. Opin. Green Sustain. Chem.* **2019**, *16*, 47–56.

(225) Fan, L.; Xia, C.; Yang, F.; Wang, J.; Wang, H.; Lu, Y. Strategies in Catalysts and Electrolyzer Design for Electrochemical CO_2 Reduction toward C_{2+} Products. *Sci. Adv.* **2020**, *6* (8), 1–17.

(226) Centi, G.; Perathoner, S.; Winè, G.; Gangeri, M. Electrocatalytic Conversion of CO_2 to Long Carbon-Chain Hydrocarbons. *Green Chem.* **2007**, *9* (6), 671–678.

(227) Pander, J. E.; Ren, D.; Huang, Y.; Loo, N. W. X.; Hong, S. H. L.; Yeo, B. S. Understanding the Heterogeneous Electrocatalytic Reduction of Carbon Dioxide on Oxide-Derived Catalysts. *ChemElectroChem* **2018**, *5* (2), 219–237.

(228) Nitopi, S.; Bertheussen, E.; Scott, S. B.; Liu, X.; Engstfeld, A. K.; Horch, S.; Seger, B.; Stephens, I. E. L.; Chan, K.; Hahn, C.; Nørskov, J. K.; Jaramillo, T. F.; Chorkendorff, I. Progress and Perspectives of Electrochemical CO_2 Reduction on Copper in Aqueous Electrolyte. *Chem. Rev.* **2019**, *119* (12), 7610–7672.

(229) Francke, R.; Schille, B.; Roemelt, M. Homogeneously Catalyzed Electroreduction of Carbon Dioxide—Methods, Mechanisms, and Catalysts. *Chem. Rev.* **2018**, *118* (9), 4631–4701.

(230) Costentin, C.; Drouet, S.; Robert, M.; Savéant, J.-M. A Local Proton Source Enhances CO_2 Electroreduction to CO by a Molecular Fe Catalyst. *Science (80).* **2012**, *338* (6103), 90–94.

(231) Schilter, D. Homogeneous Catalysis: Synthetic Models Close in on Enzymes. *Nat. Rev. Chem.* **2018**, *2* (1), 1–1.

(232) Feng, D.-M.; Zhu, Y.-P.; Chen, P.; Ma, T.-Y. Recent Advances in Transition-Metal-Mediated Electrocatalytic CO_2 Reduction: From Homogeneous to Heterogeneous Systems. *Catalysts* **2017**, *7* (12), 1–18.

(233) Costentin, C.; Passard, G.; Robert, M.; Savéant, J.-M. Ultraefficient Homogeneous Catalyst for the CO_2-to-CO Electrochemical Conversion. *Proc. Natl. Acad. Sci.* **2014**, *111* (42), 14990–14994.

(234) Ahmed, M. E.; Rana, A.; Saha, R.; Dey, S.; Dey, A. Homogeneous Electrochemical Reduction of CO_2 to CO by a Cobalt Pyridine Thiolate Complex. *Inorg. Chem.* **2020**, *59* (8), 5292–5302.

(235) Zhang, X.; Guo, S.-X.; Gandionco, K. A.; Bond, A. M.; Zhang, J. Electrocatalytic Carbon Dioxide Reduction: From Fundamental Principles to Catalyst Design. *Mater. Today Adv.* **2020**, *7*, 1–24.

(236) Pei, Y.; Zhong, H.; Jin, F. A Brief Review of Electrocatalytic Reduction of CO_2 — Materials, Reaction Conditions, and Devices. *Energy Sci. Eng.* **2021**, *9* (7), 1012–1032.

(237) Boettcher, S. W.; Oener, S. Z.; Lonergan, M. C.; Surendranath, Y.; Ardo, S.; Brozek, C.; Kempler, P. A. Potentially Confusing: Potentials in Electrochemistry. *ACS Energy Lett.* **2021**, *6* (1), 261–266.

(238) Lu, Q.; Jiao, F. Electrochemical CO_2 Reduction: Electrocatalyst, Reaction Mechanism, and Process Engineering. *Nano Energy* **2016**, *29*, 439–456.

(239) Birdja, Y. Y.; Pérez-Gallent, E.; Figueiredo, M. C.; Göttle, A. J.; Calle-Vallejo, F.; Koper, M. T. M. Advances and Challenges in Understanding the Electrocatalytic Conversion of Carbon Dioxide to Fuels. *Nat. Energy* **2019**, *4* (9), 732–745.

(240) Kuhl, K. P.; Cave, E. R.; Abram, D. N.; Jaramillo, T. F. New Insights into the Electrochemical Reduction of Carbon Dioxide on Metallic Copper Surfaces. *Energy Environ. Sci.* **2012**, *5* (5), 7050–7059.

(241) Hori, Y. CO_2-Reduction, Catalyzed by Metal Electrodes. *Handb. Fuel Cells* **2010**, 1–14.

(242) Jhong, H.-R. "Molly"; Ma, S.; Kenis, P. J. Electrochemical Conversion of CO_2 to Useful Chemicals: Current Status, Remaining Challenges, and Future Opportunities. *Curr. Opin. Chem. Eng.* **2013**, *2* (2), 191–199.

(243) Costentin, C.; Passard, G.; Savéant, J.-M. Benchmarking of Homogeneous Electrocatalysts: Overpotential, Turnover Frequency, Limiting Turnover Number. *J. Am. Chem. Soc.* **2015**, *137* (16), 5461–5467.

(244) Teeter, T. E.; Van Rysselberghe, P. Reduction of Carbon Dioxide on Mercury Cathodes. *J. Chem. Phys.* **1954**, *22* (4), 759–760.

(245) Hori, Y.; Kikuchi, K.; Suzuki, S. Production of CO and CH_4 in Electrochemical Reduction of CO_2 at Metal Electrodes in Aqueous Hydrogencarbonate Solution. *Chem. Lett.* **1985**, *14* (11), 1695–1698.

(246) Hori, Y.; Murata, A.; Takahashi, R. Formation of Hydrocarbons in the Electrochemical Reduction of Carbon Dioxide at a Copper Electrode in Aqueous Solution. *J. Chem. Soc. Faraday Trans. 1 Phys. Chem. Condens. Phases* **1989**, *85* (8), 2309–2326.

(247) Hori, Y.; Murata, A. Electrochemical Evidence of Intermediate Formation of Adsorbed CO in Cathodic Reduction of CO_2 at a Nickel Electrode. *Electrochim. Acta* **1990**, *35* (11–12), 1777–1780.

(248) Hori, Y.; Takahashi, R.; Yoshinami, Y.; Murata, A. Electrochemical Reduction of CO at a Copper Electrode. *J. Phys. Chem. B* **1997**, *101* (36), 7075–7081.

(249) Hori, Y.; Wakebe, H.; Tsukamoto, T.; Koga, O. Electrocatalytic Process of CO Selectivity in Electrochemical Reduction of CO_2 at Metal Electrodes in Aqueous Media. *Electrochim. Acta* **1994**, *39* (11–12), 1833–1839.

(250) Hori, Y. Electrochemical CO_2 Reduction on Metal Electrodes. In *Modern Aspects of Electrochemistry*; Springer New York: New York, NY, **2008**, 89–189.

(251) Kostecki, R.; Augustynski, J. Electrochemical Reduction of CO_2 at an Activated Silver Electrode. *Berichte der Bunsengesellschaft für Phys. Chemie* **1994**, *98* (12), 1510–1515.

(252) Luo, W.; Zhang, J.; Li, M.; Züttel, A. Boosting CO Production in Electrocatalytic CO_2 Reduction on Highly Porous Zn Catalysts. *ACS Catal.* **2019**, *9* (5), 3783–3791.

(253) An, X.; Li, S.; Hao, X.; Xie, Z.; Du, X.; Wang, Z.; Hao, X.; Abudula, A.; Guan, G. Common Strategies for Improving the Performances of Tin and Bismuth-Based Catalysts in the Electrocatalytic Reduction of CO_2 to Formic Acid/Formate. *Renew. Sustain. Energy Rev.* **2021**, *143*, 1–17.

(254) Xue, Y.; Guo, Y.; Cui, H.; Zhou, Z. Catalyst Design for Electrochemical Reduction of CO_2 to Multicarbon Products. *Small Methods* **2021**, *5* (10), 1–14.

(255) Zhang, W.; Hu, Y.; Ma, L.; Zhu, G.; Wang, Y.; Xue, X.; Chen, R.; Yang, S.; Jin, Z. Progress and Perspective of Electrocatalytic CO_2 Reduction for Renewable Carbonaceous Fuels and Chemicals. *Adv. Sci.* **2018**, *5* (1), 1–24.

(256) Hoshi, N.; Kato, M.; Hori, Y. Electrochemical Reduction of CO_2 on Single Crystal Electrodes of Silver Ag(111), Ag(100) and Ag(110). *J. Electroanal. Chem.* **1997**, *440* (1–2), 283–286.

(257) Taguchi, S.; Aramata, A. Surface-Structure Sensitive Reduced CO_2 Formation on Pt Single Crystal Electrodes in Sulfuric Acid Solution. *Electrochim. Acta* **1994**, *39* (17), 2533–2537.

(258) Qu, Y.; Duan, X. Progress, Challenge and Perspective of Heterogeneous Photocatalysts. *Chem. Soc. Rev.* **2013**, *42* (7), 2568–2580.

(259) Xiao, H.; Cheng, T.; Goddard, W. A.; Sundararaman, R. Mechanistic Explanation of the pH Dependence and Onset Potentials for Hydrocarbon Products from Electrochemical Reduction of CO on Cu (111). *J. Am. Chem. Soc.* **2016**, *138* (2), 483–486.

(260) Rodriguez, J. A.; Ma, S.; Liu, P.; Hrbek, J.; Evans, J.; Pérez, M. Activity of CeO_x and TiO_x Nanoparticles Grown on Au(111) in the Water-Gas Shift Reaction. *Science (80).* **2007**, *318* (5857), 1757–1760.

(261) Graciani, J.; Mudiyanselage, K.; Xu, F.; Baber, A. E.; Evans, J.; Senanayake, S. D.; Stacchiola, D. J.; Liu, P.; Hrbek, J.; Sanz, J. F.; Rodriguez, J. A. Highly Active Copper-Ceria and Copper-Ceria-Titania Catalysts for Methanol Synthesis from CO_2. *Science (80-.).* **2014**, *345* (6196), 546–550.

(262) Fu, Q.; Li, W.-X.; Yao, Y.; Liu, H.; Su, H.-Y.; Ma, D.; Gu, X.-K.; Chen, L.; Wang, Z.; Zhang, H.; Wang, B.; Bao, X. Interface-Confined Ferrous Centers for Catalytic Oxidation. *Science (80).* **2010**, *328* (5982), 1141–1144.

(263) Frese, K. W. Electrochemical Reduction of CO_2 at Intentionally Oxidized Copper Electrodes. *J. Electrochem. Soc.* **1991**, *138* (11), 3338–3344.

(264) Le, M.; Ren, M.; Zhang, Z.; Sprunger, P. T.; Kurtz, R. L.; Flake, J. C. Electrochemical Reduction of CO_2 to CH_3OH at Copper Oxide Surfaces. *J. Electrochem. Soc.* **2011**, *158* (5), E45–E49.

(265) Gao, S.; Jiao, X.; Sun, Z.; Zhang, W.; Sun, Y.; Wang, C.; Hu, Q.; Zu, X.; Yang, F.; Yang, S.; Liang, L.; Wu, J.; Xie, Y. Ultrathin Co_3O_4 Layers Realizing Optimized CO_2 Electroreduction to Formate. *Angew. Chemie Int. Ed.* **2016**, *55* (2), 698–702.

(266) Giri, S. D.; Sarkar, A.; Mahajani, S.; Suresh, A. K. Electrochemical Reduction of CO_2 on Copper Oxidized by Electrochemical Methods. *ECS Trans.* **2017**, *75* (48), 19–31.

(267) Deng, P.; Wang, H.; Qi, R.; Zhu, J.; Chen, S.; Yang, F.; Zhou, L.; Qi, K.; Liu, H.; Xia, B. Y. Bismuth Oxides with Enhanced Bismuth–Oxygen Structure for Efficient Electrochemical Reduction of Carbon Dioxide to Formate. *ACS Catal.* **2020**, *10* (1), 743–750.

(268) Gao, D.; Zhang, Y.; Zhou, Z.; Cai, F.; Zhao, X.; Huang, W.; Li, Y.; Zhu, J.; Liu, P.; Yang, F.; Wang, G.; Bao, X. Enhancing CO_2 Electroreduction with the Metal–Oxide Interface. *J. Am. Chem. Soc.* **2017**, *139* (16), 5652–5655.

(269) Dutta, A.; Kuzume, A.; Rahaman, M.; Vesztergom, S.; Broekmann, P. Monitoring the Chemical State of Catalysts for CO_2 Electroreduction: An In Operando Study. *ACS Catal.* **2015**, *5* (12), 7498–7502.

(270) Timoshenko, J.; Roldan Cuenya, B. In Situ/Operando Electrocatalyst Characterization by X-Ray Absorption Spectroscopy. *Chem. Rev.* **2021**, *121* (2), 882–961.

(271) Ait Ahsaine, H.; Zbair, M.; BaQais, A.; Arab, M. CO_2 Electroreduction over Metallic Oxide, Carbon-Based, and Molecular Catalysts: A Mini-Review of the Current Advances. *Catalysts* **2022**, *12* (5), 1–26.

(272) Lu, Q.; Rosen, J.; Jiao, F. Nanostructured Metallic Electrocatalysts for Carbon Dioxide Reduction. *ChemCatChem* **2015**, *7* (1), 38–47.

(273) Baig, N.; Kammakakam, I.; Falath, W. Nanomaterials: A Review of Synthesis Methods, Properties, Recent Progress, and Challenges. *Mater. Adv.* **2021**, *2* (6), 1821–1871.

(274) Back, S.; Yeom, M. S.; Jung, Y. Active Sites of Au and Ag Nanoparticle Catalysts for CO_2 Electroreduction to CO. *ACS Catal.* **2015**, *5* (9), 5089–5096.

(275) Gao, D.; Zhou, H.; Wang, J.; Miao, S.; Yang, F.; Wang, G.; Wang, J.; Bao, X. Size-Dependent Electrocatalytic Reduction of CO_2 over Pd Nanoparticles. *J. Am. Chem. Soc.* **2015**, *137* (13), 4288–4291.

(276) Salehi-Khojin, A.; Jhong, H.-R. M.; Rosen, B. A.; Zhu, W.; Ma, S.; Kenis, P. J. A.; Masel, R. I. Nanoparticle Silver Catalysts That Show Enhanced Activity for Carbon Dioxide Electrolysis. *J. Phys. Chem. C* **2013**, *117* (4), 1627–1632.

(277) de Lucas-Consuegra, A.; Serrano-Ruiz, J.; Gutiérrez-Guerra, N.; Valverde, J. Low-Temperature Electrocatalytic Conversion of CO_2 to Liquid Fuels: Effect of the Cu Particle Size. *Catalysts* **2018**, *8* (8), 1–11.

(278) Lates, V.; Falch, A.; Jordaan, A.; Peach, R.; Kriek, R. J. An Electrochemical Study of Carbon Dioxide Electroreduction on Gold-Based Nanoparticle Catalysts. *Electrochim. Acta* **2014**, *128*, 75–84.

(279) Herzog, A.; Bergmann, A.; Jeon, H. S.; Timoshenko, J.; Kühl, S.; Rettenmaier, C.; Lopez Luna, M.; Haase, F. T.; Roldan Cuenya, B. Operando Investigation of Ag-Decorated Cu_2O Nanocube Catalysts with Enhanced CO_2 Electroreduction toward Liquid Products. *Angew. Chemie Int. Ed.* **2021**, *60* (13), 7426–7435.

(280) Kwon, Y.; Lum, Y.; Clark, E. L.; Ager, J. W.; Bell, A. T. CO_2 Electroreduction with Enhanced Ethylene and Ethanol Selectivity by Nanostructuring Polycrystalline Copper. *ChemElectroChem* **2016**, *3* (6), 1012–1019.

(281) Zhu, W.; Zhang, Y.-J.; Zhang, H.; Lv, H.; Li, Q.; Michalsky, R.; Peterson, A. A.; Sun, S. Active and Selective Conversion of CO_2 to CO on Ultrathin Au Nanowires. *J. Am. Chem. Soc.* **2014**, *136* (46), 16132–16135.

(282) Liu, S.; Tao, H.; Zeng, L.; Liu, Q.; Xu, Z.; Liu, Q.; Luo, J.-L. Shape-Dependent Electrocatalytic Reduction of CO_2 to CO on Triangular Silver Nanoplates. *J. Am. Chem. Soc.* **2017**, *139* (6), 2160–2163.

(283) Zhu, W.; Zhang, L.; Yang, P.; Hu, C.; Luo, Z.; Chang, X.; Zhao, Z.; Gong, J. Low-Coordinated Edge Sites on Ultrathin Palladium Nanosheets Boost Carbon Dioxide Electroreduction Performance. *Angew. Chemie Int. Ed.* **2018**, *57* (36), 11544–11548.

(284) Li, F.; Chen, L.; Knowles, G. P.; MacFarlane, D. R.; Zhang, J. Hierarchical Mesoporous SnO_2 Nanosheets on Carbon Cloth: A Robust and Flexible Electrocatalyst for CO_2 Reduction with High Efficiency and Selectivity. *Angew. Chemie Int. Ed.* **2017**, *56* (2), 505–509.

(285) Luo, W.; Nie, X.; Janik, M. J.; Asthagiri, A. Facet Dependence of CO_2 Reduction Paths on Cu Electrodes. *ACS Catal.* **2016**, *6* (1), 219–229.

(286) Loiudice, A.; Lobaccaro, P.; Kamali, E. A.; Thao, T.; Huang, B. H.; Ager, J. W.; Buonsanti, R. Tailoring Copper Nanocrystals towards C_2 Products in Electrochemical CO_2 Reduction. *Angew. Chemie Int. Ed.* **2016**, *55* (19), 5789–5792.

(287) Kortlever, R.; Shen, J.; Schouten, K. J. P.; Calle-Vallejo, F.; Koper, M. T. M. Catalysts and Reaction Pathways for the Electrochemical Reduction of Carbon Dioxide. *J. Phys. Chem. Lett.* **2015**, *6* (20), 4073–4082.

(288) Tang, W.; Peterson, A. A.; Varela, A. S.; Jovanov, Z. P.; Bech, L.; Durand, W. J.; Dahl, S.; Nørskov, J. K.; Chorkendorff, I. The Importance of Surface Morphology in Controlling the Selectivity of Polycrystalline Copper for CO_2 Electroreduction. *Phys. Chem. Chem. Phys.* **2012**, *14* (1), 76–81.

(289) Suen, N.-T.; Kong, Z.-R.; Hsu, C.-S.; Chen, H.-C.; Tung, C.-W.; Lu, Y.-R.; Dong, C.-L.; Shen, C.-C.; Chung, J.-C.; Chen, H. M. Morphology Manipulation of Copper Nanocrystals and Product Selectivity in the Electrocatalytic Reduction of Carbon Dioxide. *ACS Catal.* **2019**, *9* (6), 5217–5222.

(290) Reske, R.; Mistry, H.; Behafarid, F.; Roldan Cuenya, B.; Strasser, P. Particle Size Effects in the Catalytic Electroreduction of CO_2 on Cu Nanoparticles. *J. Am. Chem. Soc.* **2014**, *136* (19), 6978–6986.

(291) Yang, F.; Deng, D.; Pan, X.; Fu, Q.; Bao, X. Understanding Nano Effects in Catalysis. *Natl. Sci. Rev.* **2015**, *2* (2), 183–201.

(292) Zhu, W.; Michalsky, R.; Metin, Ö.; Lv, H.; Guo, S.; Wright, C. J.; Sun, X.; Peterson, A. A.; Sun, S. Monodisperse Au Nanoparticles for Selective Electrocatalytic Reduction of CO_2 to CO. *J. Am. Chem. Soc.* **2013**, *135* (45), 16833–16836.

(293) Zheng, X.; De Luna, P.; García de Arquer, F. P.; Zhang, B.; Becknell, N.; Ross, M. B.; Li, Y.; Banis, M. N.; Li, Y.; Liu, M.; Voznyy, O.; Dinh, C. T.; Zhuang, T.; Stadler, P.; Cui, Y.; Du, X.; Yang, P.; Sargent, E. H. Sulfur-Modulated Tin Sites Enable Highly Selective Electrochemical Reduction of CO_2 to Formate. *Joule* **2017**, *1* (4), 794–805.

(294) Wu, Z.-Z.; Gao, F.-Y.; Gao, M.-R. Regulating the Oxidation State of Nanomaterials for Electrocatalytic CO_2 Reduction. *Energy Environ. Sci.* **2021**, *14* (3), 1121–1139.

(295) Xing, Z.; Hu, L.; Ripatti, D. S.; Hu, X.; Feng, X. Enhancing Carbon Dioxide Gas-Diffusion Electrolysis by Creating a Hydrophobic Catalyst Microenvironment. *Nat. Commun.* **2021**, *12* (1), 1–11.

(296) Lin, J.; Yan, S.; Zhang, C.; Hu, Q.; Cheng, Z. Electroreduction of CO_2 toward High Current Density. *Processes* **2022**, *10* (5), 1–33.

(297) Nguyen, D. L. T.; Lee, C. W.; Na, J.; Kim, M.-C.; Tu, N. D. K.; Lee, S. Y.; Sa, Y. J.; Won, D. H.; Oh, H.-S.; Kim, H.; Min, B. K.; Han, S. S.; Lee, U.; Hwang, Y. J. Mass Transport Control by Surface Graphene Oxide for Selective CO Production from Electrochemical CO_2 Reduction. *ACS Catal.* **2020**, *10* (5), 3222–3231.

(298) Weng, L.-C.; Bell, A. T.; Weber, A. Z. Modeling Gas-Diffusion Electrodes for CO_2 Reduction. *Phys. Chem. Chem. Phys.* **2018**, *20* (25), 16973–16984.

(299) Wang, Y.; Zhou, J.; Lv, W.; Fang, H.; Wang, W. Electrochemical Reduction of CO_2 to Formate Catalyzed by Electroplated Tin Coating on Copper Foam. *Appl. Surf. Sci.* **2016**, *362*, 394–398.

(300) Kottakkat, T.; Klingan, K.; Jiang, S.; Jovanov, Z. P.; Davies, V. H.; El-Nagar, G. A. M.; Dau, H.; Roth, C. Electrodeposited AgCu Foam Catalysts for Enhanced Reduction of CO_2 to CO. *ACS Appl. Mater. Interfaces* **2019**, *11* (16), 14734–14744.

(301) Yang, K.; Kas, R.; Smith, W. A.; Burdyny, T. Role of the Carbon-Based Gas Diffusion Layer on Flooding in a Gas Diffusion Electrode Cell for Electrochemical CO_2 Reduction. *ACS Energy Lett.* **2021**, *6* (1), 33–40.

(302) Schwartz, N.; Harrington, J.; Ziegler, K. J.; Cox, P. Effects of Electrode Support Structure on Electrode Microstructure, Transport Properties, and Gas Diffusion within the Gas Diffusion Layer. *ACS Omega* **2022**, *7* (34), 29832–29839.

(303) Rabiee, H.; Ge, L.; Zhang, X.; Hu, S.; Li, M.; Yuan, Z. Gas Diffusion Electrodes (GDEs) for Electrochemical Reduction of Carbon Dioxide, Carbon Monoxide, and Dinitrogen to Value-Added Products: A Review. *Energy Environ. Sci.* **2021**, *14* (4), 1959–2008.

(304) Jouny, M.; Luc, W.; Jiao, F. General Techno-Economic Analysis of CO_2 Electrolysis Systems. *Ind. Eng. Chem. Res.* **2018**, *57* (6), 2165–2177.

(305) Wu, B.; Chen, J.; Qian, L. Recent Advances in Heterogeneous Electroreduction of CO_2 on Copper-Based Catalysts. *Catalysts* **2022**, *12* (8), 1–27.

(306) Liu, S.; Wang, X.-Z.; Tao, H.; Li, T.; Liu, Q.; Xu, Z.; Fu, X.-Z.; Luo, J.-L. Ultrathin 5-Fold Twinned Sub-25 nm Silver Nanowires Enable Highly Selective Electroreduction of CO_2 to CO. *Nano Energy* **2018**, *45*, 456–462.

(307) Zhang, W.; Yang, S.; Jiang, M.; Hu, Y.; Hu, C.; Zhang, X.; Jin, Z. Nanocapillarity and Nanoconfinement Effects of Pipet-like Bismuth@Carbon Nanotubes for Highly Efficient Electrocatalytic CO_2 Reduction. *Nano Lett.* **2021**, *21* (6), 2650–2657.

(308) Han, L.; Song, S.; Liu, M.; Yao, S.; Liang, Z.; Cheng, H.; Ren, Z.; Liu, W.; Lin, R.; Qi, G.; Liu, X.; Wu, Q.; Luo, J.; Xin, H. L. Stable and Efficient Single-Atom Zn Catalyst for CO_2 Reduction to CH_4. *J. Am. Chem. Soc.* **2020**, *142* (29), 12563–12567.

(309) Zhang, Y.; Dong, L.-Z.; Li, S.; Huang, X.; Chang, J.-N.; Wang, J.-H.; Zhou, J.; Li, S.-L.; Lan, Y.-Q. Coordination Environment Dependent Selectivity of Single-Site-Cu Enriched Crystalline Porous Catalysts in CO_2 Reduction to CH_4. *Nat. Commun.* **2021**, *12* (1), 1–9.

(310) Yang, D.; Zhu, Q.; Chen, C.; Liu, H.; Liu, Z.; Zhao, Z.; Zhang, X.; Liu, S.; Han, B. Selective Electroreduction of Carbon Dioxide to Methanol on Copper Selenide Nanocatalysts. *Nat. Commun.* **2019**, *10* (1), 1–9.

(311) Xu, H.; Rebollar, D.; He, H.; Chong, L.; Liu, Y.; Liu, C.; Sun, C.-J.; Li, T.; Muntean, J. V.; Winans, R. E.; Liu, D.-J.; Xu, T. Highly Selective Electrocatalytic CO_2 Reduction to Ethanol by Metallic Clusters Dynamically Formed from Atomically Dispersed Copper. *Nat. Energy* **2020**, *5* (8), 623–632.

(312) Peng, C.; Luo, G.; Zhang, J.; Chen, M.; Wang, Z.; Sham, T.-K.; Zhang, L.; Li, Y.; Zheng, G. Double Sulfur Vacancies by Lithium Tuning Enhance CO_2 Electroreduction to N-Propanol. *Nat. Commun.* **2021**, *12* (1), 1–8.

(313) Marepally, B. C.; Ampelli, C.; Genovese, C.; Tavella, F.; Veyre, L.; Quadrelli, E. A.; Perathoner, S.; Centi, G. Role of Small Cu Nanoparticles in the Behaviour of Nanocarbon-Based Electrodes for the Electrocatalytic Reduction of CO_2. *J. CO_2 Util.* **2017**, *21*, 534–542.

AIM OF THE WORK

In the framework of the new generation of electrocatalysts suitable for applications in sustainable CO_2 reduction technologies, this work aims to develop novel materials synthesised from non-hazardous chemical compounds to be used as eco-friendly cathodes to carry out the reaction. Indeed, taking advantage of the mild operative conditions typical of the electrochemical CO_2 reduction approach, the studies described in this thesis have the ambitious goal of providing selective electrochemical platforms capable to work at low cathodic potentials, ensuring a low environmental impact.

In particular, they were devoted to the design of nanostructured Cu-based materials electrodeposited on carbonaceous gas diffusion supports, capable to drive the reaction towards C_1 and C_2 products using water as source of protons. Such platforms represent good candidates for the development of low-cost electrodes suitable for the artificial photosynthesis-oriented systems which in turn exploit an electrical current where electrons are preferably gained from renewables.

The initial step of this work involved the optimisation of nanostructured Cu films loaded onto the C-based supports through an easy, time-effective, and low-cost electrochemical process followed by further chemical and electrochemical treatments. The morphology of each electrocatalyst was thoroughly investigated by scanning electron microscopy, X-ray diffraction, Raman spectroscopy, and electrochemical analyses. The screening of potentials (from -0.4 to -1.1 V, *vs* RHE) and the kinetic studies were carried out using a H-type cell filled with $KHCO_3$ aqueous solution. The catalytic activities were evaluated in terms of productivity and selectivity, with the aim of defining the most promising chemical composition of the electrocatalyst, along with the "greener" reaction conditions.

Once those parameters were established, the aim shifted towards the production of a more efficient electrocatalyst able to enhance the interaction between the active phase and the reactant, so increasing the productivity towards the desired C_2 product.

To this aim, layered double hydroxides (LDHs) composed of Cu, Mg, and Al were obtained over the same supports applying again an environmental-friendly electrochemical method, whose parameters were optimised from already reported procedures. Such inorganic clays were initially used as precursors for the formation of well dispersed Cu-containing catalysts within mixed non-redox metal oxides by means of further calcination and reduction processes. Again, each electrocatalyst was tested in the most selective operative conditions and, by testing the pristine CuMgAl LDH, unprecedent results were obtained, paving the way for the use of LDHs in reduction electrochemical process.

Optimisations in terms of cations molar ratio and amount of loaded catalyst, as well as characterisations of the most promising LDH, have been carried out and outstanding results, in terms of acetic acid productivity compared to the state of the art, have been obtained. Moreover, the best electrocatalyst was investigated via *operando* and *in situ* analyses which provided the intimate details of the catalytic active surface during the course of the reaction, thus making the control over its selectivity towards acetic acid possible.

CHAPTER 2

Nanostructured Copper-based Electrodes Electrochemically Synthesised on a Carbonaceous Gas Diffusion Membrane with Catalytic Activity for the Electroreduction of CO_2

Among the new generation of electrocatalysts for the CO_2ER reaction, the nanostructured materials are gaining momentum in view thanks to their unique ability to finely tune the selectivity to the desired product. Moreover, to reduce the great investment related to the use of metal electrodes, the carbonaceous materials represent the most promising alternative in terms of sustainability, availability, and scalability. In this scenario, the following chapter reports a comparative study among several nanostructured Cu-based electrodes with different oxidation states, loaded on a carbonaceous gas diffusion layer, in order to evaluate the most promising catalyst for the CO_2ER reaction in liquid phase.

The content of this chapter has been adapted from the following publication:

M. Serafini, F. Mariani, A. Fasolini, E. Scavetta, F. Basile, and D. Tonelli, "Nanostructured Copper-Based Electrodes Electrochemically Synthesized on a Carbonaceous Gas Diffusion Membrane with Catalytic Activity for the Electroreduction of CO_2", *ACS Applied Materials & Interfaces* **2021, *13*** (48), 57451-57461

2.1 Introduction

The global effort in pursuing effective decarbonisation strategies is depicting new scenarios towards alternative production chains.

In this context, the fascinating concept of solar-driven chemistry, realised with photochemical systems either including inorganic [1–7] or organic bio-hybrid [8] components, is attracting much attention thanks to the biomimetic approach towards a sustainable process, which culminates in the concept of artificial leaves [2,9,10]. In such a system, light is absorbed at a photoanode to generate electricity that is used *in situ* for the electroreduction of CO_2 to chemicals, thus ideally eliminating the need of any external power supply. To date, the design of lightweight, low-cost and low-power consuming electrocatalytic platforms for high-throughput CO_2 electrocatalytic reduction represents a major challenge for a future integration in the aforementioned artificial leaf. In this context, this work aims to develop novel active materials for cathode where the CO_2ER takes place, targeting future integration with solar-driven electrochemical cells [11].

Of particular interest is the direct production of acetic acid that is nowadays mainly obtained by industrial multistep chemical processes. Among them, Monsanto and Cativa chemical routes are the most common technologies used for the large-scale production of acetic acid which involve the use of precious metals such as rhodium or iridium-based homogeneous catalysts, respectively, within harsh operative conditions [12]. Indeed, both processes are based on liquid phase carbonylation reactions where methanol, derived from the oxidation of the natural gas, reacts with an excess of carbon monoxide at temperatures of 423 to 473 K and pressures of 30 to 60 atm, respectively. Although the Rh-based catalyst provides high selectivity, CO-deficient areas of the plant often cause an instability of the catalyst leading to the formation of inactive species or the loss of Rh as the insoluble RhI_3, along with the water gas shift reaction as side phenomenon.

Those limitations imposed strict rules in the whole reactor's configuration in order to preserve the efficiency of the reaction, and for this reason, in 1996 the catalyst was replaced by an iridium/iodide compound, and this change is known as the Cativa process. The process represents a step forward to the Monsanto industrial configuration, since the cheaper catalyst was found to be more robust, soluble, and stable in the same reaction conditions. Such new experimental conditions provided faster reactions which are essential to meet the current acetic acid's global demand of approximately 15 million tons per year [13]. Indeed, the main consumption of acetic acid mainly derives from the production of (i) vinyl acetate monomer, used in polymer industries, (ii) acetic anhydride, used as typical acetylation agent in textile industries, and (iii) C_1-C_4 acetates. Moreover, the acetic acid is widely employed as an excellent polar protic solvent.

However, the safety and environmental hazards of the current methodologies are a matter of serious concern. To this purpose, many researchers are working on developing sustainable and environmentally benign processes employing a lower supply of energy and a simpler design to produce acetic acid in substantial amount. To achieve the goal, the consumption of CO_2 and syngas likely offers an excellent alternative as a sustainable feedstock to develop innovative technologies, along with heterogenous catalysts that will simplify the separation steps, in view of commercial developments. One of these is represented by the electrochemical CO_2 conversion. Such an approach, under liquid or gas phase conditions, is a reaction by which hydrocarbons can be obtained at ambient temperature and atmospheric pressure, thus closing the carbon cycle with the production of added-value commodity chemicals, using electricity derived preferably from renewables. However, in order to produce acetic acid, which is a C_2 product, two parameters are essential: the active phase of the electrocatalyst and the experimental conditions, which influence the overall selectivity; therefore, it is crucial the choice of the material, the type of electrolyte and its pH, and the experimental set-up.

Due to its unique ability to catalyse CO_2ER towards a number of hydrocarbons, aldehydes and alcohols requiring more than two electrons transfers with substantial Faradaic Efficiencies (FE), Cu has been overall recognised as the gold standard among pure metal catalysts since 1985 [14–16].

In particular, Cu-based electrode interfaces are able to stabilise the chemisorbed $CO_2^{\cdot-}$ radical anions and CO species, which are the key intermediates in the initial phase of the catalytic CO_2 conversion and in the subsequent process of hydrocarbon and alcohol formation, respectively. This not only increases the CO surface concentration, thereby promoting those CO_2ER pathways involving C−C coupling reactions, but also blocks the reaction sites for the parasitic hydrogen evolution reaction (HER) [17,18]. Recent studies concerning liquid-phase CO_2ER have reported on the fundamental role of nano and micro-structure [19–22], as well as redox state [23,24] of Cu-based cathode materials in improving catalyst's selectivity and activity.

It has been showed that metallic Cu obtained after reduction of Cu_2O, which was formed by electropolishing and subsequent thermal annealing of a polycrystalline Cu foil, displayed enhanced current densities and Faradaic Efficiencies with respect to the pristine Cu foil [25]. The more active Cu catalyst was produced *in situ* during CO_2ER at -0.5 V *vs* RHE and led to formate production. The effect of the orientation and thickness of Cu_2O films electrodeposited on commercial Cu plates for CO_2ER performed at -1.1 V *vs* RHE was investigated by online electrochemical mass spectroscopy and XRD [23]. On the one hand, the selectivity towards the main product (formic acid) was demonstrated to largely depend on the film thickness rather than the orientation. On the other hand, the reaction was found to be actually catalysed by *in situ* formation of nanostructured Cu domains during the progress of the reaction itself.

The influence of CuO nanoparticles (NPs) morphology synthesised by hydrothermal method was studied during CO_2ER at -1.7 V *vs* RHE [26]. Again, *in situ* reduction to metallic Cu was reported, leading to good selectivity towards ethanol, while different electrocatalytic activities

were observed depending on the initial CuO NPs morphologies. Dendritic Cu catalysts electrodeposited on technical Cu mesh supports were also studied for the CO_2 electroreduction showing good Faradaic selectivity to formate and ethylene at -0.7 V and -1.1 V *vs* RHE, respectively [18]. Subsequent thermal annealing led to > C_1 alcohols formation (EtOH and n-PrOH at -1.0 V *vs* RHE).

Thermal and electrochemical activations of copper foils to form oxide-based catalysts for CO_2ER have been recently compared by Giri *et al.* [27]. Interestingly, the authors observed no relevant differences between the oxidation methods and showed, by XPS and XRD analyses, which all oxides reduced back to Cu^0 within the first few minutes of reaction. Higher currents and Faradaic Efficiencies were obtained from the activated samples and were ascribed to the increased surface area after Cu activation. Overall, these works suggest that the CO_2ER actually proceeds on Cu^0 sites that form during the first stages of the reaction. Nevertheless, the redox state and morphology of the starting oxides affect the reaction outcome in terms of selectivity and chemical nature of the products.

In other recent studies, the morphological evolution of electrochemically deposited cuprous oxide nanocubes during CO_2ER has been monitored using liquid cell transmission electron microscopy [28] (*in situ* TEM). Interestingly, pulsed electrolysis conditions were chosen to continuously regenerate Cu(I) species and the combination of Cu(100) domains, defect sites and surface Cu_2O was found to enhance the CO_2ER reaction pathway leading to C_{2+} products [24]. Similarly, high C_2 Faradaic efficiency (80%) was reported towards acetic acid and ethanol using a 3D dendritic Cu^0/Cu_2O composite electrochemically synthesised on a Cu foil, upon application of a reduction potential as low as -0.4 V *vs* RHE [29].

Efforts in the replacement of bulk metal cathodes with lightweight and low-cost carbonaceous supports, especially large-area gas diffusion electrodes, represent a step forward in the overall design of artificial photosynthesis-oriented systems.

The first attempts involving Cu-based catalysts for CO_2ER date back to the 90s and were motivated by the increased mass fixation of CO_2 provided by the porous and 3D structure of gas diffusion layers (GDLs) [30,31]. In more recent years, only a few works on liquid-phase CO_2ER catalysts based on Cu^0 NPs, either alone [32] or deposited on CNTs [4,33,34], and loaded on GDLs have been reported, where formic and acetic acids were the major products. However, to date the role of Cu morphology and redox state on CO_2ER products distribution has not yet been investigated on GDL supports, which is a crucial step to pave the way for the use of such low-cost and high surface area supports in the challenging electrochemical reaction.

In addition to the catalyst material, the chemical composition of the electrolyte employed for the CO_2ER plays a main role in the selectivity of this reaction. Aqueous electrolytes have been overall recognised as the best media to perform the reaction in terms of cost-effectiveness, sustainability, and availability [35]. However, the use of aqueous electrolytes causes some limitations in the overall reaction efficiency. This is because of the scarce CO_2 solubility in aqueous media at ambient conditions (~34 mM, at pH 7) and the presence of the competitive hydrogen evolution reaction (HER). Moreover, since the electrochemical CO_2 reduction needs relatively high cathodic potentials that favour the HER, the local pH at the electrode-electrolyte interface in aqueous environment tends to be significantly different from the bulk one. Such a difference is caused by the production of OH^- during the CO_2 reduction reaction (*e.g.*, $CO_2 + 2e^- + H_2O \rightarrow CO + 2OH^-$) and the simultaneous hydrogen evolution reaction ($H_2O + 2e^- \rightarrow H_2 + 2OH^-$) [36].

Starting from the earlier studies of Hori *et al.* [17,37], the role of the pH has been thoroughly investigated on Cu surface. Indeed, he demonstrated for the first time that the reaction selectivity towards C_1 or C_2 products is strongly dependent on the employed pH.

In particular, he discovered that the production of CH_4 was strongly pH dependent, while the production of C_2H_4 was independent of pH. Indeed, the production of C_1 products was inhibited at high pH values favouring the selectivity towards C_2. Such evidences were also confirmed by the group of Koper [38,39], who described two different pathways (pH dependent and independent), related to different rate determining steps (RDSs). The pH dependent pathway promoted, at low pH condition, the production of methane through the adsorbed $*CO_2^-$ species while, at high pH, stimulated the dimerization of CO towards the production of ethylene (C_2 products). Contrarily, the pH independent route, based on the adsorption of $*OCCO^-$ species derived from CO dimerization, preferentially promoted the formation of C_2 products. Hence, based on these experimental evidences, in order to favour the production of C_2 products and reduce the competitive HER, a higher local pH is preferred instead of an acidic environment. Therefore, to promote this shift in aqueous electrolytes, two main strategies can be exploited: the use of neutral or alkaline electrolytes and a different buffer strength (concentration of the salt).

The most widely employed electrolyte to test the catalytic activities of a target electrocatalyst in liquid phase CO_2ER is $KHCO_3$ [4,17,40,41]. Zhong *et al.* [42] carried out studies on the effect of CO_2 bubbling inside different electrolytes, *i.e.*, $KHCO_3$, K_2CO_3, KOH, KCl, and HCl. Along with theoretical calculations, the Authors demonstrated that the best electrolytes to perform the CO_2ER were $KHCO_3$ and KCl because they were capable to provide a high ratio of active carbonates species, *i.e.*, H_2CO_3 or HCO_3^-, which were assumed to favour a higher efficiency. Moreover, they provided stable pH values after 10 min of bubbling, maintaining neutral or slightly alkaline conditions for the $KHCO_3$ and an acidic pH for KCl, while avoiding strong pH variations up to 4-5 units as registered with KOH or K_2CO_3. More recently, Marcandalli *et al.* [43] investigated the importance of acid-base equilibria in hydrogen carbonate solutions on Au electrodes, and found out the fundamental role of HCO_3^- species acting as further source of

CO_2. A similar conclusion was observed also by Zhu *et al.* [44]. Indeed, they stated that the presence of HCO_3^- likely equilibrates the dissolved CO_2 thus promoting a higher CO_2 concentration at the surface of the electrode.

Besides, together with the type of electrolyte, the buffer strength is another parameter to consider. To this regard, Hori *et al.* [45] carried out several studies on differently concentrated solutions of $KHCO_3$ on polycrystalline Cu electrodes, demonstrating that the production of C_2 products, *i.e.*, C_2H_4 or CH_3CH_2OH was favoured by $KHCO_3$ solutions at lower concentration. The less concentrated $KHCO_3$ possessed a lower buffer strength, thus causing the pH to naturally increase at the surface of the electrode. However, recent studies on the effect of $KHCO_3$ concentration also have suggested that it has to be sufficiently high to guarantee a moderate electric conductivity directly affecting the reaction efficiency [46]. Indeed, concentrations below 0.1 M likely lower the conductivity of the solution, thus disfavouring electrochemical reactions.

Moreover, further investigations on the electrolyte highlighted that also the nature of the cation present in the electrolyte likely plays an important role. Several studies have been carried out by the group of Koper to investigate this issue in terms of reaction selectivity. Pérez-Gallent *et al.* [47] revealed that the formation of the hydrogenated dimer intermediate (OCCOH) was related to the size of the cation. Indeed, it was preferentially formed at low overpotential by employing smaller ions such as Li^+, K^+, and Na^+. The cation effect is, therefore, explained as a catalytic promotion effect capable to stabilise specific intermediates.

Such experimental evidences were also confirmed by density-functional theory calculations (DFT) that demonstrated the promotor effect of adsorbed K^+ on Cu electrode, which favours paths involving the $*CHO^-$ intermediate that can lead to C_2 products [48].

For those reasons, to obtain C_2 products, preferably in liquid phase, many research groups have chosen to employ aqueous $KHCO_3$ solutions, thanks to the ability to better buffer the local pH at the electrolyte-electrode interface, promoting a neutral pH [49].

Finally, the cell configuration where the CO_2 electroreduction takes place represents another fundamental aspect since the mass transport plays a central role for the progress of the reaction. As previously stated, a gas diffusion layer as support for the Cu active phase was chosen to replace the bulk metal electrode and provide high surface area. Such systems are suitable for both liquid and gaseous reaction conditions, even if one or the other determines which product can be obtained.

In 2015, Ampelli *et al.* [33] revealed that performing the CO_2ER in liquid and gaseous phase, employing the same electrocatalyst, the products selectivity considerably changed. Indeed, by using an electrolyte-less configuration (no electrolyte in the cathodic part), hydrocarbons and alcohols up to C_3-C_4 were detected in gas phase conditions, while acetic acid was mainly detected in liquid phase. According to the issues related to the liquid phase reaction and the use of aqueous electrolyte, the $KHCO_3$ solutions were maintained under a constant CO_2 bubbling in order to preserve the pH of the bulk solution and the reactant availability, thus keeping constant the boundary operating conditions during the whole test [42].

In this work, a set of nanostructured Cu catalysts has been loaded over a carbonaceous GDL (Toray carbon paper, shortly named CP) by simple and highly reproducible procedures, including first the Cu^0 electrodeposition and then a chemical or electrochemical oxidative treatment, leading to the formation of a pristine Cu^0/CP and of its oxidised forms Cu_2O-Cu^0/CP, CuO_x-Cu^0/CP and $Cu(OH)_2$-Cu^0/CP, respectively.

The materials have been exploited for CO_2ER in liquid phase to produce acetic acid as the main product, on the basis of the suitable conditions reported in literature.

The catalytic performances in terms of productivity and selectivity towards formic and acetic acids depend on the electrocatalyst morphology and Cu redox state, which can be finely tuned modifying the experimental parameters of the oxidation treatment.

2.2 Materials and Methods

2.2.1 Chemicals and Materials

Toray Carbon Paper (TGP-H-60), Nafion membrane N-115 (0.125 mm thick, ≥ 0.90 meq/g exchange capacity), copper tape and ammonium nitrate were purchased from Alfa Aesar. Copper nitrate trihydrate ($Cu(NO_3)_2 \cdot 3H_2O$), sulfuric acid, ethanol (96.0 – 97.2%), potassium hydroxide, hydrogen peroxide, ammonium persulfate, potassium hydrogen carbonate and phenol were purchased from Sigma-Aldrich. Pure carbon dioxide (≥ 99.9%) was acquired by Rivoira (S.r.l.). Deuterium oxide (99.96%) was purchased from Eurisotop. Gas sampling bags (Tedlar Bags) were obtained from Supelco. All chemicals were of reagent grade or higher.

2.2.2 Apparatus

The copper electrodeposition and the electrochemical characterisations of the support were carried out in a conventional three electrode cell and all potentials were controlled by a potentiostat (CH Instrument 660 C). 4 cm^2 sized Toray Carbon Paper was used as the working electrode, while a saturated calomel electrode (SCE) and a Pt gauze were used as the reference and counter electrodes, respectively. With the exception of the electrocatalytic tests, all the potentials are quoted *vs* SCE. The morphology and the structure of the catalysts were investigated by Scanning Electron Microscopy (SEM) using the E-SEM Zeiss EVO 50 Series Instrument. Energy Dispersive X-ray Spectroscopy (EDS) measurements were performed with an Oxford INCA system equipped with a 30 mm^2 Silicon Drift Detector. Raman spectra were recorded with the Renishaw Raman RM1000 equipped with a Leica DMLM optical

microscope. The excitation wavelength came from an argon laser adjusted at 514.5 nm with an outpower power of 25 mW. This power was reduced as needed by neutral density filters in order to prevent the sample damage. The crystalline phases and the dimensions of the crystallites were analysed by X-ray diffraction spectroscopy (XRD) using a PW1050/81 diffractometer (Philips/Malvern, Royston, UK) coupled with a graphite monochromator in the diffracted beam and controlled by a PW1710 unit (Cu Kα, λ = 0.15418 nm). The electrochemical CO_2 reduction reaction tests were carried out in a low volume, two-compartment electrochemical (H-type) cell (Pine Research Instrumentation, Inc.). The GDLs coated with the catalysts were used as the working electrodes, an Ag/AgCl (KCl sat.) electrode was used as the reference and a Pt gauze as the counter electrodes. ^{1}H-NMR spectra were recorded by means of an Inova 600 spectrometer (600 MHz, D_2O) coupled with a Triple Resonance Probe. Gaseous products were detected by a Thermo Focus GC with a carbon molecular sieve column (CARBOSPHERE 80/100 6*1/8) equipped with a TCD detector.

2.2.3 Pretreatment of the Carbonaceous Support

A total geometrical surface area of 4 cm^2 of Toray carbon paper (CP) was obtained from a 19 x 19 cm foil. Before copper deposition, the carbonaceous membrane was soaked in 1 M H_2SO_4 followed by treatment in pure EtOH for well-defined times, whose optimisation will be discussed in Section 3.1.2.

2.2.4 Electrodeposition of Cu^0 on the Carbon Paper Electrode

The electrodeposition of metal copper was performed in a conventional three electrode cell by applying a constant potential of -0.4 V *vs* SCE for 500 s. The electrolytic solution was composed of 0.15 M $Cu(NO_3)_2 \cdot 3H_2O$ and 0.70 M NH_4NO_3. The pre-treated CP was employed as the working electrode and coupled with a Pt gauze and SCE as counter and reference electrodes, respectively.

The as-obtained Cu^0 thin layer was carefully washed in mono-distilled H_2O and then dried at 333 K overnight. The pristine metal copper electrocatalyst was named Cu^0/CP.

2.2.5 Oxidative Treatment of the Pristine Cu^0/CP

Once the Cu^0 electrocatalyst had been obtained, the copper oxidation state was tuned by means of simple chemical and electrochemical methods. Three different oxidised catalysts were obtained as follows:

a. The Cu_2O-Cu^0/CP catalyst was achieved by applying a constant potential of -0.4 V *vs* SCE for 720 s in 0.5 M KOH aqueous solution, obtaining a thin Cu_2O film over the metal copper deposit.

b. The $Cu(OH)_2$-Cu^0/CP and the CuO_x-Cu^0/CP catalysts were chemically obtained. Indeed, Cu^0/CP electrodes were soaked for 20 min in two different 2.5 M NaOH solutions adding either 0.1 M $(NH_4)_2S_2O_8$ in order to obtain the copper hydroxide, or 0.1 M H_2O_2 to obtain a mixture of copper oxides, along with a metal copper layer that, in both cases, was still present.

The morphologies and the structures of each electrocatalyst were thoroughly investigated by SEM-EDS, Raman and X-ray diffraction analysis.

2.2.6 Liquid Phase CO_2 Electroreduction Tests

The electrochemical reduction tests were performed in a H-type cell equipped with a proton exchange polymeric membrane (Nafion-115). Both sides of the cell were filled with 0.3 M $KHCO_3$ as the electrolyte. The cathodic side was pre-saturated with a constant flux of pure CO_2 (20 mL min^{-1}) for 30 min, which was maintained at 5 mL min^{-1} during the reaction.

An Ag/AgCl (KCl sat.) electrode and a Pt gauze were located in the anodic part of the cell, while the electrocatalyst was placed in the cathodic side (Figure 2.1). All the applied potentials used for the CO_2ER are referred to the reversible hydrogen electrode (RHE).

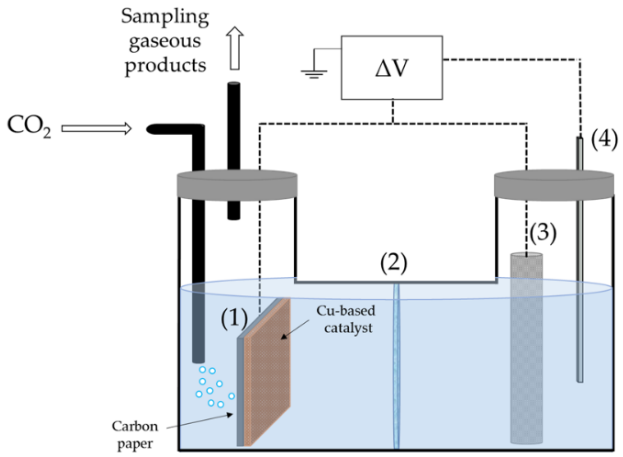

Figure 2.1. Scheme of the reaction set-up for the liquid phase CO_2ER. (1) Working electrode, (2) Nafion membrane, (3) counter electrode – Pt gauze, (4) reference electrode – Ag/AgCl (KCl sat.). Electrolyte 0.3 M $KHCO_3$

The liquid products were analysed by a quantitative H^1-NMR analysis, adding phenol as the internal standard and deuterium oxide to provide an internal lock signal. Gaseous products were collected in a gas sampling bag for all the duration of the electrocatalytic test and analysed by gas chromatography. When different reaction times were investigated, a new catalyst was electrodeposited each time. All the electrocatalytic tests were carried out as single tests.

2.3 Results and Discussion

2.3.1 Carbonaceous Support for the Catalysts

2.3.1.1 Morphology and XRD Characterisation

Toray Carbon Paper was chosen as the conductive support on which the electrocatalyst was deposited. Mostly known for its large use as a gas diffusion layer (GDL) in the proton exchange membrane fuel cells (PEMFC), the CP structure is composed of three main features [50].

The long, thin and randomly distributed fibers provide good electrical conductivity and act as the active phase during electrodeposition, while the void regions among them assure a good carbon dioxide transfer, in both liquid and gas phases. The third feature is ascribed to a carbon binder, which guarantees strength and durability of the fibers. The bare CP was morphologically investigated by SEM, as shown in Figure 2.2a.

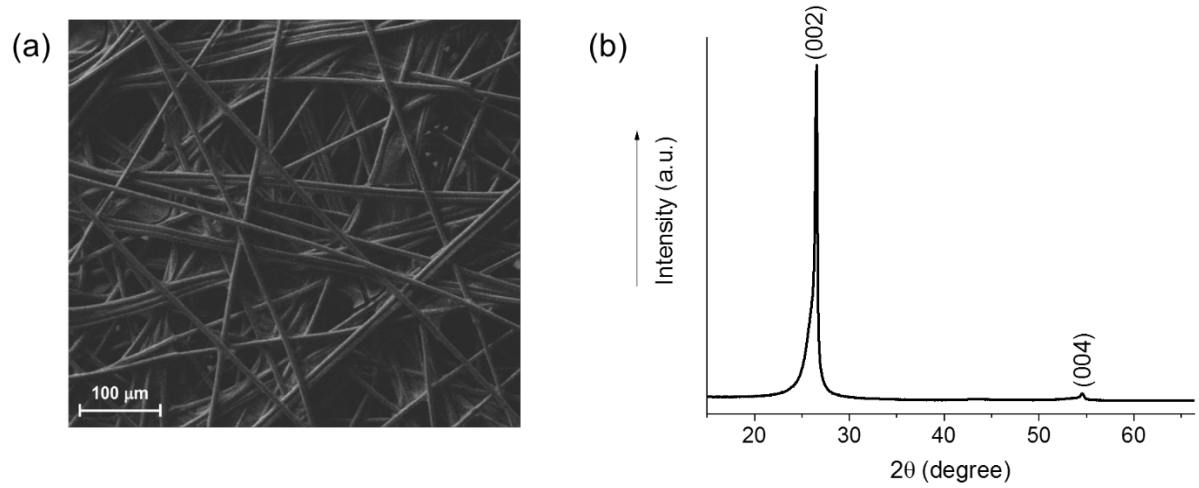

Figure 2.2. SEM image (a) and XRD diffraction pattern (b) of the pristine Toray carbon paper surface

The majority of the carbon fibers can be individually visualised with an average diameter of 7 µm, but also fibers linked together by the carbon binder can be distinguished, forming larger areas of conductive fibers. Moreover, X-ray diffraction analysis was conducted in order to evaluate the crystalline structure of the carbon support. The diffraction pattern, which is given in Figure 2.2b, was compared to the standard ICSD. The reflection pattern was assigned to hexagonal graphite (ICSD No 98-005-3029) [51], which shows the most intense signal at 26.5° and another one which is less intense at 54.6°, corresponding to (002) and (004) planes, according to Miller indices, respectively.

2.3.1.2 Optimisation of the Carbon Gas Diffusion Layer Pretreatment

The cleaning procedure of the catalyst support is a fundamental step to obtain a reproducible and well adherent coating. In this study, an already reported pre-treatment was adopted [52] that guaranteed: (i) an effective cleaning of the carbon support from organic and inorganic impurities without altering the structure of the fibers, (ii) an increase of its hydrophilicity, (iii) good reproducibility of the electrodeposition process, and (iv) short preparation times. 1 M H_2SO_4 and pure EtOH sequential baths were used for this purpose. We tested five treatment combinations in both acidic and alcoholic environments upon variation of the residence times. The effect of the pretreatment was investigated by Raman spectroscopy (Figure 2.3) and the attention was focused on the two typical bands of the carbonaceous materials: the "D-band" (1354 cm^{-1}), which represents the vibration of the defects inside the crystalline structure, and the "G-band" (1581 cm^{-1}) that is related to the C-C vibrations of graphite (Figure 2.3a).

(a)

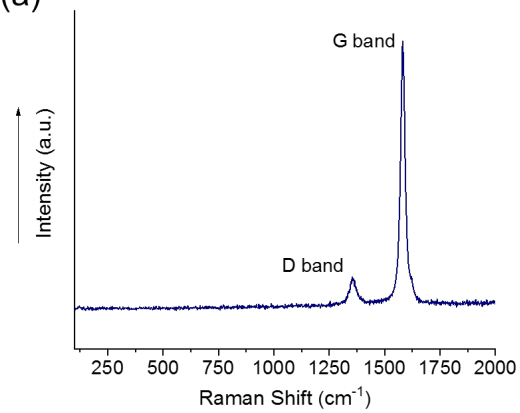

(b)

Pre-treatment method	*R value*
None	0.29
24h 1M H_2SO_4 + 24h pure EtOH	0.24
2h 1M H_2SO_4 + 1h pure EtOH	0.19
8h pure EtOH	0.21
8h 1M H_2SO_4	0.25

Figure 2.3. (a) Typical D and G bands referred to the disordered and ordered carbonaceous structure and (b) R values obtained for different pre-treatments

The ratio between them, known as the "R-value" [53], indicates the degree of ordered graphite crystallites inside the structure.

In Figure 2.3b is displayed the R-value (I_D/I_G) related to the five samples coming from the different pretreatments. Overall, the Toray Carbon Paper after acidic and alcoholic treatments for 2 h and 1 h, respectively, reported the lowest ratio (R-value = 0.19), which means that the disordered carbonaceous components on the surface were reduced, thus favouring a greater contribution of the crystalline structure. Therefore, the aforementioned pre-treatment was chosen for the GDL support. Finally, an electrochemically active surface area (ECSA) evaluation was performed using cyclic voltammetry (CV) for the chosen pre-treated CP. A potential range of 100 mV centred around the open circuit value was set and several CVs with different scan rates were recorded, obtaining an average ECSA of 39 cm^2 and a roughness factor (RF) of 9.75. The increase of the ECSA in comparison to the geometrical area is fully explained by the fibers structure of the paper.

2.3.2 Copper-based Catalysts Electrodeposited on the GDL

2.3.2.1 Synthesis and Morphological/Structural Characterisation of the Cu^0/CP Electrocatalyst

The electrodeposition of a thin layer of metal copper over the carbonaceous membrane was performed by applying a constant voltage for a well-defined time, as reported in Figure 2.4a.

The reaction that occurred at the CP, used as the working electrode, is the following:

$$Cu(NO_3)_2 + 2e^- \rightarrow Cu^0 + 2NO_3^- \quad (1)$$

The progress of the reaction was investigated recording SEM images at different times in order to follow the evolution of the Cu^0 deposition over the carbon fiber.

The nucleation of sub-micrometric copper particles started after 1.5 s, as shown in Figure 2.4b, and a maximum current density of 21.7 mA cm^{-2} was recorded.

Afterwards, the current density began to decrease and reached a constant value of 15.6 mA cm^{-2}, due to the diffusion processes [54], while the particles were still growing (Figure 2.5) until the end of the deposition process. Besides, as the particles started to increase their dimensions, it can be noticed that crystal agglomerates rather than large single crystals mainly formed.

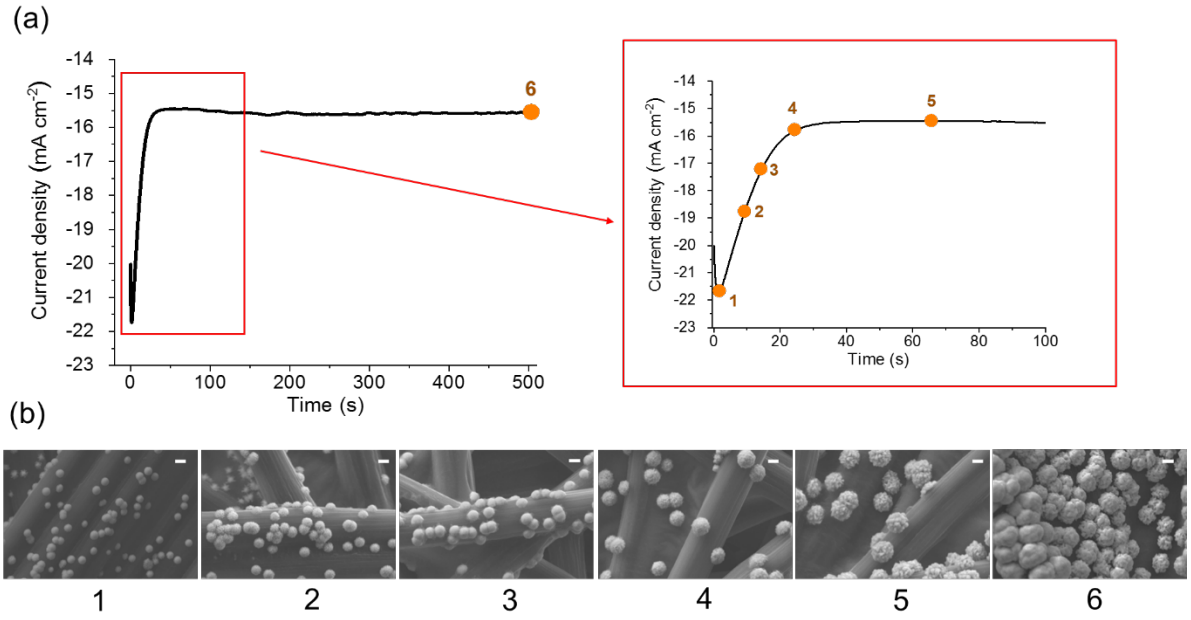

Figure 2.4. (a) Chronoamperometric curve (i *vs* t) recorded during the metal copper deposition over the carbonaceous support of 4 cm^2 size and (b) SEM images obtained at the six different times as shown (scale bar = 1 µm)

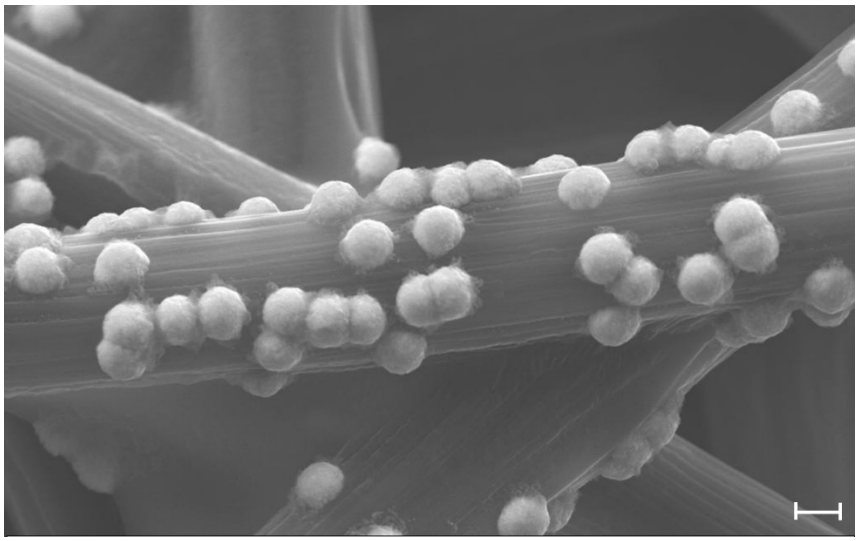

Figure 2.5. Growth of the metal copper particles over the carbon fiber (17 s passed) scale bar = 2 µm

After 500 s, a homogeneous covering of the conducting fibers was achieved and the metal copper deposit showed good adhesion to the 3D carbonaceous substrate (Figure 2.6).

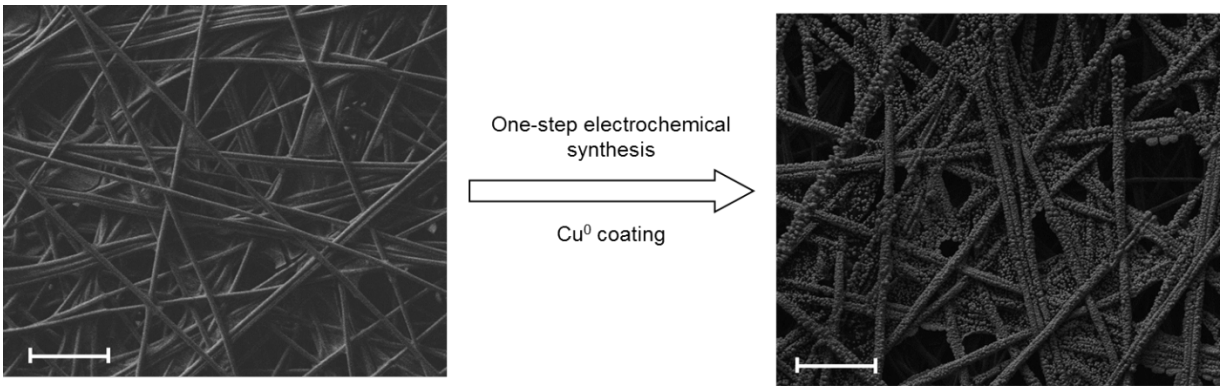

Figure 2.6. SEM images of the thin metal copper deposition over the carbon fiber support. Scale bar = 100 µm

Moreover, the reproducibility of the Cu mass was investigated, obtaining an average of (10 ± 1) mg for 20 electrodepositions. Interestingly, the Cu^0 coating occurred only on the superficial fibers, leaving the underlying ones completely uncovered.

Due to the poor interactions of carbon dioxide with the bare fibers, this fact could facilitate the passage of CO_2 through the 3D structure of the carbon paper to reach the thin catalyst surface oriented towards the anode, where protons are produced. X-ray diffraction spectroscopy was performed on the as-obtained electrocatalyst (Figure 2.7).

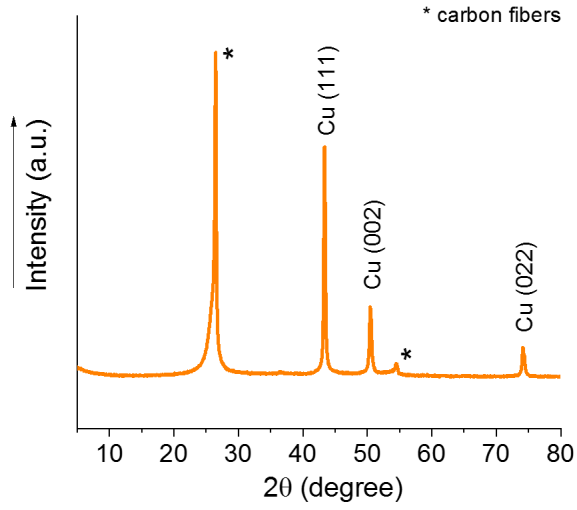

Figure 2.7. X-ray diffraction pattern of the copper deposit over the fibers

The XRD pattern exhibited three distinct reflections ascribable to the Cu^0 cubic crystal system (ICSD No 98-006-2848) within (111), (002) and (022) crystalline planes at 43.6°, 50.6° and 74.2° (2θ) [55]. Moreover, an average size of 36 nm for the Cu crystallites was achieved by applying the Scherrer's equation, as given below:

$$\overline{CS} = \frac{K \cdot \lambda}{\beta \cdot cos\theta} \quad (2)$$

where K represents the Scherrer's constant (0.9), λ is the radiation wavelength, β is the full-width at half-maximum and θ is the Bragg's angle.

2.3.2.2 Electrochemical Characterisation of Cu^0/CP Electrocatalyst

Figure 2.8a shows the linear sweep voltammetry (LSV) study carried out on the Cu^0/CP electrocatalyst, performed in a typical three electrode cell filled with 0.3 M $KHCO_3$, either saturated with N_2 (inert condition) or CO_2 (reaction condition). CO_2 was bubbled for at least 20 min to ensure a constant pH of the electrolyte [42]. The potential was scanned from 0 to -1.5 V *vs* SCE, at 10 mV s^{-1}.

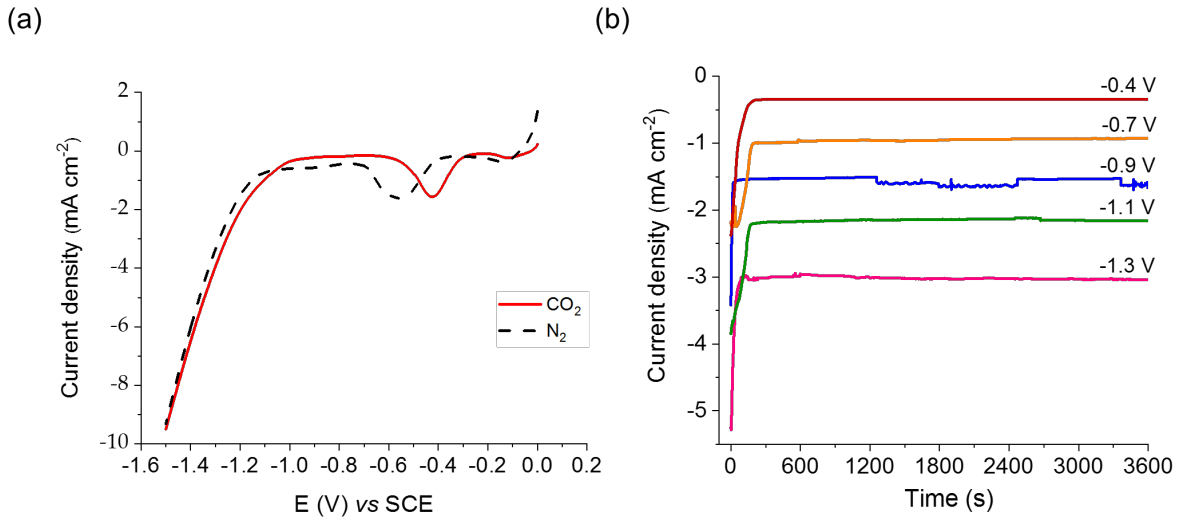

Figure 2.8. (A) LSV curves of the Cu^0/CP electrocatalyst in CO_2 (red line) and N_2 (black dashed line) saturated 0.3 M $KHCO_3$. (b) Current densities for CO_2ER recorded at five Cu^0/CP electrodes at the shown potentials (V *vs* RHE) with CO_2 bubbling of 5 mL min^{-1}

It can be noticed that the onset potential at which the hydrogen evolution reaction (HER) takes place is slightly anticipated in the presence of CO_2 (from -1.1 V to -0.95 V *vs* SCE). According to Dongare *et al.* [32], the current density recorded with the N_2 saturated electrolyte is ascribable to the catalyst electroreduction itself coupled with the hydrogen evolution. On the other hand, the maximum current density recorded after the onset potential shown in the red-curve (CO_2 saturated electrolyte) was slightly higher, probably due to the contribution of the carbon dioxide reduction.

The Faradaic peaks observed at -0.42 V (red curve) and -0.55 V *vs* SCE (black curve) can be associated with the reduction of surface Cu oxides locally formed during the LSV characterisation. Due to the lower pH of the CO_2 saturated electrolyte, the reduction of oxidised Cu species results facilitated, occurring at less cathodic potential. Figure 2.8b shows several chronoamperometric curves recorded at a Cu^0/CP electrode during CO_2ER in different potential-controlled electrolysis conditions with CO_2 continuously flowing. Herein, the current densities rapidly decreased from the very first step of the reaction until a plateau value, which linearly increased as the applied potential was more cathodic (R^2 = 0.998). Differently from other literature reports [32], the potential increase did not lead to significant disturbance in the recorded current.

2.3.2.3 Oxidative Functionalisation and Characterisation of the Cu^0/CP-derived Electrocatalysts

Once the Cu^0-based gas diffusion electrode was fully investigated, simple chemical and electrochemical methods were employed to selectively change the copper redox couple acting as active phase. A first functionalisation of the Cu^0 layer was achieved by performing a potential-controlled electrochemical oxidation at -0.4 V *vs* SCE in 0.5 M KOH as electrolyte for 12 min, leading to the Cu_2O-Cu^0/CP catalyst.

The potential for the electrochemical oxidation was selected on the basis of a cyclic voltammetry study on the pristine Cu^0/CP catalyst, as shown in Figure 2.9, which was in accordance with the literature [56].

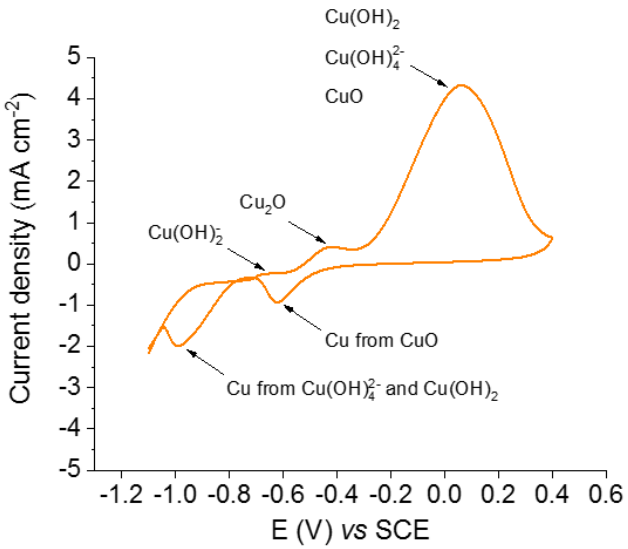

Figure 2.9. CV study on the Cu^0/CP electrocatalyst in 0.5 m KOH, scan rate 50 mv s^{-1}, N_2 atmosphere. Peaks assigned from a reported study [56]

Two further copper oxide-based electrocatalysts were obtained by simple chemical oxidations, soaking the pristine Cu^0/CP in strong oxidising mixtures for a relatively short time. The species produced on the pristine metal copper layer were $Cu(OH)_2$ and CuO_x, depending on the chemical nature of the oxidant.

A comprehensive morphological and structural characterisation of the copper-derived samples is reported in Figure 2.10.

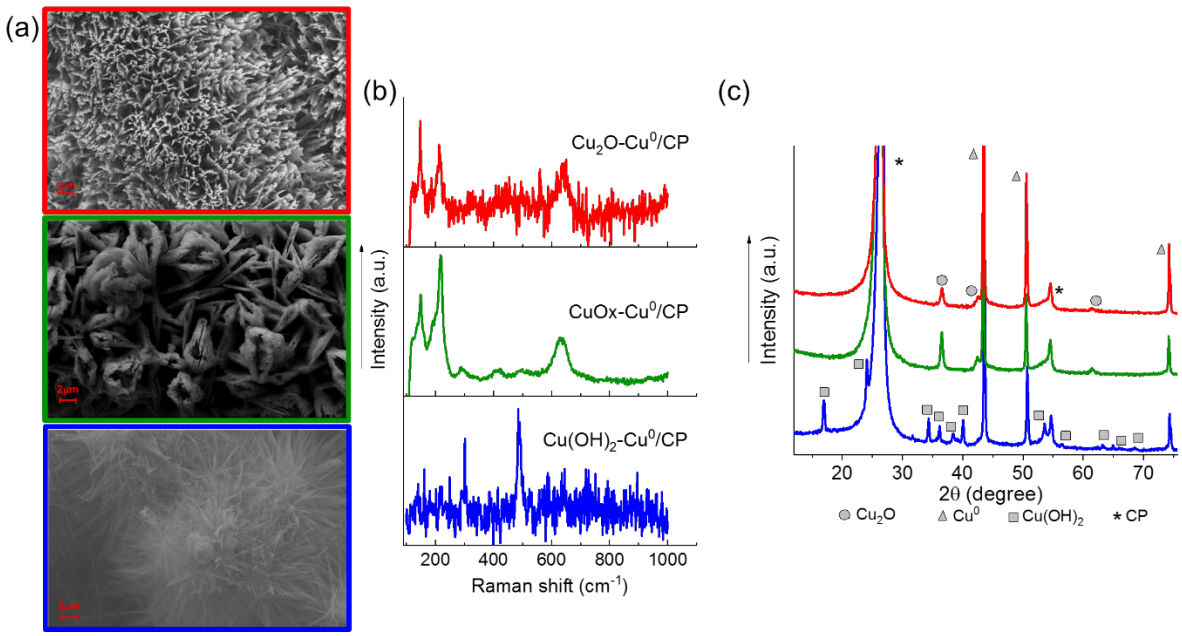

Figure 2.10. (a) SEM images, (b) Raman spectra and (c) X-ray diffraction patterns of the oxidised copper species derived from the pristine Cu^0/CP: Cu_2O-Cu^0/CP (red line), CuOx-Cu^0/CP (green line) and $Cu(OH)_2$-Cu^0/CP (blue line)

If compared to the metal copper deposit above described, the SEM images highlight different morphologies which are typical of the oxidised species, while the corresponding Raman and X-ray diffraction patterns reveal the nature of each catalyst.

In Figure 2.10, the red-evidenced catalyst was confirmed to be Cu_2O-Cu^0/CP by XRD, Raman analyses and SEM image revealed fibers fully covered by thin and dense flaps with a thickness lower than 100 nm and arranged perpendicularly with respect to the fibers. The electrochemical oxidative treatment has converted the spherical metal copper particles in a segmented nanosheets-like coating characterised by a strong increase of both the surface area of the active material and the void spaces. The X-ray diffraction pattern showed the typical reflections at 36.6°, 42.5° and 61.7° (2θ) (ICSD No. 98-006-2467) [57], referred to the crystalline planes (111), (002), (022), respectively, likewise of the pristine Cu^0/CP catalyst crystal structure.

Moreover, compared to the crystallites size of the metal copper deposit, the average dimension of the cuprite crystallites was only 3 nm larger, with an average value around 39 nm. In addition, the Raman spectrum displayed the typical peaks of cuprous oxide at 147, 212 and 641 cm^{-1} with much lower intensities than those recorded for the other catalysts [58], thus suggesting the presence of a very thin oxidised layer over the pristine metal copper. The catalyst obtained by chemical oxidation in a mixture of H_2O_2 30% *v/v* and NaOH (Figure 2.10, green-evidenced) had a uniform shuttle-like microstructure, similarly to the CuO nanoparticles obtained by a sol-gel method developed by Narsinga Rao *et al.* [59]. Contrary to their nanoparticles, which were 800 nm length with a thickness of 130 nm, the length of a single shuttle was quite higher around 8-7 μm with a thickness lower than 600 nm. The Raman analysis displayed the presence of a broad peak at 288 cm^{-1} with a shoulder at 334 cm^{-1}, ascribable to the CuO species [60], in addition to the typical peaks of Cu_2O. Moreover, optical microscope images (not showed) revealed the coexistence of weak blue thin fibers growing from the copper deposit along the fibers, similar to the one that will be described just below. Those singular components were hard to analyse because of their smaller sizes, but it was also possible to confirm the presence of $Cu(OH)_2$ species (see below). Therefore, by employing a relatively mild chemical oxidation, we were able to obtain an electrocatalyst in which the surface of the metal copper layer was fully covered by all three copper-oxide species Cu_2O, CuO and $Cu(OH)_2$. Due to the small crystallites size of the hydroxide and the bulk nature of the technique, the XRD pattern recorded for this catalyst only highlighted Cu_2O and Cu^0 crystalline planes without showing the typical reflections of tenorite species. The average crystallites dimension for Cu_2O resulted 28 nm, thus confirming a smaller size than the others. The third catalyst was produced in a stronger oxidising condition, soaking the Cu^0/CP in a mixture of ammonium persulfate and sodium hydroxide (blue-evidenced). In this case, the SEM image highlighted the formation of a flower-like structure, where the spherical agglomerates of the metal copper were surrounded by very thin needles,

which the further structural characterisations confirmed to be copper hydroxide. In particular, the Raman spectrum exhibited the characteristic peak at 490 cm^{-1} [61], while the XRD analysis showed a multitude of peaks at 17.0°,24.1°, 34.4°, 36.2°, 38.4°, 40.1°,53.6°, 56.5°, 63.3°, 64.9°, 68.62° (2θ) (ICSD 98-002-8484) [62] referred to the (020), (021), (002), (111), (022), (130), (132), (151), (200), (152) and (221) crystalline planes, respectively, with an average crystallites size of 49 nm.

2.3.3 Liquid Phase CO_2 Electroreduction Tests

2.3.3.1 Perfomances of the Potentiostatic Electroreduction

The optimised nanostructured electrocatalysts were tested for the reduction of carbon dioxide in liquid phase, as detailed in the material section, using the electrochemical setup showed in Figure 2.1. The pristine Cu^0/CP catalyst was employed to carry out a complete screening of the potentials applied during 1h reaction. The reactions occurring at the electrocatalyst surface are shown in Table 2.1, together with their standard reduction potentials.

Table 2.1. CO_2ER products with standard potentials calculated via the Gibbs free energy. Reported from Zhao *et al*. [63]

Reaction	E^0 *(V) vs RHE*
$2H^+ + 2e^- \rightarrow H_{2(g)}$	0.0
$CO_2 + 2e^- + 2H^+ \rightarrow CO_{(g)} + H_2O$	-0.10
$CO_2 + 2e^- + 2H^+ \rightarrow HCOOH_{(aq)}$	-0.12
$2CO_2 + 8e^- + 8H^+ \rightarrow CH_3COOH_{(aq)} + 2H_2O$	+0.11

The products distribution as a function of the applied potentials is reported in Figure 2.11.

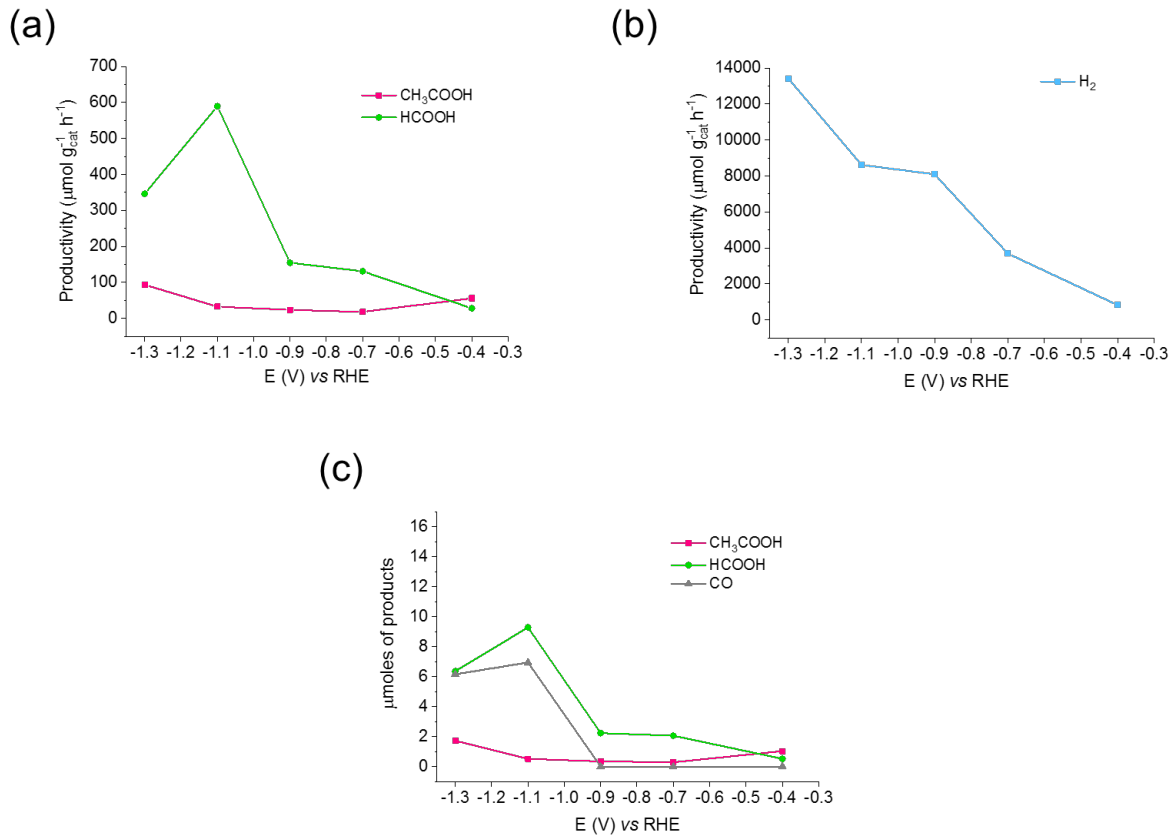

Figure 2.11. Product distribution obtained during the screening of the applied potentials using the pristine Cu^0/CP electrocatalyst. (a) Productivities of liquid products; (b) productivity of H_2 and (c) detected moles of CO_2ER products

It is worth to note that -1.1 V was reported as the potential value at which the highest amount of CO_2 reduction products can be obtained, as stated by Kuhl *et al.* [64], and, in our case, the best formic acid productivity and selectivity were obtained. Differently, acetic acid was the major product obtained at the least cathodic potential (-0.4 V *vs* RHE). Moreover, in the latter condition, the lowest amount of H_2 as side product was detected. Therefore, these two potentials leading to the most interesting reaction outcomes were investigated during the following tests with the oxidised electrocatalysts. The resulting products distributions are showed in Figure 2.12 and the recorded current densities are reported in Table 2.2.

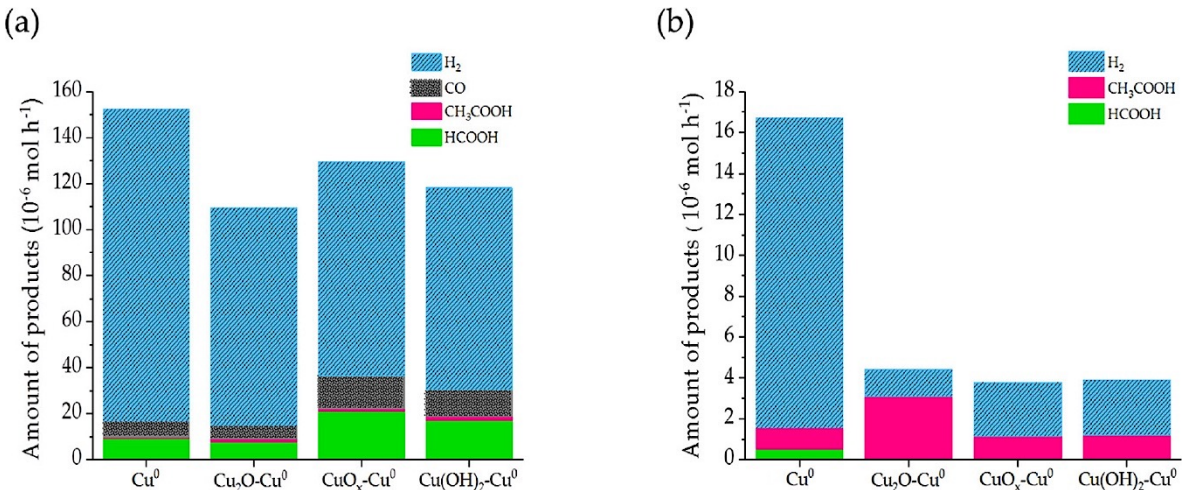

Figure 2.12. CO_2ER products distribution for 1h reaction at (a) -1.1 V *vs* RHE and (b) -0.4 V *vs* RHE

Table 2.2. Recorded current densities corresponding to the reactions whose product distributions are reported in Figure 2.12

Potential (V vs RHE)	*Electrocatalyst*	J_{tot} *(mA cm^{-2})*
-1.1	Cu^0	2.20
	Cu_2O-Cu^0	2.58
	CuOx-Cu^0	2.08
	$Cu(OH)_2$-Cu^0	2.32
-0.4	Cu^0	0.38
	Cu_2O-Cu^0	0.46
	CuOx-Cu^0	0.93
	$Cu(OH)_2$-Cu^0	0.62

Comparing the results at the two voltages, the first evidence that stands out is the different products distribution.

Indeed, by setting the most cathodic potential (-1.1 V *vs* RHE), shown in Figure 2.12a, hydrogen is observed as the main gaseous product, especially for the pristine Cu^0/CP electrode, but its presence is due to a side reaction (HER) with no carbon dioxide involved, and a fair amount of carbon monoxide is present. On the other hand, considering the liquid phase, H^1-NMR analysis revealed the presence of formic acid as the main product and of a small amount of acetic acid. The Faradaic efficiency (FE) was ~ 80% for hydrogen evolution, ~ 4, 7, and 1 %, for CO, $HCOO^-$ and CH_3COO^- production, respectively.

When using the other three catalysts based on the oxidised species of copper, the same products and an analogous behaviour was pointed out, but the FE for the hydrogen evolution decreased to a value of ~ 50%, regardless of the employed catalyst.

The greatest amounts of CO (14.4 μmol h^{-1}) and HCOOH (21.0 μmol h^{-1}) were obtained using the CuOx-Cu^0/CP electrocatalyst, and they progressively decreased when the catalysts were $Cu(OH)_2$-Cu^0/CP and Cu_2O-Cu^0/CP. Therefore, by applying the most cathodic potential, it was not possible to select the electrocatalyst fulfilling the best compromise between the total moles of products from CO_2ER and selectivity to useful products (such as acetic and formic acid). Therefore, a lower cathodic potential (-0.4 V *vs* RHE) was applied. In such a case, the only detected gaseous compound was hydrogen for all the tested catalysts, in much lower amounts with respect to the previous results, and, interestingly, the H^1-NMR analysis revealed appreciable amounts of acetic acid as the only reduced species in liquid phase.

Again, at the Cu^0/CP electrode the highest amount of hydrogen was evolved, so confirming that metal Cu alone does not favour the CO_2 electroreduction. Indeed, at less cathodic potentials as highlighted in Figure 2.12b, the selectivity for acetate production was very good, and the electrocatalyst that provided the greatest amount of acetate was the Cu_2O-Cu^0/CP. In particular, the produced μmoles were three times higher than the values obtained with the other two electrocatalysts based on oxidised species of copper, and meanwhile the hydrogen evolution

was the lowest. In such a case the FE was ~ 8 and 76% for hydrogen and acetate production, respectively, so confirming the good selectivity of the catalyst for CO_2 electroreduction to CH_3COO^-. Therefore, the Cu_2O-Cu^0/CP represented the most active nanostructured catalyst by applying a relatively low cathodic potential, suitable for the application discussed in the Introduction section. Moreover, other literature reports [24,29] have found out the copper redox couple Cu^I/Cu^0 is the most active one in favouring the C_2 pathway.

2.3.3.2 Cu_2O-Cu^0/CP versus Cu^0/CP Productivity

The results obtained with the most promising electrocatalyst at the two limit reference potentials were compared and the productivity towards the formation of the reduced species was investigated (Figure 2.13). To this purpose, the μmoles production of each compound was referred to the grams of the loaded catalyst (considering the electrodeposited Cu) per hour of reaction. The total amount of copper electrodeposited over the carbonaceous support was calculated by the Faraday's equation:

$$\text{Mass of } Cu^0 = \frac{(\text{A.M.})\cdot Q}{F\cdot Z} \qquad (3)$$

where, A.M. is the atomic mass of Cu (63.546 g mol^{-1}), Q is the total amount of charge passed during the electrodeposition, F is the Faraday's constant (96,485 C mol^{-1}) and Z is the number of the exchanged electrons.

The H_2 production was not considered in the calculation of the productivity because no carbon dioxide is involved during the occurrence of this reaction.

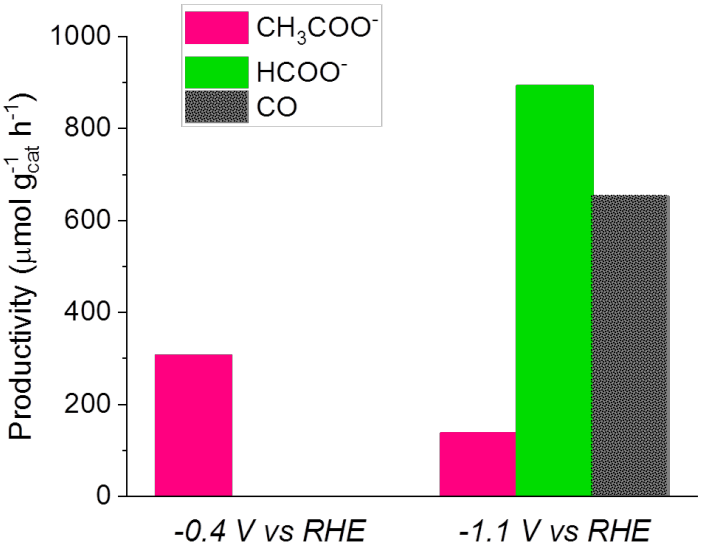

Figure 2.13. CO_2ER productivity using Cu_2O-Cu^0/CP electrocatalyst at the two limit reference potentials

The productivity graph clearly shows the different behaviour of the Cu_2O-Cu^0/CP electrocatalyst when different cathodic potentials were applied. Interestingly, at -0.4 V *vs* RHE the only reduced detected products is acetate with a relatively high productivity of 308 μmol g_{cat}^{-1} h^{-1}, whereas at -1.1 V the productivities result 653, 894 and 139 μmol g_{cat}^{-1} h^{-1} for CO, $HCOO^-$ and CH_3COO^-. All the productivities calculated at the two potentials, when working with Cu_2O-Cu^0/CP or Cu^0/CP electrocatalysts, are collected in Table 2.3 to emphasise the remarkable change of activity and selectivity passing from the reduced to the partly oxidised state of copper. In particular, at both potentials the total productivity is higher for the Cu_2O-Cu^0/CP electrocatalyst, and the same holds also for the carbon selectivity towards acetate production, resulting 8.2 % (*vs* 3.1% for Cu^0/CP) at -1.1 V and practically 100% at -0.4 V. In the following, a tentative explanation of the better performance of the Cu_2O-Cu^0/C than Cu^0/CP electrode to produce useful chemicals will be given.

Table 2.3. Productivity (μmol g_{cat}^{-1} h^{-1}) obtained for Cu_2O-Cu^0/CP and Cu^0/CP electrocatalysts at -1.1 and -0.4 V

Potential (V vs RHE)	*Electrocatalyst*	*CO*	*HCOOH*	*CH_3COOH*
-1.1	Cu_2O-Cu^0/CP	653	894	139
	Cu^0/CP	441	590	33
-0.4	Cu_2O-Cu^0/CP	nd	nd	308
	Cu^0/CP	nd	28	56

One of the first works that suggested the key role of Cu^+ species in the selective reduction of CO_2 was published by Mistry *et al.* [65], who developed Cu electrocatalysts using a plasma treatment which produced a stable cuprous oxide layer (Cu_2O) on the surface of a Cu foil. Also Roberts *et al.* [66] reported a copper surface structured *in situ* using an oxidative–reductive reaction leading to Cu_2O, which was subsequently reduced to Cu^0 in a cubic structure. This catalyst displayed an exceptional ability to catalyse CO_2 reduction favouring C–C coupling, which leads to multicarbon products.

More recently Zhu *et al.* [29] fabricated a 3D dendritic copper-cuprous oxide composite which displayed a noticeable selectivity to C_2 products (acetic acid and ethanol). They attributed the optimum performance of the catalyst to the many exposed active sites in the 3D dendritic structure and to a suitable Cu^I/Cu^0 ratio.

Based on these evidences, the higher activity and the outstanding selectivity of the electrocatalyst Cu_2O-Cu^0/CP over Cu^0/CP can be attributed to the following features, considering that the CO_2 reduction is a surface process and its efficiency is related to the density of active sites on the catalyst:

1) the proper Cu^I/Cu^0 ratio of the catalytic active sites, determined by the electrochemical synthesis above described. In this regard, the coexistence of Cu^I and Cu^0 species at the electrocatalyst surface was predicted to lead to enhanced *CO dimerization, and therefore to C_2 products [67].
2) the structure of the Cu_2O coating, which is preserved also after the application of the cathodic potential at which the CO_2ER occurs (shown in Figure 2.10a), constituted of a segmented nanosheets morphology. This structure is characterised by a very high surface area of the active material in respect to the spherical metal copper particles and by many void spaces. The high surface area should guarantee a huge number of active sites produced by the reduction of the Cu_2O film to Cu^0, presumably in the form of non-homogenous nanoparticles with enhanced grain boundaries which improve the catalytic performance, as already reported [68].

Overall, the nanosheets-like structure is likely to favour the CO_2 mass transport throughout the catalyst surface and should guarantee a vast electrochemical interface for CO_2 activation and reduction. According to the literature, CO_2 adsorbs on the active sites of the catalyst and is reduced to *CO intermediates that can be more strongly bound on the Cu surface and converted into C_2 products by *CO dimerization [32]. That means that *CO dimerization is the key step in the selective reduction of CO_2 to acetic acid and this process requires a longer residence time than the one necessary to follow the C_1 pathway which produces HCOOH ($2H^+$, $2e^-$).

Moreover, fiber copper electrodes with a three-dimensional porous hollow structure were introduced by Kas *et al.* [69] to study the electrochemical reduction of CO_2, highlighting the importance of the void spaces to remarkably increase the electrocatalytic performance due to the optimal mass transport conditions for those reactions in which at least one gas-phase reactant is involved. The fact that at the most cathodic potential a noticeable productivity of

CO and HCOOH is observed also at Cu_2O-Cu^0/CP electrode, despite the better selectivity for acetate with respect to the Cu^0/CP electrode, is thus explainable.

At high overpotentials, the current density increases due to the higher rate of both CO_2 reductions to CO and HER. Consequently, a significant reduction of the CO_2 concentration at the electrode surface takes place, the reactant is under diffusion control and the formation of gaseous products limits the formation of multi-carbon liquid products, like acetate, at high concentration.

2.3.3.3 CH_3COO^- Production over Time using Cu_2O-Cu^0/CP

Although many studies have been carried out to synthesise new materials as catalysts for the electrochemical reduction of CO_2, in most cases, the final products are formate and carbon monoxide, which require further reduction to become useful chemicals. Focusing the attention on acetate, which is the only product apart from hydrogen when the catalyst is Cu_2O-Cu^0/CP and the applied potential is -0.4 V *vs* RHE, electroreductions of different duration (15 min, 30 min and 1 h, Figure 2.14) were performed to study the formation kinetics of this product. Table 2.4 shows the trend of the produced μmoles during the CO_2ER in $KHCO_3$ 0.3 M and continuous CO_2 feed.

Table 2.4. Acetate production over time at -0.4 V *vs* RHE in $KHCO_3$ 0.3 M and continuous CO_2 flow using Cu_2O-Cu^0/CP

Time (min)	J_{tot} *(mA cm^{-2})*	CH_3COO^- *(μmol)*
15	0.60	0.172
30	0.44	0.344
60	0.46	3.09

From the table, it can be noticed that during the first 30 min the production rate of acetate is constant, whereas in the following 30 min it increases very rapidly. In Figure 2.14 the chronoamperometric responses recorded for the three experiments are shown.

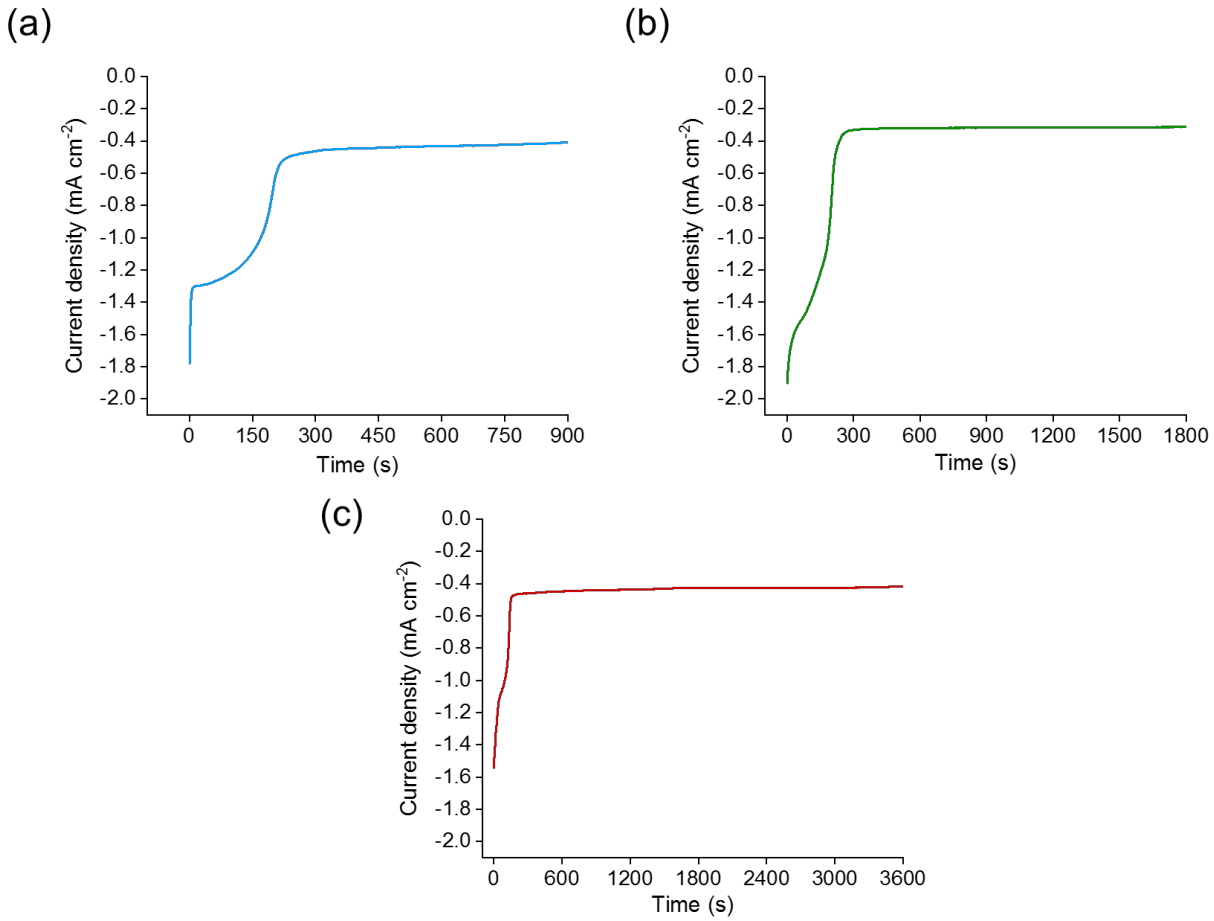

Figure 2.14. Current densities recorded at Cu_2O-Cu^0/CP electrode during CO_2ER at -0.4 V *vs* RHE and 0.3 M $KHCO_3$ as electrolyte after (a) 15 min, (b) 30 min and (c) 1h time of reaction

Looking at the Figure 2.14a, a rapid decrease of the current density recorded at the beginning of the potential application is observed and such a behaviour is due to a reduction of the electrocatalyst itself to covert Cu^I into Cu^0 to obtain a constant ratio of the two oxidation states (activation phase of the electrocatalyst). Immediately after this step, the current stabilises due to the adsorption/reduction of CO_2 on the active sites of the catalyst, followed by a slow further decrease, related to the mass transport limitation, until a stable value is recorded. Meanwhile, also the hydrogen evolution reaction occurs, since the reduction of CO_2 takes place in aqueous

solution, although the applied potential is low and the catalyst displays the lowest activity towards HER in respect to the others investigated in this work. In fact, an evident hydrogen evolution started after ~ 200 s, which was visible to the naked eye.

Consequently, the electrolysis carried out for shorter times suffered most from the initial process related to the catalyst activation and the beginning of the HER, thus resulting in a lower acetate production. By applying the potential -0.4 V for a longer time (1 h) the acetate production remarkably increased during the second half an hour (2.75 *vs* 0.344 μmoles) caused by a higher activity of the Cu^{I}/Cu^{0} centres to promote *CO dimerization. However, extending the reaction time to 3 or 5 hours, the production of acetate started to decrease. The reasons could be related to a spurious phenomenon due to a possible stripping of the product by the CO_2 stream or to a poisoning of the catalyst surface induced by cathodic deposition of some metal impurities during the CO_2ER or by graphitic carbon species formed via decomposition of intermediates [32,36,70].

2.3.3.4 Re-usability and Stability of Cu_2O-Cu^0/CP Electrode

After 1h CO_2ER at -0.4 V *vs* RHE, the reusability of the working electrode was also studied. It was disassembled, washed with bi-distilled water, dried under nitrogen, and subjected again to the same electrochemical oxidative process to convert Cu to Cu_2O, as described in the Experimental section. Then, it was re-used for a second reaction run under the same conditions.

The Faradaic efficiency of acetate during the second CO_2ER resulted slightly increased (from 76% to 84%) and the productivity slightly decreased from 308 to 245 μmol g_{cat}^{-1} h^{-1}. This preliminary experiment, which needs further studies, gives evidence of the possibility to re-use the electrode after a proper activation process and the Toray carbon paper in not damaged during the disassembling process.

The stability of the optimised catalyst was also investigated over time during 5h reaction upon application of -0.4 V *vs* RHE. The recorded current density plot is showed in Figure 2.15 and highlights no relevant degradation due to prolonged use, as a relative standard deviation (%RSD) of only 9% on the average J_{tot} value was obtained during the whole reaction time.

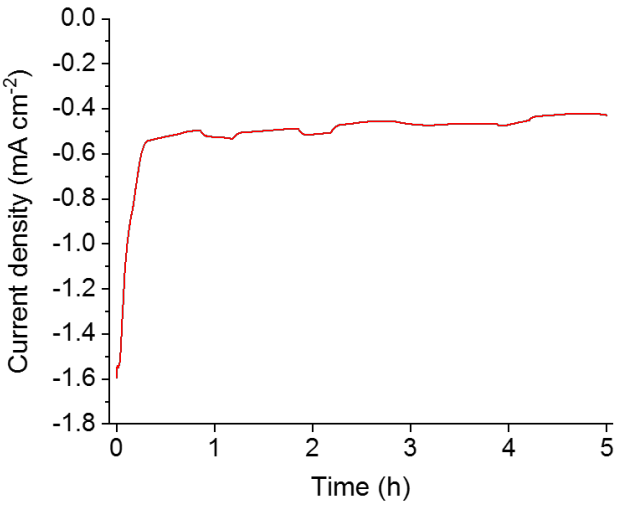

Figure 2.15. Recorded current density during 5h reaction using Cu_2O-Cu^0/CP at -0.4 V *vs* RHE

2.3.3.5 Comparison of Cu_2O-Cu^0/CP Performance with State-of-the-art Catalysts

In order to compare the performance of the most effective electrocatalyst described in this work, that can reduce CO_2 to liquid products, a short overview of other Cu based catalysts reported in the literature is shown in Table 2.5. It was not easy to get the data since the comparison must involve similar experimental conditions, especially the use of a gas diffusion layer based on carbonaceous paper, the application of a constant potential, and a continuous CO_2 feed delivered during the liquid phase reaction. Furthermore, the parameters used in literature to describe the performance of the catalysts are different and expressed in a different way.

Table 2.5. Overview of Cu based electrocatalysts

Electrocatalyst	*Potential (V vs RHE)*	*Electrolyte*	*Products*	*FE (%)*	*Productivity*	*Reference*
Porous Cu^0 NPs	-0.9	0.1 M $KHCO_3$	Formic acid Acetic acid Ethanol n-propanol	40	1460 μM h^{-1} 10 μM h^{-1} 67 μM h^{-1} 26 μM h^{-1}	32
Dendritic Cu^0-Cu_2O composite	-0.7	0.1 M KCl	Acetic acid Ethanol	28.6 13.2		29
Cu^0 NPs on carbon nanotubes	~ - 1.35	0.5 M $KHCO_3$	Formic acid Acetic acid	28.5 71.5 (C-based)	3.07 μmol h^{-1} (total carbon productivity)	34
Cu_2O/GDL	~ -0.85	0.5 M $KHCO_3$	Formic acid Acetic acid	8.1 0.5	24 μmol h^{-1} 0.6 μmol h^{-1}	71
Cu_2O-Cu^0/GDL	-0.4	0.3 M $KHCO_3$	Acetic acid	76	3.09 μmol h^{-1}	This work

Some observations can be done from the data in the table. When the catalyst is based on Cu NPs, the main product is formic acid unless the NPs are supported on carbon nanotubes; on the contrary, if the catalyst contains both Cu^I and Cu^0 centres, the electrocatalytic reduction activity towards acetic acid is favoured, but depending on the applied potential. In fact, the major selectivity of the electrochemically produced Cu_2O-Cu^0 [71] operating at ~ -0.85 V *vs* RHE is towards formate, while with the optimum electrocatalyst proposed in this work it is possible to obtain only acetic acid with a high FE and an appreciable productivity, working at a low cathodic potential of -0.4 V.

2.4 Conclusions

In this research, affordable and easily-synthesised nanostructured Cu-based electrodes with notable catalytic activities towards the electroreduction of carbon dioxide at ambient condition were reported. The combination of non-critical raw materials and reproducible synthesis/activation procedures, which provides a noteworthy and selective production of added-value chemicals from a waste product, represents a good choice for the application in solar-driven chemistry [2] and future scalability. Herein, a fully covered 4 cm^2 sized Cu^0-based electrocatalyst was successfully obtained by a simple electrochemical deposition on a carbonaceous gas diffusion membrane. Compared to most of the electrocatalysts employed in the state of the art [7,18,24,29], the optimised electrode has a higher geometrical surface area, thus overcoming critical steps of reproducibility and providing a scalable approach. Electrochemical and chemical methods are effective strategies to selectively tune the active phase of the pristine catalyst. Therefore, different copper redox couples were obtained by further and simple oxidative functionalisation of the pristine Cu^0/CP, maintaining an average crystallites dimension of less than 40 nm. The catalytic activity of each electrocatalyst towards the liquid phase electrochemical reduction of CO_2 was thoroughly investigated at two limit reference potentials. A selectivity towards the formation of acetic acid as the main liquid product was obtained by applying the lowest voltage (-0.4 V *vs* RHE) at the Cu_2O-Cu^0/CP electrocatalyst, thus resulting the most promising material. Indeed, in this case the most stable current density was observed that may be due to the decrease of the parasitic hydrogen evolution reaction, in favour of useful products formation. Despite the reaction mechanisms at the basis of CO_2ER are still under debate, we can hypothesise that the use of Cu^I/Cu^0 couple as active phase preferentially drives the reaction pathway towards C-C bond formation [4,29,66,67] under mild reaction conditions.

In conclusion, the possibility to easily produce nanostructured, large-area and low-cost electrocatalysts with promising catalytic activities was demonstrated in view of industrially relevant applications.

2.5 References

(1) Centi, G.; Perathoner, S.; Winè, G.; Gangeri, M. Electrocatalytic Conversion of CO_2 to Long Carbon-Chain Hydrocarbons. *Green Chem.* **2007**, *9* (6), 671-678.

(2) Bensaid, S.; Centi, G.; Garrone, E.; Perathoner, S.; Saracco, G. Towards Artificial Leaves for Solar Hydrogen and Fuels from Carbon Dioxide. *ChemSusChem* **2012**, *5* (3), 500–521.

(3) Genovese, C.; Ampelli, C.; Perathoner, S.; Centi, G. Electrocatalytic Conversion of CO_2 to Liquid Fuels Using Nanocarbon-Based Electrodes. *J. Energy Chem.* **2013**, *22* (2), 202–213.

(4) Genovese, C.; Ampelli, C.; Perathoner, S.; Centi, G. Mechanism of C–C Bond Formation in the Electrocatalytic Reduction of CO_2 to Acetic Acid. A Challenging Reaction to Use Renewable Energy with Chemistry. *Green Chem.* **2017**, *19* (10), 2406–2415.

(5) Prajapati, A.; Singh, M. R. Assessment of Artificial Photosynthetic Systems for Integrated Carbon Capture and Conversion. *ACS Sustain. Chem. Eng.* **2019**, *7* (6), 5993–6003.

(6) Wang, Q.; Warnan, J.; Rodríguez-Jiménez, S.; Leung, J. J.; Kalathil, S.; Andrei, V.; Domen, K.; Reisner, E. Molecularly Engineered Photocatalyst Sheet for Scalable Solar Formate Production from Carbon Dioxide and Water. *Nat. Energy* **2020**, *5* (9), 703–710.

(7) Wang, X.; Gao, C.; Low, J.; Mao, K.; Duan, D.; Chen, S.; Ye, R.; Qiu, Y.; Ma, J.; Zheng, X.; Long, R.; Wu, X.; Song, L.; Zhu, J.; Xiong, Y. Efficient Photoelectrochemical CO_2 Conversion for Selective Acetic Acid Production. *Sci. Bull.* **2021**, *66* (13), 1296–1304.

(8) Gai, P.; Yu, W.; Zhao, H.; Qi, R.; Li, F.; Liu, L.; Lv, F.; Wang, S. Solar-Powered Organic Semiconductor–Bacteria Biohybrids for CO_2 Reduction into Acetic Acid. *Angew. Chemie Int. Ed.* **2020**, *59* (18), 7224–7229.

(9) Zhang, G.; Liu, B.; Wang, T.; Gong, J. Artificial Leaves for Solar Fuels. *Chinese J. Chem.* **2021**, *39* (6), 1450–1458.

(10) Amao, Y.; Shuto, N.; Furuno, K.; Obata, A.; Fuchino, Y.; Uemura, K.; Kajino, T.; Sekito, T.; Iwai, S.; Miyamoto, Y.; Matsuda, M. Artificial Leaf Device for Solar Fuel Production. *Faraday Discuss.* **2012**, *155*, 289–296.

(11) Fan, L.; Xia, C.; Yang, F.; Wang, J.; Wang, H.; Lu, Y. Strategies in Catalysts and Electrolyzer Design for Electrochemical CO_2 Reduction toward C_{2+} Products. *Sci. Adv.* **2020**, *6* (8), 1–17.

(12) Jones, J. H. The Cativa^{TM} Process for the Manufacture of Acetic Acid. *Platin. Met. Rev.* **2000**, *44* (2), 94–105.

(13) Manyar, H.; Deshmukh, G. Production Pathways of Acetic Acid and Versatile Applications in Food Industry. *Intech Open* **2020**, 1–11.

(14) Nitopi, S.; Bertheussen, E.; Scott, S. B.; Liu, X.; Engstfeld, A. K.; Horch, S.; Seger, B.; Stephens, I. E. L.; Chan, K.; Hahn, C.; Nørskov, J. K.; Jaramillo, T. F.; Chorkendorff, I. Progress and Perspectives of Electrochemical CO_2 Reduction on Copper in Aqueous Electrolyte. *Chem. Rev.* **2019**, *119* (12), 7610–7672.

(15) Hori, Y.; Kikuchi, K.; Suzuki, S. Production of CO and CH_4 in Electrochemical Reduction of CO_2 at Metal Electrodes in Aqueous Hydrogencarbonate Solution. *Chem. Lett.* **1985**, *14* (11), 1695–1698.

(16) Xue, Y.; Guo, Y.; Cui, H.; Zhou, Z. Catalyst Design for Electrochemical Reduction of CO_2 to Multicarbon Products. *Small Methods* **2021**, *5* (10), 1–14.

(17) Hori, Y. Electrochemical CO_2 Reduction on Metal Electrodes. In *Modern Aspects of Electrochemistry*; Springer New York: New York, NY, **2008**; 89–189.

(18) Rahaman, M.; Dutta, A.; Zanetti, A.; Broekmann, P. Electrochemical Reduction of CO_2 into Multicarbon Alcohols on Activated Cu Mesh Catalysts: An Identical Location (IL) Study. *ACS Catal.* **2017**, *7* (11), 7946–7956.

(19) de Lucas-Consuegra, A.; Serrano-Ruiz, J.; Gutiérrez-Guerra, N.; Valverde, J. Low-Temperature Electrocatalytic Conversion of CO_2 to Liquid Fuels: Effect of the Cu Particle Size. *Catalysts* **2018**, *8* (8), 1–11.

(20) Liu, S.; Huang, S. Size Effects and Active Sites of Cu Nanoparticle Catalysts for CO_2 Electroreduction. *Appl. Surf. Sci.* **2019**, *475*, 20–27.

(21) Cui, H.; Guo, Y.; Guo, L.; Wang, L.; Zhou, Z.; Peng, Z. Heteroatom-Doped Carbon Materials and Their Composites as Electrocatalysts for CO_2 Reduction. *J. Mater. Chem. A* **2018**, *6* (39), 18782–18793.

(22) Duan, Y.-X.; Meng, F.-L.; Liu, K.-H.; Yi, S.-S.; Li, S.-J.; Yan, J.-M.; Jiang, Q. Amorphizing of Cu Nanoparticles toward Highly Efficient and Robust Electrocatalyst for CO_2 Reduction to Liquid Fuels with High Faradaic Efficiencies. *Adv. Mater.* **2018**, *30* (14), 1–7.

(23) Kas, R.; Kortlever, R.; Milbrat, A.; Koper, M. T. M.; Mul, G.; Baltrusaitis, J. Electrochemical CO_2 Reduction on Cu_2O-Derived Copper Nanoparticles: Controlling the Catalytic Selectivity of Hydrocarbons. *Phys. Chem. Chem. Phys.* **2014**, *16* (24), 12194–12201.

(24) Arán-Ais, R. M.; Scholten, F.; Kunze, S.; Rizo, R.; Roldan Cuenya, B. The Role of in Situ Generated Morphological Motifs and Cu(i) Species in C_{2+} Product Selectivity during CO_2 Pulsed Electroreduction. *Nat. Energy* **2020**, *5* (4), 317–325.

(25) Li, C. W.; Kanan, M. W. CO_2 Reduction at Low Overpotential on Cu Electrodes Resulting from the Reduction of Thick Cu_2O Films. *J. Am. Chem. Soc.* **2012**, *134* (17), 7231–7234.

(26) Chi, D.; Yang, H.; Du, Y.; Lv, T.; Sui, G.; Wang, H.; Lu, J. Morphology-Controlled CuO Nanoparticles for Electroreduction of CO_2 to Ethanol. *RSC Adv.* **2014**, *4* (70), 37329–37332.

(27) Giri, S. D.; Mahajani, S. M.; Suresh, A. K.; Sarkar, A. Electrochemical Reduction of CO_2 on Activated Copper: Influence of Surface Area. *Mater. Res. Bull.* **2020**, *123*, 1–8.

(28) Arán-Ais, R. M.; Rizo, R.; Grosse, P.; Algara-Siller, G.; Dembélé, K.; Plodinec, M.; Lunkenbein, T.; Chee, S. W.; Cuenya, B. R. Imaging Electrochemically Synthesized Cu_2O Cubes and Their Morphological Evolution under Conditions Relevant to CO_2 Electroreduction. *Nat. Commun.* **2020**, *11* (1), 1–8.

(29) Zhu, Q.; Sun, X.; Yang, D.; Ma, J.; Kang, X.; Zheng, L.; Zhang, J.; Wu, Z.; Han, B. Carbon Dioxide Electroreduction to C_2 Products over Copper-Cuprous Oxide Derived from Electrosynthesized Copper Complex. *Nat. Commun.* **2019**, *10* (1), 1–11.

(30) Cook, R. L.; MacDuff, R. C.; Sammells, A. F. High Rate Gas Phase CO_2 Reduction to Ethylene and Methane Using Gas Diffusion Electrodes. *J. Electrochem. Soc.* **1990**, *137* (2), 607–608.

(31) Ikeda, S.; Ito, T.; Azuma, K.; Ito, K.; Noda, H. Electrochemical Mass Reduction of Carbon Dioxide Using Cu-Loaded Gas Diffusion Electrodes I. Preparation of Electrode and Reduction Products. *Denki Kagaku oyobi Kogyo Butsuri Kagaku* **1995**, *63* (4), 303–309.

(32) Dongare, S.; Singh, N.; Bhunia, H. Electrocatalytic Reduction of CO_2 to Useful Chemicals on Copper Nanoparticles. *Appl. Surf. Sci.* **2021**, *537*, 1–8.

(33) Ampelli, C.; Genovese, C.; Marepally, B. C.; Papanikolaou, G.; Perathoner, S.; Centi, G. Electrocatalytic Conversion of CO_2 to Produce Solar Fuels in Electrolyte or Electrolyte-Less Configurations of PEC Cells. *Faraday Discuss.* **2015**, *183*, 125–145.

(34) Marepally, B. C.; Ampelli, C.; Genovese, C.; Tavella, F.; Veyre, L.; Quadrelli, E. A.; Perathoner, S.; Centi, G. Role of Small Cu Nanoparticles in the Behaviour of Nanocarbon-Based Electrodes for the Electrocatalytic Reduction of CO_2. *J. CO_2 Util.* **2017**, *21*, 534–542.

(35) Sharifi Golru, S.; Biddinger, E. J. Effect of Additives in Aqueous Electrolytes on CO_2 Electroreduction. *Chem. Eng. J.* **2022**, *428*, 1–21.

(36) Kas, R.; Kortlever, R.; Yılmaz, H.; Koper, M. T. M.; Mul, G. Manipulating the Hydrocarbon Selectivity of Copper Nanoparticles in CO_2 Electroreduction by Process Conditions. *ChemElectroChem* **2015**, *2* (3), 354–358.

(37) Hori, Y.; Takahashi, R.; Yoshinami, Y.; Murata, A. Electrochemical Reduction of CO at a Copper Electrode. *J. Phys. Chem. B* **1997**, *101* (36), 7075–7081.

(38) Calle-Vallejo, F.; Koper, M. T. M. Theoretical Considerations on the Electroreduction of CO to C_2 Species on Cu(100) Electrodes. *Angew. Chemie Int. Ed.* **2013**, *52* (28), 7282–7285.

(39) Schouten, K. J. P.; Qin, Z.; Pérez Gallent, E.; Koper, M. T. M. Two Pathways for the Formation of Ethylene in CO Reduction on Single-Crystal Copper Electrodes. *J. Am. Chem. Soc.* **2012**, *134* (24), 9864–9867.

(40) Kumar, B.; Llorente, M.; Froehlich, J.; Dang, T.; Sathrum, A.; Kubiak, C. P. Photochemical and Photoelectrochemical Reduction of CO_2. *Annu. Rev. Phys. Chem.* **2012**, *63* (1), 541–569.

(41) Ramírez-Valencia, L. D.; Bailón-García, E.; Carrasco-Marín, F.; Pérez-Cadenas, A. F. From CO_2 to Value-Added Products: A Review about Carbon-Based Materials for Electro-Chemical CO_2 Conversion. *Catalysts* **2021**, *11* (3), 1–67.

(42) Zhong, H.; Fujii, K.; Nakano, Y.; Jin, F. Effect of CO_2 Bubbling into Aqueous Solutions Used for Electrochemical Reduction of CO_2 for Energy Conversion and Storage. *J. Phys. Chem. C* **2015**, *119* (1), 55–61.

(43) Marcandalli, G.; Villalba, M.; Koper, M. T. M. The Importance of Acid–Base Equilibria in Bicarbonate Electrolytes for CO_2 Electrochemical Reduction and CO Reoxidation Studied on Au(hkl) Electrodes. *Langmuir* **2021**, *37* (18), 5707–5716.

(44) Zhu, S.; Jiang, B.; Cai, W.-B.; Shao, M. Direct Observation on Reaction Intermediates and the Role of Bicarbonate Anions in CO_2 Electrochemical Reduction Reaction on Cu Surfaces. *J. Am. Chem. Soc.* **2017**, *139* (44), 15664–15667.

(45) Hori, Y.; Murata, A.; Takahashi, R. Formation of Hydrocarbons in the Electrochemical Reduction of Carbon Dioxide at a Copper Electrode in Aqueous Solution. *J. Chem. Soc. Faraday Trans. 1 Phys. Chem. Condens. Phases* **1989**, *85* (8), 2309–2326.

(46) Zhong, H.; Fujii, K.; Nakano, Y. Effect of $KHCO_3$ Concentration on Electrochemical Reduction of CO_2 on Copper Electrode. *J. Electrochem. Soc.* **2017**, *164* (9), F923–F927.

(47) Pérez-Gallent, E.; Marcandalli, G.; Figueiredo, M. C.; Calle-Vallejo, F.; Koper, M. T. M. Structure- and Potential-Dependent Cation Effects on CO Reduction at Copper Single-Crystal Electrodes. *J. Am. Chem. Soc.* **2017**, *139* (45), 16412–16419.

(48) Akhade, S. A.; McCrum, I. T.; Janik, M. J. The Impact of Specifically Adsorbed Ions on the Copper-Catalyzed Electroreduction of CO_2. *J. Electrochem. Soc.* **2016**, *163* (6), F477–F484.

(49) Lu, Q.; Jiao, F. Electrochemical CO_2 Reduction: Electrocatalyst, Reaction Mechanism, and Process Engineering. *Nano Energy* **2016**, *29*, 439–456.

(50) Zamel, N.; Li, X.; Shen, J. Correlation for the Effective Gas Diffusion Coefficient in Carbon Paper Diffusion Media. *Energy & Fuels* **2009**, *23* (12), 6070–6078.

(51) Holfmann, H. U.; Wilm, D. Über Die Kristallstruktur Von Kohlenstoff. *Z. Elektrochem.* **1936**, *42* (7b), 504–522.

(52) Ma, X.; Li, X.; Jagadale, A. D.; Hao, X.; Abudula, A.; Guan, G. Fabrication of $Cu(OH)_2$@NiFe-Layered Double Hydroxide Catalyst Array for Electrochemical Water Splitting. *Int. J. Hydrogen Energy* **2016**, *41* (33), 14553–14561.

(53) Liu, J.; Tian, Y.; Chen, Y.; Liang, J.; Zhang, L.; Fong, H. A Surface Treatment Technique of Electrochemical Oxidation to Simultaneously Improve the Interfacial Bonding Strength and the Tensile Strength of PAN-Based Carbon Fibers. *Mater. Chem. Phys.* **2010**, *122* (2–3), 548–555.

(54) Grujicic, D.; Pesic, B. Electrodeposition of Copper: The Nucleation Mechanisms. *Electrochim. Acta* **2002**, *47* (18), 2901–2912.

(55) Young, J. F. T. XXVIII. The Crystal Structure of Various Heusler Alloys by the Use of X-Rays. *London, Edinburgh, Dublin Philos. Mag. J. Sci.* **1923**, *46* (272), 291–305.

(56) Giri, S. D.; Sarkar, A. Electrochemical Study of Bulk and Monolayer Copper in Alkaline Solution. *J. Electrochem. Soc.* **2016**, *163* (3), H252–H259.

(57) Zav'yalova, A. A.; Imamov, R. M.; Pinsker, Z. G. Production and Investigation of Thin Films of Cu_2O. *Kristallografiya* **1964**, *9* (6), 413–415.

(58) Deng, Y.; Handoko, A. D.; Du, Y.; Xi, S.; Yeo, B. S. In Situ Raman Spectroscopy of Copper and Copper Oxide Surfaces during Electrochemical Oxygen Evolution Reaction: Identification of Cu^{III} Oxides as Catalytically Active Species. *ACS Catal.* **2016**, *6* (4), 2473–2481.

(59) Narsinga Rao, G.; Yao, Y. D.; Chen, J. W. Superparamagnetic Behavior of Antiferromagnetic CuO Nanoparticles. *IEEE Trans. Magn.* **2005**, *41* (10), 3409–3411.

(60) Rashad, M.; Rüsing, M.; Berth, G.; Lischka, K.; Pawlis, A. CuO and Co_3O_4 Nanoparticles: Synthesis, Characterizations, and Raman Spectroscopy. *J. Nanomater.* **2013**, *2013*, 1–6.

(61) Wang, J.; Zhu, L.; Ji, L.; Chen, Z. Preparation of Nanostructured $Cu(OH)_2$ and CuO Electrocatalysts for Water Oxidation by Electrophoresis Deposition. *J. Mater. Res.* **2018**, *33* (5), 581–589.

(62) Oswald, H. R.; Reller, A.; Schmalle, H. W.; Dubler, E. Structure of Copper(II) Hydroxide, $Cu(OH)_2$. *Acta Crystallogr. Sect. C Cryst. Struct. Commun.* **1990**, *46* (12), 2279–2284.

(63) Zhao, X.; Du, L.; You, B.; Sun, Y. Integrated Design for Electrocatalytic Carbon Dioxide Reduction. *Catal. Sci. Technol.* **2020**, *10* (9), 2711–2720.

(64) Kuhl, K. P.; Cave, E. R.; Abram, D. N.; Jaramillo, T. F. New Insights into the Electrochemical Reduction of Carbon Dioxide on Metallic Copper Surfaces. *Energy Environ. Sci.* **2012**, *5* (5), 7050–7059.

(65) Mistry, H.; Varela, A. S.; Bonifacio, C. S.; Zegkinoglou, I.; Sinev, I.; Choi, Y.-W.; Kisslinger, K.; Stach, E. A.; Yang, J. C.; Strasser, P.; Cuenya, B. R. Highly Selective Plasma-Activated Copper Catalysts for Carbon Dioxide Reduction to Ethylene. *Nat. Commun.* **2016**, *7* (1), 1–9.

(66) Roberts, F. S.; Kuhl, K. P.; Nilsson, A. High Selectivity for Ethylene from Carbon Dioxide Reduction over Copper Nanocube Electrocatalysts. *Angew. Chemie* **2015**, *127* (17), 5268–5271.

(67) Xiao, H.; Goddard, W. A.; Cheng, T.; Liu, Y. Cu Metal Embedded in Oxidized Matrix Catalyst to Promote CO_2 Activation and CO Dimerization for Electrochemical Reduction of CO_2. *Proc. Natl. Acad. Sci.* **2017**, *114* (26), 6685–6688.

(68) Kwon, Y.; Lum, Y.; Clark, E. L.; Ager, J. W.; Bell, A. T. CO_2 Electroreduction with Enhanced Ethylene and Ethanol Selectivity by Nanostructuring Polycrystalline Copper. *ChemElectroChem* **2016**, *3* (6), 1012–1019.

(69) Kas, R.; Hummadi, K. K.; Kortlever, R.; de Wit, P.; Milbrat, A.; Luiten-Olieman, M. W. J.; Benes, N. E.; Koper, M. T. M.; Mul, G. Three-Dimensional Porous Hollow Fibre Copper Electrodes for Efficient and High-Rate Electrochemical Carbon Dioxide Reduction. *Nat. Commun.* **2016**, *7* (1), 1–7.

(70) Hori, Y.; Konishi, H.; Futamura, T.; Murata, A.; Koga, O.; Sakurai, H.; Oguma, K. "Deactivation of Copper Electrode" in Electrochemical Reduction of CO_2. *Electrochim. Acta* **2005**, *50* (27), 5354–5369.

(71) de Brito, J. F.; Genovese, C.; Tavella, F.; Ampelli, C.; Boldrin Zanoni, M. V.; Centi, G.; Perathoner, S. CO_2 Reduction of Hybrid Cu_2O–Cu/Gas Diffusion Layer Electrodes and Their Integration in a Cu-based Photoelectrocatalytic Cell. *ChemSusChem* **2019**, *12* (18), 4274–4284.

CHAPTER 3

Cu-based Electrocatalysts Derived from CuMgAl Layered Double Hydroxides Synthesised on Carbonaceous Gas Diffusion Membrane for the Electrochemical CO_2 Reduction

Thanks to the comparative studies among different nanostructured copper species, it was possible to highlight the importance of the electrocatalyst's morphology, along with the oxidation state of the active phase, in terms of CO_2ER productivity. A substantial catalytic activity towards the production of acetic acid was obtained with the nanostructured Cu_2O/Cu^0 electrocatalyst upon application of a very low potential. Indeed, such a Cu-based film displayed both the presence of many void spaces over its surface, which likely favoured the diffusion of CO_2, and an optimal ratio between Cu^+ and Cu^0 oxidation states, that has been widely demonstrated to be the main responsible for the C-C coupling.

In the present chapter, further optimisations of the Cu-based catalysts will be described and discussed. In particular, with the carbonaceous support unchanged, several Cu-based electrocatalysts, derived from Cu-based Layered Double Hydroxide (LDH) precursors, were obtained by means of electrochemical and chemical procedures, with the aim to improve the catalytic activity by enhancing the basicity of the overall catalyst. The main purpose of the work described in this chapter was to increase the productivity of acetic acid, in terms of mmol g_{cat}^{-1} h^{-1}, favouring the catalyst's interaction with CO_2 due to its acidic nature and promoting an alkaline environment at the electrode-electrolyte interface, which suppressed the competitive H_2 evolution. Moreover, employing a Cu-based electrocatalyst derived from a hydrotalcite structure favoured the dispersion of the active phase, thus increasing the available surface area and, therefore, its catalytic activity.

3.1 Introduction

The catalytic activity of a material towards the CO_2ER reaction, as already discussed, is sensitive to the nature of the active sites, which in turn is governed by the local size, shape, crystal face, and chemical composition of the particles concerned [1,2]. However, one of the main issues that needs to be overcome when a nanostructured catalyst is employed relies on the preservation of its stability during the reaction [3]. Moreover, when the heterogeneous electrochemical CO_2 reduction reaction is carried out in aqueous phase, the interaction between the gaseous reactant and the active surface of the electrode is generally very low [4]. Indeed, by using water as source of proton, the solubility of carbon dioxide is approximately 34 mM, as discussed in Chapter 1, and its gaseous nature limits the mass transport towards the surface of the electrode [5], thus lowering the availability of CO_2. Besides the experimental set-up conditions, *i.e.*, the employed cell or the electrolyte pH, modifications in the chemical composition and structure of the catalyst can provide an easy way to alleviate these restrictions. Such changes aim to (i) facilitate the interaction between the electrocatalyst and CO_2, enhancing the reactant availability, (ii) increase the dispersion of the catalytic active phase, making the available active surface more prone to activate the CO_2 molecule, (iii) maintain the stability of the catalyst, and (iv) generate locally a suitable environment. Although the aforementioned nanostructured Cu-based films through the porous nature of the GDL have already shown high selectivity towards the production of acetic acid, the interaction with the reactant was likely guaranteed in terms of CO_2 residence time but, from a chemical point of view, the electrocatalyst could not favour a proper interaction in terms of adsorption, due to the scarce affinity with the acidic CO_2. This issue was mainly due to the lack of basic sites within the Cu active species [6]. Moreover, the homogeneous Cu-containing coating likely suffers from the poor dispersion of Cu species that can be subjected to sintering phenomena

during the reaction [7]. For this reason, an efficient strategy is represented by the use of more complex structures that can facilitate and improve the reaction performances [8].

In the context of the chemical CO_2 reduction reactions, the metal oxides are the most widely employed materials for the formation of the metal-based supported catalysts and find their major applications in the CO_2 reforming [9] and hydrogenation reactions.

In 2017, Han *et al.* [10,11] investigated the CO_2 desorption from different metal oxides supports by means of temperature programmed desorption studies (CO_2-TPD), in order to evaluate their effect on the reforming of methane reaction (DRM). They reported that Al_2O_3 exhibited the highest value around 33.7 μmol g^{-1}, due to its amphoteric nature, followed by MgO (12.8 μmol g^{-1}), ZrO_2 (7.6 μmol g^{-1}), TiO_2 (1.2 μmol g^{-1}), and SiO_2 (2.1 μmol g^{-1}) thus demonstrating the CO_2 adsorption capacity of Al_2O_3 and MgO species. Indeed, the general idea was to employ metal-based particles, preferably nano-sized, that displayed (i) good interactions with the basic layer in which they were dispersed that in turn guaranteed their stability, and (ii) a higher catalytic activity towards the target reaction thanks to the better achieved dispersion, also favoured by the enhanced interaction with the gaseous reactant. Al_2O_3 is a well know catalyst support employed for CO_2 hydrogenation reactions thanks to its ability to improve metal NPs dispersion and density of active sites [12,13]. Moreover, Bach *et al.* [14] have recently reported the benefits of the addition of 5 wt% MgO as promoter of basicity in the catalyst Ni/Al_2O_3 for the CH_4 dry reforming, thus improving the catalytic activity.

Therefore, MgO-Al_2O_3 metal oxides are considered as promising materials to increase the interaction between the active phase and the reactant when acid-base interactions are needed, along with a substantial dispersion of the supported active catalyst to enhance its stability.

The traditional methods to achieve the metal oxides supported catalysts includes co-precipitations [15], hydrothermal [16] or sol-gel methods [17]. However, such methods suffer from the poor active phase dispersion or the aggregation of the nanoparticles [8].

Hence, a more efficient strategy to obtain supported metal-based catalytic systems could be found in a class of compounds that has been widely studied for catalytic purposes, thanks to their alkaline nature and the intriguing structural composition, namely Layered Double Hydroxides. Also known as hydrotalcite-like compounds, Layered Double Hydroxides (LDHs) are anionic clays with molecular formula $[M(II)_{1-x}\,M(III)_x(OH)_2]^{x+}(A^{n-}_{x/n}) \cdot mH_2O$, coming from the natural hydrotalcite $Mg_6Al_2(OH)_{16}(CO_3) \cdot 4H_2O$. They consist of lamellas where the cations are octahedrally coordinated with OH^- forming layered structures, and anions are intercalated among the layers in order to balance their overall positive charge due to the partial substitution of M(II) with M(III) [18–20]. The easy tunability of metal ions and the possibility to exchange the interlayer anions make LDHs attractive alternatives for applications in catalysis [18,21–24], photocatalysis [25–27], electrochemical oxygen evolution [28,29], electrochemical sensors [30–32], biology [33] and separation processes [34].

Concerning their application in catalysis, LDHs are mostly employed as catalyst precursors for the preparation of metal-based catalysts, since the homogeneous distribution of the metal cations within the LDH brucite-type layers allows the formation of well dispersed small metal particles that are stabilised inside a thermally stable oxide matrix species, upon calcination and reduction processes.

Even in this case, such precursors are mainly used for the preparation of catalysts suitable for the reforming of methane towards syngas [35,36] or for CO_2 hydrogenation to methane or methanol [37,38]. Fasolini *et al.* [35] described the synthesis of Rh-based catalysts derived from a RhMgAl LDH active for the oxy-reforming of methane. By exploiting the nature of the LDH and the proper calcination and reduction conditions, they were able to achieved well-dispersed and stable metal Rh particles with high surface area, so improving the availability of the metal after reduction, an issue often found when the catalyst is prepared by coprecipitation and calcination at high temperature [39].

In addition, several studies have been also carried out on the Cu-containing LDHs precursors. As an example, Kühl *et al.* [40] described the synthesis of LDHs precursors composed of Cu, Zn, and Al which were designed for the methanol steam reforming reaction. The LDHs were obtained by co-precipitations methods inside microemulsion droplets and then subjected to further calcination and reduction processes, which allowed to obtain the final composite material made of Cu nanoparticles supported on $ZnAl_2O_4$. In this way, a higher BET surface area of the LDH precursors and the calcined sample was obtained compared to the one of the conventionally co-precipitated reference catalyst, and this result led to higher performances for the methanol steam reforming reaction.

Focusing the attention on the CO_2 conversion, Chen *et al.* [8] reported the benefits that a catalyst based on Cu NPs supported on MgO/Al_2O_3, which was synthesised starting from CuMgAl LDH precursors, has brought to the production of CO from the carbon dioxide, in contrast to the same catalyst non-derived from LDH precursors. In particular, it showed higher stability and conversion. Similarly, Li *et al.* [38] reported the synthesis of Ga^{3+}-modified Cu/ZnO based catalysts starting from a series of $(CuZn)_{1-x}Ga_x$-CO_3 LDH nanosheets precursors. Such materials, upon reduction, displayed greater Cu surface areas and dispersions if compared to the same catalyst synthesised from a hydroxyl-carbonate precursor phase, which contained the same metals and was obtained by a conventional co-precipitation method.

Hence, the studies employed for the chemical CO_2 conversion processes can be a starting point for applications in electrocatalysis, following the same synthesis protocol. However, while for the thermal approach, the metal oxides species are directly used as a support for the active phase, the electrochemical process needs a conductive support in order to promote the reaction. For this reason, it is necessary to employ a different strategy for the synthesis of the material, with known chemical composition, to obtain a homogeneous LDH film precursor which guarantees also a good adhesion to the conductive support.

Therefore, the synthesis of the LDH precursors can be also obtained by means of electrochemical techniques. Indeed, such an approach has recently emerged as an affordable strategy for the coating of specific support otherwise achieved with further treatments, *i.e.*, the addition of binding materials like epoxy resins, mineral oil, or PVC membrane [41]. Thanks to its high speed, simplicity, and low-cost, the LDHs electrochemical synthesis allows the deposition of a well adherent, homogeneous coating [42]. Moreover, it offers the possibility to obtain large-area surfaces [43]. The most common electrochemical methods by which the LDH precursors can be obtained are: (i) potentiostatic, (ii) galvanostatic, (iii) and potentiodynamic methods [44]. Such methods will be described in the following chapter. In this context, Basile and his coworkers [45] described for the first time the synthesis of a Rh-based catalyst derived from a RhMgAl hydrotalcite precursors which was electrochemically obtained on a FeCrAlY foam. In this way, a Rh-dispersion over a layer of MgAl oxides species supported on a metal foam was easily achieved upon calcination and reduction of the electrocatalyst without the addition of extra binding compounds.

In this chapter, the optimisation of the electrochemical synthesis of CuMgAl LDH/CP precursors will be described. The precursor composition was chosen as the best option on the basis of the studies performed on the basicity of Mg and Al oxides [10] and their remarkable performances as CO_2 sorbents [46,47]. The LDH precursors were subjected to further calcination and reduction steps, and the procedures were optimised in order to achieve a Cu^0 active phase well dispersed on a mixed oxides layer which in turn was supported on a three-dimensional electrode. In particular, we synthesised layer double oxides (LDO) based materials, namely CuMgAl LDO/CP and Cu^0-MgAl LDO/CP. Besides, a different chemical reduction was also tested in KNO_2 on the pristine LDH in order to design milder operative conditions for producing metal Cu, while preserving the LDH structure.

Such a system was referred as Cu^0-MgAl LDH/CP. Finally, since the redox couple Cu^+/Cu^0 has been pointed out to be the main responsible for the CO_2 reduction to C_2 products, a final electrochemical oxidation was performed on both the reduced electrocatalysts by employing the procedure described in Chapter 2 (Paragraph 2.2.5), namely Cu_2O/Cu^0-MgAl LDO/CP and Cu_2O/Cu^0-MgAl LDH/CP, respectively. Each synthesised material, starting from the LDH precursor to the final Cu_2O/Cu^0 (LDH-derived) electrocatalysts, was tested for the liquid phase CO_2ER working at a potential (-0.4 V *vs* RHE) which had resulted the most selective for acetic acid production. Such materials were electrochemically loaded on the usual carbonaceous gas diffusion membranes with the aim of comparing the catalytic activities of the new materials with those displayed by the Cu-based films, described in the previous chapter, in terms of acetic acid productivity and selectivity.

3.2 Materials and Methods

3.2.1 Chemicals and Materials

Toray Carbon Paper (TGP-H-60), Nafion membrane N-115 (0.125 mm thick, ≥ 0.90 meq/g exchange capacity); magnesium nitrate hexahydrate ($Mg(NO_3)_2 \cdot 6H_2O$), ammonium nitrate (NH_4NO_3), and copper tape were purchased from Alfa Aesar. Copper nitrate trihydrate ($Cu(NO_3)_2 \cdot 3H_2O$), aluminium nitrate nonahydrate ($Al(NO_3)_3 \cdot 9H_2O$), sulfuric acid (H_2SO_4 96% - 98%), ethanol (CH_3CH_2OH 96.0 – 97.2%), potassium hydrogen carbonate ($KHCO_3$), potassium hydroxide, potassium nitrite, and phenol were purchased from Sigma-Aldrich. Deuterium oxide (99.96%) was purchased from Eurisotop. Pure carbon dioxide (≥ 99.9%) was acquired by Rivoira (S.r.l.). Gas sampling bags (Tedlar Bags) were obtained from Supelco. All chemicals were of reagent grade or higher.

3.2.2 Apparatus

The deposition of the layered double hydroxide precursors and the further oxidation were electrochemically carried out in a conventional three-electrode cell, connected to a potentiostat (CH Instrument 660 C). The cell for the electrodeposition included: a 4 cm^2 sized Toray Carbon Paper (CP) used as working electrode; an aqueous saturated calomel electrode (SCE) as reference electrode, and a Pt gauze as counter electrode. All the applied potentials were referred to the SCE except for the electrochemical CO_2 reduction tests for which they were quoted *vs* the reversible hydrogen electrode (RHE). After the deposition, the samples were calcined in a muffle and reduced in a tubular reactor. The morphology and the structure of the catalytic films loaded on the carbonaceous support were investigated by Scanning Electron Microscopy (SEM analysis) using the E-SEM Zeiss EVO 50 Series instrument. Such an instrument includes an Oxford INCA system equipped with a 30 mm^2 Silicon Drift Detector which allowed to perform Energy Dispersive X-ray Spectroscopy (EDS) measurements. Moreover, X-ray diffraction analyses (XRD) were carried out using a PW1050/81 diffractometer (Philips/Malvern, Royston, UK) coupled with a graphite monochromator in the diffracted beam and controlled by a PW1710 unit (Cu Kα, $\lambda = 0.15418$ nm). The electrochemical CO_2 reduction reaction tests and the analyses of the products were carried out using the same equipment described in Chapter 2 (Paragraph 2.2.2).

3.2.3 Preparation of the Electrocatalysts

Similarly to the Cu-based electrocatalysts described in Chapter 2, a geometrical surface area of 4 cm^2 of Toray carbon paper (CP) was cut out from a 19 x 19 cm foil and each piece were pre-treated using the following optimised procedure: 2 h in 1 M H_2SO_4, 1 h in pure EtOH, and thoroughly rinsed with distilled H_2O. Even in this case, the carbonaceous support was referred as gas diffusion layer (GDL).

The preliminary evaluation of the best procedure to electrochemically synthesise the CuMgAl layered double hydroxide precursors is discussed in Paragraph 3.3.1. The optimal electrodeposition process used for the synthesis of all the investigated electrocatalysts included a potentiodynamic method adapted from an already published procedure [44,48,49]. A freshly prepared 0.03 M solution containing the nitrate salts of Cu^{2+}, Mg^{2+}, and Al^{3+} was prepared with molar ratios of Cu: Mg: Al = 1.5: 1.5: 1. Then, a variable potential from 0.0 to -1.4 V was applied with a scan rate of 30 mV s^{-1}. The as-obtained Cu-based LDH thin layer was thoroughly rinsed in distilled H_2O and dried to a constant weight. This electrocatalyst was referred to as CuMgAl LDH/CP. Afterwards, the LDH precursor was calcined for 3 h and chemically reduced in a gaseous mixture of H_2/N_2 (10/90 mL min^{-1}). For these steps, different temperatures and times were evaluated and the optimised experimental conditions will be discussed in Paragraphs 3.3.2 and 3.3.3, where the calcined samples will be referred to as CuMgAl layered double oxides (LDOs), while the sample subjected to the further reduction treatment as Cu^0 – MgAl LDO/CP. Finally, the latter sample was electrochemically oxidised using an already optimised procedure previously described in Chapter 2 (Paragraph 2.2.5). Briefly, the oxidation was achieved by applying a constant potential of -0.4 V *vs* SCE for 720 s in 0.5 M KOH solution, in order to obtain a copper oxidation to Cu^+. After the oxidation, the sample was rinsed and dried to constant weight. The last described sample was named as Cu_2O/Cu^0 – MgAl LDO/CP. The morphology and the structure of each electrocatalyst were thoroughly investigated by SEM-EDS and X-ray diffraction analysis.

3.2.4 Chemical Reduction of the CuMgAl LDH Precursors in Liquid Phase

The reduction of the CuMgAl LDH/CP precursors was carried out also chemically, employing a KNO_2 solution at different times and temperatures. In particular, the chemical reductions were performed as follows:

- Sample immersed for 30 min, in 0.1 M KNO_2 at 298K
- Sample immersed for 1h and 30 min, in 0.1 M KNO_2 at 298K
- Sample immersed for 1h and 30 min, in 0.1 M KNO_2 at 333K

At the end of each reduction process, the sample was thoroughly rinsed with distilled water and dried until constant weight. The sample obtained from the third treatment was named as Cu^0 – MgAl LDH/CP. Then, an electrochemical oxidation, as described before, was performed in order to achieve a final catalyst composition that likely includes the Cu^+/Cu^0 active redox couple (Cu_2O/Cu^0 – MgAl LDH/CP). Even in this case, the morphology and the structure of each electrocatalyst were thoroughly investigated by SEM-EDS and X-ray diffraction analysis.

3.2.5 Liquid Phase CO_2 Electroreduction Tests

The electrochemical CO_2 reduction tests were performed using the same experimental set-up reported in Chapter 2, which has been thoroughly described in Paragraph 2.2.6. All the electrocatalytic tests were carried out as single tests so as to investigate the catalytic activity of each material at -0.4 V *vs* RHE, unless otherwise stated.

3.3 Results and Discussion

3.3.1 Optimisation of the Electrochemical Synthesis of CuMgAl LDH Precursors over the Carbonaceous Membrane

Preliminary attempts to electrosynthesise the CuMgAl LDH/CP precursors were carried out through a potentiostatic deposition, which is the most commonly used in literature [42,43,45,50].

Starting from the composition of the electrolytic bath employed for the Cu^0-based films electrodepositions, $Mg(NO_3)_2 \cdot 6H_2O$ and $Al(NO_3)_3 \cdot 9H_2O$ salts were added in order to achieve a final molar ratio between divalent (Mg^{2+} + Cu^{2+}) and trivalent cations of 6: 1.

In particular, the electrolytic bath for the potentiostatic electrodeposition included:

- 0.15 M $Cu(NO_3)_2 \cdot 3H_2O$
- 0.70 M NH_4NO_3
- 0.15 M $Mg(NO_3)_2 \cdot 6H_2O$
- 0.05 M $Al(NO_3)_3 \cdot 9H_2O$

According to the studies performed by Cavani *et al.* [18] on the Cu-containing LDH synthesised through chemical processes, a unitary molar ratio between the divalent cations had to be preserved in order to achieve a hydrotalcite structure. Interestingly, they reported that the only way to synthesise a layered double hydroxide with copper as divalent cation was to add a second divalent cation. However, as long as the molar ratio between Cu^{2+}/M(II) was equal or lower than 1, a hydrotalcite with structural copper can be formed. On the contrary, when the amount of copper exceeded the moles of M(II), the formation of other Cu compounds was energetically more favoured than the LDH. In this work, the concentrations of Cu^{2+} and Mg^{2+} in the electrolytic bath have been kept equal. Once it was prepared, two attempts of electrodeposition were performed, varying the applied potential in order to evaluate the best one.

The catalysts were loaded on the carbonaceous membrane upon application of -0.4 and -1.0 V *vs* SCE for 500 s. The former procedure employed the same electrodeposition parameters already described for the Cu-based films, while for the latter sample a more cathodic potential was chosen. According to Gualandi *et al.* [44], the most commonly employed potentials for the potentiostatic electrodeposition of the LDHs vary from -1.1 to -0.9 V *vs* SCE, but the synthesised LDHs in that paper did not contain an easily reducible cation such as Cu^{2+} . Indeed, at these cathodic potentials the main reactions are the reduction of nitrates and water which favour the formation of the layered double hydroxides through a complex multistep process [51–54], schematically illustrated in Figure 3.1.

All the first occurring reactions (1 – 5) involve the consumption of H^+ ions and/or the generation of OH^-.

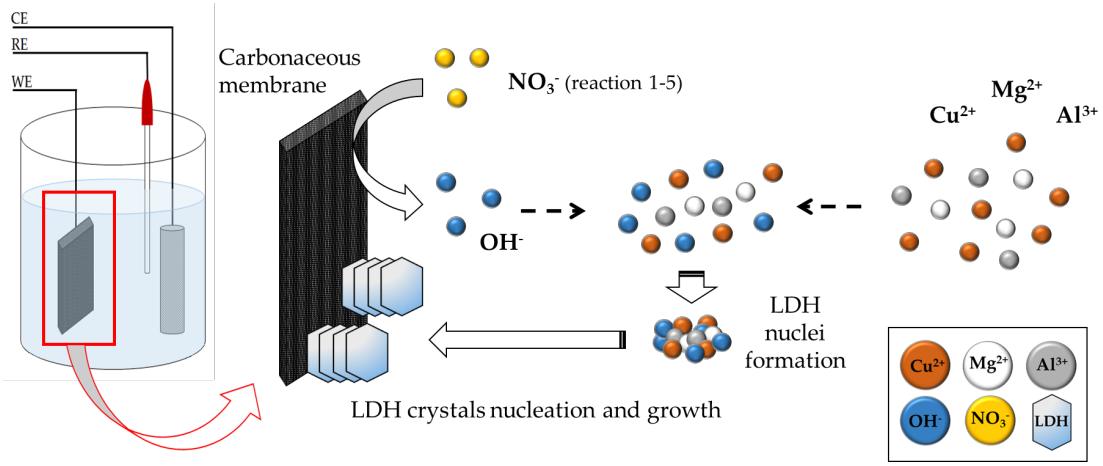

Figure 3.1. Scheme of the processes occurring at the working electrode

$$2H^+ + 2e^- \rightarrow H_2 \qquad E^0 = 0.0\ V \qquad (1)$$

$$NO_3^- + 2H^+ + 2e^- \rightarrow NO_2^- + H_2O \qquad E^0 = 0.93\ V \qquad (2)$$

$$NO_3^- + 10H^+ + 8e^- \rightarrow NH_4^+ + 3H_2O \qquad E^0 = 0.36\ V \qquad (3)$$

$$2H_2O + 2e^- \rightarrow H_2 + 2OH^- \qquad E^0 = -0.83\ V \qquad (4)$$

$$NO_3^- + H_2O + 2e^- \rightarrow NO_2^- + 2OH^- \qquad E^0 = 0.01\ V \qquad (5)$$

The generated hydroxide ions diffuse towards the bulk solution, while the cations species present in the electrolytic bath diffuse towards the electrode surface, so forming the first LDH nuclei. Once the amount of produced OH^- equalises the one removed by the cations precipitation, the nucleation and growth of the crystals take place at the electrode surface.

The rate of the LDH precipitation strongly depends on the presence of defects on the electrode surface, which act as nucleation centres, and on the oversaturation degree of the solution [44].

As a result, by applying -0.4 V *vs* SCE for 500 s, a black and not adherent deposit was obtained over the carbonaceous membrane and the X-ray diffraction pattern, shown in Figure 3.2a, displayed no peak attributable to the hydrotalcite structure [18,55]. However, the presence of Cu^0 and Cu oxides can be confirmed. In particular, the peaks at 43.5°, 50.6°, and 74.3° (2θ) were referred to the (111), (002), and (022) Cu crystal facets, respectively [56], while the peak at 36.7° (2θ) was consistent with the presence of cuprite (Cu_2O).

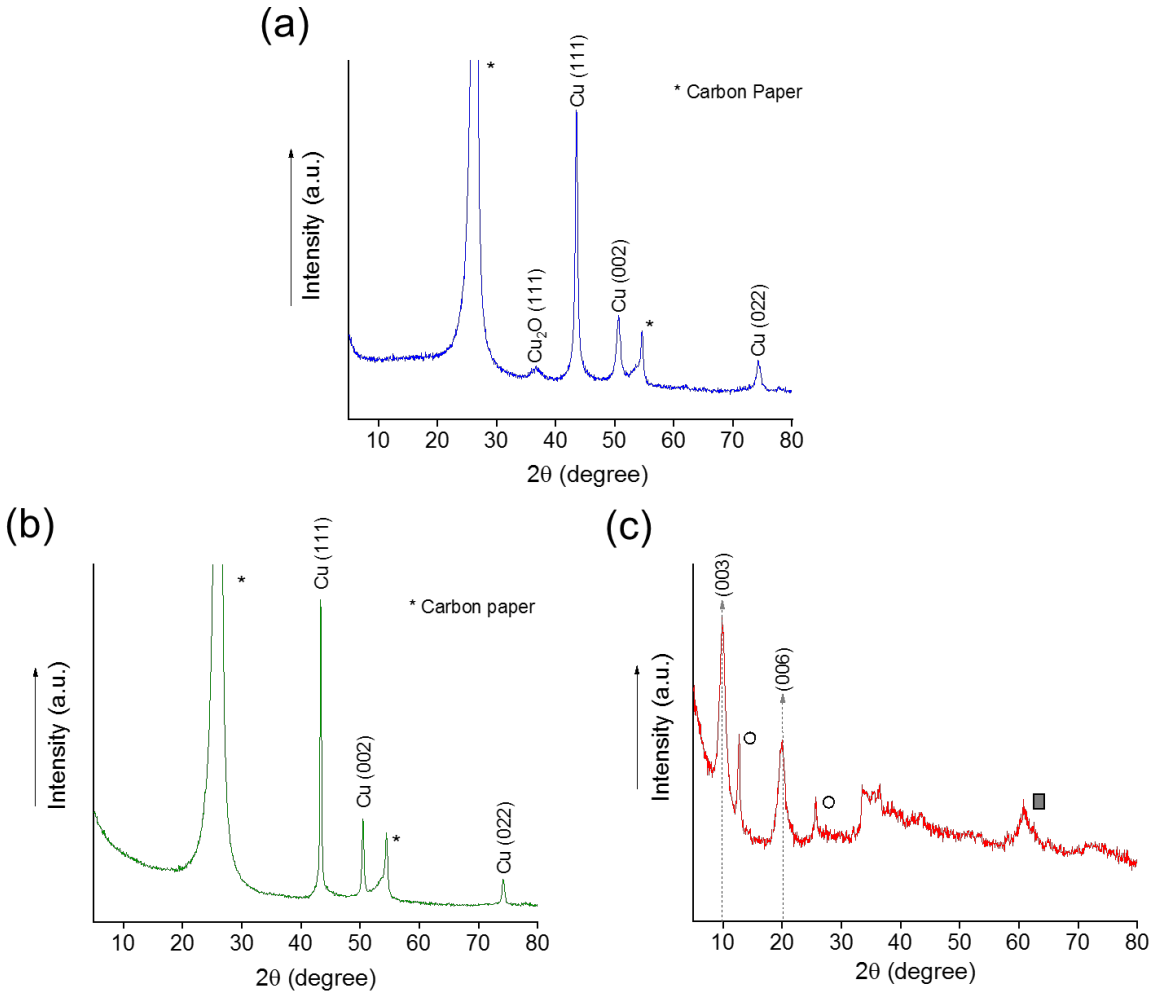

Figure 3.2. X-ray diffraction patterns of the deposit over the GDL achieved upon application of (a) -0.4 V *vs* SCE and (b) -1.0 V *vs* SCE for 500 s; (c) X-ray diffraction patterns of the powder detached from the support during the electrodeposition at -1.0 V *vs* SCE for 500 s

Hence, the presence of different cations in the electrolytic bath did not substantially change the outcome of the deposition: at -0.4 V *vs* SCE, it was possible to obtain Cu^0 as the main phase. However, unlike the Cu^0-based film described in Chapter 2, the solid deposit included also Cu^I species. Such a difference was likely due to the presence of a higher concentration of nitrates compared to the electrolytic bath previously used.

Besides, a different result was obtained when -1.0 V *vs* SCE was applied [55]. In this case, a thick layer visible to the naked eye was observed during the electrodeposition process which detached from the conductive support once the electrode was removed from the electrolyte. The solid deposit dispersed in the electrolyte was filtered and dried in air.

Later, X-ray diffraction analyses were performed both on the surface of the carbonaceous membrane and on the collected blue powder. In the former case, the XRD analysis revealed that the solid deposit remaining on the surface of the GDL was essentially composed of metal copper (Figure 3.2b), while in the latter, it has highlighted the presence of the layered double hydroxide, containing NO_3^- as interlayer anion confirmed by the reflections at 10.04° and 20.08° (2θ) indexed as (003) and (006), respectively (Figure 3.2c) [18,55,57]. Moreover, the reflections marked with the circle at 12.7° and 25.7° (2θ) are in agreement with the presence of synthetic Gerhardtite, a mineral species with chemical formula $Cu_2(OH)_3NO_3$ [58,59], of which they represent the (001) and (002) crystal planes, respectively. Finally, the reflection at 60.8° (2θ), marked with a rectangle, can be referred to both species as it can be related to the (040) reflection of the Gerhardtite structure, but it can be also referred to the (110) crystal plane of the LDH [60,61]. However, from a qualitative point of view, some considerations can be made. Focusing the attention on the intensity, according to Guillou *et al.* [58], the reflection at 60.8° ascribable to $Cu_2(OH)_3NO_3$ should be much lower than the one recorded at 25.7°, while the (110) reflection of the layered double hydroxide should display a greater intensity [31].

Moreover, the crystallites sizes were calculated for all the reflections through the Scherrer's equation (Chapter 2, Paragraph 2.3.2.1, Equation 2). As a result, the crystallites sizes obtained from the reflections at 12.7° and 25.7° (2θ), related to Gerhardtite, corresponded to similar values, around 38 nm, while those associated to the LDH structure, and measured at 10.04° and 20.08° (2θ), resulted 16 and 13 nm, respectively. The crystallites size calculated using the full width at the half maximum of the reflection at 60.8° (2θ) was 11 nm. By comparing each crystallites size, it can be stated that the reflection recorded in the XRD pattern of the detached powder, at the highest 2θ, is consistent with the (110) crystal plane of the hydrotalcite structure.

Hence, from the experimental evidences, it can be stated that the use of potentiostatic methods for the electrosynthesis of the three-metal LDH has shown some critical issues, especially in terms of adhesion, and thus a different approach has been investigated.

In particular, the electrodeposition of the Cu-containing LDH precursors films over the carbonaceous support was carried out with a potentiodynamic method (Cyclic voltammetry, CV), by adapting an already reported procedure [49].

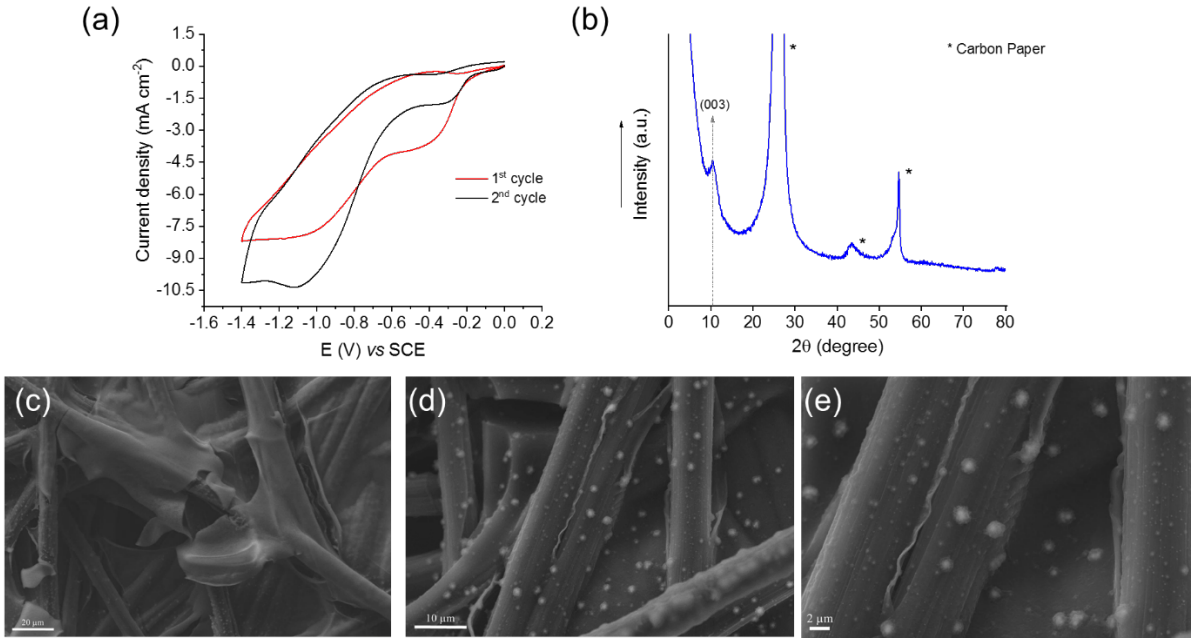

Figure 3.3. (a) Potentiodynamic deposition of the Cu-containing LDH film over the carbonaceous gas diffusion electrode; (b) X-ray diffraction pattern and (c), (d), and (f) SEM images of a CuMgAl 1.5: 1.5: 1 LDH/CP electrodeposited film

The voltammograms recorded during the electrodeposition process of the CuMgAl LDH/CP, displayed in Figure 3.3a, show the presence of two cathodic peaks: one at -0.40 V, slightly anticipated at -0.28 V in the second cathodic sweep segment, and the other at -1.03 V. By comparing the deposition curves recorded with and without the Cu^{2+} species in the electrolytic bath, shown in Figure 3.4, it is worth noting that, while the most cathodic peak is present in both traces relative to the MgAl LDH/CP and the CuMgAl LDH/CP electrodepositions, the

less cathodic peak can be seen only in the Cu-containing electrolytic solutions. Thus, it can be stated that the peak at -0.4 V is ascribable to the reduction of copper ions.

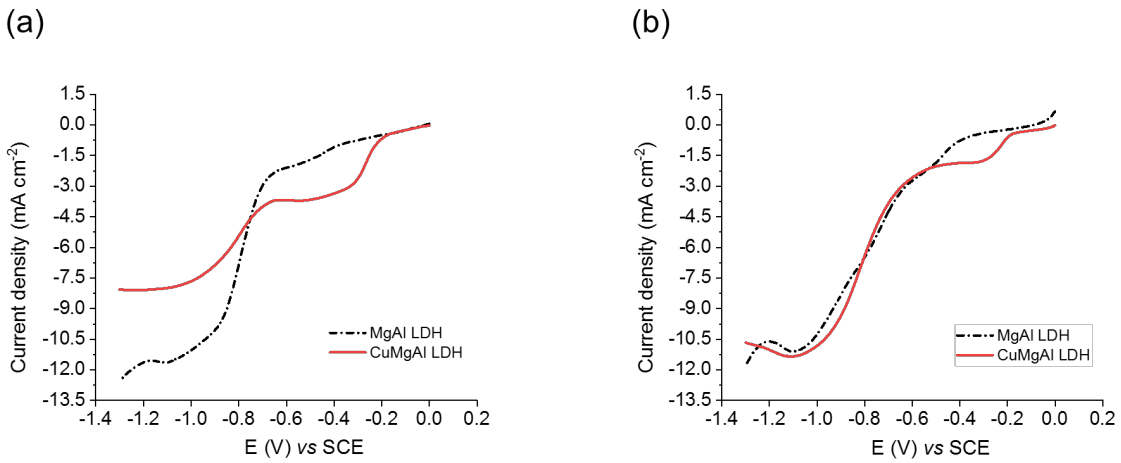

Figure 3.4. (a) Comparison of the first and (b) the second sweeps recorded during the electrodeposition of MgAl 3: 1 LDH and CuMgAl 1.5: 1.5: 1 LDH

Moreover, it was observed that the current related to this peak decreases after the first deposition cycle (Figure 3.3a), while that associated to the peak at -1.03 V strongly increases. Therefore, we can assume that a partial reduction of the copper species occurs as soon as the cathodic potential is applied so hindering, in some way, the reduction of nitrates which is favoured during the second deposition cycle on the CP electrode modified with metal copper. The first evidence of the presence of the layered double hydroxide structure, obtained with this potentiodynamic method, was given by the X-ray diffraction analysis (Figure 3.3b) that shows the typical diffraction of the LDH phase, containing NO_3^- as interlayer anion, at 10.4° indexed as (003) [18,55]. Differently from the previous XRD pattern recorded on the powder, it was possible to see only the (003) reflection, as it generally represents the most intense one. The (006) reflection, visible in Figure 3.2c, was likely hidden by the signal related to the carbonaceous support in Figure 3.3b. Moreover, the SEM images highlighted that the carbon fibers were homogeneously covered by a solid deposit (Figures 3.3 c-e) that remained attached to the surface of the conductive support, even after being dried.

Different morphologies can be recognised within the same deposit: a thin veil that covers the fibers and well-dispersed spherical particles, which are visible when the veil is not present. Their chemical compositions were investigated through EDS analyses, carried out for both the morphologies. On the one hand, the analyses carried out on the veil revealed the compresence of Cu, Mg, and Al with molar ratios that reflect approximately those of the electrolytic bath, *i.e.*, 1.2: 1.2: 1 *vs* 1.5: 1.5: 1. On the other hand, the analyses performed on the spherical particles revealed higher amounts of Cu and Mg than Al, and thus the pristine molar ratio was not maintained, suggesting the deposition of a defective LDH structure displaying cations molar ratios of 1.3 for Cu/Mg, 2.5 for Cu/Al and 1.8 for Mg/Al and a total molar ratio between divalent and trivalent cations of 4.3. Further analyses on the ternary nature of the electrochemically synthesised LDH will be discussed in Chapter 4 (Paragraph 4.3.1).

Despite the presence of defective LDH structures localised in the spherical particles, a homogeneous and well-adherent deposit was obtained by applying a potentiodynamic procedure, which allowed to load a very low amount of catalyst (~ 1.14 mg). Indeed, the final purpose of this work was to use the LDH structure as precursor to achieve a well-dispersed active phase over an alkaline support and thus no further optimisation of the electrochemically synthesised material has been performed. Hence, starting from the just described precursor, further chemical modifications were optimised to achieve the final catalyst.

3.3.2 Optimisation of the LDH Precursor Calcination and Morphological Study

Once the LDH precursors were successfully loaded on the GDL, the samples were subjected to a calcination process in order to obtain the oxides species of each cation. Differently from the already reported procedures for the LDH calcination [45,62,63], the one to be applied to the CuMgAl LDH electrodeposited on the carbonaceous membrane must be modified. Indeed, according to the literature, the calcination is commonly carried out at 1173 or 673 K, but the carbon fibers of the support cannot withstand to such temperatures. For this reason, different temperatures were tested, with the aim to avoid possible alterations of the physical features of the membrane. The calcination was initially carried out at 773 K for 3h, with a temperature ramp of 2.5 K min^{-1} (Figure 3.5b). The temperature was chosen on the basis of a previous study on the calcination of CuMgAl LDH [64], while the time was selected considering the carbonaceous nature of the support as the first tried temperature of 773 K was already a too high temperature.

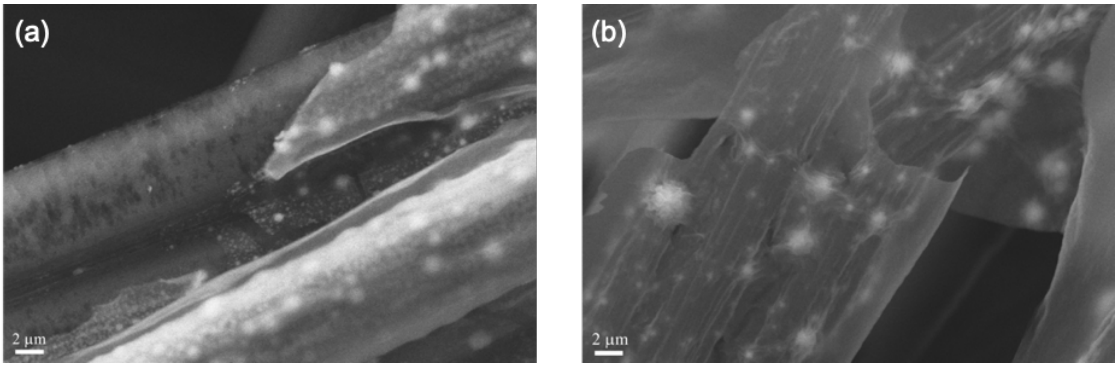

Figure 3.5. SEM images of the CuMgAl LDO/CP precursor at two different temperatures: (a) 773 K with a temperature ramp of 2.5 K min^{-1} and (b) 623 K with a temperature ramp of 2 K min^{-1} (3h each)

As shown in Figure 3.5a, the thermal treatment at 773 K for 3h caused an initial damage of the carbon fibers, visible in the upper part of the bare fiber. For this reason, a lower temperature was chosen to perform the calcination in order to preserve the integrity of the support. Figure 3.5b showed the image recorded after the calcination of the LDH precursor at 663 K for 3h.

In this case, the temperature ramp was lowered of 0.5 K min^{-1} (2 K min^{-1} *vs* 2.5 K min^{-1}), to guarantee a long enough time to the thermal treatment to be effective. As highlighted by the SEM images, the solid deposit obtained in the latter case has spherical particles of higher dimensions when compared to the pristine LDH precursors and to the ones obtained at 773 K. Indeed, focusing the attention on the greatest particle visible on the left side of Figure 3.5b, the diameter was around 3.5 μm, while the greatest particles of the LDH precursors were around 2.0 μm and those coming from the first calcined catalyst (773 K) were 1.0 μm. While the increase of the particles sizes after calcination is a well-known phenomenon [65], the unexpected decrease of the particles dimensions in the catalysts calcined at 773 K led to hypothesise a possible thermal strain due to the unstable condition of the carbonaceous support, which in turn has likely caused a damage of the LDH film. Moreover, to corroborate the fact that the carbon fibers treated at 663 K have not undergone any sort of damages, and meantime the calcination has occurred, other SEM images were recorded (Figure 3.6). However, in both cases, the thermal treatment seems to cause a partial detachment of the catalyst layer from the support.

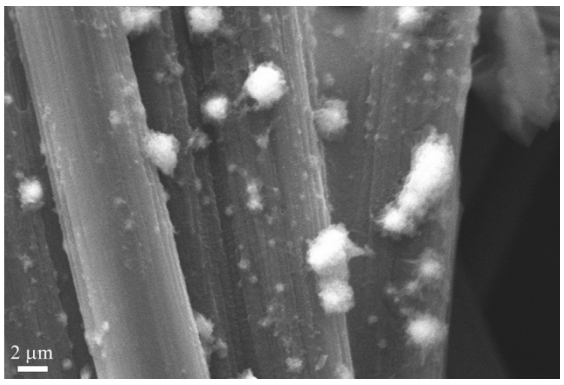

Figure 3.6. Carbon fibers of the CuMgAl LDO/CP obtained after calcination at 663 K

Therefore, the CuMgAl LDO obtained after the calcination at 663 K was chosen as the material to be further investigated and X-ray diffraction analysis was performed to validate the conversion of the LDH precursors into oxides species. Figure 3.7 displays the X-ray diffraction pattern recorded on the solid film.

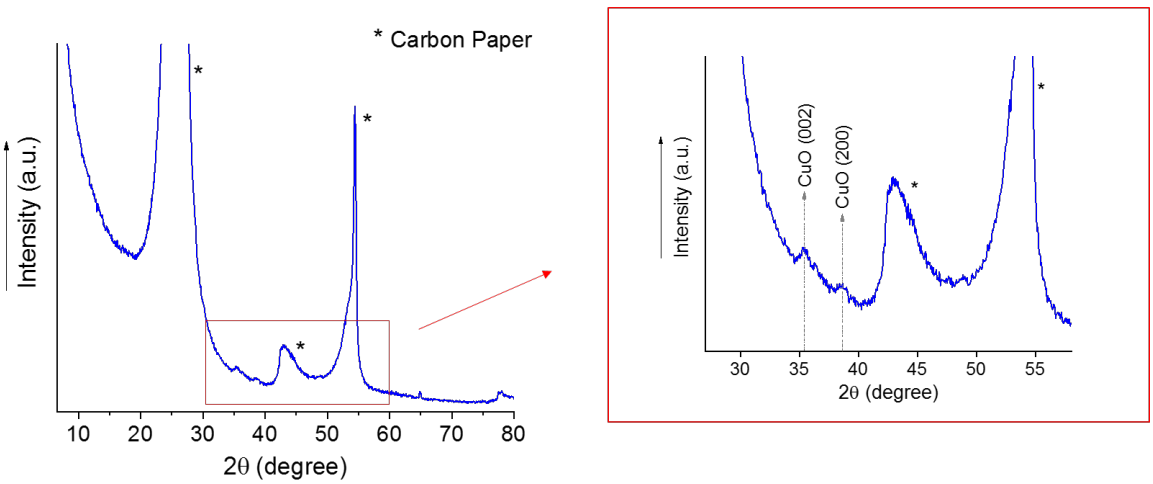

Figure 3.7. X-ray diffraction pattern recorded for the CuMgAl LDO/CP obtained at 663 K for 3h (2 K min^{-1})

The X-ray diffraction pattern evidences the presence of the CuO species, displaying its typical reflections at 35.4° and 38.9° (2θ) [66], while the reflections related to the LDH structure disappeared. Moreover, focusing the attention at higher angles, two smaller reflections can be observed (Figure 3.8).

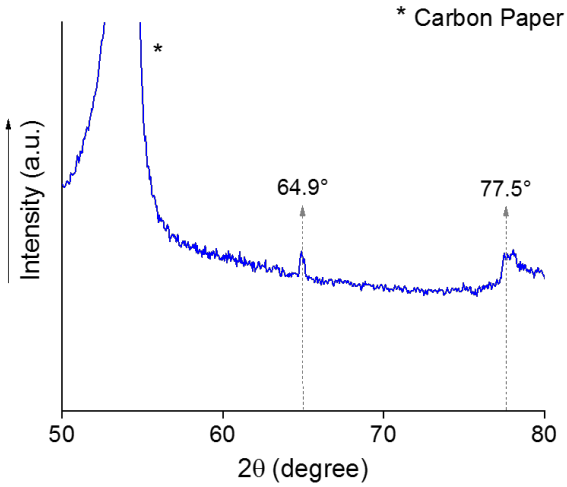

Figure 3.8. X-ray diffraction pattern recorded for the CuMgAl LDO/CP – focused at higher angles

The nature of these reflections is not easy to assign because of their low intensities. However, some hypotheses can be stated on the basis of the literature. The first reflection at 64.9° (2θ) can be referred to the presence of a $CuAl_2O_4$ spinel species [67] which can be likely formed in presence of Cu^{2+} inside the hydrotalcite structure, as CuO may be derived from its

decomposition [18]. However, this hypothesis needs to be confirmed since spinel species are usually achieved upon calcination at temperatures over 1023 K. While, the second reflection at 77.5° (2θ) can be explained in two ways. On the one hand, it is consistent with the presence of the $CuAl_2O_4$ spinel species that usually displayed a second reflection at 77.4° (2θ). On the other hand, such a diffraction can be referred also to the MgO species [68]. Since a correct assignment is difficult, as already said, it can be assumed that the CuMgAl LDO includes CuO species and mixed oxides species of Mg and Al, regardless their chemical composition or crystalline structure.

Therefore, the CuMgAl LDO/CP obtained at 663 K was employed as the optimised calcined electrocatalyst, and used for the further reduction and oxidation processes.

3.3.3 Optimisation of the CuMgAl LDO Reduction and Morphological Study

Since it was demonstrated that the carbonaceous support did not stand temperatures higher than 663 K, the experimental conditions tested for the reduction involved equal or lower temperatures. To date, the most widely used process to perform the reduction of a catalyst exploits hydrogen [8,18,69,70]. The samples were subjected to two reduction procedures.

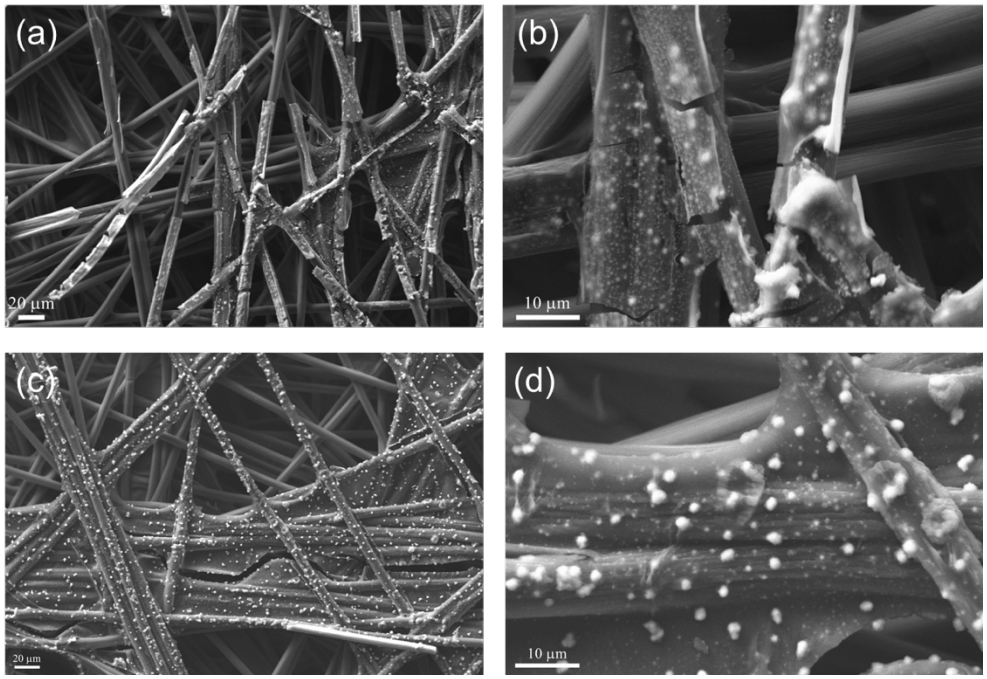

Figure 3.9. Reduced CuMgAl LDO with gaseous H_2/N_2 (10/90 mL min^{-1}) at (a), (b) 578 K for 3h (10 K min^{-1}) and (c), (d) at 663 K for 3h (2 K min^{-1})

The former was carried out at 578 K for 3h with a temperature ramp of 10 K min^{-1} [70], while the latter was performed at 663 K for 3h using a lower temperature ramp of 2 K min^{-1}. SEM analyses were achieved for both the reduced electrocatalysts.

In Figures 3.9 a-b, the CuMgAl LDO appears completely broken and detached from the fibers while, in Figures 3.9 c-d the catalyst is more uniform and adherent to the support even though it was obtained at a higher temperature. The reason for this difference likely relies on the different temperature ramp. Indeed, by applying 10 K min^{-1} the thin layer, that after the calcination was less adherent to the support, likely has suffered from a thermal stress which caused the homogeneous veil to crack, thus losing cohesion. Contrarily, even if a higher temperature was employed, the lower temperature ramp used in the second attempt of reduction has preserved the integrity of the layer, maintaining well-dispersed spherical particles along the fibers.

Hence, the second experimental condition was chosen as the best option to obtain a uniform catalyst adherent to the carbon fibers and further investigation was performed by X-ray diffraction analyses in order to verify the presence of metallic copper.

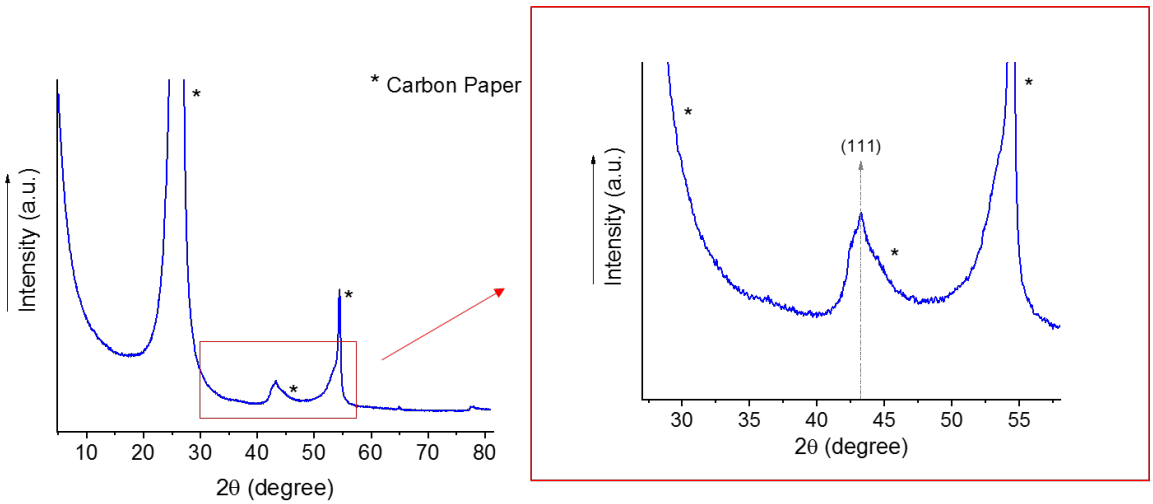

Figure 3.10. X-ray diffraction pattern of the reduced CuMgAl LDO at 578 K for 3h (H_2/N_2 10/90 mL min^{-1})

In Figure 3.10 is shown the XRD pattern achieved for the reduced LDO sample. Although there are no evident and well-defined reflections, the only evidence of the presence of Cu^0 is the shape of the reflection at 43.2° (2θ). Indeed, such a reflection, generally attributed to the carbonaceous support, has the same position of the Cu^0 crystal plane (111) but, if it is coming from the carbon fibers, the highest part of the peak is generally wide, while in this case, its shape tends to be sharper. This can be explained considering both the very low amount of metal copper and the possible presence of nanometric Cu^0 coming from the reduction, which make the shape of the metal copper reflection not to emerge from the broad signal of the support. Moreover, moving to higher angles, the presence of the reflections at 64.9° and 77.4° (2θ) was verified (Figure 3.11), so confirming the presence of the previously obtained oxides species that were not reduced in the selected experimental condition while the reflection related to the tenorite species (CuO) disappeared (Figure 3.10).

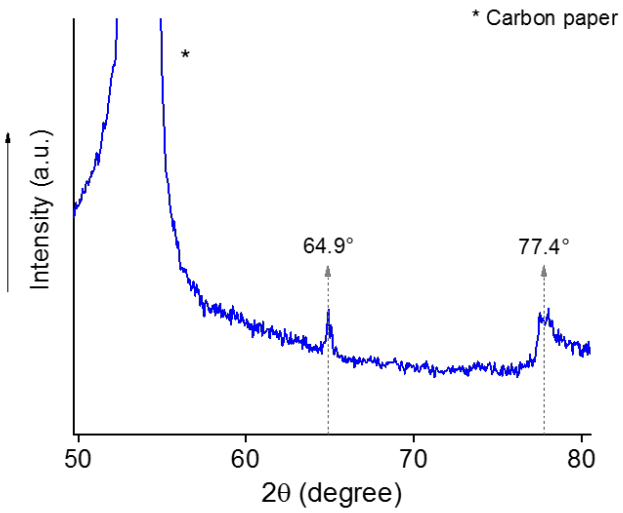

Figure 3.11. XRD pattern of the reduced CuMgAl LDO – focused at higher angles

To further verify the presence of metal copper within the reduced electrocatalyst, EDS analysis was performed on the spherical particles spread along the fibers (Figure 3.12). The analysis on position 1 confirmed the presence of Cu as the estimated atomic percentages (atomic %) for each cation were: Mg 0.05%, Al 0.04%, and Cu 1.42%.

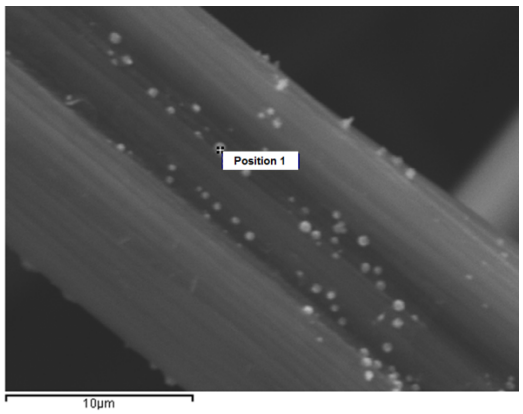

Figure 3.12. EDS analysis of the smaller spherical particles along the fibers

Due to the small thickness of the catalytic layer and its very low mass, it was not possible to perform other morphological evaluations.

Therefore, the CuMgAl LDO reduced at 578 K for 3h, and exposed to a mixture of H_2/N_2 (10/90 mL min^{-1}) with a temperature ramp of 2 K min^{-1} was chosen as the optimised reduced electrocatalyst which allowed to achieve metal Cu species within Mg/Al mixed oxides.

The last chemical treatment performed on the catalyst was the electrochemical oxidation, carried out to achieve the same redox active couple Cu^{+}/Cu^{0} that was studied in Chapter 2.

3.3.4 Morphological Study of the Electrochemical Oxidised Cu^{0}-MgAl LDO Electrocatalyst

The electrochemical oxidation of the reduced CuMgAl LDO/CP was carried out using the same procedure as employed to obtain the $Cu_2O/Cu^{0}/CP$ described in Chapter 2 (Paragraph 2.2.5). Similarly to the previous electrocatalysts, the morphological characterisations were performed essentially to verify if the metal copper was oxidised to Cu_2O, but since the catalytic layer was very thin, as already mentioned, X-ray diffraction was the only performed analysis.

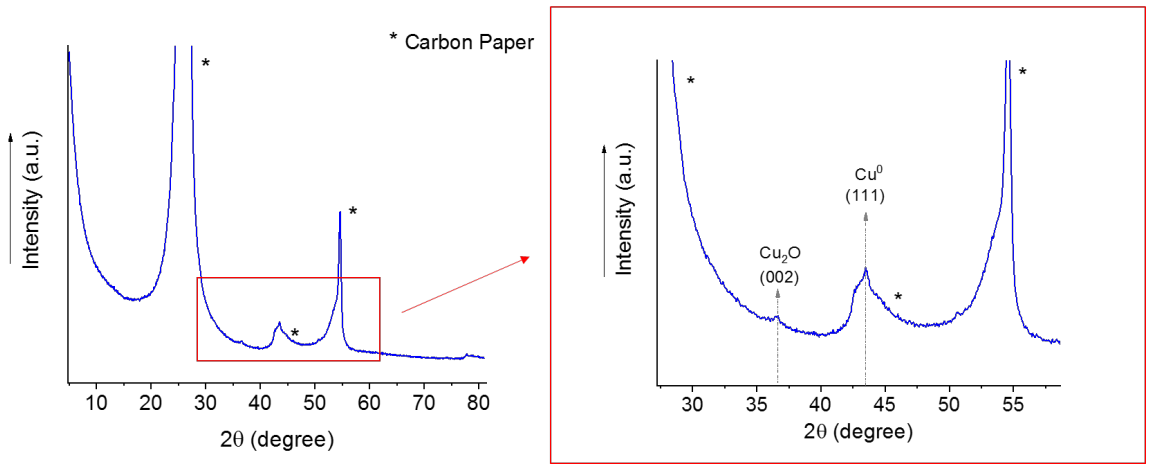

Figure 3.13. X-ray diffraction pattern of the oxidised Cu^{0}-MgAl LDO

As shown in the diffraction pattern (Figure 3.13), the presence of cuprite was verified by the very small reflection at 36.6° (2θ) [71], which was the only experimental evidence. Indeed, the signal at 43.2° (2θ) keeps the same shape displayed in the Cu^{0} – MgAl LDO/CP electrocatalyst, and this observation suggests that the metal copper was subjected only to a partial oxidation, similarly to the Cu-based film, thus making the contribution of the Cu_2O species particularly

scarce. Besides, even in this case, it was possible to recognise the presence of the mixed oxides species once more moving to higher angles.

Although experimental evidences of the effective copper oxidation were likely limited, the fact that no other species were identified, except for the previously obtained ones, led to hypothesise that a Cu_2O/Cu^0 - MgAl LDO was achieved. Further investigations, *e.g.*, by X-ray photoelectron spectroscopy, could help in identifying the chemical composition.

Once the just described electrocatalyst was obtained, the catalytic activity of all the materials synthesised was tested in order to evaluate if the utilisation of Mg and Al, both inside the LDH structure and as a mixed oxides-based support for the Cu active species, could improve the productivity in acetic acid if compared with the electrocatalysts that contained only Cu.

3.3.5 Direct Reduction of the LDH Precursors in Liquid Phase

A chemical reduction in liquid phase in mild operative conditions was also carried out in order to find an alternative route to obtained a well-dispersed Cu active phase supported on a basic layer, regardless the type of the alkaline sites. Here, the mild operative conditions were chosen to avoid the use of high temperature and better preserve the conductivity of the carbonaceous material. X-ray diffraction and SEM-EDS analyses were performed on each catalyst. As a result, the first experimental evidence of the presence of Cu was achieved by EDS analyses on the sample immersed in 0.1 M KNO_2 for 1h and 30 min at 333 K, as shown in Figure 3.14. The other samples did not show the presence of copper within the LDH structure.

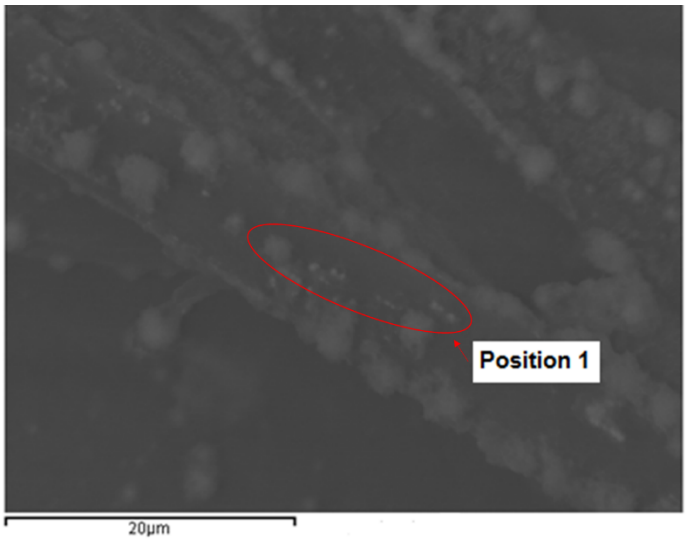

Figure 3.14. SEM images of the CuMgAl LDH/CP reduced in 0.1 M KNO_2 at 333K for 1h and 30 min

The SEM image shows the presence of small and bright particles along with larger spherical particles previously attributed to the LDH structure. Here, the EDS analysis confirmed the presence of copper since the atomic % of each cation was: 5.7 for Mg, 5.0 for Al, and 21.5 for Cu. Similarly to the previous morphological studies, the experimental evidences were not strongly detailed. However, it can be hypothesised that a partial reduction has occurred for this sample.

Later, the partially reduced sample was subjected to the further electrochemical oxidation, like the reduced sample exposed to H_2. In this case, a morphological evaluation of the possible presence of Cu_2O was carried out by X-ray diffraction analysis (Figure 3.15).

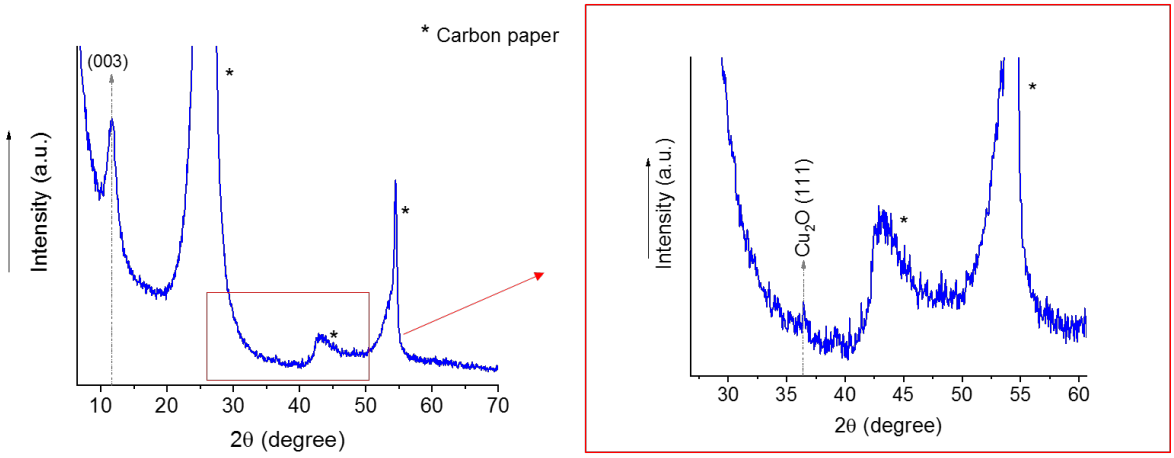

Figure 3.15. X-ray diffraction pattern of the Cu_2O/Cu^0 – MgAl LDH/CP

Since the LDH precursors had not been subjected to calcination prior to the reduction in KNO_2, the hydrotalcite structure was preserved, as confirmed by the presence of the (003) reflection. However, the analysis revealed also a partial oxidation of copper, evidenced from the slight reflection at 36.7° (2θ) thus suggesting that the achieved sample included a minimum amount of Cu^+/Cu^0 active redox couple within the preserved LDH structure.

3.3.6 Electrocatalytic Tests

A preliminary investigation was carried out on the hydrogen evolution reaction, which is known to be the side reaction of the CO_2ER [72,73].

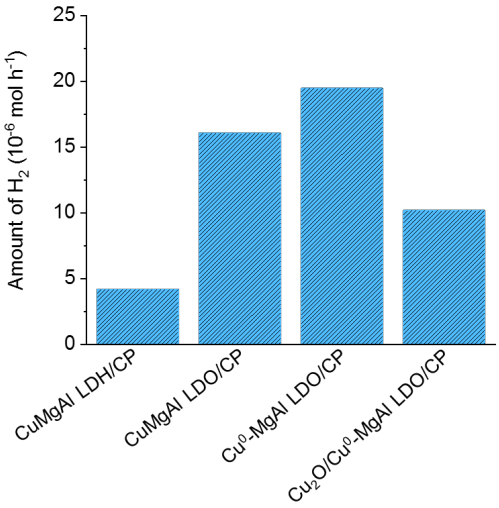

Figure 3.16. H_2 evolution during CO_2ER reaction tests at -0.4 V *vs* RHE in 0.3 M $KHCO_3$, 1h reaction

Similarly to the CO_2ER tests discussed in Chapter 2 (Paragraph 2.3.3.1), the only gaseous product obtained at this low cathodic potential was hydrogen, whose distribution among different materials is shown in Figure 3.16. The H_2 productivity was not calculated as no carbon dioxide was involved during the occurrence of this reaction. Here, its highest production was obtained by employing the Cu^0-MgAl LDO/CP electrocatalyst, which was the sample that displayed the presence of metal copper within the Mg/Al oxides species. Such a result confirmed that when Cu^0 was the only active phase, even in the presence of basic sites, the CO_2 electroreduction was not favoured but, on the contrary, the H_2 evolution preferably occurred, as demonstrated also with the Cu^0/CP. Contrarily, the pristine CuMgAl LDH/CP displayed the lowest H_2 production, interestingly lower than the final optimised materials. Therefore, from the preliminary study of the HER the electrocatalyst that did not undergo any thermal treatments best suppressed this side reaction, likely in favour of a higher CO_2 reduction products selectivity.

To confirm this hypothesis, quantitative H^1-NMR analyses on the collected liquid phases were performed and the values of the productivities were calculated as shown in Figure 3.17.

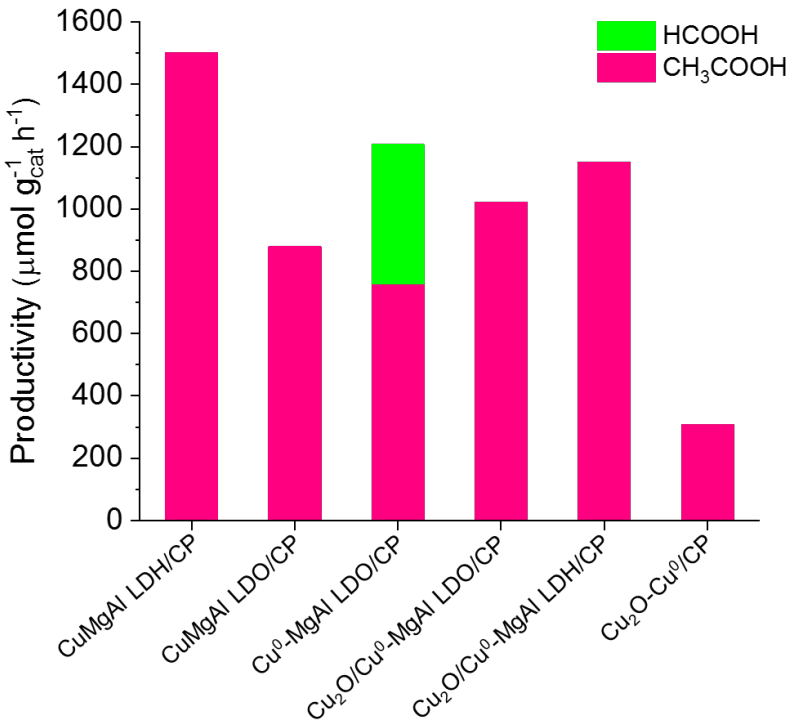

Figure 3.17. CO_2ER productivity at -0.4 V *vs* RHE in 0.3 M $KHCO_3$, 1h reaction

For any tested catalyst, acetic acid was the only product found in liquid phase, with the exception of the reduced electrocatalyst (Cu^0-MgAl LDO/CP). In such a case, also formic acid was detected, and, therefore, this electrocatalyst containing only Cu^0 species as the active phase displayed the worst selectivity. Remarkably, the final optimised electrocatalyst (Cu_2O-Cu^0-MgAl LDO/CP), which was supposed to be the most active, displayed a CH_3COOH productivity only slightly higher than the calcined and reduced samples: 1.0 $mmol_{CH3COOH}$ g_{cat}^{-1} h^{-1} *vs* 0.9 and 0.8 $mmol_{CH3COOH}$ g_{cat}^{-1} h^{-1} achieved when using CuMgAl LDO/CP and Cu^0-MgAl LDO/CP, respectively. Such results led to hypothesise that the overall amount of Cu^+/Cu^0 active redox couple, formed during the final electrochemical oxidation, was not enough to guarantee an effective improvement of the acetic acid production. Moreover, all those samples were subjected to several thermal treatments that, even if the optimised conditions have ensured the integrity of the conductive support, has likely caused partial

detachment of the catalytic layer. Such an issue, already highlighted by the SEM images previously shown, was also probably responsible for the higher H_2 evolution.

The decrease of the catalytic activities due to the thermal treatments was clearly confirmed by the unexpected results achieved with the non-treated sample, *i.e.*, CuMgAl LDH/CP, which displayed the highest productivity in acetic acid (1.5 $mmol_{CH3COOH}$ g_{cat}^{-1} h^{-1}), and, meantime, the lowest H_2 evolution. Such electrocatalyst was tested twice, in order to give a preliminary indication of the experiment reproducibility. The same productivity was obtained in both experiments. Beyond all the expectations, since pristine Layered Double Hydroxides are generally employed in electrochemical oxidation processes [28,29], the experimental evidences obtained in this work reveal that the CuMgAl LDH synthesised with a potentiodynamic method, even in presence of a defective LDH structure, has outstanding catalytic activities also for an electrochemical reduction process. Moreover, it was the only sample that, compared to the other investigated materials, did not undergo a further thermal or chemical treatment. That has surely guaranteed a constant adhesion of the catalytic layer to the carbon support, thus decreasing undesired resistances which could lower the overall efficiency. However, as already demonstrated by our previous work and as widely reported in literature [74–76], the C-C coupling is thought to be favoured in presence of the Cu^+/Cu^0 active redox couple. As Cu is likely be present in its oxidised form, *i.e.*, Cu^{2+} inside the LDH structure, the remarkable selectivity towards a C_2 product exhibited by the pristine CuMgAl LDH/CP led to hypothesise the presence of other copper species within the material. For this reason and on the basis of the achieved results, further investigations of the chemical and morphological composition of CuMgAl LDH, as well as the optimisation of its synthesis to guarantee a well-defined structure without defects, will be reported and discussed in Chapter 4.

Moreover, the productivity in acetic acid obtained with the catalyst coming from CuMgAl LDH/CP after chemical reduction in KNO_2, where it was assumed the presence of the active

redox couple Cu^{+}/Cu^{0} within the LDH structure, was higher than the ones found out for all the other treated samples, but still lower than the pristine CuMgAl LDH/CP.

Such an evidence confirmed, on the one hand, that any sort of treatment carried out on the pristine LDH inevitably caused a decrease of the catalytic performances. On the other hand, the presence of the Cu^{+}/Cu^{0} species within the LDH structure of the material submitted to the chemical reduction and its great catalytic performance contribute to support the idea that the pristine LDH (or LDH precursor) likely has almost the same chemical composition of the Cu_2O/Cu^{0} – MgAl LDH/CP.

Finally, the CH_3COOH productivities obtained with all the LDH-based electrocatalysts were compared to the most promising electrocatalyst previously studied, *i.e.*, the Cu_2O-Cu^{0}/CP, and from Figure 3.17, it was clearly demonstrated the benefits of the presence of alkaline sites together with the Cu active phase. In fact, they, both in form of oxides or hydroxides, favoured the interaction with the carbon dioxide, due to its acidic nature, thus enhancing its availability at the surface of the electrode. Indeed, the CH_3COOH productivity was increased from 0.31 $mmol_{CH3COOH}\ g_{cat}^{-1}\ h^{-1}$ when the electrocatalyst was Cu_2O-Cu^{0}/CP to 1.5 $mmol_{CH3COOH}\ g_{cat}^{-1}\ h^{-1}$ when using CuMgAl LDH/CP precursor. Although the consideration is based only on the experimental evidences just discussed, since it was not possible to perform a quantitative evaluation of the different basicity, such a behaviour is consistent with a recently reported transport modelling by Jouny *et al.* [77]. Indeed, they claimed the possibility to easily promote the formation of C_2 products in the presence of an alkaline environment near the electrode–electrolyte interface, which supresses the HER. Moreover, it can be hypothesised that the addition of a metal oxides support not only increased the local pH at the surface of the electrode but also guaranteed a better distribution of the Cu, regardless which species were present; that enhanced the available surface area with a consequent higher catalytic activity if compared to the compact films previously described in Chapter 2.

3.4 Conclusions

In this thesis work Cu-based electrocatalysts derived from LDH precursors were synthesised, characterised and tested for the CO_2ER, displaying substantial catalytic activities. At first, a three-metals based Layered Double Hydroxide, composed of Cu, Mg, and Al, was successfully synthesised by means of a simple, low time-consuming, and highly reproducible electrochemical deposition. Indeed, through a potentiodynamic approach, it was possible to obtain a homogeneous film well adherent on a 3D carbonaceous membrane (CP), designed to guarantee a better dispersion of the active phase. By means of X-ray diffraction and SEM-EDS analyses, the hydrotalcite structure was confirmed and the morphology of the CuMgAl LDH/CP precursor was investigated, pointing out both the spherical particles and the veil-like structures. The pristine LDH was then subjected to further thermal treatments in order to achieve the well-known catalysts, generally employed for the thermal CO_2 conversion reactions [35–38]. Such treatments, performed on the entire materials, were optimised to preserve the conductivity of the support and a sufficient adhesion between the catalytic layer and the carbon fibers. Since Cu^+/Cu^0 couple has been recognised as the main redox active one responsible for the C-C coupling, the final supported electrocatalyst was electrochemically oxidised until a Cu_2O/Cu^0-MgAl LDO/CP was obtained. As a result, except for the electrocatalyst reduced in hydrogen (Cu^0-MgAl LDO/CP) that confirmed the scarce activity of Cu^0 alone towards the CO_2ER, all the catalysts displayed selectivity towards acetic acid, outpacing the previous results obtained with the Cu_2O-Cu^0/CP. Surprisingly, the highest catalytic activity was achieved with the pristine CuMgAl LDH/CP, which led to hypothesise a possible presence of different Cu species within the material as such. Moreover, the higher catalytic activity exhibited by the materials which possess a LDH structure, compared to the mixed oxides derived forms, was also confirmed when employing the Cu_2O/Cu^0-MgAl LDH/CP electrocatalyst.

Such results demonstrate that, by virtue of the homogeneous distribution of the metal cations within the LDH layers which presumably is preserved after the chemical/thermal treatments, and the enhanced affinity CO_2 due to the higher alkalinity of LDHs, such electrocatalysts may become emerging materials, both in the field of thermal conversion and in the electrochemical CO_2 reduction. In particular, the remarkable results achieved with the pristine catalyst suggest the high potential of LDHs not only as catalysts precursors but also as promising catalysts that guarantee a high dispersion of the active phases and, consequently, a greater activity for CO_2ER.

3.5 References

(1) Keil, F. J. Complexities in Modeling of Heterogeneous Catalytic Reactions. *Comput. Math. with Appl.* **2013**, *65* (10), 1674–1697.

(2) Gao, D.; Cai, F.; Wang, G.; Bao, X. Nanostructured Heterogeneous Catalysts for Electrochemical Reduction of CO_2. *Curr. Opin. Green Sustain. Chem.* **2017**, *3*, 39–44.

(3) Raaijman, S. J.; Arulmozhi, N.; Koper, M. T. M. Morphological Stability of Copper Surfaces under Reducing Conditions. *ACS Appl. Mater. Interfaces* **2021**, *13* (41), 48730–48744.

(4) Nguyen, D. L. T.; Lee, C. W.; Na, J.; Kim, M.-C.; Tu, N. D. K.; Lee, S. Y.; Sa, Y. J.; Won, D. H.; Oh, H.-S.; Kim, H.; Min, B. K.; Han, S. S.; Lee, U.; Hwang, Y. J. Mass Transport Control by Surface Graphene Oxide for Selective CO Production from Electrochemical CO_2 Reduction. *ACS Catal.* **2020**, *10* (5), 3222–3231.

(5) Lin, J.; Yan, S.; Zhang, C.; Hu, Q.; Cheng, Z. Electroreduction of CO_2 toward High Current Density. *Processes* **2022**, *10* (5), 1–33.

(6) Durst, J.; Rudnev, A.; Dutta, A.; Fu, Y.; Herranz, J.; Kaliginedi, V.; Kuzume, A.; Permyakova, A. A.; Paratcha, Y.; Broekmann, P.; Schmidt, T. J. Electrochemical CO_2 Reduction - A Critical View on Fundamentals, Materials and Applications. *Chimia (Aarau)*. **2015**, *69* (12), 769–776.

(7) Reske, R.; Mistry, H.; Behafarid, F.; Roldan Cuenya, B.; Strasser, P. Particle Size Effects in the Catalytic Electroreduction of CO_2 on Cu Nanoparticles. *J. Am. Chem. Soc.* **2014**, *136* (19), 6978–6986.

(8) Chen, Y.; Hong, H.; Cai, J.; Li, Z. Highly Efficient CO_2 to CO Transformation over Cu-Based Catalyst Derived from a CuMgAl-Layered Double Hydroxide (LDH). *ChemCatChem* **2021**, *13* (2), 656–663.

(9) Abou Rached, J.; Cesario, M. R.; Estephane, J.; Tidahy, H. L.; Gennequin, C.; Aouad, S.; Aboukaïs, A.; Abi-Aad, E. Effects of Cerium and Lanthanum on Ni-Based Catalysts for CO_2 Reforming of Toluene. *J. Environ. Chem. Eng.* **2018**, *6* (4), 4743–4754.

(10) Han, J. W.; Park, J. S.; Choi, M. S.; Lee, H. Uncoupling the Size and Support Effects of Ni Catalysts for Dry Reforming of Methane. *Appl. Catal. B Environ.* **2017**, *203*, 625–632.

(11) Aziz, M. A. A.; Jalil, A. A.; Wongsakulphasatch, S.; Vo, D.-V. N. Understanding the Role of Surface Basic Sites of Catalysts in CO_2 Activation in Dry Reforming of Methane: A Short Review. *Catal. Sci. Technol.* **2020**, *10* (1), 35–45.

(12) Xie, T.; Wang, J.; Ding, F.; Zhang, A.; Li, W.; Guo, X.; Song, C. CO_2 Hydrogenation to Hydrocarbons over Alumina-Supported Iron Catalyst: Effect of Support Pore Size. *J. CO_2 Util.* **2017**, *19*, 202–208.

(13) Lam, E.; Corral-Pérez, J. J.; Larmier, K.; Noh, G.; Wolf, P.; Comas-Vives, A.; Urakawa, A.; Copéret, C. CO_2 Hydrogenation on Cu/Al_2O_3 : Role of the Metal/Support Interface in Driving Activity and Selectivity of a Bifunctional Catalyst. *Angew. Chemie Int. Ed.* **2019**, *58* (39), 13989–13996.

(14) Bach, V. R.; de Camargo, A. C.; de Souza, T. L.; Cardozo-Filho, L.; Alves, H. J. Dry Reforming of Methane over $Ni/MgO–Al_2O_3$ Catalysts: Thermodynamic Equilibrium Analysis and Experimental Application. *Int. J. Hydrogen Energy* **2020**, *45* (8), 5252–5263.

(15) Sanches, S. G.; Flores, J. H.; da Silva, M. I. P. Cu/ZnO and $Cu/ZnO/ZrO_2$ Catalysts Used for Methanol Steam Reforming. *Mol. Catal.* **2018**, *454*, 55–62.

(16) Liao, M.; Guo, C.; Guo, W.; Hu, T.; Xie, J.; Gao, P.; Xiao, H. One-Step Growth of $CuO/ZnO/CeO_2/ZrO_2$ Nanoflowers Catalyst by Hydrothermal Method on Al_2O_3 Support for Methanol Steam Reforming in a Microreactor. *Int. J. Hydrogen Energy* **2021**, *46* (14), 9280–9291.

(17) Mohtashami, Y.; Taghizadeh, M. Performance of the ZrO_2 Promoted Cu-ZnO Catalyst Supported on Acetic Acid-Treated MCM-41 in Methanol Steam Reforming. *Int. J. Hydrogen Energy* **2019**, *44* (12), 5725–5738.

(18) Cavani, F.; Trifirò, F.; Vaccari, A. Hydrotalcite-Type Anionic Clays: Preparation, Properties and Applications. *Catal. Today* **1991**, *11* (2), 173–301.

(19) Forano, C.; Hibino, T.; Leroux, F.; Taviot-Guého, C. Chapter 13.1 Layered Double Hydroxides. *Developments in Clay Science, Vol. 1* **2006**, *1*, 1021–1095.

(20) Tonelli, D.; Gualandi, I.; Musella, E.; Scavetta, E. Synthesis and Characterization of Layered Double Hydroxides as Materials for Electrocatalytic Applications. *Nanomaterials* **2021**, *11* (3), 1–20.

(21) Basile, F.; Basini, L.; Fornasari, G.; Gazzano, M.; Trifirò, F.; Vaccari, A. Anionic Clays as Precursors of Noble Metal Based Catalysts for Methane Activation. In *Preparation of Catalysts VII* **1998**, *118*, 31–40.

(22) Basile, F.; Fornasari, G.; Gazzano, M.; Vaccari, A. Rh, Ru and Ir Catalysts Obtained by HT Precursors: Effect of the Thermal Evolution and Composition on the Material Structure and Use. *J. Mater. Chem.* **2002**, *12* (11), 3296–3303.

(23) Tabanelli, T.; Cocchi, S.; Gumina, B.; Izzo, L.; Mella, M.; Passeri, S.; Cavani, F.; Lucarelli, C.; Schütz, J.; Bonrath, W.; Netscher, T. Mg/Ga Mixed-Oxide Catalysts for Phenol Methylation: Outstanding Performance in 2,4,6-Trimethylphenol Synthesis with Co-Feeding of Water. *Appl. Catal. A Gen.* **2018**, *552*, 86–97.

(24) De Maron, J.; Eberle, M.; Cavani, F.; Basile, F.; Dimitratos, N.; Maireles-Torres, P. J.; Rodriguez-Castellón, E.; Tabanelli, T. Continuous-Flow Methyl Methacrylate Synthesis over Gallium-Based Bifunctional Catalysts. *ACS Sustain. Chem. Eng.* **2021**, *9* (4), 1790–1803.

(25) Mohapatra, L.; Parida, K. A Review on the Recent Progress, Challenges and Perspective of Layered Double Hydroxides as Promising Photocatalysts. *J. Mater. Chem. A* **2016**, *4* (28), 10744–10766.

(26) Khalil, M.; Gunlazuardi, J.; Ivandini, T. A.; Umar, A. Photocatalytic Conversion of CO_2 Using Earth-Abundant Catalysts: A Review on Mechanism and Catalytic Performance. *Renew. Sustain. Energy Rev.* **2019**, *113*, 1–16.

(27) Fasolini, A.; Sangiorgi, N.; Tosi Brandi, E.; Sangiorgi, A.; Mariani, F.; Scavetta, E.; Sanson, A.; Basile, F. Increased Efficiency and Stability of Dye-Sensitized Solar Cells (DSSC) Photoanode by Intercalation of Eosin Y into Zn/Al Layered Double Hydroxide. *Appl. Clay Sci.* **2021**, *212*, 1–10.

(28) Vlamidis, Y.; Scavetta, E.; Gazzano, M.; Tonelli, D. Iron vs Aluminum Based Layered Double Hydroxides as Water Splitting Catalysts. *Electrochim. Acta* **2016**, *188*, 653–660.

(29) Dionigi, F.; Zeng, Z.; Sinev, I.; Merzdorf, T.; Deshpande, S.; Lopez, M. B.; Kunze, S.; Zegkinoglou, I.; Sarodnik, H.; Fan, D.; Bergmann, A.; Drnec, J.; Araujo, J. F. de; Gliech, M.; Teschner, D.; Zhu, J.; Li, W.-X.; Greeley, J.; Cuenya, B. R.; Strasser, P. In-Situ Structure and Catalytic Mechanism of NiFe and CoFe Layered Double Hydroxides during Oxygen Evolution. *Nat. Commun.* **2020**, *11* (1), 1–10.

(30) Ballarin, B.; Seeber, R.; Tonelli, D.; Vaccari, A. Electrocatalytic Properties of Nickel(II) Hydrotalcite-Type Anionic Clay: Application to Methanol and Ethanol Oxidation. *J. Electroanal. Chem.* **1999**, *463* (1), 123–127.

(31) Scavetta, E.; Tonelli, D. Amperometric Sensors Based on Synthetic Hydrotalcites and Their Application for Ethanol Detection in Beer. *Electroanalysis* **2005**, *17* (4), 363–370.

(32) Gualandi, I.; Tessarolo, M.; Mariani, F.; Arcangeli, D.; Possanzini, L.; Tonelli, D.; Fraboni, B.; Scavetta, E. Layered Double Hydroxide-Modified Organic Electrochemical Transistor for Glucose and Lactate Biosensing. *Sensors* **2020**, *20* (12), 1–14.

(33) Choy, J.; Choi, S.; Oh, J.; Park, T. Clay Minerals and Layered Double Hydroxides for Novel Biological Applications. *Appl. Clay Sci.* **2007**, *36* (1–3), 122–132.

(34) Millange, F.; Walton, R. I.; Lei, L.; O'Hare, D. Efficient Separation of Terephthalate and Phthalate Anions by Selective Ion-Exchange Intercalation in the Layered Double Hydroxide $Ca_2Al(OH)_6 \cdot NO_3 \cdot 2H_2O$. *Chem. Mater.* **2000**, *12* (7), 1990–1994.

(35) Fasolini, A.; Abate, S.; Barbera, D.; Centi, G.; Basile, F. Pure H_2 Production by Methane Oxy-Reforming over Rh-Mg-Al Hydrotalcite-Derived Catalysts Coupled with a Pd Membrane. *Appl. Catal. A Gen.* **2019**, *581* (May), 91–102.

(36) Kim, K. Y.; Lee, J. H.; Lee, H.; Noh, W. Y.; Kim, E. H.; Ra, E. C.; Kim, S. K.; An, K.; Lee, J. S. Layered Double Hydroxide-Derived Intermetallic $Ni_3GaC_{0.25}$ Catalysts for Dry Reforming of Methane. *ACS Catal.* **2021**, *11* (17), 11091–11102.

(37) Dewangan, N.; Hui, W. M.; Jayaprakash, S.; Bawah, A.-R.; Poerjoto, A. J.; Jie, T.; Jangam, A.; Hidajat, K.; Kawi, S. Recent Progress on Layered Double Hydroxide (LDH) Derived Metal-Based Catalysts for CO_2 Conversion to Valuable Chemicals. *Catal. Today* **2020**, *356*, 490–513.

(38) Li, M. M.-J.; Chen, C.; Ayvalı, T.; Suo, H.; Zheng, J.; Teixeira, I. F.; Ye, L.; Zou, H.; O'Hare, D.; Tsang, S. C. E. CO_2 Hydrogenation to Methanol over Catalysts Derived from Single Cationic Layer CuZnGa LDH Precursors. *ACS Catal.* **2018**, *8* (5), 4390–4401.

(39) Basile, F.; Fornasari, G.; Rosetti, V.; Trifirò, F.; Vaccari, A. Effect of the Mg/Al Ratio of the Hydrotalcite-Type Precursor on the Dispersion and Activity of Rh and Ru Catalysts for the Partial Oxidation of Methane. *Catal. Today* **2004**, *91–92*, 293–297.

(40) Kühl, S.; Friedrich, M.; Armbrüster, M.; Behrens, M. Cu,Zn,Al Layered Double Hydroxides as Precursors for Copper Catalysts in Methanol Steam Reforming – pH-Controlled Synthesis by Microemulsion Technique. *J. Mater. Chem.* **2012**, *22* (19), 9632–9638.

(41) Scavetta, E.; Berrettoni, M.; Seeber, R.; Tonelli, D. [Ni/Al-Cl]-Based Hydrotalcite Electrodes as Amperometric Sensors: Preparation and Electrochemical Study. *Electrochim. Acta* **2001**, *46* (17), 2681–2692.

(42) Shamsayei, M.; Yamini, Y.; Asiabi, H.; Khataei, M. M. Electrodeposition of Layered Double Hydroxide Intercalated with 2,3-Dimercaptopropane Sulfonate on Carbon Cloth and Application for Effective Uptake of Heavy Metals. *Appl. Clay Sci.* **2020**, *196*, 1–12.

(43) Scavetta, E.; Mignani, A.; Prandstraller, D.; Tonelli, D. Electrosynthesis of Thin Films of Ni, Al Hydrotalcite Like Compounds. *Chem. Mater.* **2007**, *19* (18), 4523–4529.

(44) Gualandi, I.; Vlamidis, Y.; Mazzei, L.; Musella, E.; Giorgetti, M.; Christian, M.; Morandi, V.; Scavetta, E.; Tonelli, D. Ni/Al Layered Double Hydroxide and Carbon Nanomaterial Composites for Glucose Sensing. *ACS Appl. Nano Mater.* **2019**, *2* (1), 143–155.

(45) Basile, F.; Benito, P.; Fornasari, G.; Monti, M.; Scavetta, E.; Tonelli, D.; Vaccari, A. Novel Rh-Based Structured Catalysts for the Catalytic Partial Oxidation of Methane. *Catal. Today* **2010**, *157* (1–4), 183–190.

(46) Li, L.; Wen, X.; Fu, X.; Wang, F.; Zhao, N.; Xiao, F.; Wei, W.; Sun, Y. MgO/Al_2O_3 Sorbent for CO_2 Capture. *Energy & Fuels* **2010**, *24* (10), 5773–5780.

(47) Yang, Z.; Wei, J.; Zeng, G.; Zhang, H.; Tan, X.; Ma, C.; Li, X.; Li, Z.; Zhang, C. A Review on Strategies to LDH-Based Materials to Improve Adsorption Capacity and Photoreduction Efficiency for CO_2. *Coord. Chem. Rev.* **2019**, *386*, 154–182.

(48) Musella, E.; Gualandi, I.; Scavetta, E.; Rivalta, A.; Venuti, E.; Christian, M.; Morandi, V.; Mullaliu, A.; Giorgetti, M.; Tonelli, D. Newly Developed Electrochemical Synthesis of Co-Based Layered Double Hydroxides: Toward Noble Metal-Free Electro-Catalysis. *J. Mater. Chem. A* **2019**, *7* (18), 11241–11249.

(49) Musella, E.; Gualandi, I.; Giorgetti, M.; Scavetta, E.; Basile, F.; Rivalta, A.; Venuti, E.; Corticelli, F.; Christian, M.; Morandi, V.; Tonelli, D. Electrosynthesis and Characterization of Layered Double Hydroxides on Different Supports. *Appl. Clay Sci.* **2021**, *202*, 1–12.

(50) Gupta, V.; Gupta, S.; Miura, N. Potentiostatically Deposited Nanostructured Co_xNi_{1-x} Layered Double Hydroxides as Electrode Materials for Redox-Supercapacitors. *J. Power Sources* **2008**, *175* (1), 680–685.

(51) Indira, L.; Kamath, P. V. Electrogeneration of Base by Cathodic Reduction of Anions: Novel One-Step Route to Unary and Layered Double Hydroxides (LDHs). *J. Mater. Chem.* **1994**, *4* (9), 1487–1490.

(52) Scavetta, E.; Ballarin, B.; Giorgetti, M.; Carpani, I.; Cogo, F.; Tonelli, D. Electrodes Modified by One-Step Electrosynthesis of Ni/Al-NO_3 Double Layered Hydroxide. *J. New Mater. Electrochem. Syst.* **2004**, *7* (1), 43–50.

(53) Gualandi, I.; Solito, A. G.; Scavetta, E.; Tonelli, D. Electrochemical Pretreatment of Pt Surface: Modification with Co/Al Layered Double Hydroxide for Analytical Applications. *Electroanalysis* **2012**, *24* (4), 857–864.

(54) Gualandi, I.; Monti, M.; Scavetta, E.; Tonelli, D.; Prevot, V.; Mousty, C. Electrodeposition of Layered Double Hydroxides on Platinum: Insights into the Reactions Sequence. *Electrochim. Acta* **2015**, *152*, 75–83.

(55) Monti, M.; Benito, P.; Basile, F.; Fornasari, G.; Gazzano, M.; Scavetta, E.; Tonelli, D.; Vaccari, A. Electrosynthesis of Ni/Al and Mg/Al Layered Double Hydroxides on Pt and FeCrAlloy Supports: Study and Control of the pH near the Electrode Surface. *Electrochim. Acta* **2013**, *108*, 596–604.

(56) Young, J. F. T. XXVIII. The Crystal Structure of Various Heusler Alloys by the Use of X-Rays. *London, Edinburgh, Dublin Philos. Mag. J. Sci.* **1923**, *46* (272), 291–305.

(57) Musella, E.; Gualandi, I.; Scavetta, E.; Gazzano, M.; Rivalta, A.; Venuti, E.; Christian, M.; Morandi, V.; Tonelli, D. Electrochemical Approach for the Production of Layered Double Hydroxides with a Well-Defined Co/Me^{III} Ratio. *Chem. – A Eur. J.* **2019**, *25* (71), 16301–16310.

(58) Guillou, N.; Louër, M.; Louër, D. An X-Ray and Neutron Powder Diffraction Study of a New Polymorphic Phase of Copper Hydroxide Nitrate. *J. Solid State Chem.* **1994**, *109* (2), 307–314.

(59) Pereira, D. C.; Faria, D. L. A. de; Constantino, V. R. L. Cu^{II} Hydroxy Salts: Characterization of Layered Compounds by Vibrational Spectroscopy. *J. Braz. Chem. Soc.* **2006**, *17* (8), 1651–1657.

(60) Malherbe, F.; Bigey, L.; Forano, C.; de Roy, A.; Besse, J.-P. Structural Aspects and Thermal Properties of Takovite-like Layered Double Hydroxides Pillared with Chromium Oxo-Anions. *J. Chem. Soc. Dalt. Trans.* **1999**, *21*, 3831–3839.

(61) Molano-Mendoza, M.; Donneys-Victoria, D.; Marriaga-Cabrales, N.; Angel Mueses, M.; Puma, G. L.; Machuca-Martínez, F. Dataset on Infrared Spectroscopy and X-Ray Diffraction Patterns of Mg–Al Layered Double Hydroxides by the Electrocoagulation Technique. *Data Br.* **2019**, *27*, 1–11.

(62) Benito, P.; Nuyts, G.; Monti, M.; De Nolf, W.; Fornasari, G.; Janssens, K.; Scavetta, E.; Vaccari, A. Stable Rh Particles in Hydrotalcite-Derived Catalysts Coated on FeCr Alloy Foams by Electrosynthesis. *Appl. Catal. B Environ.* **2015**, *179*, 321–332.

(63) Ho, P.; Scavetta, E.; Tonelli, D.; Fornasari, G.; Vaccari, A.; Benito, P. Hydrotalcite-Type Materials Electrodeposited on Open-Cell Metallic Foams as Structured Catalysts. *Inorganics* **2018**, *6* (3), 1–18.

(64) Mokhtar, M.; Alhashedi, B. F. A.; Kashmery, H. A.; Ahmed, N. S.; Saleh, T. S.; Narasimharao, K. Highly Efficient Nanosized Mesoporous CuMgAl Ternary Oxide Catalyst for Nitro-Alcohol Synthesis: Ultrasound-Assisted Sustainable Green Perspective for the Henry Reaction. *ACS Omega* **2020**, *5* (12), 6532–6544.

(65) Phromma, S.; Wutikhun, T.; Kasamechonchung, P.; Eksangsri, T.; Sapcharoenkun, C. Effect of Calcination Temperature on Photocatalytic Activity of Synthesized TiO_2 Nanoparticles via Wet Ball Milling Sol-Gel Method. *Appl. Sci.* **2020**, *10* (3), 1–13.

(66) Asbrink, S.; Waskowska, A. CuO: X-Ray Single-Crystal Structure Determination at 196 K and Room Temperature. *J. Phys. Condens. Matter* **1991**, *3* (42), 8173–8180.

(67) O'Neill, H. S. t. C.; James, M.; Dollase, W. A.; Redfern, S. A. T. Temperature Dependence of the Cation Distribution in $CuAl_2O_4$ Spinel. *Eur. J. Mineral.* **2005**, *17* (4), 581–586.

(68) Karki, B. B.; Stixrude, L.; Clark, S. J.; Warren, M. C.; Ackland, G. J.; Crain, J. Structure and Elasticity of MgO at High Pressure. *Am. Mineral.* **1997**, *82* (1–2), 51–60.

(69) Tanasoi, S.; Tanchoux, N.; Urdă, A.; Tichit, D.; Săndulescu, I.; Fajula, F.; Marcu, I.-C. New Cu-Based Mixed Oxides Obtained from LDH Precursors, Catalysts for Methane Total Oxidation. *Appl. Catal. A Gen.* **2009**, *363* (1–2), 135–142.

(70) Maslova, V.; Quadrelli, E. A.; Gaval, P.; Fasolini, A.; Albonetti, S.; Basile, F. Highly-Dispersed Ultrafine Pt Nanoparticles on Microemulsion-Mediated TiO_2 for Production of Hydrogen and Valuable Chemicals via Oxidative Photo-Dehydrogenation of Glycerol. *J. Environ. Chem. Eng.* **2021**, *9* (2), 1–10.

(71) Zav'yalova, A. A.; Imamov, R. M.; Pinsker, Z. G. Production and Investigation of Thin Films of Cu_2O. *Kristallografiya* **1964**, *9* (6), 413–415.

(72) Hori, Y. Electrochemical CO_2 Reduction on Metal Electrodes. In *Modern Aspects of Electrochemistry*; Springer New York: New York, NY, **2008**, 89–189.

(73) Rahaman, M.; Dutta, A.; Zanetti, A.; Broekmann, P. Electrochemical Reduction of CO_2 into Multicarbon Alcohols on Activated Cu Mesh Catalysts: An Identical Location (IL) Study. *ACS Catal.* **2017**, *7* (11), 7946–7956.

(74) Zhu, Q.; Sun, X.; Yang, D.; Ma, J.; Kang, X.; Zheng, L.; Zhang, J.; Wu, Z.; Han, B. Carbon Dioxide Electroreduction to C_2 Products over Copper-Cuprous Oxide Derived from Electrosynthesized Copper Complex. *Nat. Commun.* **2019**, *10* (1), 1–11.

(75) Mistry, H.; Varela, A. S.; Bonifacio, C. S.; Zegkinoglou, I.; Sinev, I.; Choi, Y.-W.; Kisslinger, K.; Stach, E. A.; Yang, J. C.; Strasser, P.; Cuenya, B. R. Highly Selective Plasma-Activated Copper Catalysts for Carbon Dioxide Reduction to Ethylene. *Nat. Commun.* **2016**, *7* (1), 1–8.

(76) Roberts, F. S.; Kuhl, K. P.; Nilsson, A. High Selectivity for Ethylene from Carbon Dioxide Reduction over Copper Nanocube Electrocatalysts. *Angew. Chemie* **2015**, *127* (17), 5268–5271.

(77) Jouny, M.; Luc, W.; Jiao, F. High-Rate Electroreduction of Carbon Monoxide to Multi-Carbon Products. *Nat. Catal.* **2018**, *1* (10), 748–755.

CHAPTER 4

Electrosynthesised CuMgAl Layered Double Hydroxides as New Catalysts for the Electrochemical Reduction of CO_2

The results obtained with the Cu-based electrocatalysts derived from CuMgAl layered double hydroxides precursors outpaced those of the $Cu^{0-I/II}$ films in terms of CH_3COOH productivity, mainly due to the addition of basic sites, *i.e.*, Mg/Al oxides species. Among them, the highest catalytic activity was obtained with the pristine CuMgAl LDH, electrochemically loaded on the carbonaceous membrane. Indeed, such a material, which had not been subjected to any further calcination or reduction process, displayed a CH_3COOH productivity 5 times higher than those obtained before. For this reason, the attention was focused on the use of this Layered Double Hydroxide as electrocatalyst for the CO_2ER. Initially, further investigations were carried out to characterised the exact morphological and chemical compositions since the previous results led to hypothesise the presence of different copper species within the LDH structure. Then, starting from the first synthesised LDH, *i.e.*, the CuMgAl 1.5: 1.5: 1, optimisations in terms of cations molar ratios and amounts of loaded catalyst were carried out with the ultimate goal to find the most promising CuMgAl LDH electrocatalysts suitable for the CH_3COOH production during the CO_2ER reaction.

The content of this chapter has been adapted from the following patent application:

D. Tonelli, E. Scavetta, F. Mariani, M. Serafini, A. Fasolini, and F. Basile "*Rivestimenti catalitici a base di idrossidi doppi a strato contenenti: Cu, Mg e Al, ottenibili per via elettrochimica, per impieghi quali la riduzione elettrochimica dell'anidride carbonica*", Italian Patent Application No 102022000025860, filed on December 16th, 2022.

4.1 Introduction

The Layered Double Hydroxides (LDHs) are a class of compounds employed in many fields such as medicine, environment, biotechnology, and electrochemistry [1]. Concerning the last application mentioned, they can be exploited for a wide range of purposes like supercapacitors [2], sensors [3], electrocatalysts for the oxygen evolution reaction (OER) [4], or as light-sensitive electrodes for applications in solar and fuel cells [5].

However, not all the LDHs are suitable for the electrochemical applications since one of the main requirements of the materials employed in this field is the electrical conductivity. To this aim, redox active species can be added to the hydrotalcite structure and, generally, they are transition metals, like Co, Ni, and Mn [6–8], which are easily involved in Faradaic reactions. However, in order to be used as electrochemically active materials, the LDHs need to be supported over conductive supports that can be made of metal [9] or carbon [10]. Typically, the coating is obtained by depositing a fixed amount of a colloidal suspension of a chemically synthesised LDH, which is then let dry in air, and sometimes a binder is added to improve the adhesion to the conductive support [1,11]. Since those methods generally suffer from scarce mechanical properties or little conductivity, the films of the hydrotalcite can be grown directly on the electrode. The most interesting approach is the electrochemical deposition, as described in the previous chapter, which can be carried out in different ways: (i) potentiostatic synthesis which involves the application of a fixed cathodic potential (generally between -0.9 and -1.1 V *vs* SCE) for a well-defined period of time, (ii) galvanostatic synthesis which exploits a fixed current instead of a fixed potential difference, and (iii) potentiodynamic synthesis for which the deposition is stimulated by cyclic voltammetry [3]. The last route allows to restore the concentration gradient originating after the LDH precipitation, thus enhancing the control on the M^{II} and M^{III} cations molar ratio. Since the charge transport in the LDH occurs through the phenomena of the electron hopping and anions movement [12], both the chemically synthesised

and the *in situ* grown materials display a better performance in strong alkaline solutions and are generally employed as anode modifiers to catalyse oxidation processes. Moreover, thanks to their large surface area, adjustable band gap, wide-range light absorption, low cost, and notable recyclability, LDH compounds and their derivatives can be employed also as visible-light driven photocatalysts suitable not only for photo-oxidation processes, *i.e.*, oxygen evolution reaction or pollutants degradation [13], but also as photocatalysts for the hydrogen evolution reaction [14]. In this context, a recently and promising application is the use of the redox-active LDHs as cathodes for the photocatalytic CO_2 reduction [15–17]. Depending on the final composition of the layered materials, the photocatalytic CO_2 conversion can be finely tuned to the desired product, including CO, CH_4, or CH_3OH. Interestingly, Ahmed *et al.* [18] demonstrated that the addition of Cu to ZnAl and ZnGa LDHs improved the photocatalytic activities, as it extended the LDHs absorption to visible light and switched the selectivity from CO towards the production of CH_3OH.

However, due to their high CO_2 sorption capability, which is dependent on their layered morphology, and their high affinity to carbonate anions, nowadays the interest for LDHs compounds is not limited to the photocatalytic processes, but also to the electrochemical CO_2 conversion. However, since LDHs display a relatively low electrical conductivity compared to metals, very few studies have been performed on the pristine layered double hydroxides as cathode materials for CO_2ER. Nevertheless, in these papers, H_2, CO and HCOOH were obtained as major products. Li *et al.* [19] reported a comparison between a Cu/MgAl and a Au/MgAl LDH obtained by a co-precipitation method. The respective active component (Cu and Au) was added by two different routes: copper was added to the LDH through a pre-intercalation of EDTA, while gold was added by an ion exchange process. Once the inks of the catalysts were obtained, they were loaded on a bulk glassy carbon electrode (1.8 cm^2).

The catalytic performances for the CO_2ER were investigated in two different electrolytes ($KHCO_3$ and alcohol amine solution, containing ethanolamine and diethanol amine). Applying a fixed potential from -0.3 to -0.5 V *vs* RHE to the Cu/MgAl LDH and from -0.45 to -0.7 V *vs* RHE to the Au/MgAl LDH in $KHCO_3$, the Authors obtained a large variety of products, including H_2, CO, CH_4, and HCOOH. On the contrary, upon application of a potential in the same ranges to both LDHs in the alcohol amine solution, only gaseous products were obtained, *i.e.*, H_2 and CO. Iwase *et al.* [20] reported the use of a bimetallic layered double hydroxide made of Cu and Al, obtained by a co-precipitation method and loaded on a carbonaceous gas diffusion layer (1.89 cm^2). The electrocatalyst, tested in a gas diffusion electrode set-up [21] under galvanostatic conditions (50 mA), led to the production of CO, HCOOH and H_2 as major products and ethylene and ethanol as minor ones. Overall, these works demonstrated the possibility to use either ternary and bimetallic Cu-based layered double hydroxides as electrocatalysts for the CO_2ER. However, both syntheses were based on complex and time-consuming co-precipitation methods at relatively high temperatures that require further processing to load the LDHs on the conductive support. Moreover, they mainly displayed productivity towards C_1 products with relatively scarce selectivity.

In this work it has been carried out an optimisation of the electrochemically synthesised nanostructured CuMgAl LDHs-based materials for the direct use in the CO_2ER reaction, whose outstanding performances have been reported in the previous chapter. In addition to the earlier characterisations, the morphology of the resulting materials was thoroughly investigated by SEM-EDS, X-Ray diffraction and Raman spectroscopy. Such investigations have proved that, through a simple, one-step, and highly reproducible potentiodynamic procedure, it was possible to obtain, not only a CuMgAl LDH, but also a composite material with an intimate contact between the layered hydroxide and Cu^0/Cu_2O species, without needing further calcination and reduction processes.

The electrocatalytic properties of the composite, that previously had served as a precursor, have been studied during potentiostatic CO_2ER in liquid phase ($KHCO_3$). It has been evaluated the effect of the catalyst composition, particularly (i) different molar ratios between divalent and trivalent cations, (ii) different amount of loaded catalyst on the carbonaceous support and (iii) different ratios between each cation on the resulting catalytic performances. For the sake of brevity, the investigated materials will be named indicating the molar ratios among cations in the electrolytic solution used for their electrodeposition. The optimised catalyst, *i.e.*, CuMgAl 2: 1: 1 LDH/CP, reached a productivity in acetic acid of 2.0 mmol g_{cat}^{-1} h^{-1} at a low applied potential (-0.4 V *vs* RHE). This result confirmed the hypotheses made in the previous chapter, where it was assumed the possible presence of different copper species within the LDH structure in the pristine precursor which led to remarkable results. Here, the beneficial effects of combining a well-defined ratio among the three cations present in LDH layers with highly dispersed copper species allowed to obtain a selectivity of almost 100% in the liquid products, a little amount of hydrogen detected in the gaseous phase, and an enhanced productivity, if compared not only to the nanostructured Cu^0/Cu_2O films, but also to the CuMgAl 1.5: 1.5: 1 LDH and its derivatives.

4.2 Materials and Methods

4.2.1 Chemicals and Materials

Nafion membrane N-115 (0.125 mm thick, ≥ 0.90 meq/g exchange capacity), Toray Carbon Paper (TGP-H-60), magnesium nitrate hexahydrate ($Mg(NO_3)_2 \cdot 6H_2O$), and copper tape were purchased from Alfa Aesar. Copper nitrate trihydrate ($Cu(NO_3)_2 \cdot 3H_2O$), aluminium nitrate nonahydrate ($Al(NO_3)_3 \cdot 9H_2O$), sulfuric acid (96% - 98%), ethanol (96.0 – 97.2%), potassium hydrogen carbonate, and phenol were purchased from Sigma-Aldrich. Deuterium oxide (99.96%) was purchased from Eurisotop. All chemicals were of reagent grade or higher.

Pure carbon dioxide (≥ 99.9%) was acquired by Rivoira (S.r.l.). Gas sampling bags (Tedlar Bags) were obtained from Supelco. All chemicals were of reagent grade or higher.

4.2.2 Apparatus

The electrodeposition of the layered double hydroxides was carried out in a conventional three-electrode cell connected to a potentiostat (CH Instrument 660 C). 4 cm^2 sized Toray Carbon Paper (CP) and a Pt gauze were used as the working and counter electrodes, respectively. Electrode potentials were referred to an aqueous saturated calomel electrode (SCE), with the exception of the electrocatalytic tests for which the potentials were quoted to the reversible hydrogen electrode, RHE. The morphology and the structure of the electrocatalysts were investigated by Scanning Electron Microscopy (SEM) and by Field Emission Scanning Electron Microscopy (SEM-FEG) using the E-SEM Zeiss EVO 50 Series instrument and a LEO 1530 ZEISS instrument equipped with Schottky emitter and an "In-lens" detectors for secondary electrons imaging. Energy Dispersive X-ray Spectroscopy (EDS) measurements were performed with an Oxford INCA system equipped with a 30 mm^2 Silicon Drift Detector and a Brucker Quantax 200 Detector. X-ray diffraction analyses (XRD) were carried out using a PW1050/81 diffractometer (Philips/Malvern, Royston, UK) coupled with a graphite monochromator in the diffracted beam and controlled by a PW1710 unit (Cu Kα, λ = 0.15418 nm) and a PANalytical X'Pert PRO diffractometer equipped with a fast-solid state X'Celerator detector. Cu Kα radiation was used (λ=0.15418 nm) at 40 mA, 40 kV. The 2θ range was investigated from 3.5° to 80° with a step size of 0.066° and time/step of 300 s. Raman spectra were recorded with a micro-spectrometer Raman RM1000 (Renishaw/Thermo Fisher, New Mills, Wotton-under-Edge, Gloucestershire, UK) equipped with a Leica DMLM optical microscope and a CCD detector. The excitation wavelength came from an Ar^+ laser (λ = 514.5 nm) with an output power of 25 mW.

This power was reduced as needed by neutral density filters in order to prevent the sample damage. The electrochemical CO_2 reduction reaction tests were carried out in a two-compartment electrochemical (H-type) cell (Pine Research Instrumentation, Inc.). The carbonaceous membranes (CP) coated with the electrocatalysts were used as the working electrodes, while a Ag/AgCl (KCl sat.) electrode and a Pt gauze were used as the reference and counter electrodes, respectively. Gaseous products were detected by a Thermo Focus GC (TCD detector) with a carbon molecular sieve column (CARBOSPHERE 80/100 6' x 1/8''). ^{1}H-NMR spectra were recorded by means of an Inova 600 spectrometer (600 MHz) coupled with a Triple Resonance Probe.

4.2.3 Electrodeposition of CuMgAl Layered Double Hydroxides on the Carbon Paper Electrode

Each piece of the 4 cm^2 carbonaceous membrane was pre-treated using the procedure optimised for the Cu-based films, described in Chapter 3.

The three-metals LDHs were deposited on the cleaned carbonaceous supports in the same experimental conditions as described in Chapter 3. In this case, different freshly prepared 0.03 M solutions containing the nitrate salts of Cu^{2+}, Mg^{2+}, and Al^{3+} were obtained by varying the ratio between the total moles of the divalent metals and those of the trivalent metal, whose optimisation will be discussed in Paragraph 4.3.2. Analogously, a variable potential from 0.0 to -1.4 V was applied with a scan rate of 30 mV s^{-1}. The as-obtained Cu-containing LDH thin layer was thoroughly rinsed in distilled H_2O and dried to a constant weight.

4.2.4 Electrocatalytic Tests

The liquid phase electrochemical CO_2 reduction tests were performed using the procedure described in Chapter 2 (Paragraph 2.2.6). All the electrocatalytic tests were carried out as single tests, unless otherwise stated.

4.3 Results and Discussion

4.3.1 Morphological and Structural Characterisation of the CuMgAl Layered Double Hydroxide Electrodeposited on Gas Diffusion Membranes

The electrodepositions of the Cu-containing LDH films over the carbonaceous support were carried out by cyclic voltammetry, as described in Chapter 3 (Paragraph 3.3.1). During the catalyst optimisation, the role of both the cations molar ratios inside the electrolytic bath and the number of the deposition cycles (see Paragraph 4.3.2) on the catalytic performance were investigated. Before each deposition, the carbonaceous membrane was pre-treated following the usual procedure (Chapter 2, Paragraph 2.3.1).

The morphological and structural characterisations reported in this chapter are referred to the CuMgAl 2: 1: 1 LDH/CP, chosen as a representative benchmark of all the Cu-containing LDH samples synthesised. Figure 4.1 displays the cyclic voltammograms recorded during the electrodeposition.

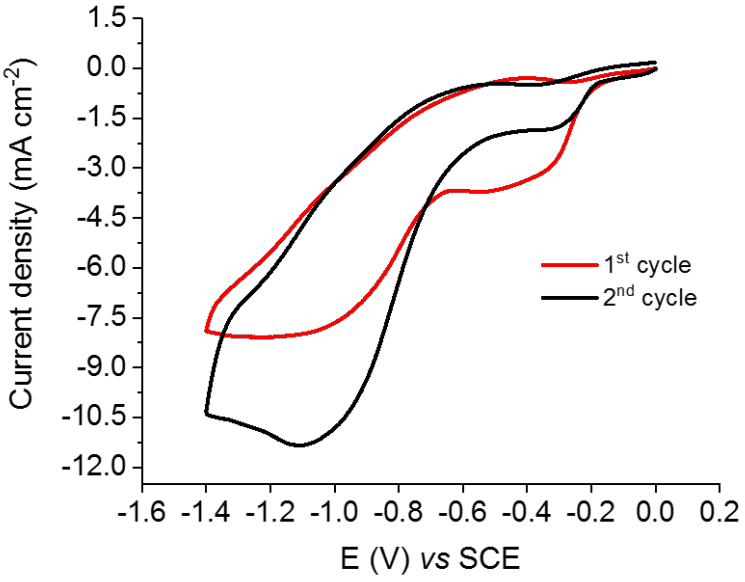

Figure 4.1. CVs recorded during the electrodeposition of the CuMgAl 2: 1: 1 LDH/CP

As shown, the trend of the current was the same as for the CuMgAl 1.5: 1.5: 1 LDH, suggesting that, even in this case, a partial reduction of copper occurred from the very beginning. In the previous characterisation it was considered that the reduced copper, visible in the first cathodic peaks of both cycles, was inside the layered double hydroxide structures since there were no evidences of Cu species in the X-ray diffraction pattern. However, the outstanding catalytic activities led to hypothesise that these reduction peaks could cause the deposition of other copper species within the Cu-containing LDH structure. For this reason, further investigations were performed.

As a preliminary test, a CV characterisation was performed with the aim of confirming the presence of copper. From the voltammogram recorded in basic solution (Figure 4.2) it was possible to evidence the typical redox waves associated to the different Cu species [22] , likely present along with the LDH structure, thus confirming the above mentioned hypothesis.

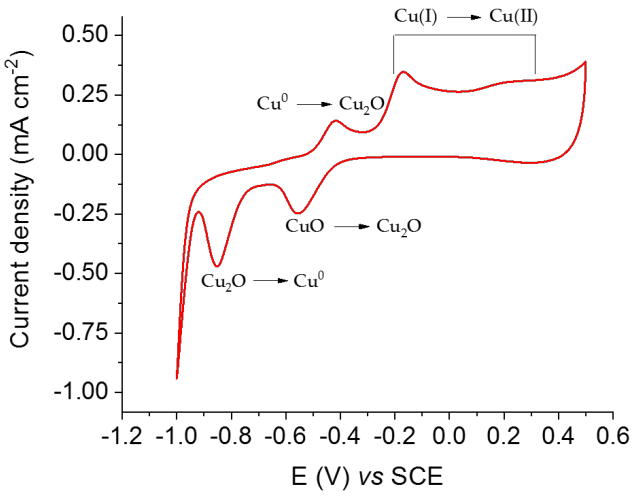

Figure 4.2. CV characterisation of the CuMgAl 2: 1: 1 LDH/CP electrocatalyst in 1 M NaOH, scan rate 50 mV s^{-1} (N_2 atmosphere)

Moreover, the less cathodic peak recorded during the second scan (Figure 4.1), which is anticipated compared to the one of the first cycle (-0.28 V instead of -0.4 V), as already discussed in the previous chapter, can be associated with the deposition of copper onto a film already present on the conductive support, according to the literature evidences for Pt and

stainless steel [23]. Therefore, to assess thoroughly the morphology and the chemical nature of the electrodeposited material, further XRD and SEM-EDS analyses were performed.

At the beginning, a X-ray diffraction pattern was recorded to confirm the presence of the layered double hydroxide corresponding to the 2: 1: 1 molar ratio (Figure 4.3a). In the same way as the one achieved for the LDH with molar ratio 1.5: 1.5: 1, the XRD pattern displays the typical reflection at 10.4° (2θ) indexed as (003) reflection. However, in this case, it is possible to observe also the second reflection related to the (006) reflection at 21.2° (2θ), and this evidence means that the crystallinity of the LDH structure is higher than the one achieved with a different molar ratio. Both 2θ values were consistent with the presence of NO_3^- as interlayer anion [24,25].

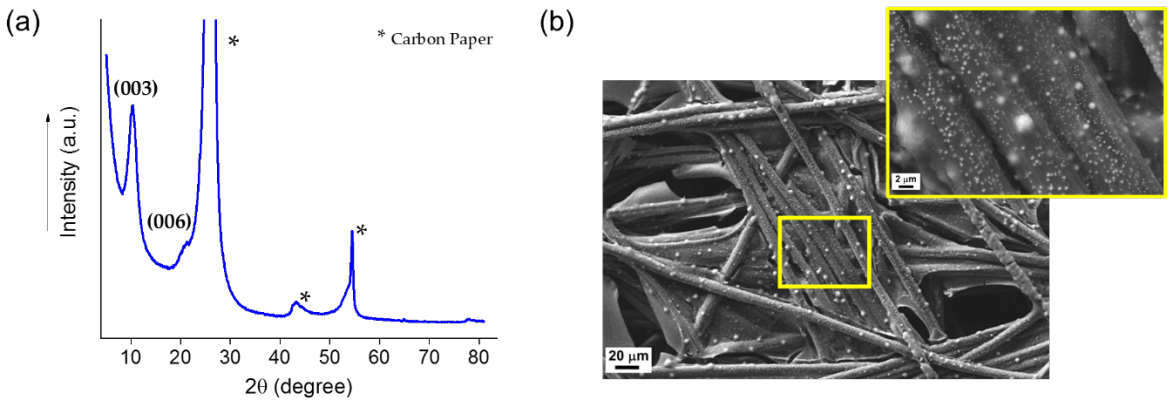

Figure 4.3. (a) X-ray diffraction pattern and (b) SEM images of a CuMgAl 2: 1: 1 LDH/CP electrodeposited film

The Bragg angle of (003) reflection was used both to calculate the perpendicular dimension of the crystallites [26] and the relevant d-spacing. Such values are reported in the paragraphs describing the compositions investigated for each LDH (Paragraphs 4.3.2.1 and 4.3.2.3). However, from the X-ray diffraction analysis alone it was not possible to confirm the ternary nature of the electrodeposited LDH or to determine the presence of additional Cu species.

Moreover, the SEM picture reported in Figure 4.3b highlights that, after electrodeposition of the LDH, the carbon fibers of the support are homogeneously covered by a micro and nano structured coating which exhibits different morphological features, like the previously obtained material (Chapter 3, Paragraph 3.3.1, Figure 3.3). For these reasons, further investigations were performed by EDS and SEM-FEG imaging of a freshly prepared CuMgAl 2: 1: 1 LDH/CP. The results obtained with the SEM-FEG imaging are shown in Figure 4.4.

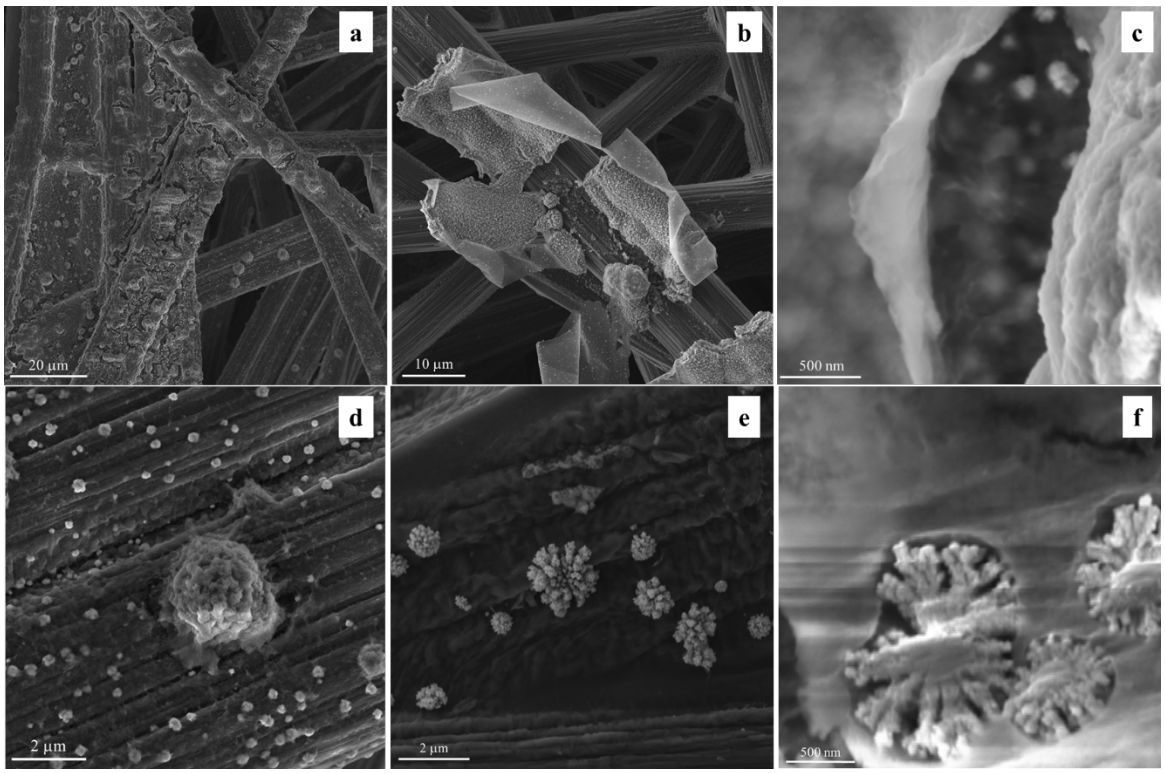

Figure 4.4. (a), (b), (c) SEM-FEG images of the layered deposit on the fibers; SEM-FEG images of the discrete particles with cauliflower-like (d) and coral-like (e, f) shapes

Figure 4.4a highlights the presence of a thin veil covering the superficial fibers, which was partially evident from the SEM image shown in Figure 4.3b. Focusing on this thin film coating the fibers, the SEM pictures of a point where its continuity is interrupted are reported in Figure 4.4b and c, and clearly show its veil-like conformation with an estimated thickness of few tens of nm. Moreover, Figure 4.5a again highlights the layered nature of the fibers coating, which is a typical feature of the LDHs morphology [7].

The EDS analyses carried out in position 1 (Figure 4.5a) confirmed the ternary nature of the LDH with cations molar ratios of 1.4 for Cu/Mg, 1.8 for Cu/Al and 1.3 for Mg/Al, and a total molar ratio between divalent and trivalent cations of 3.0, thus suggesting a very good match with the expected 2: 1: 1 ratio.

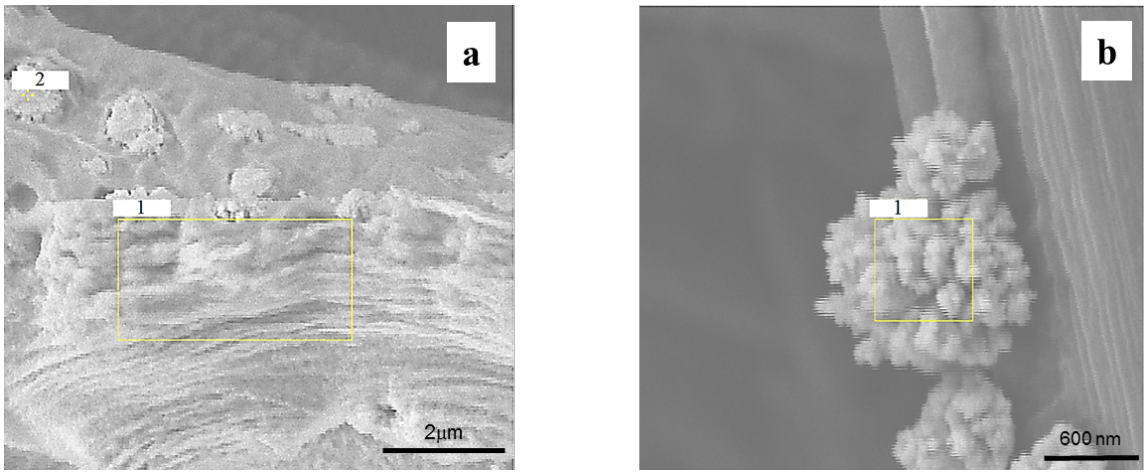

Figure 4.5. EDS analyses of the CuMgAl2: 1: 1 LDH/CP: (a) layered deposit and (b) coral-like particle

However, in addition to the LDH veil, Figures 4.4 d-f show the presence of discrete particles with different morphologies that are located both on the fibers and incorporated in the LDH structure. In particular, the smallest round particles decorating the fibers in Figure 4.4d were found to consist of Cu only by EDS analysis. Differently, in the coral-like particles (Figure 4.4e) Cu/oxidised Cu species (68% Cu and 16% O atomic%, Figure 4.5b, position 1) were detected.

To further investigate the chemical nature of the coral-like structures, Raman analysis was carried out along the fiber (Figure 4.6a) and at a coral-like particle (Figure 4.6b).

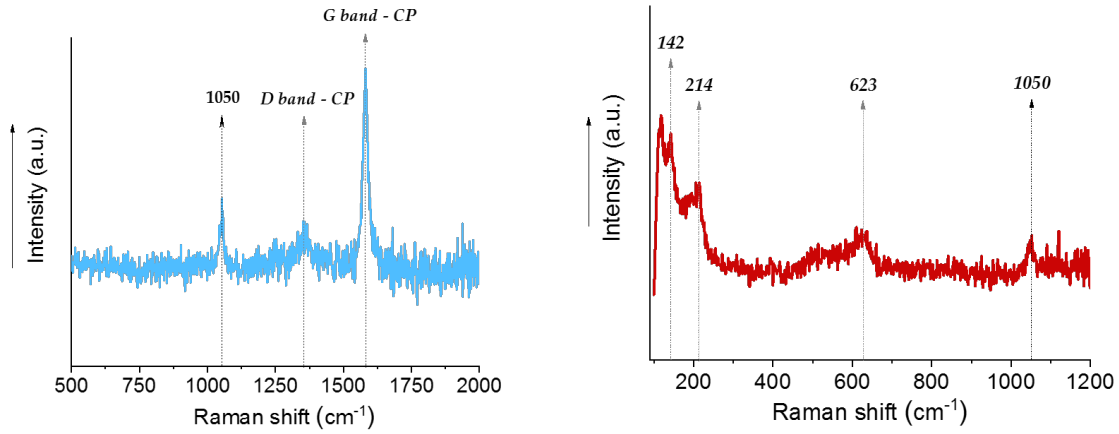

Figure 4.6. Raman spectra recorded for the CuMgAl 2: 1: 1 LDH film: (a) along the carbon fibers and (b) at the coral-like particles

The results were consistent with the presence of Cu_2O species, displaying the typical peaks at 142, 214 and 626 cm^{-1} [27,28] in the position of the particle. On the contrary, the analysis performed along the fibers shows the characteristic peak of the NO_3^- stretching [10,29], highlighting the presence of the layered double hydroxide veil with nitrate anions in the interlayer, together with the typical peaks related to the carbon fibers (1354 cm^{-1} "D-band" and 1581 cm^{-1} "G-band" [30]).

Instead, cauliflower-like particles, which could be also ascribed to a typical LDH morphology [31], were observed (Figure 4.4d) where Cu, Mg and Al were detected by punctual EDS analysis and EDS mapping (Figure 4.7) without respecting the 2: 1: 1 ratio (cations molar ratios of 0.60 for Cu/Mg, 1.5 for Cu/Al and 2.5 for Mg/Al), thus suggesting the deposition of a defective LDH, likewise the previous analyses performed on the particles assumed as spherical (Chapter 3, Paragraph 3.3.1).

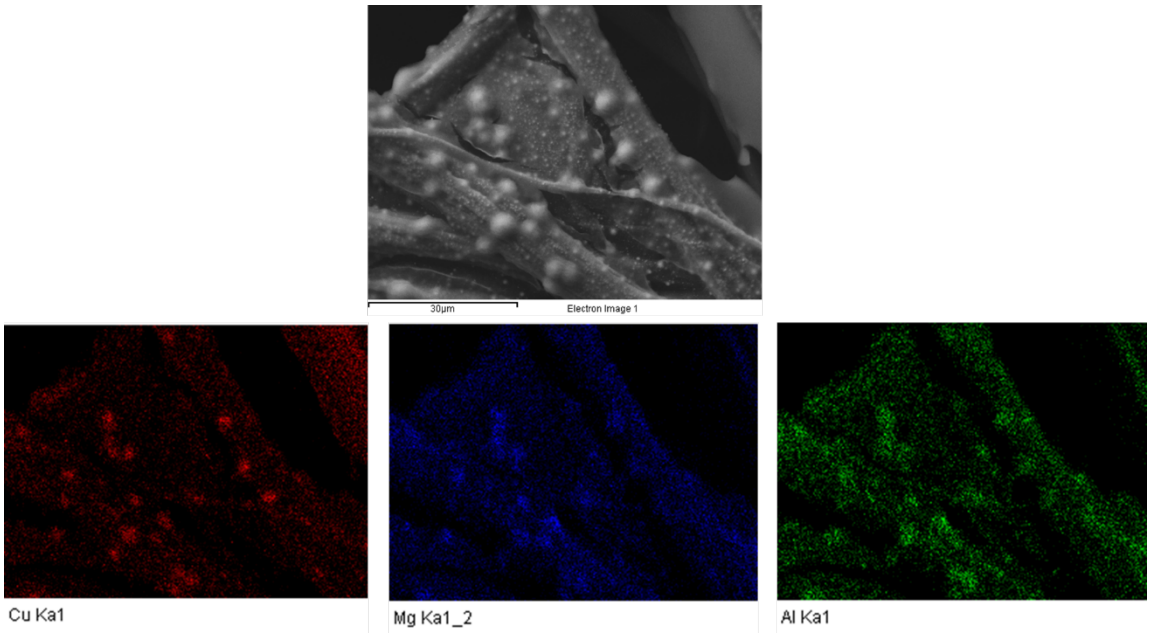

Figure 4.7. EDS mapping of the cations' distribution of the CuMgAl 2: 1: 1 LDH/CP electrodeposited film

Differently, as already shown in Figures 4.4f and 4.5a, the coral-like particles were also found to be incorporated inside the pores present in the LDH veil and EDS analysis in position 2 of Figure 4.5a confirmed that they are made of Cu/oxidised Cu species, similarly to those spread over the fibers (57% Cu and 8% O atomic %).

These results confirm that the electrochemically synthesised material on CP fibers is composed of both ternary CuMgAl LDH and different copper-based particles, as hypothesised in the previous chapter. In conclusion, the electrodeposition process allowed to create an intimate contact among Cu/Cu_2O species and a ternary CuMgAl LDH.

4.3.2 Optimisation of the CuMgAl Electrocatalyst and Catalytic Tests Performance

The optimisation of the electrocatalyst formulation and properties was carried out by evaluating the following parameters: (i) molar ratio between total M(II) and M(III), (ii) amount of the loaded catalyst, and (iii) molar ratios among the three cations, as already stated in the introduction of this chapter. Each electrocatalyst was tested during the liquid phase CO_2ER for a 1h reaction at -0.4 V *vs* RHE, especially to estimate the selectivity towards the production of

acetic acid. The choice of these conditions was made on the basis of the outcomes of the previous tests, likewise the reactions performed in Chapter 3. In this case, the productivity will be given as mmol g_{cat}^{-1} h^{-1} instead of μmol g_{cat}^{-1} h^{-1}.

4.3.2.1 Effect of the Total M(II) and M(III) Ratio

The first parameter investigated was the molar ratio between the divalent cations (Cu and Mg) and the trivalent one (Al). In fact, this parameter can deeply influence the catalytic activity of LDH and LDH-derived catalysts in different processes [7,9,32,33]. A set of electrocatalysts was synthesised starting from two different electrolytic baths keeping a total molar concentration of 0.03 M:

I. M(II): M(III) = 6: 1, corresponding to the molar ratio Cu: Mg: Al = 3: 3: 1 (CuMgAl 3: 3: 1 LDH/CP)

II. M(II): M(III) = 3: 1, corresponding to the molar ratio Cu: Mg: Al = 1.5: 1.5: 1 (CuMgAl 1.5: 1.5: 1 LDH/CP)

The as prepared LDH films were investigated by SEM analyses (Figure 4.8).

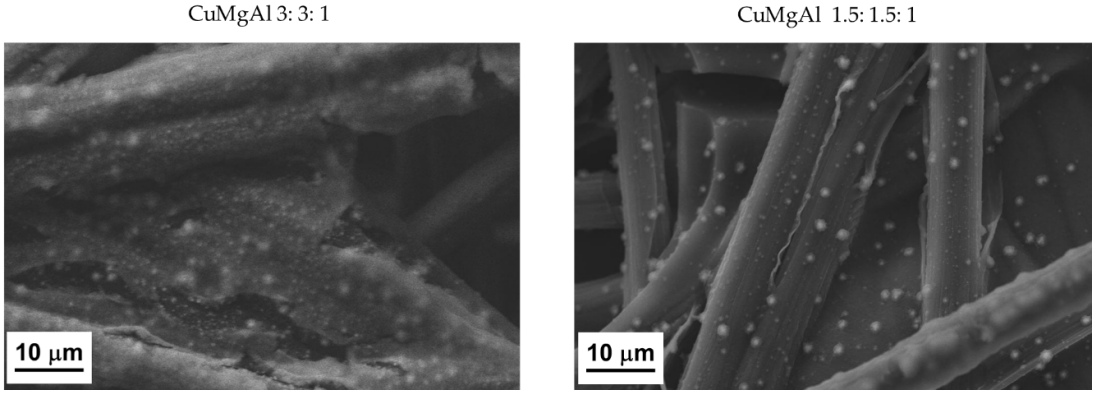

Figure 4.8. SEM images of CuMgAl LDHs synthesised from electrolytic solutions containing different molar ratios of cations

The 4 cm^2 area of the membrane was fully covered by the electrocatalyst in both cases but the most homogeneous film was achieved by employing the latter cations composition. Indeed, the 6: 1 molar ratio led to a covering that appeared broken and scarcely attached to the carbon fiber.

Contrarily, when using the 3: 1 molar ratio, the material appeared more uniformly distributed along the fibers and the film well adherent to the CP. Deeper investigations on the electrosynthesised LDH veil for each material were performed using SEM-FEG analysis. As shown in Figure 4.9, the electrodeposited LDH veils along the fibers have a porous structure.

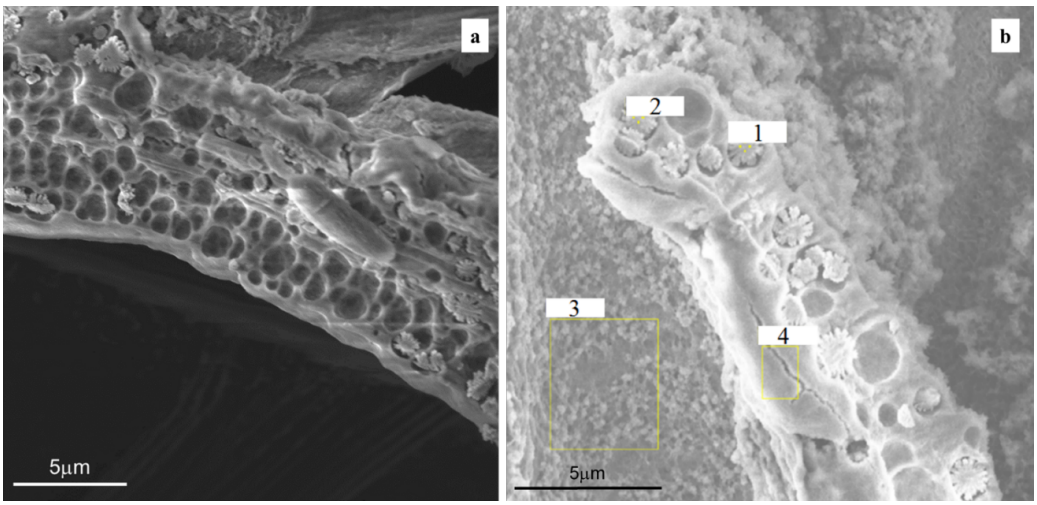

Figure 4.9. SEM-FEG images of (a) CuMgAl 2: 1: 1 LDH/CP and (b) CuMgAl 3: 3: 1 LDH/CP

Interestingly, the 3: 3: 1 CuMgAl LDH presents a higher amount of incorporated coral-like particles and a new flat structure near the layered one which was subjected to further EDS investigations (see the following discussion).

(a)

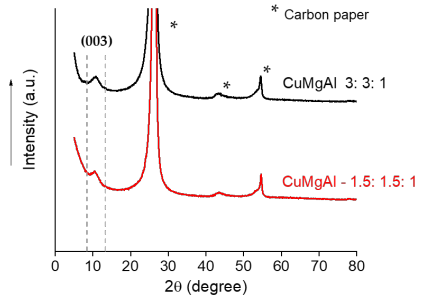

(b)

Cu^{2+}: Mg^{2+}: Al^{3+} (electrolytic bath)	Cu/Mg	Cu/Al	Mg/Al	M^{2+}/M^{3+}
3 : 3 : 1	0.7	1.9	2.8	4.7
1.5 : 1.5 : 1	1.0	1.2	1.2	2.4

(c)

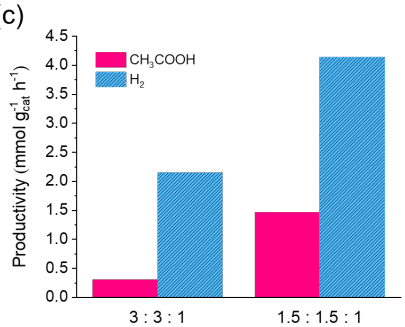

Figure 4.10. (a) X-ray diffraction patterns of the electrosynthesised CuMgAl LDHs with different cations molar ratios; (b) Estimated total M(II)/M(III) ratio from EDS analyses; (c) CO_2ER products distribution at -0.4 V *vs* RHE (1h reaction) for the two different LDH compositions

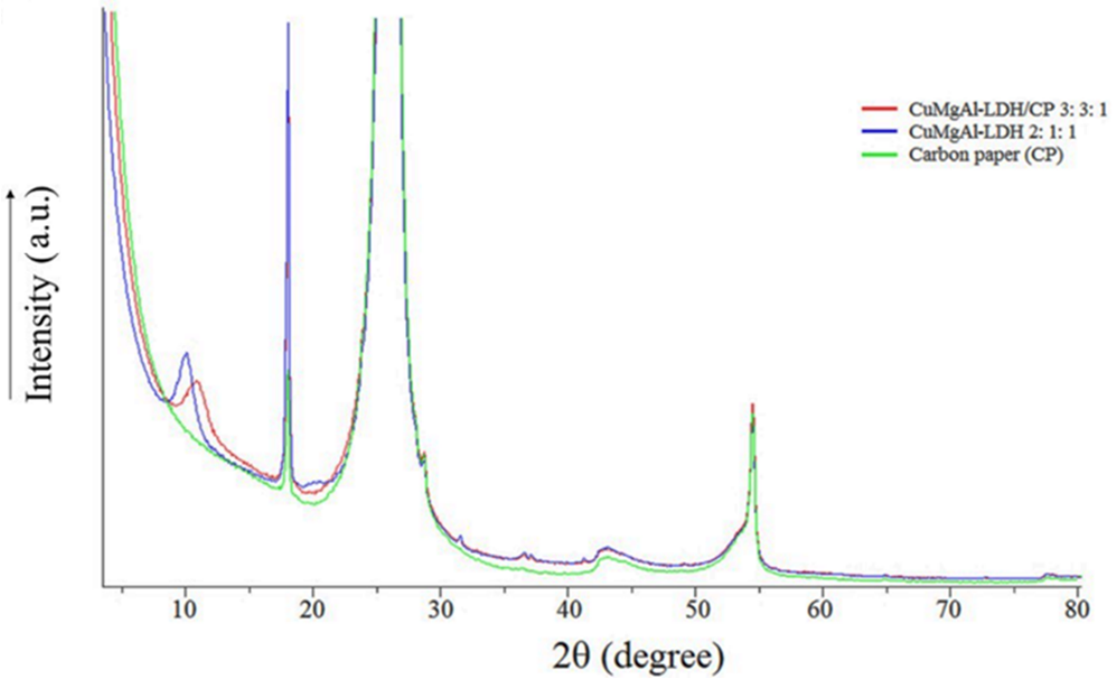

Figure 4.11. X-ray diffraction patterns of CuMgAl 2: 1: 1 LDH/CP (blue line), CuMgAl 3: 3: 1 LDH/CP (red line), and carbon paper (green line)

Figure 4.10a and Figure 4.11 show the X-ray diffraction spectra of each sample and the presence of the layered double hydroxide structure is confirmed by the reflection indexed as (003), which shows a slight change in the 2θ position.

In both cases, an average crystallites size of 19.5 nm was calculated by using the Scherrer's formula from the full width at half maximum of (003) reflection peak, with a shape factor K=1 [34]. Contrarily, the interlayer spaces, estimated by the angular position of the (003) reflection peak, obtained for the CuMgAl 3: 3: 1 LDH/CP was lower than the one relative to the CuMgAl 1.5: 1.5: 1 LDH/CP, *e.g.*, 8.1 *vs* 8.8 Å, which are both typical values of the nitrate anions [24]. The reason for this difference was demonstrated by the studies carried out in 1983 by Miyata [35] and later by Marappa *et al.* [36]. Indeed, they both defined the increase of the interlayer spacing inside Mg/Al based layered double hydroxides containing NO_3^- as anion as a result of the increase of the *x* component in the general formula $[(M^{II})_{1-x}(M^{III})_x(OH)_2]^{x+}(A^{m-}_{x/m}) \cdot nH_2O]$, and thus of the increase of LDH layer positive charge. The two papers reported that for a value of x = 0.3, the basal spacing increases up to 8.8 Å, while for lower values of x (*i.e.*, x = 0.2)

the basal spacing reaches values around 8.0 Å. Commonly, nitrate ions are shown to intercalate with their molecular plane inclined at an angle of ~ 70° to the metal hydroxide layer when the positive charge is high, due to the inclusion of a larger number of anions that have to pack closer together, whereas, when *x* is small, the plane formed by the NO_3^- results parallel to the basic layer. Therefore, concerning the two investigated LDHs, the increase of the interlayer space is in agreement with the increase of the molar fraction of Al^{3+}, which enhances the amount of negative ions (NO_3^- or CO_3^{2-}) required to balance the excess of positive charge.

Besides, the EDS analysis (Figure 4.10b) reports that the composition of the CuMgAl 1.5: 1.5: 1 LDH film is the one that better reflects that of the synthetic bath solution, confirming again that the best molar ratio between the total amount of M(II) and M(III) in this three-cations LDH is 3: 1, in accordance with the literature [7]. Indeed, several inconsistencies were observed for the supposed 6: 1 LDH. Although the X-ray diffraction analysis demonstrated again the presence of the layered double hydroxide structure, the EDS analysis achieved in position 3 (Figure 4.9b) revealed the presence of several Cu/Al oxides species nearby the LDH structure, where the estimated molar ratio among the cations did not match with that of the electrolytic solution. Such evidences suggest the presence of a defective layered double hydroxide deposit over the carbon fibers, where the cations ratio approaches 4: 1 or 5: 1. Therefore, it can be stated that using a higher molar ratio between divalent and trivalent cations in the electrolytic bath solution led to the formation of (i) a lower interlayer space, (ii) a defective LDH structure, and (iii) undesired oxides species.

Finally, in order to investigate the effect of the total cations' molar ratio on the electrocatalytic performance, the two LDHs were tested for the liquid phase electrochemical CO_2 reduction (Figure 4.10c). Both electrocatalysts led to the production of acetic acid at -0.4 V *vs* RHE as the main liquid product but, the highest productivity was achieved with the CuMgAl 1.5: 1.5: 1 LDH/CP that outperformed the other material by 5 times (1.5 $mmol_{CH3COOH}$ g_{cat}^{-1} h^{-1} *vs* 0.3

$mmol_{CH3COOH}\ g_{cat}^{-1}\ h^{-1}$). This result comes from two main features, *i.e.*, the final molar ratio in the electrocatalyst and the interlayer distance. On one hand, the 3: 1 molar ratio used in the electrolytic bath solution led to the formation of a more controlled LDH structure, as the mean ratio in the deposited material reflected the one of the solution. On the other hand, a higher interlayer space obtained with the 3: 1 LDH may favour the diffusion of the carbon dioxide inside the structure. This phenomenon may lead to the formation of a higher concentration of carbon sources in contact with the active phases, resulting in a higher production of acetic acid. Indeed, the presence of carbonates inside the LDH structure was confirmed by the X-ray diffraction analysis performed after the reaction, which will be discussed in Paragraph 4.3.3.

For these reasons, further optimisations of the material to be tested for CO_2ER were carried out employing 3: 1 as the molar ratio between the total M(II) and the M(III).

4.3.2.2 Effect of the Amount of the Loaded Catalyst

Once the best molar ratio between M(II) and M(III) was identified, the effect of different amounts of electrocatalyst loaded on the carbonaceous membrane was explored. In this case, the electrocatalyst composition, CuMgAl 1.5: 1.5: 1 LDH/CP was investigated by varying the numbers of deposition cycles.

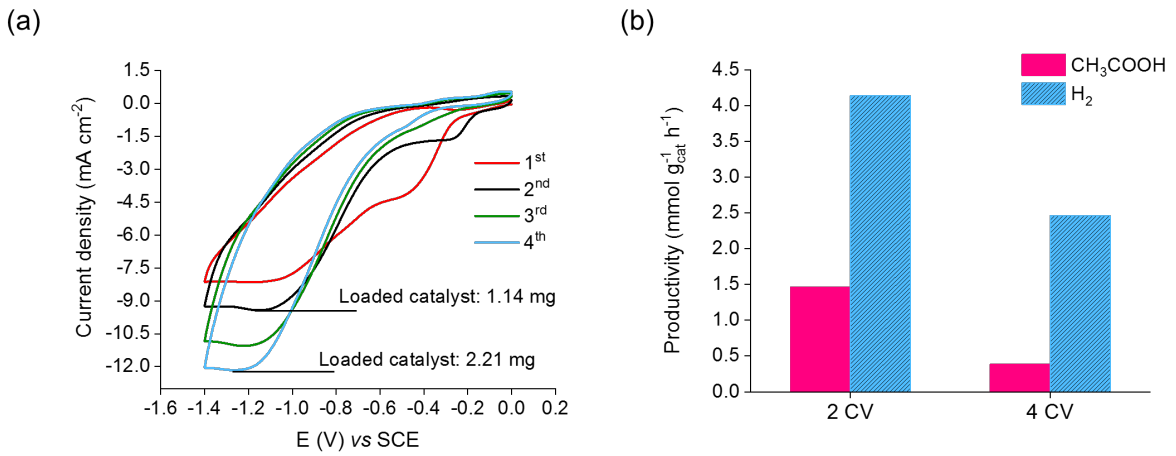

Figure 4.12. (a) Current densities recorded during the electrodeposition processes; (b) CO_2ER products distribution at -0.4 V *vs* RHE (1h reaction) for the different amounts of loaded catalyst

Figure 4.12a shows that increasing the numbers of CV cycles, the amount of loaded catalyst proportionally increased with the current density. A mass increment of 94% was observed between the second and the fourth electrodeposition cycle (1.14 mg against 2.21 mg).

By comparing the outcomes of the catalytic tests, it can be noticed that a higher productivity per gram of catalyst was obtained by the sample on which the lower amount of electrocatalyst was loaded (Figure 4.12b). Indeed, the selective applied potential led again to the formation of acetic acid as the main liquid product, and the productivity values obtained with the two loading were 1.5 mmol g_{cat}^{-1} h^{-1} *vs* 0.4 mmol g_{cat}^{-1} h^{-1}. The presence of a ticker layer of LDH containing a higher amount of non-redox active centres (Mg and Al) produced a less conductive material where the charge transfer from the conductive support to the active redox species (Cu) is likely to be hindered and the H^+ diffusion towards the electroactive surface area of the electrode is limited, thus resulting in a decrease of the catalytic activity. Indeed, after the second cycle of deposition, the peak related to the nitrate reduction started to increase at the expense of the peak related to copper deposition that slowly disappeared, suggesting the prevalent formation of the ternary LDHs. In this way, the coral-like Cu^0/Cu_2O particles are likely more covered by non-active species (Mg and Al) causing a change at the electrode/electrolyte interface that affects negatively the activation processes [37,38]. Therefore, the 2 cycles electrodeposition was chosen for the preparation of CuMgAl 1.5: 1.5: 1 LDH/CP and this sample was employed for further optimisations.

4.3.2.3 Effect of the Cu/Mg/Al Molar Ratios

Lastly, a set of CuMgAl LDHs where the total M(II)/M(III) molar ratio was 3: 1 was prepared using 2 deposition cycles in order to the investigate the effect of the molar ratios among cations. Three different synthetic bath solutions were employed for the electrosynthesis of the catalysts, and precisely:

I. Cu: Mg: Al = 1: 2: 1, corresponding to a theoretical CuMgAl 1: 2: 1 LDH/CP

II. Cu: Mg: Al = 1.5: 1.5: 1, corresponding to a theoretical CuMgAl 1.5: 1.5: 1 LDH/CP

III. Cu: Mg: Al = 2: 1: 1, corresponding to a theoretical CuMgAl 2: 1: 1 LDH/CP

(a)

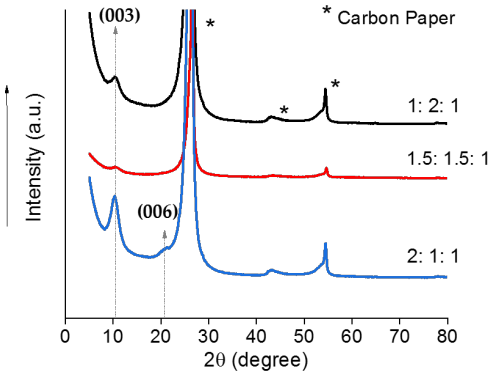

(b)

Cu^{2+}: Mg^{2+}: Al^{3+} (electrolytic bath)	Cu/Mg	Cu/Al	Mg/Al	M^{2+}/M^{3+}
1 : 2 : 1	0.4	1.0	2.6	3.6
1.5 : 1.5 : 1	1.0	1.2	1.2	2.4
2 : 1 : 1	2.2	2.0	0.9	2.9

Figure 4.13. (a) X-ray diffraction patterns of the CuMgAl LDHs with different cations ratios; (b) Estimated cations ratios from EDS analyses on the electrosynthesised films

X-ray diffraction analyses were carried out (Figure 4.13a). All spectra show the typical reflection at 10.4° (2θ) indexed as (003) with no change in the position of the Bragg's angle, a feature ascribable to the similar ion radius of Mg^{2+} (0.72 Å) and Cu^{2+} (0.73 Å) [39]. However, it is worth noting that the intensity of the reflection (003) for the 2: 1: 1 sample was the highest, compared to the other materials, and it is the only case in which it was also possible to observe the second order reflection (006), thus suggesting a higher crystallinity of this LDH.

However, the obtained d-spacing value was always 8.5 Å, since the amount of Al was the same for all samples and the different ratio of the divalent cations did not influence the d value to a significant extent (see discussion in Paragraph 4.3.2.1).

A substantial difference among the films was found in the crystallite size and in the estimated ratios obtained by the EDS analyses (Figure 4.13b). The average crystallite dimensions calculated considering the reflection at 10.4° (2θ), for the CuMgAl 1: 2: 1, CuMgAl 1.5: 1.5: 1, and CuMgAl 2: 1: 1 were 120.9, 19.5, and 9.9 nm, respectively.

This trend was also confirmed by the SEM analyses (Figure 4.14), which not only showed the presence of a very homogeneous covering along the fibers with well dispersed particles in all three electrocatalysts, but also clearly displayed a decrease in the particles sizes by increasing the amount of copper inside the electrolytic solution.

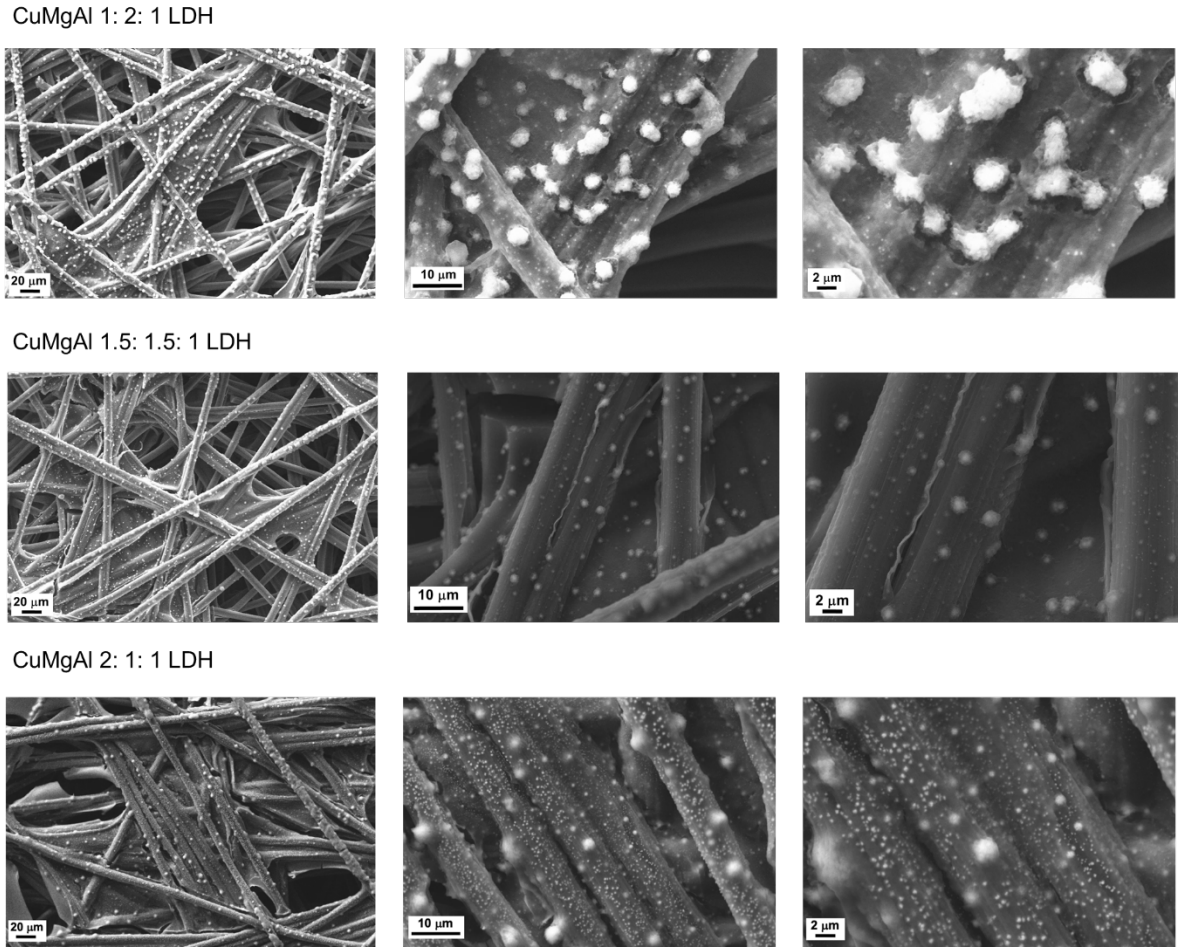

Figure 4.14. SEM images of the CuMgAl LDHs with different molar ratios among cations

Moreover, the estimated molar ratios among Cu/Mg/Al and between the total amount of M(II) and M(III) obtained with the EDS analyses (Figure 4.13b) pointed out that the CuMgAl 2: 1: 1 LDH/CP catalyst exactly reflected the composition of the electrolytic bath solution unlike the other two LDHs. Only by providing a double amount of copper, the nominal ratio was maintained. Finally, the as obtained electrocatalysts were tested for the liquid phase CO_2ER (Figure 4.15) in order to choose the best electrocatalyst in terms of its activity.

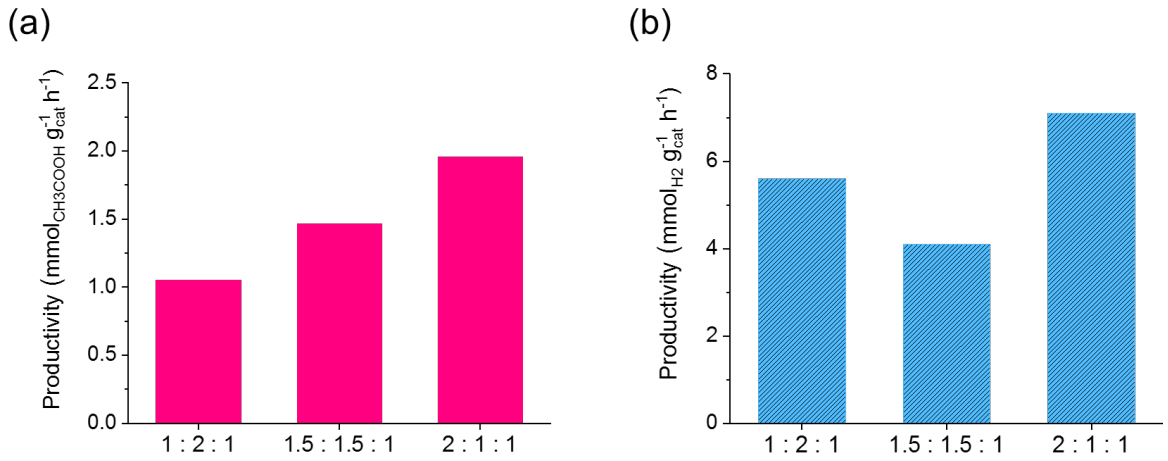

Figure 4.15. (a) CH_3COOH production and (b) hydrogen production at -0.4V *vs* RHE (1h reaction)

Again, the CO_2 reduction tests led to the selective formation of acetic acid, but significant results were obtained concerning the productivity. Indeed, the greatest production of CH_3COOH was obtained by the electrocatalyst that displayed the most crystalline structure and the lower sizes of the crystallite. In particular, the production increased from a value of 1.1 $mmol_{CH3COOH}$ g_{cat}^{-1} h^{-1} obtained with the CuMgAl 1: 2: 1 LDH/CP catalyst up to 2.0 $mmol_{CH3COOH}$ g_{cat}^{-1} h^{-1} obtained with the CuMgAl 2: 1: 1 LDH/CP. Moreover, the relative standard deviations (% RSD) were 32 % and 0.36 % (N=2), respectively, indicating the higher reproducibility of the reaction carried out on the CuMgAl 2: 1: 1 LDH/CP. Hydrogen was the only gaseous compound detected. In this case, a non-linear trend was observed.

As far as the acetic acid production is concerned it is reasonable to state that the higher is the molar ratio of Cu with respect to the other non-redox active species (Mg and Al), the higher is the acetic acid production. Table 4.1 shows the current recorded during the CO_2ER employing the three LDHs containing different cations molar ratios. Again, the highest current density was recorded for the CuMgAl 2: 1: 1 LDH.

Table 4.1. Current densities recorded during the CO_2ER for the LDHs based on different cations molar ratios (N=2)

Electrocatalyst	$J \pm \Delta J$ *(mA* mg_{cat}^{-1}*)*
CuMgAl 1: 2: 1 LDH/CP	0.84 ± 0.08
CuMgAl 1.5: 1.5: 1 LDH/CP	1.00*
CuMgAl 2: 1: 1 LDH/CP	1.10 ± 0.06

*the values of the recorded current densities were the same, considering the sensitivity of the instrument

This feature favoured both the production of CH_3COOH and the evolution of hydrogen thus demonstrating that both processes are best catalysed by the same LDH, *i.e.*, the one containing the highest amount of Cu.

Overall, the results obtained highlight that:

I. The intimate contact between the ternary CuMgAl LDHs and the Cu^0/Cu_2O particles enhances the production of acetic acid. This suggests that the presence of the LDH structure increases the availability of the carbon sources at the surface and inside the electrocatalysts.

II. The higher interlayer space obtained with the total cations' molar ratio of 3: 1 is likely to favour the entrance of CO_2 inside the layered structures, thus enhancing the amount of carbonates species and the subsequent acetate production.

III. The higher amount of nano-sized particles and nanometric crystallite sizes, together with the higher crystallinity of the CuMgAl 2: 1: 1 LDH/CP led to the formation of a more active material.

IV. The higher amount of coral-like particles in CuMgAl 2: 1: 1 LDH/CP (Figure 4.14) suggests that the dominant presence of active Cu^+/Cu^0 redox couple species is capable to favourably drive the reaction pathway towards the C-C bond formation.

Besides, for the sake of clarity, in Table 4.2 is shown a comparison between the catalytic performances of the most promising Cu-based catalysts loaded on carbonaceous support (GDL), similarly to the one reported in Chapter 2, Paragraph 2.3.3.5. Here the productivity is expressed in mmol g_{cat}^{-1} h^{-1} and the best performances obtained with the CuMgAl LDH-derived and CuMgAl LDH-based catalysts have been added.

Table 4.2. Overview of the productivity in liquid phase of Cu-based catalysts over GDL

Electrocatalyst	*Potential (V vs RHE)*	*Electrolyte*	*Products*	*Productivity*	*Reference*
Porous Cu^0 NPs	-0.9	0.1 M $KHCO_3$	Formic acid Acetic acid	182.5 mM g_{cat}^{-1} h^{-1} 1.2 mM g_{cat}^{-1} h^{-1}	40
Cu^0 NPs on CNT (impregnation)	~-0.8	0.5 M $KHCO_3$	Formic acid Acetic acid	0.21 mmol g_{cat}^{-1} h^{-1} 0.21 mmol g_{cat}^{-1} h^{-1}	41
Cu^0 NPs on CNT (Cu nanowires)	~ - 1.35	0.5 M $KHCO_3$	Formic acid Acetic acid	2.6 mmol g_{cat}^{-1} h^{-1} 0.57 mmol g_{cat}^{-1} h^{-1}	42
Cu_2O	~ -0.85	0.5 M $KHCO_3$	Formic acid Acetic acid	20 mmol g_{cat}^{-1} h^{-1} 0.5 mmol g_{cat}^{-1} h^{-1}	43
Cu_2O-Cu^0	-0.4	0.3 M $KHCO_3$	Acetic acid	0.31 mmol g_{cat}^{-1} h^{-1}	27
Cu_2O/Cu^0 – MgAl LDO	-0.4	0.3 M $KHCO_3$	Acetic acid	1.02 mmol g_{cat}^{-1} h^{-1}	Chapter 3
Cu_2O/Cu^0 – MgAl LDH	-0.4	0.3 M $KHCO_3$	Acetic acid	1.15 mmol g_{cat}^{-1} h^{-1}	Chapter 3
CuMgAl 2: 1: 1 LDH	-0.4	0.3 M $KHCO_3$	Acetic acid	2.0 mmol g_{cat}^{-1} h^{-1}	This chapter

4.3.3 Potentials Screening using CuMgAl 2: 1: 1 LDH/CP and Stability over Time

To summarise, the Cu-containing LDH, synthesised by 2 electrodeposition cycles, and with a molar ratio between M(II) and M(III) of 3: 1 and ratios among cations of 2: 1: 1, was chosen as the optimised electrocatalyst and, therefore, a study of the different applied potentials during the CO_2ER and an evaluation of its stability over time were performed.

A potentials screening was carried out in order to evaluate (i) the effective selectivity towards the acetic acid at -0.4 V *vs* RHE, (ii) the possibility to obtain other reduction products from CO_2 by applying both a less cathodic potential and a more cathodic one. To this purpose, -0.2 and -0.8 V *vs* RHE were selected for the screening and the achieved results were compared to those obtained at -0.4 V *vs* RHE in the liquid phase CO_2ER.

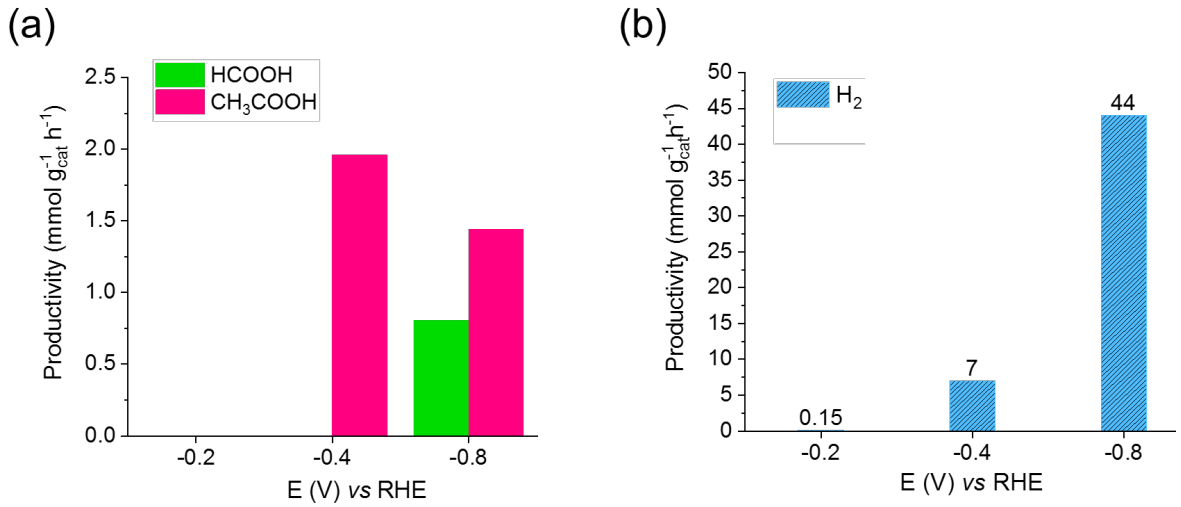

Figure 4.16. CO_2ER (a) liquid and (b) gaseous products distribution for a 1h reaction at different applied potentials using the CuMgAl 2: 1: 1 LDH/CP

The as obtained products distribution is shown in Figure 4.16. As a result, by applying the most cathodic potential (-0.8 V), the selectivity towards acetic acid was reduced, and the formation of formic acid was pointed out. Such shift in the selectivity will be investigated in Chapter 5 through *operando* and *in situ* analyses. Moreover, as the potential was more cathodic, a higher amount of hydrogen was evidenced, so hindering the production of acetic and formic acids or

of other reduction products. On the other hand, the reaction at -0.2 V *vs* RHE produced only a small amount of hydrogen. However, the least cathodic applied overpotential was not enough for the reduction of carbon dioxide to start and no liquid products were detected. Therefore, -0.4 V *vs* RHE was again confirmed to be the most selective potential for the production of acetic acid in the liquid phase CO_2ER with the experimental set-up used in this work. However, comparing the best results obtained with the Cu_2O-Cu^0/CP electrocatalyst, which up to date was our best performing catalyst, the acetic acid production was higher for the optimised CuMgAl 2: 1: 1 LDH/CP electrocatalyst (0.31 mmol g_{cat}^{-1} h^{-1} *vs* 2.0 mmol g_{cat}^{-1} h^{-1}). Indeed, the Cu containing layered double hydroxide acted as a catalyst for the electroreduction of CO_2 in liquid phase, coupling the presence of different active phases of copper with the basicity of the Mg and Al hydroxides, which likely favours the interaction with CO_2 [40]. Moreover, the 3D structure of the carbonaceous gas diffusion membrane joined with the lamellar assembly of the LDH was able to most favour the diffusion of the gaseous compound at the electrode surface and, thanks to the higher affinity to carbonates as interlayer anion [19], the LDH acted as a concentrator for the CO_2 during the reaction.

In order to confirm the entrance of carbonates in the lamellar structure and if the crystallinity was maintained after a 1h reaction at -0.4 V *vs* RHE, X-ray diffraction analysis was also recorded right after the reaction (Figure 4.17).

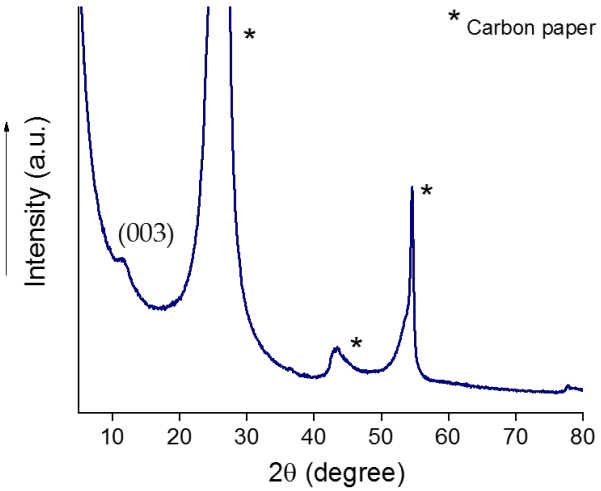

Figure 4.17. X-ray diffraction pattern of the CuMgAl 2: 1: 1 LDH/CP electrodeposited film after a 1h reaction at -0.4 V *vs* RHE

The diffraction pattern shows the presence of a broad reflection indexed as the basal (003), confirming the maintenance of the structure, while the (006) reflection disappears. However, the intensity of the 003 reflection was lower than the one recorded for the pristine LDH, thus suggesting a loss of crystallinity during the CO_2 reduction process, while the nanostructure of the electrocatalyst was preserved, since the average size of the crystallites only grew up from 9.9 nm to 25.6 nm. This slight change can be attributed to a sintering process which has been widely proved in the literature for nanoparticle dimensions < 25 nm [41,42]. It is also worth noting the shift of the Bragg angle of reflection (003) from 10.4° to 11.7° (2θ) and the decrease of the d-spacing from 8.5 Å to 7.6 Å which is typical of the CO_3^{2-} interlayer anion, which confirms the effective adsorption/entrance of the carbon dioxide inside the LDH structure during the reaction.

Finally, the stability of the CuMgAl 2: 1: 1 LDH/CP electrocatalyst was studied over time at -0.4 V *vs* RHE. Figure 4.18 shows the recorded current density during a 5h reaction and demonstrates no degradation of the sample even if the catalyst had been working for a longer time, with a relative standard deviation of 5% on the average J_{tot} value.

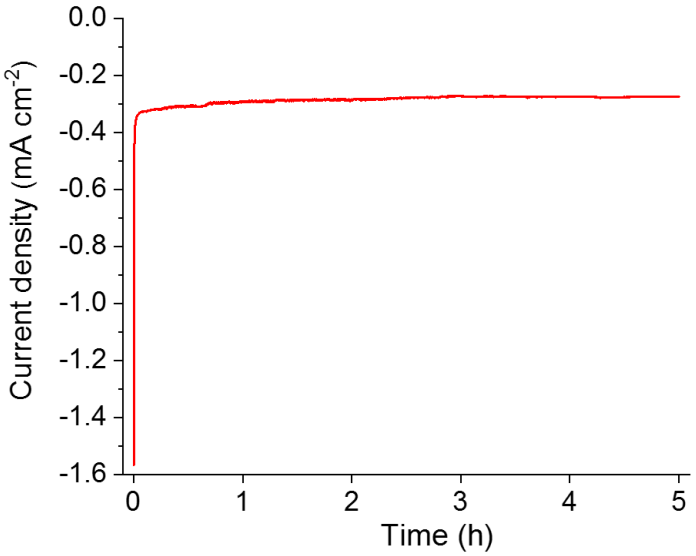

Figure 4.18. Recorded current density during 5h reaction using CuMgAl 2: 1: 1 LDH/CP at -0.4 V *vs* RHE

4.4 Conclusions

Outstanding performances towards the electrochemical CO_2 reduction were obtained by using new CuMgAl LDHs based materials. Unlike the LDHs, already reported in the state of the art, [19,20] that are synthesised by the standard co-precipitation methods, the here designed materials were directly loaded on a carbonaceous gas diffusion membrane by means of a simple, low time-consuming, and highly reproducible electrochemical deposition, as already discussed in the previous chapters. The attention was focused on the morphology of each electrocatalyst and, after a thorough investigation, it was proven the existence of a composite material displaying an intimate contact between a nanostructured ternary CuMgAl LDH, in the form of both layered veils and cauliflower-like particles and Cu^0/Cu_2O species, in the form of coral-like particles.

Furthermore, several parameters were investigated to establish which was the most active electrocatalyst composition evaluating the performances in terms of acetic acid productivity, during a potentiostatic CO_2 reduction at -0.4V *vs* RHE for 1h. As a result, all catalysts displayed selectivity towards the production of acetic acid, concerning the liquid products. The highest activity was displayed by the CuMgAl 2: 1: 1 LDH/CP, which outpaced the results previously obtained with the Cu_2O-Cu^0/CP electrocatalyst, with the Cu-based derived electrocatalysts, and with the CuMgAl LDH having a cations molar ratio 1.5: 1.5: 1. Such a result demonstrates once again the high potential of the LDHs, alone or coupled with different copper active phases, as electrocatalysts for the CO_2 reduction and also the possibility to enhance their catalytic performances to produce high added-value commodities with optimum productivities by adjusting their morphological and chemical composition.

4.5 References

(1) Tonelli, D.; Gualandi, I.; Musella, E.; Scavetta, E. Synthesis and Characterization of Layered Double Hydroxides as Materials for Electrocatalytic Applications. *Nanomaterials* **2021**, *11* (3), 1–20.

(2) Jing, C.; Dong, B.; Zhang, Y. Chemical Modifications of Layered Double Hydroxides in the Supercapacitor. *ENERGY Environ. Mater.* **2020**, *3* (3), 346–379.

(3) Gualandi, I.; Vlamidis, Y.; Mazzei, L.; Musella, E.; Giorgetti, M.; Christian, M.; Morandi, V.; Scavetta, E.; Tonelli, D. Ni/Al Layered Double Hydroxide and Carbon Nanomaterial Composites for Glucose Sensing. *ACS Appl. Nano Mater.* **2019**, *2* (1), 143–155.

(4) Vlamidis, Y.; Scavetta, E.; Gazzano, M.; Tonelli, D. Iron vs Aluminum Based Layered Double Hydroxides as Water Splitting Catalysts. *Electrochim. Acta* **2016**, *188*, 653–660.

(5) Fasolini, A.; Sangiorgi, N.; Tosi Brandi, E.; Sangiorgi, A.; Mariani, F.; Scavetta, E.; Sanson, A.; Basile, F. Increased Efficiency and Stability of Dye-Sensitized Solar Cells (DSSC) Photoanode by Intercalation of Eosin Y into Zn/Al Layered Double Hydroxide. *Appl. Clay Sci.* **2021**, *212* (May), 1–10.

(6) Musella, E.; Gualandi, I.; Scavetta, E.; Rivalta, A.; Venuti, E.; Christian, M.; Morandi, V.; Mullaliu, A.; Giorgetti, M.; Tonelli, D. Newly Developed Electrochemical Synthesis of Co-Based Layered Double Hydroxides: Toward Noble Metal-Free Electro-Catalysis. *J. Mater. Chem. A* **2019**, *7* (18), 11241–11249.

(7) Musella, E.; Gualandi, I.; Scavetta, E.; Gazzano, M.; Rivalta, A.; Venuti, E.; Christian, M.; Morandi, V.; Tonelli, D. Electrochemical Approach for the Production of Layered Double Hydroxides with a Well-Defined Co/Me^{III} Ratio. *Chem. – A Eur. J.* **2019**, *25* (71), 16301–16310.

(8) Wang, H.; Xiang, X.; Li, F. Facile Synthesis and Novel Electrocatalytic Performance of Nanostructured Ni–Al Layered Double Hydroxide/Carbon Nanotube Composites. *J. Mater. Chem.* **2010**, *20* (19), 3944–3952.

(9) Basile, F.; Benito, P.; Fornasari, G.; Monti, M.; Scavetta, E.; Tonelli, D.; Vaccari, A. Novel Rh-Based Structured Catalysts for the Catalytic Partial Oxidation of Methane. *Catal. Today* **2010**, *157* (1–4), 183–190.

(10) Musella, E.; Gualandi, I.; Giorgetti, M.; Scavetta, E.; Basile, F.; Rivalta, A.; Venuti, E.; Corticelli, F.; Christian, M.; Morandi, V.; Tonelli, D. Electrosynthesis and Characterization of Layered Double Hydroxides on Different Supports. *Appl. Clay Sci.* **2021**, *202*, 1–12.

(11) Scavetta, E.; Berrettoni, M.; Seeber, R.; Tonelli, D. [Ni/Al-Cl]-Based Hydrotalcite Electrodes as Amperometric Sensors: Preparation and Electrochemical Study. *Electrochim. Acta* **2001**, *46* (17), 2681–2692.

(12) Tonelli, D.; Scavetta, E.; Giorgetti, M. Layered-Double-Hydroxide-Modified Electrodes: Electroanalytical Applications. *Anal. Bioanal. Chem.* **2013**, *405* (2–3), 603–614.

(13) Fu, S.; Zheng, Y.; Zhou, X.; Ni, Z.; Xia, S. Visible Light Promoted Degradation of Gaseous Volatile Organic Compounds Catalyzed by Au Supported Layered Double Hydroxides: Influencing Factors, Kinetics and Mechanism. *J. Hazard. Mater.* **2019**, *363*, 41–54.

(14) Li, S.; Wang, L.; Li, Y.; Zhang, L.; Wang, A.; Xiao, N.; Gao, Y.; Li, N.; Song, W.; Ge, L.; Liu, J. Novel Photocatalyst Incorporating Ni-Co Layered Double Hydroxides with p-Doped CdS for Enhancing Photocatalytic Activity towards Hydrogen Evolution. *Appl. Catal. B Environ.* **2019**, *254*, 145–155.

(15) Razzaq, A.; Ali, S.; Asif, M.; In, S.-I. Layered Double Hydroxide (LDH) Based Photocatalysts: An Outstanding Strategy for Efficient Photocatalytic CO_2 Conversion. *Catalysts* **2020**, *10* (10), 1–43.

(16) Flores-Flores, M.; Luévano-Hipólito, E.; Martínez, L. M. T.; Morales-Mendoza, G.; Gómez, R. Photocatalytic CO_2 Conversion by MgAl Layered Double Hydroxides: Effect of Mg^{2+} Precursor and Microwave Irradiation Time. *J. Photochem. Photobiol. A Chem.* **2018**, *363*, 68–73.

(17) Zhu, L.; Qiao, Z. $SrTiO_3$@NiFe LDH Core–Shell Composites for Photocatalytic CO_2 Conversion. *RSC Adv.* **2022**, *12* (17), 10592–10597.

(18) Ahmed, N.; Shibata, Y.; Taniguchi, T.; Izumi, Y. Photocatalytic Conversion of Carbon Dioxide into Methanol Using Zinc–Copper–M(III) (M=aluminum, Gallium) Layered Double Hydroxides. *J. Catal.* **2011**, *279* (1), 123–135.

(19) Li, L.; Yang, J.; Li, L.; Huang, Y.; Zhao, J. Electrolytic Reduction of CO_2 in $KHCO_3$ and Alkanolamine Solutions with Layered Double Hydroxides Intercalated with Gold or Copper. *Electrochim. Acta* **2022**, *402*, 1–11.

(20) Iwase, K.; Hirano, T.; Honma, I. Copper Aluminum Layered Double Hydroxides with Different Compositions and Morphologies as Electrocatalysts for the Carbon Dioxide Reduction Reaction. *ChemSusChem* **2022**, *15* (2), 1–6.

(21) Schröder, J.; Mints, V. A.; Bornet, A.; Berner, E.; Fathi Tovini, M.; Quinson, J.; Wiberg, G. K. H.; Bizzotto, F.; El-Sayed, H. A.; Arenz, M. The Gas Diffusion Electrode Setup as Straightforward Testing Device for Proton Exchange Membrane Water Electrolyzer Catalysts. *JACS Au* **2021**, *1* (3), 247–251.

(22) Caballero-Briones, F.; Artés, J. M.; Díez-Pérez, I.; Gorostiza, P.; Sanz, F. Direct Observation of the Valence Band Edge by in Situ ECSTM-ECTS in p-Type Cu_2O Layers Prepared by Copper Anodization. *J. Phys. Chem. C* **2009**, *113* (3), 1028–1036.

(23) Coetzee, C.; Tadie, M.; Dorfling, C. Evaluating the Effect of Molecular Properties of Polyacrylamide Reagents on Deposit Growth in Copper Electrowinning. *Hydrometallurgy* **2020**, *195*, 1–12.

(24) Cavani, F.; Trifirò, F.; Vaccari, A. Hydrotalcite-Type Anionic Clays: Preparation, Properties and Applications. *Catal. Today* **1991**, *11* (2), 173–301.

(25) Monti, M.; Benito, P.; Basile, F.; Fornasari, G.; Gazzano, M.; Scavetta, E.; Tonelli, D.; Vaccari, A. Electrosynthesis of Ni/Al and Mg/Al Layered Double Hydroxides on Pt and FeCrAlloy Supports: Study and Control of the pH near the Electrode Surface. *Electrochim. Acta* **2013**, *108*, 596–604.

(26) Gevers, B. R.; Naseem, S.; Leuteritz, A.; Labuschagné, F. J. W. J. Comparison of Nano-Structured Transition Metal Modified Tri-Metal MgMAl–LDHs (M = Fe, Zn, Cu, Ni, Co) Prepared Using Co-Precipitation. *RSC Adv.* **2019**, *9* (48), 28262–28275.

(27) Serafini, M.; Mariani, F.; Fasolini, A.; Scavetta, E.; Basile, F.; Tonelli, D. Nanostructured Copper-Based Electrodes Electrochemically Synthesized on a Carbonaceous Gas Diffusion Membrane with Catalytic Activity for the Electroreduction of CO_2. *ACS Appl. Mater. Interfaces* **2021**, *13* (48), 57451–57461.

(28) Huang, Y.; Han, Y.; Sun, J.; Zhang, Y.; Han, L. Dual Nanocatalysts Co-Decorated Three-Dimensional, Laser-Induced Graphene Hybrid Nanomaterials Integrated with a Smartphone Portable Electrochemical System for Point-of-Care Non-Enzymatic Glucose Diagnosis. *Mater. Today Chem.* **2022**, *24*, 1–10.

(29) Cosano, D.; Esquivel, D.; Romero-Salguero, F. J.; Jiménez-Sanchidrián, C.; Ruiz, J. R. Use of Raman Spectroscopy to Assess Nitrate Uptake by Calcined LDH Phases. *Colloids Surfaces A Physicochem. Eng. Asp.* **2020**, *602*, 1–6.

(30) Liu, J.; Tian, Y.; Chen, Y.; Liang, J.; Zhang, L.; Fong, H. A Surface Treatment Technique of Electrochemical Oxidation to Simultaneously Improve the Interfacial Bonding Strength and the Tensile Strength of PAN-Based Carbon Fibers. *Mater. Chem. Phys.* **2010**, *122* (2–3), 548–555.

(31) Amini, R.; Asadpour-Zeynali, K. Cauliflower-like $NiCo_2O_4$−Zn/Al Layered Double Hydroxide Nanocomposite as an Efficient Electrochemical Sensing Platform for Selective Pyridoxine Detection. *Electroanalysis* **2020**, *32* (6), 1160–1169.

(32) Fasolini, A.; Abate, S.; Barbera, D.; Centi, G.; Basile, F. Pure H_2 Production by Methane Oxy-Reforming over Rh-Mg-Al Hydrotalcite-Derived Catalysts Coupled with a Pd Membrane. *Appl. Catal. A Gen.* **2019**, *581*, 91–102.

(33) Scavetta, E.; Mignani, A.; Prandstraller, D.; Tonelli, D. Electrosynthesis of Thin Films of Ni, Al Hydrotalcite Like Compounds. *Chem. Mater.* **2007**, *19* (18), 4523–4529.

(34) Klug, H. P.; Alexander, L. E. X-Ray Diffraction Procedures for Polycrystalline and Amorphous Materials. *2nd Ed. John Wiley Sons* **1974**, 618–708.

(35) Miyata, S. Anion-Exchange Properties of Hydrotalcite-Like Compounds. *Clays Clay Miner.* **1983**, *31* (4), 305–311.

(36) Marappa, S.; Radha, S.; Kamath, P. V. Nitrate-Intercalated Layered Double Hydroxides – Structure Model, Order, and Disorder. *Eur. J. Inorg. Chem.* **2013**, *2013* (12), 2122–2128.

(37) Monteiro, M. C. O.; Dattila, F.; Hagedoorn, B.; García-Muelas, R.; López, N.; Koper, M. T. M. Absence of CO_2 Electroreduction on Copper, Gold and Silver Electrodes without Metal Cations in Solution. *Nat. Catal.* **2021**, *4* (8), 654–662.

(38) Lu, S.; Wang, Y.; Xiang, H.; Lei, H.; Xu, B. Bin; Xing, L.; Yu, E. H.; Liu, T. X. Mass Transfer Effect to Electrochemical Reduction of CO_2: Electrode, Electrocatalyst and Electrolyte. *J. Energy Storage* **2022**, *52*, 1–20.

(39) Jia, M.; Zhang, Y.; Bao, Y.; Wang, J.; Xu, A. Recyclable CuMgAl Hydrotalcite for Oxidative Esterification of Aldehydes with Alkylbenzenes. *Green Chem. Lett. Rev.* **2018**, *11* (3), 230–236.

(40) Dongare, S.; Singh, N.; Bhunia, H. Electrocatalytic Reduction of CO_2 to Useful Chemicals on Copper Nanoparticles. *Appl. Surf. Sci.* **2021**, *537*, 1–8.

(41) Genovese, C.; Ampelli, C.; Perathoner, S.; Centi, G. Mechanism of C–C Bond Formation in the Electrocatalytic Reduction of CO_2 to Acetic Acid. A Challenging Reaction to Use Renewable Energy with Chemistry. *Green Chem.* **2017**, *19* (10), 2406–2415.

(42) Marepally, B. C.; Ampelli, C.; Genovese, C.; Tavella, F.; Veyre, L.; Quadrelli, E. A.; Perathoner, S.; Centi, G. Role of Small Cu Nanoparticles in the Behaviour of Nanocarbon-Based Electrodes for the Electrocatalytic Reduction of CO_2. *J. CO_2 Util.* **2017**, *21*, 534–542.

(43) de Brito, J. F.; Genovese, C.; Tavella, F.; Ampelli, C.; Boldrin Zanoni, M. V.; Centi, G.; Perathoner, S. CO_2 Reduction of Hybrid Cu_2O–Cu/Gas Diffusion Layer Electrodes and Their Integration in a Cu-based Photoelectrocatalytic Cell. *ChemSusChem* **2019**, *12* (18), 4274–4284.

(44) Hadj-Abdelkader, N. E. H.; Beltrao-Nunes, A.-P.; Belkhadem, F.; Benselka, N.; Roy, R.; Azzouz, A. New Insights in MgAl and MgFe-LDH Affinity towards Carbon Dioxide – Role of the Hydrophilic Character on CO_2 Retention Strength. *Appl. Clay Sci.* **2020**, *198*, 1–10.

(45) Goodman, E. D.; Schwalbe, J. A.; Cargnello, M. Mechanistic Understanding and the Rational Design of Sinter-Resistant Heterogeneous Catalysts. *ACS Catal.* **2017**, *7* (10), 7156–7173.

(46) Wu, L.; Kolmeijer, K. E.; Zhang, Y.; An, H.; Arnouts, S.; Bals, S.; Altantzis, T.; Hofmann, J. P.; Costa Figueiredo, M.; Hensen, E. J. M.; Weckhuysen, B. M.; van der Stam, W. Stabilization Effects in Binary Colloidal Cu and Ag Nanoparticle Electrodes under Electrochemical CO_2 Reduction Conditions. *Nanoscale* **2021**, *13* (9), 4835–4844.

CHAPTER 5

In Situ/Operando Studies of the Electrochemical Reduction of CO_2 by CuMgAl LDH Catalysts on Gold Electrodes

In the previous chapter the optimal composition of the CuMgAl LDH electrocatalyst that allowed to obtain an outstanding performance for the production of acetic acid during the CO_2ER reaction has been defined. Here, preliminary investigations on the intimate details of the electrocatalyst's surface and variations that occurred during the production of liquid products by employing a CuMgAl 2: 1: 1 LDH electrocatalyst were carried out. In particular, coupling an *operando* spectroscopic analysis with *in situ* measurements, a relation between the superficial changes of the catalytic layer, also consequent to a possible intermediates' adsorption, and the selectivity of the reaction upon application of different potentials has been successfully established. To do so, the liquid products' distribution at the electrode-electrolyte interface by means of *in situ* H^1-NMR has been investigated, while *operando* Surface Enhanced Raman Spectroscopy (SERS) was used to follow the chemical state of the active layer along with the possible formation of adsorbed intermediates. Differently from the previous tests, the ternary LDH was electrodeposited over an Au support, since the SERS analysis needed a roughened surface to enhance the signals. For this reason, an initial optimisation of the catalyst electrodeposition on a different support was performed. Besides, using *in situ* H^1-NMR analyses, a preliminary evaluation has been also carried out on which was the carbon source that due to the presence of the electrocatalyst is able to promote the formation of the target products.

The experiments described and discussed in this chapter were carried out during a research stay in the Leiden Institute of Chemistry (NL), at the Catalysis and Surface Chemistry (CASC) research group of Prof. Marc T.M. Koper.

5.1 Introduction

Notably, one of the major challenges of the electrochemical CO_2 reduction is revealing the dynamic processes at the basis of the reaction mechanism. Differently from the water splitting reaction, the CO_2ER is more complicated due to the wide range of intermediates/products that can be formed by multiple H^+/e^- transfer processes [1]. Since the reaction outcomes are strictly dependent on the active sites and the local pH generated at the electrode-electrolyte interface, it is essential to understand which type of changes the electrocatalytic layer undergo during the reaction and thus to identify possible active intermediates herein adsorbed. Along with the electrocatalyst optimisation, the control over the reaction mechanism that occurred at the catalyst surface will offer the possibility to selectively tune the reaction towards the desired CO_2 reduction product. Typically, *ex situ* spectroscopic, diffraction, or microscopic techniques are employed to explore the catalytic activities, durability, and selectivity of a material, providing base understandings [2]. However, they could give estimations that may be not sufficient to reveal mechanistic details of the electrochemical processes. Recently, *in situ* and *operando* techniques of spectroscopic or microscopic nature have gained a great interest as promising approaches to investigate the electrocatalyst, along with the binding modes of the intermediates, during the course of CO_2ER reactions [3,4]. In particular, since the ability of Cu-based electrocatalyst to yield C_{2+} products has been widely demonstrated, great efforts are being making in order to shift the selectivity of an employed material towards the formation of C-C coupling, investigating the effects of the reaction environment, *i.e.*, catalytic layer, local pH, and applied potential on the products' distribution [5,6]. To these purposes, *operando* and *in situ* X-ray absorption (XAS) [7], X-ray photoelectron (XPS) [8], infrared [4], and Raman [9] spectroscopies are considered the most promising techniques to provide such information. Indeed, thanks to such mechanistic studies, it is nowadays overall accepted that the selectivity of Cu-based electrocatalysts is strongly dependent on the adsorption properties of the

intermediates such as *CO, *OCHO, and *COOH, which in turn are related to the structural and chemical composition of the electrocatalyst [10].

To date, it is generally recognised that there are two main pathways of reaction which allowed, on one hand, the formation of C_1 products, *i.e.,* CO, HCOOH, CH_4, or CH_3OH, and, on the other hand, the C_{2+} products, *i.e.*, C_2H_4, CH_3CH_2OH, or CH_3COOH. Figure 5.1 shows an example of typical C_1 and $C_{2/2+}$ (products with 2 or more carbon atoms) pathways on the Cu catalyst surface.

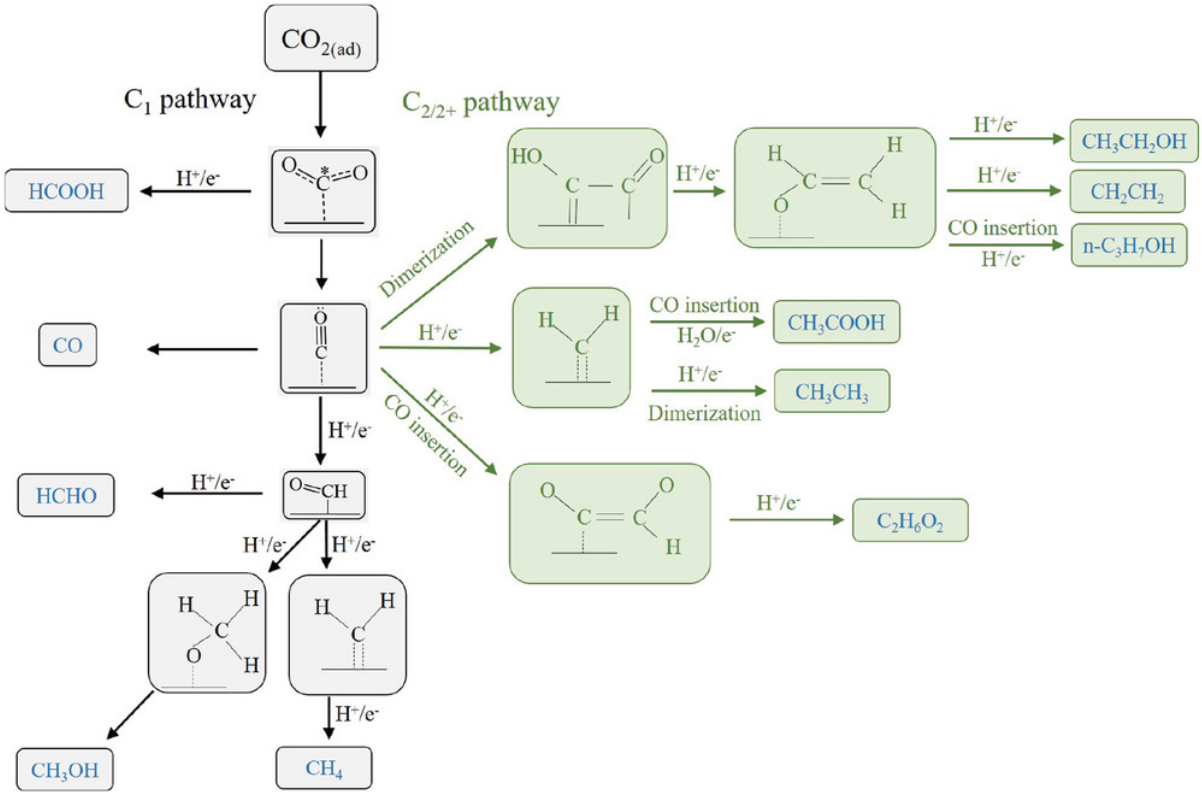

Figure 5.1. C_1 and $C_{2/2+}$ pathways on the Cu-based electrocatalyst. Reproduced with permission from Quan *et al.* [10], © 2021 The Authors. Advanced Science published by Wiley-VCH GmbH

Although the C_1 reaction pathways are simpler and better defined, those for C_{2+} products are more complex and strongly dependent on the electrocatalyst surface and the employed reaction's conditions. This is because the C-C coupling is kinetically disfavoured compared to the formation of C-H or H-H bonds [11], as lower energies are required for their formation [12].

As suggested by several *in situ* infrared spectroscopic studies [13,14], the most widely accepted pathway towards C_{2+} products involves the formation of *CO, which is also considered as the rate limiting step, since it can dimerize in *OCCO species or be hydrogenated to produce *CHO intermediates [15]. Moreover, a higher coverage of *CO over the electrocatalytic surface may likely enhance the probability of the C-C coupling occurrence and thus favour the C_{2+} pathway [16]. To achieve the goal, several studies have been performed which have highlighted the importance of an alkaline environment at the electrode-electrolyte interface. As an example, Moradzaman *et al.* [17] demonstrated by *in situ* attenuated total reflection surface-enhanced infrared absorption spectroscopy that an enhanced *CO coverage of the surface of an oxide-derived Cu electrode was achieved by increasing the electrolyte's pH, which resulted in a higher production of C_2H_4 instead of CH_4. Similarly, Gunathunge *et al.* [18] revealed the coexistence of two different CO adsorption sites over a Cu-based electrocatalyst in alkaline pH, including *CO atop and bridge sites, the former active towards the CO_2 reduction while the latter completely inert. However, the quantification of the *CO coverage on the electrode's surface is still a great challenge [16,19].

Furthermore, along with the alkaline environment at the electrode-electrolyte interface, the chemical composition of Cu based catalyst plays an important role, and it is crucial to investigate the effects of different chemical states of surface ions on the products' distribution and selectivity. In particular, one of the main issues concerns the possible role of surface copper oxide as active catalyst towards C_{2+} products for which there are still open debates and conflicting ideas. As an example, Mistry *et al.* [20] revealed by means of *in situ* X-ray absorption near edge structure (XANES) spectroscopy that Cu^+ species survived even after the beginning of the CO_2 reduction. Here, the Cu^+ was considered to be the main responsible for the production of C_2H_4.

Similarly, Eilert *et al.* [21] proposed that residual subsurface oxygen changed the structure of the oxide derived Cu electrocatalyst, shifting the selectivity towards C_2 products. Differently, Ren *et al.* [22] revealed by *in situ* Raman analyses that upon application of the cathodic potential the Cu_2O-based electrocatalyst was fully reduced to Cu^0 within few minutes, thus suggesting metal copper as real active phase. Additional *in situ* Raman analyses have demonstrated that restructuring processes upon cycling from oxidising to reducing potentials were useful to enhance the selectivity towards C_2 products [23]. Moreover, *operando* Raman spectroscopy was useful in the identification of a direct correlation between the potential-dependent *CO coverage, the preferred C–C coupling, and the selectivity to C_{2+} products [16].

Therefore, by applying different *in situ/operando* techniques, it was possible to obtain a wide range of information regarding both the adsorbed active intermediates and the chemical state of the electrocatalyst.

Raman spectroscopy represents one of the most highly versatile technique for determining the chemical composition of a target sample without altering it [24]. Briefly, the surface of a material is irradiated by a light source with frequency ν_0 and its inelastic photons' scattering, known as Raman scattering, displays shifted frequencies compared to the pristine irradiating light. Such frequencies (ν_1) are characteristic of the atomic vibrational modes associated to the irradiated sample, resulting in its spectroscopic fingerprints. Since the employed light sources are generally photons within the visible range, Raman spectroscopy possesses unique advantages for *operando* analyses of electrode materials. Indeed, it includes (i) non-destructive light sources, (ii) the possibility to add window materials transparent to visible light, *i.e.*, quartz in the electrochemical cell for *operando* analyses, and (iii) a spectrum acquisition time scale which allows a sufficient time resolution. Moreover, electrolytes that usually display stronger infrared signals (*e.g.*, H_2O), have moderate Raman signals, so facilitating the identification of the test material [25].

The technique requires roughed surfaces (typically metals, *e.g.,* Cu or Au), in order to decrease the SERS background signals, while the main drawbacks consist in the great gas evolution and the difficult interpretation of the spectrum if many peaks are present [26]. Indeed, no single *in situ/operando* method is able to provide a complete picture of the interface. In this chapter, an *operando* Raman study was carried out during the reaction performed with the CuMgAl 2: 1: 1 LDH electrocatalyst and an *in situ* sampling of the liquid at the electrode-electrolyte interface was performed for a following to H^1-NMR analysis (*in situ* H^1-NMR). That was aimed to characterise the catalyst surface during the reaction and to evaluate the quantitative results of the catalytic tests in terms of liquid products, *i.e.*, HCOOH and CH_3COOH.

A relation between the changes of the chemical state of copper, induced by the potential, and the different selectivity towards the C_1 and C_2 compounds was finally proposed, along with a preliminary evaluation of the possible role of CO_3^{2-} in the CO_2 reduction process achieved with a LDH material.

5.2 Materials and Methods

5.2.1 Chemicals and Materials

Copper nitrate trihydrate ($Cu(NO_3)_2 \cdot 3H_2O$), aluminium nitrate nonahydrate ($Al(NO_3)_3 \cdot 9H_2O$), iso-propanol (≥ 99.9 %), potassium hydrogen carbonate ($KHCO_3$), potassium nitrate (KNO_3), deuterium oxide, phenol, and potassium chloride were purchased from Sigma Aldrich. Magnesium nitrate hexahydrate ($Mg(NO_3)_2 \cdot 6H_2O$) was obtained from Alfa Aesar. H_2 (5.0 purity), Ar (6.0 purity), and CO_2 (4.5 purity) were purchased from Linde. A Selemion™ AMVN ion exchange membrane was purchased from AGC Engineering Co. All chemicals were of reagent grade or higher.

5.2.2 Apparatus

The electrochemical deposition and the roughening of the Au electrode were carried out in a conventional three-electrode cell connected to a potentiostat (Biologic SP300) coupled with an EC-Lab software. The conventional three-electrode cell included: a Au polycrystalline disk (diameter = 6 or 3.6 mm) used as working electrode; a gold wire used as counter electrode and a HydroFlex® reversible hydrogen electrode (RHE) or a home-made RHE, used as reference electrode. The CuMgAl LDH films electrodeposited over the Au disk were investigated by X-ray diffraction spectroscopy carried out with a Philips X'Pert diffractometer, equipped with the X'Celerator (Cu Ka, λ = 0.15418 nm) in steps of 0.021 and 8 s counting time between 8 and 80. The CO_2 electroreduction tests for the *in situ* sampling of the liquid products were performed in a typical H-cell, filled with a 0.3 M $KHCO_3$ solution and connected to an Autolab PGSTAT12. The working electrode compartment included the modified Au disk and the HydroFlex® RHE used as working and reference electrodes, respectively, while a platinum wire was placed in the other side of the cell. The two compartments were divided by an AMVN membrane. The liquid samples were collected through an *in situ* fraction collector FRC-10A, which allowed to collect 60 $\mu L\ min^{-1}$ of liquid closed to the surface of the electrode, and analysed by a Bruker AV-III HD 600 MHz NMR spectrometer equipped with a TXI cryoprobe. Scanning Electron Microscopy (SEM) studies were achieved by means of a E-SEM Zeiss EVO 50 Series Instrument. *Operando* Surface Enhanced Raman Spectroscopy (SERS) analyses of the CO_2 electroreduction reaction were carried out using a HR-800 (LabRam HR, Horiba Yobin Yvon) spectrometer integrated with a confocal microscope. The laser beam was focused through an objective lens on the working electrode in a vertical arrangement [27] (for details see the cited reference). The spectra were recorded by excitation with a He-Ne laser at a wavelength of 632.8 nm, without filters added. The experiments were performed in a home-made glass cell, with a quartz window at the bottom, connected to a Micro Autolab III.

5.2.3 Pretreatment of the Au Disk

The Au polycrystalline disk was mechanically polished on a Buehler micro-polishing cloth (8 inches) with decreasing sizes of diamond polishing suspensions, namely, 3µm, 1 µm and 0.25µm. Then, the electrode was sonicated in pure isopropanol followed by ultrapure water, 5 min each. Finally, it was dried with compressed air.

5.2.4 Electrodeposition of the CuMgAl 2: 1: 1 LDH Films

The Cu-containing LDH films were deposited on the cleaned Au electrode by adapting the same procedure used for the electrodeposition on the carbonaceous gas diffusion membrane (GDL) [28–30]. The electrodeposition solution was prepared using the nitrate salts of each cation, $Cu(NO_3)_2 \cdot 3H_2O$, $Mg(NO_3)_2 \cdot 6H_2O$, $Al(NO_3)_3 \cdot 9H_2O$, with a total concentration of 30 mM and keeping molar ratios among Cu, Mg, and Al of 2: 1: 1. The working electrode was in contact with the electrodeposition solution with a hanging meniscus configuration, unlike the experimental set-up used for the GDL support where the electrode was completely dipped in the electrolytic bath. The electrodeposition of the LDH film was carried out by cyclic voltammetry in a potential window from 0.365 to -1.0 V *vs* RHE, which differs from the already optimised conditions (from 0.456 to -0.943 V *vs* RHE) due to the different electrodeposition set-up conditions.

The as-obtained electrocatalyst was thoroughly rinsed in ultrapure H_2O and dried in Ar to a constant weight. The achieved electrocatalyst was named CuMgAl 2: 1: 1 LDH/Au.

5.2.5 Electrocatalytic Tests

The liquid phase CO_2 electrochemical reduction tests were performed in a H-type cell, where the working electrode was separated from the counter electrode by an ion exchange membrane.

The compartment of the reference electrode was physically separated from the working electrode but connected through the electrolyte. A 0.3 M $KHCO_3$ solution was employed as the supporting electrolyte. Both sides of the cell were pre-saturated with a constant flux of pure CO_2 (20 mL min^{-1}) for 30 min which was maintained at 5 mL min^{-1} during the reaction occurrence. All the applied potentials used for the CO_2ER were referred to the RHE. During the electrochemical reduction the cell was not tightly sealed and thus only liquid products were collected *in situ* and analysed by a quantitative H^1-NMR analysis, adding phenol as the internal standard and deuterium oxide to provide an internal lock signal.

5.2.6 Operando Surface Enhanced Raman Spectroscopy Analysis

In situ Surface Enhanced Raman Spectroscopy (SERS) measurements were carried out during the electrochemical CO_2 reduction reaction in liquid phase. Prior to the electrodeposition of the LDH film, the Au disk was roughened by 30 oxidation-reduction cycles (ORC) in 0.5 M KCl. During the ORC the electrode was held at +1.81 V and 0 V *vs* RHE for 5 and 20 s, respectively. Prior to the oxidation-reduction cycles, the electrode was kept at the OCP potential for 20 s. The investigated potentials were chosen on the basis of the potentials to be applied during the electrocatalytic tests in order to relate the peaks recorded during the *operando* Raman analysis with the liquid outcomes of the reaction.

5.3 Results and Discussion

5.3.1 Electrochemical Synthesis of the CuMgAl 2: 1: 1 LDH over the Au Disk

At the beginning, preliminary attempts for the CuMgAl 2: 1: 1 LDH electrodeposition were performed. Due to the different electrodeposition set-up, it was necessary to find the proper parameters in order to achieve the same material whose synthesis had already been optimised on the 4 cm^2 sized carbonaceous membrane (GDL).

Indeed, different conductive supports and reference electrodes are usually responsible for several variations during electrochemical processes [30,31].

The electrodeposition of the Cu-containing LDH films over gold electrodes was carried out by cyclic voltammetry starting from 0.365 to -1.0 V *vs* RHE (scan rate = 30 mV s^{-1}).

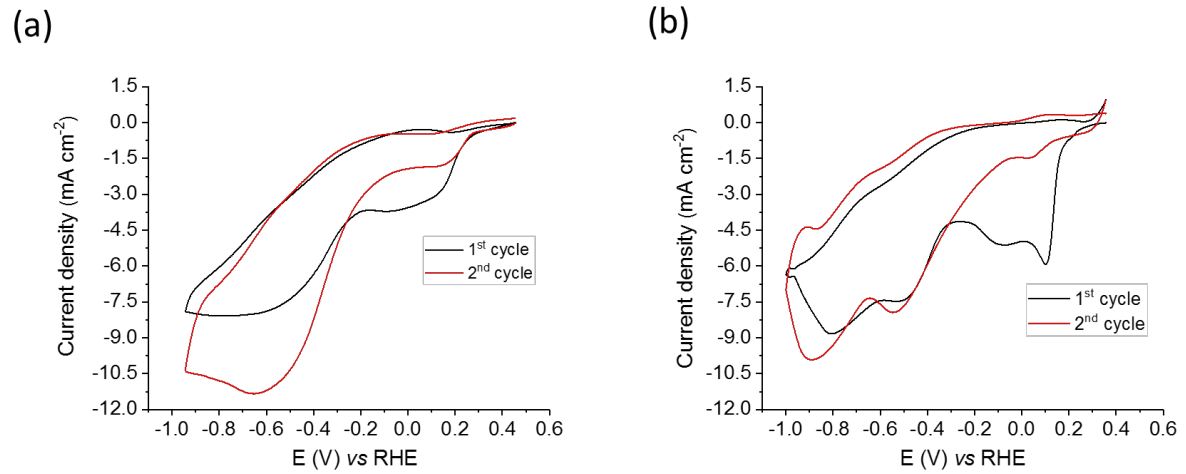

Figure 5.2. Electrodeposition of CuMgAl 2: 1: 1 LDH over (a) Carbon Paper - 4 cm^2 and (b) over Au - 0.28 cm^2

Figure 5.2 shows a comparison between the electrodeposition achieved on the carbonaceous membrane (Figure 5.2a) and the one achieved on the Au support (Figure 5.2b). Focusing on the recorded current densities, it can be stated that the amount of the loaded electrocatalyst on the gold support, should be slightly lower. However, since the mass of the electrode was much higher than that of the electrodeposited catalytic film, it was impossible to weigh precisely the catalyst mass. Unlike the material synthesised on the carbonaceous membrane, namely CuMgAl LDH/CP, the voltammograms recorded during the electrodeposition over Au presented four cathodic peaks: two at +0.1 and -0.08 V *vs* RHE, one of which disappeared during the second cycle, and two more cathodic peaks at -0.5 and -0.8 V *vs* RHE.

Comparing these peaks with the ones recorded during the electrodeposition on CP, it can be hypothesised that they are referred to the reduction of the same species, *i.e.*, copper (less cathodic peaks) and nitrate (more cathodic peaks).

Indeed, the larger peaks observed employing the carbonaceous material may likely include the systems of the two peaks, which are well resolved when the electrode is made of a more conductive material. Moreover, to validate the idea that they can be ascribable to the same species it is worth noting the behaviour recorded during the second scan. Here, the less cathodic peak recorded in Figure 5.2b is slightly anticipated likewise the one obtained in Figure 5.2a, thus suggesting that, even in the electrodeposition on Au, a partial reduction of the Cu species occurs as soon as the cathodic potential is applied and it can be related to the deposition of copper onto a film already present on the metal support. Moreover, a similar trend was observed also for the nitrates reduction which was hindered by the copper reduction during the first scan and favoured during the second one (for a more detailed discussion see Chapter 3, Paragraph 3.3.1).

To further investigate the nature of the less cathodic peaks, an electrodeposition was carried out upon application of a narrower range of potential, from +0.256 V to -0.350 V *vs* RHE, employing the solution containing the nitrate salts of each cation as electrolyte. This was aimed to avoid the nitrate reduction and consequently the pH increase next to the electrode-electrolyte interface. A homogeneous film was achieved on the surface of the Au support, and the recorded CVs (Figure 5.3) displayed two reduction peaks in the first scan and one peak in the other three cycles, which was decreasing in intensity and shifted towards an intermediate potential value, in a way similar to what happened when the deposition was performed in a broader potential window (Figure 5.2b).

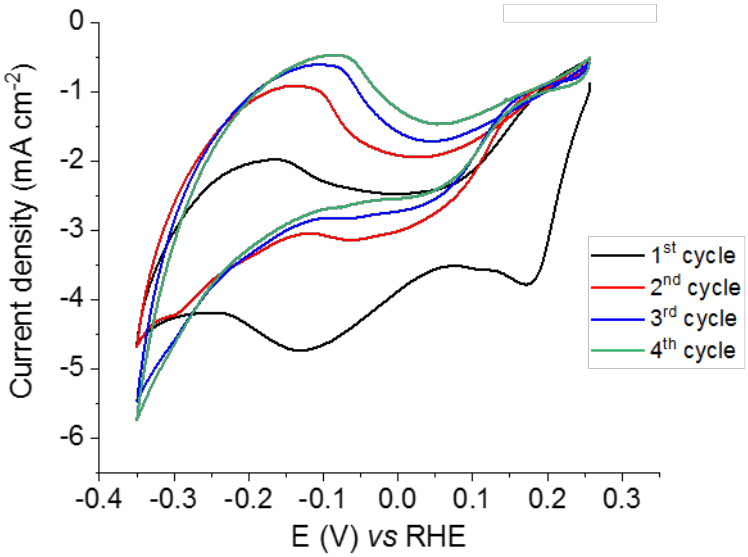

Figure 5.3. Voltammograms recorded during the electrodeposition of only Cu species on Au

Assuming that those peaks were consistent with the copper reduction, as already discussed in Chapter 3 (Paragraph 3.3.1), to confirm their nature, a CV characterisation was carried out in alkaline condition and compared with the one recorded employing Cu^0/CP electrocatalyst (Figure 5.4). For the sake of clarity, the applied potentials during the electrochemical characterisation on the new film was referred to a saturated calomel electrode (SCE) even though it was carried out employing a HydroFlex® reversible hydrogen electrode (RHE).

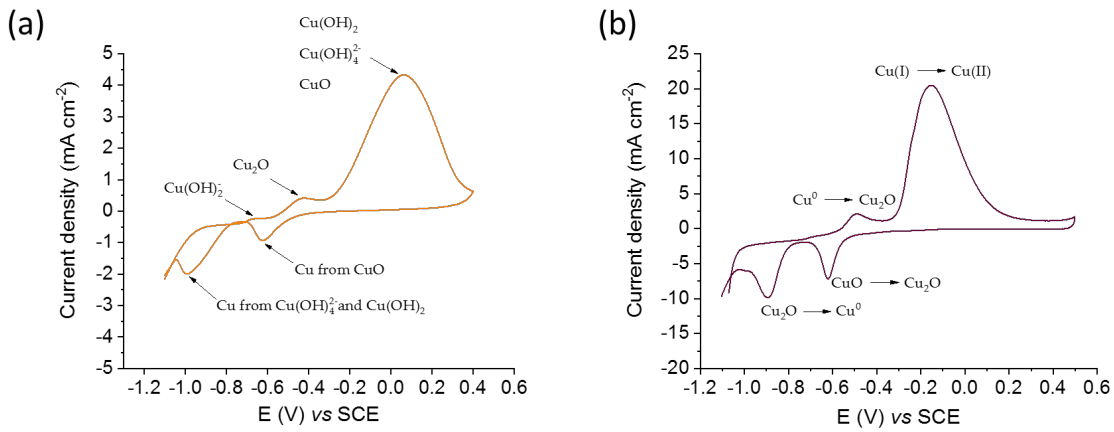

Figure 5.4. CV study on the (a) Cu^0/CP and (b) Cu-containing film/Au in 0.5 M KOH, scan rate 50 mV s^{-1}, N_2 atmosphere. Peaks assigned from a reported study [32]

As a result, the voltammogram obtained for the film electrodeposited on Au displayed the same peaks as those present in the Cu^0/CP characterisation, except for a slight shift of the potentials likely due to the different employed support.

The presence of the LDH structure was investigated by performing X-ray diffraction analysis (Figure 5.5) on two different samples which were prepared by 2 or 4 deposition cycles.

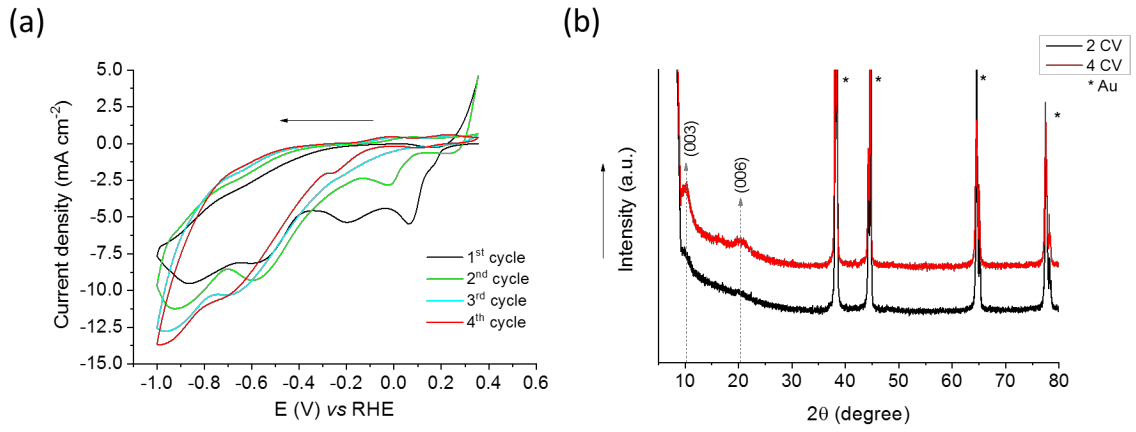

Figure 5.5. (a) Electrodeposition of CuMgAl 2: 1: 1 LDH/Au by using 4 CVs and (b) X-ray diffraction patterns for the materials synthesised by 2 or 4 CVs

Focusing the attention on the recorded current densities for the 4 CVs electrodeposition (Figure 5.5a), it can be noticed the same trend as already observed using CP as conductive support (Chapter 4, Paragraph 4.3.2.2), thus suggesting an increase of the loaded catalyst on the conductive support, upon cycling.

X-ray diffraction spectra were recorded on both samples (Figure 5.5b) and the clearest evidence of the LDH structure was obtained with the 4 CVs electrocatalyst. Indeed, it displays the typical reflections of the layered double hydroxide (003) and (006) at 10.3° and 20.9° (2θ), respectively [33], along with the reflections of the gold support at 38.4°, 44.8°, 64.5°, and 77.4° (2θ) [34]. Moreover, the corresponding d-spacing of the (003) reflection is 8.6, typical of the NO_3^- inside the structure [35].

The confirmed presence of the LDHs, together with the evidences of the copper species, led to hypothesise that a material similar to the one based on CuMgAl LDH/was obtained also on the Au support. However, SEM analyses revealed that the morphology has a completely different structure (Figure 5.6). Indeed, it was not possible to determine the presence of coral- or cauliflower-like particles referred to the presence of Cu^0 and Cu_2O, but only a homogeneous and well-adherent coating where the EDS analyses revealed the presence of all three cations with a good match with the cations' molar ratios in the electrolytic bath of 2: 1: 1 (1.9 for Cu/Mg, 1.7 Cu/Al, and 0.9 for Mg/Al). The different morphology is consistent with the different nature of the support, both in terms of morphology and conductivity.

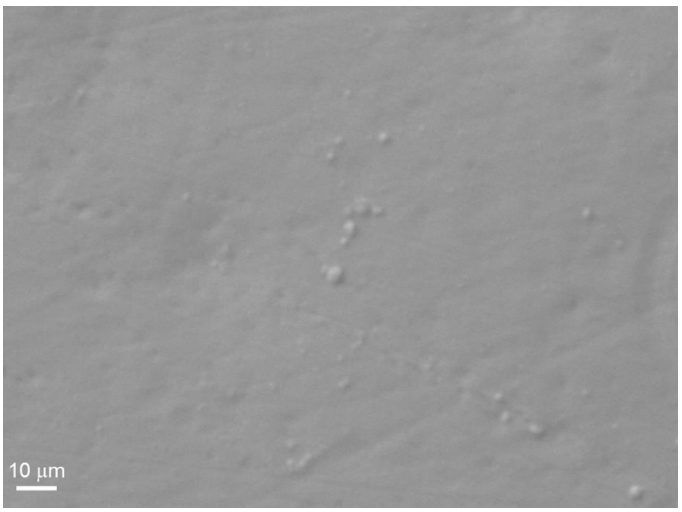

Figure 5.6. SEM image of the electrodeposited CuMgAl 2: 1: 1 LDH/Au

Therefore, except for the morphological characterisation it can be assumed that the electrocatalyst achieved on Au possessed the same chemical composition of the one electrosynthesised on the carbon paper (Cu species and ternary CuMgAl LDHs). Moreover, since a clearer evidence of the LDH crystal structure was achieved by performing a 4 CVs electrodeposition, this material was chosen for further studies.

5.3.2 Studies of the Catalytic Activities at the Electrode-Electrolyte Interface

Once the electrodeposition on Au had been optimised, several tests on the catalytic performances for the electrochemical CO_2 reduction were performed. The tests were carried out to confirm the selectivity trend of the Cu-based layered double hydroxides towards acetic and formic acid and the possible presence of other reaction outcomes studied through an initial screening of potentials. The products distribution at the electrode-electrolyte interface was evaluated by applying an *in situ* sampling which was submitted to H^1-NMR to analyse the liquid phase. Moreover, kinetic studies have been performed to investigate the product distribution during time at a fixed applied potential.

Such studies were conducted only on the liquid products since the final purpose was to study the possible reaction mechanism concerning the acetic and formic acid production.

5.3.2.1 Screening of the Potentials

An initial evaluation of the catalytic performances using the CuMgAl LDH/Au electrocatalyst was carried out by applying fixed potentials from 0 to -1.4 V *vs* RHE for 10 min each (potential step = 0.2 V), in order to verify the achievable products in dependence on the potential. Each potential was applied consecutively, without restoring the open circuit potential (OCP) between the tests, and the same deposit was employed during the entire experiment. Moreover, by sampling close to the electrode surface, it was possible to collect a minimum amount of liquid (at a rate of 60 μL min^{-1}), so that the total volume sampled was 0.6 mL for each potential, which was finally analysed with quantitative H^1-NMR.

Figure 5.7 displays the products distribution concerning the liquid phase referred to the different applied potentials.

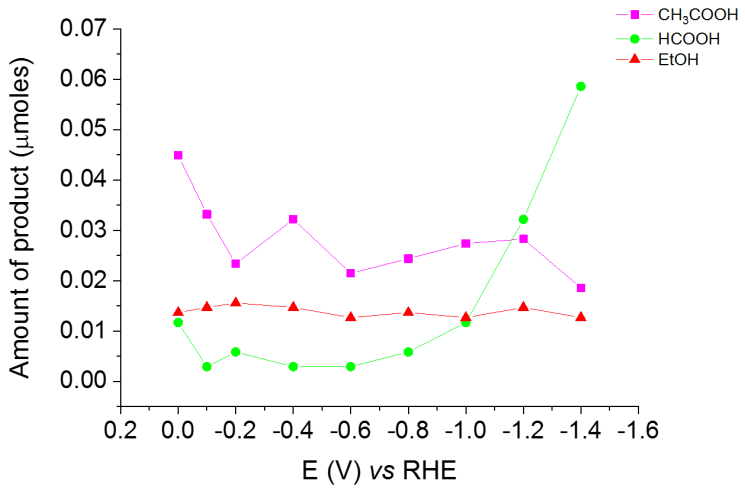

Figure 5.7. Liquid products distribution at the different applied potentials

(Reaction time for each potential = 10 min)

As a result, it was possible to confirm the presence of acetic and formic acids, even at very low potentials such as 0 V *vs* RHE, and also traces of ethanol were detected. In particular, the results can be summarised as follows:

- CH_3COOH – two peaks of production and high selectivity were observed at 0 and -0.4 V *vs* RHE, followed by a decrease as the potential became more cathodic.
- HCOOH – production increased as the potential became more cathodic than -1.0 V *vs* RHE.
- CH_3CH_2OH – the production seemed to be independent from the applied potential

Concerning the production of ethanol, since it displayed an independent trend regardless the applied potential, two main hypotheses may be advanced. It could come from (i) an impurity derived from the treatment process of the Au support, *e.g.,* traces in the diamond polishing suspensions, or (ii) the promotion of a different mechanism, *e.g.*, a disproportion such as the Cannizzaro reaction [36]. However, once excluded any possible impurity source, and due to the very low amount detected during the semi-quantitative analyses at the interface, the presence of ethanol was not investigated further.

On the other hand, from a preliminary evaluation, the production trend related to the formic and acetic acids seemed to confirm the one observed in the studies described in Chapter 2, where the liquid products were determined in the bulk electrolyte. Similarly, the production of acetic acid was favoured at low applied potentials while the formation of formic acid was enhanced in more reducing conditions. Indeed, from an empirical point of view, it can be hypothesised that the production of acetic acid occurs as soon as the cathodic potential is applied and thus it is favoured by the partially reduced species of the electrocatalyst, while the production of formic acid becomes significant at potentials more cathodic than -1.0 V *vs* RHE. In order to investigate a possible reaction mechanism, kinetic studies at the most representative potentials were carried out.

Moreover, it was thoroughly investigated the production at 0 V since the applied potential generated a very low current density (~ 0.056 mA cm^{-2}, once it reached the plateau).

5.3.2.2 Kinetic Studies at Fixed Potential

Starting from the initial evaluation of the products distribution at the electrolyte-electrode interface carried out by *in situ* measurements, three potentials were chosen as the most representative to further investigate the distribution of the target products over time (1 h of reaction). The liquid samples were analysed every 10 min of reaction, which allowed to carefully follow the reaction outcomes. Figure 5.8 displays the achieved results concerning (i) 0 V, considered as the initial potential at which the reduction started, (ii) -0.4 V since at this value the second peak in the acetic acid production occurred, and (iii) -0.8 V considered as the initial potential at which the formic acid production started to increase.

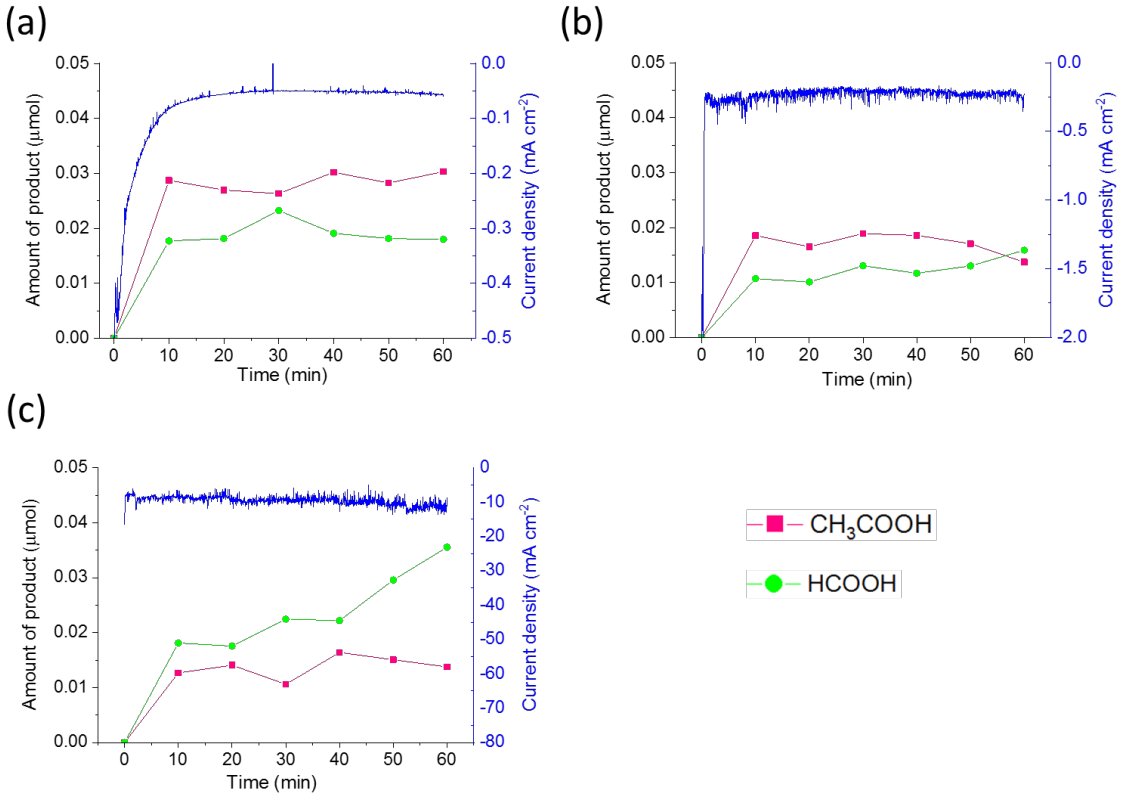

Figure 5.8. Kinetic studies at fixed applied potentials (a) 0 V, (b) -0.4 V, and (c) -0.8 V *vs* RHE

Figure 5.8a shows the products distribution during 1h reaction at 0 V *vs* RHE. On the one hand, a fair selectivity to acetic could be evidenced, as the amount of CH_3COOH was two times higher than HCOOH. Surprisingly, the low potential led to a constant production of both acids during time, suggesting that their formation is independent from each other.

Such an experimental evidence is consistent with the already reported theory concerning the two different reaction pathways, namely C_1 and C_2 route [37,38]. Moreover, it can be hypothesised that the employed experimental conditions led to the coexistence of catalytic species capable to promote both the formic acid production and the C-C coupling to obtain acetic acid.

Moving to the kinetic study at -0.4 V (Figure 5.8b), a change in the products selectivity was observed. Indeed, as soon as the cathodic potential was applied, the acetic acid was again the main product but it started to decrease at the end of reaction and the selectivity shifted towards formic acid.

Such an experimental evidence suggests that after 45-50 min of reaction the catalytic species capable to promote the C-C coupling was outpaced by the species responsible for the C_1 pathway. The final kinetic study (Figure 5.8c) clearly demonstrated a different trend of the reaction outcomes, showing an increasing production of formic acid and a lower and constant production of acetic acid. Moreover, the more cathodic potential led to the formation of the lowest amount of acetic acid, if compared to the other two potentials, thus suggesting the decreased activity of the catalytic sites for the CO dimerization.

Therefore, with the aim of better understanding if the different reaction mechanisms originate from changes in the chemical composition of the catalytic layer or from different adsorbed intermediates on its surface, several electrocatalytic tests were carried out while performing *Operando* Surface Enhanced Raman spectroscopy (SERS).

5.3.3 Operando Studies of the CO_2 Electroreduction Reaction

SERS analyses were performed on the surface of the electrocatalyst during several electrochemical CO_2 reduction reactions carried out in liquid phase. The main purpose of these studies was to investigate the existence of relation between the variations of the chemical composition of the catalytic surface, once the potential has been applied, and the changed selectivity towards liquid products.

Since the copper oxides species and the hydrotalcite structures have substantial Raman shifts between 100 and 1200 cm^{-1} [39–41], Raman spectra were recorded at the different applied potentials (*vs* RHE) in this range (Figure 5.9).

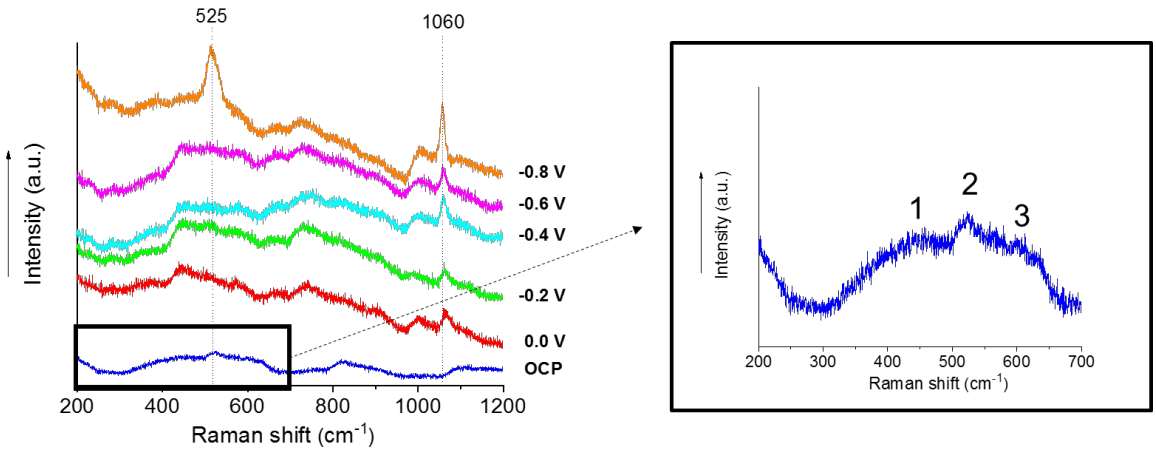

Figure 5.9. *Operando* Raman spectra recorded on the CuMgAl LDH/Au during CO_2ER at different applied potentials

The spectra revealed the presence of a peak at 1060 cm^{-1} as soon as the potential was applied. In fact, except for the spectrum recorded at the open circuit potential (*i.e.*, +0.6 V *vs* RHE) which is the equilibrium potential that the working electrode spontaneously assumes once it has been immersed into the electrolyte, it was always possible to observe that peak, which is consistent with the presence of adsorbed CO_3^{2-} species at the surface of the electrocatalyst [42,43]. Since it was not possible to point out the peak related to the presence of HCO_3^-, which was supposed to be around 1012-1020 cm^{-1} [44,45], it may be assumed that the pH at the electrode-electrolyte interface, as soon as 0 V was applied, reached very alkaline values.

Moreover, it is worth noting that no peak related to the intercalated NO_3^- anions inside the LDH structure (1050 cm^{-1} [30,46]) was observed at the OCP potential. Besides, referring to the OCP spectrum, it can be observed a wide group of peaks at very low Raman shifts which are consistent with the presence of Cu_2O (1 – 450 cm^{-1}; 2 – 523 cm^{-1}; 3 – 610 cm^{-1}) [16,42,47] at the surface of the electrocatalyst. Such an evidence confirmed a similar chemical composition of the catalyst both on gold and carbonaceous supports. Surprisingly, upon application of the most cathodic potential (-0.8 V), the peak at 525 cm^{-1} prevailed over the others.

In such conditions the formic acid formation starts to increase (Figure 5.7), as well as the selectivity for this product (Figure 5.8c) and that suggests the presence of a copper species that favours its production. According to the literature, the Raman peak at 525 cm^{-1} may not only be indicative of the cuprite but also of "cathodically" formed $CuO_x/Cu(OH)_y$ species [42,48,49]. The high intensity of this peak related to the prevalence of formic acid in the reaction outcomes led to hypothesise a connection between the two data. Moreover, the presence of such a peak, slightly evident from the beginning (OCP), may justify the presence of formic acid even at low applied potentials, albeit in much smaller quantities.

In order to support this hypothesis and verify if the production of formic acid was related to the prevalence of the peak at 525 cm^{-1}, SERS analyses were carried out during a kinetic study at fixed potential. In particular, -0.4 V was chosen as the most representative value since a change in the selectivity from acetic to formic acid was observed at the end of the reaction. Moreover, even if the selectivity towards formic acid was predominant at -0.8 V and thus it was supposed to be easier to identify the aforementioned peak, it was not possible to achieve good Raman spectra at this potential due to the strong H_2 evolution that constantly caused focus losses.

Figure 5.10 shows the recorded spectra at different reaction steps and they were divided in dependence on the Raman shift range for the sake of clarity.

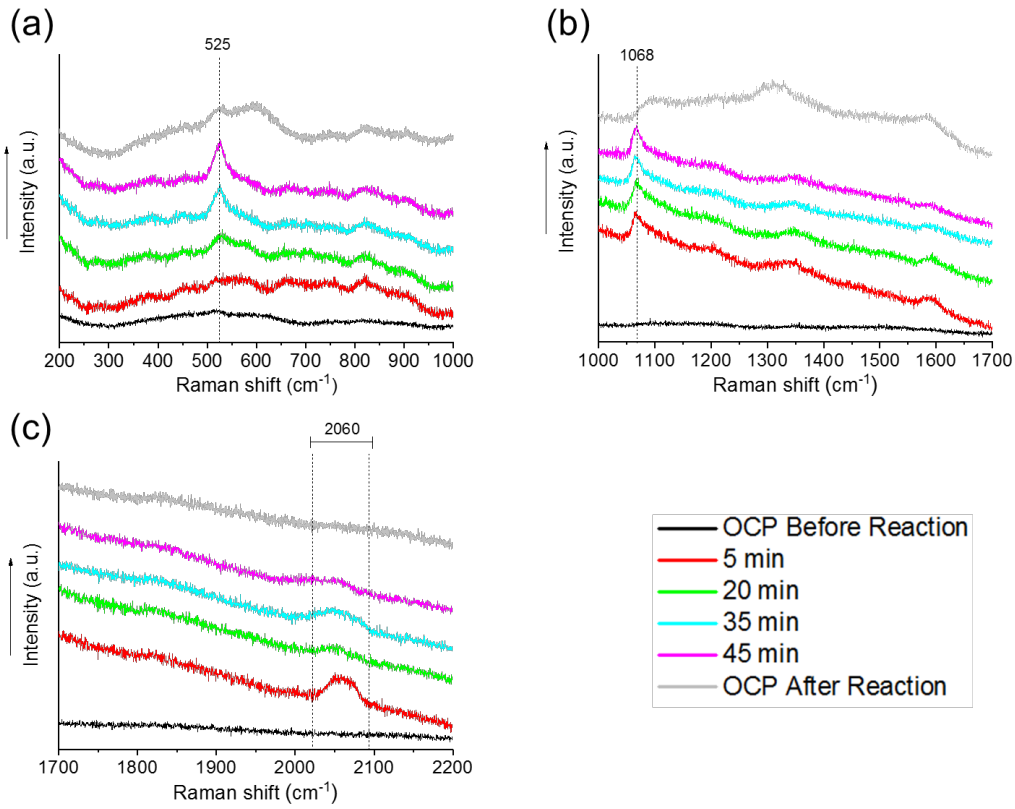

Figure 5.10. *Operando* Surface Enhance Raman spectra recorded on the CuMgAl LDH/Au during CO_2ER at -0.4 V *vs* RHE, 1h reaction

As a result, Figure 5.10a clearly highlights the growth of the peak at 525 cm^{-1} which disappeared as soon as the reaction was turned off. The peak started to grow after 20 min of reaction and kept increasing with time. Comparing this result with the quantitative kinetic study at -0.4 V for 1h, it is worth noting that the production of formic acid started to increase after 45 min of reaction, finally outpacing the production of acetic acid. This experimental evidence is also consistent with the spectra recorded in different reduction conditions (Figure 5.9) and it supports that the $CuO_x/Cu(OH)_y$ species may be involved in the production of formic acid. Interestingly, once the system returned to the OCP, that was similar to the one recorded at the beginning of the experiment, the peak related to the $CuO_x/Cu(OH)_y$ species decreased, displaying the same intensity of the initial condition.

This trend suggested the reversible nature of the production of such species, which is favoured upon application of more cathodic potentials, otherwise less predominant, highlighting their *in situ* formation.

Besides, Figure 5.10b shows the constant contribution of the carbonate anions adsorbed on the surface. However, the peak disappeared once the reaction was turned off, thus suggesting the restored bulk pH (~7.1) next to the surface of the electrode. This behaviour is consistent with the studies reported in the state of the art, confirming the local pH variation towards an alkaline environment as soon as the CO_2ER and HER evolved [50].

Moreover, it has been evaluated the presence of *CO on the surface of the electrocatalyst which is supposed to be fundamental for the CO_2 reduction development [51,52]. Figure 5.10c reports a wide Raman shift around 2060 cm^{-1} which can be assigned to the adsorption of *CO on the atop sites of the catalytic layer [42]. Recently, it has been demonstrated that the atop-bound *CO favoured the development of the CO_2ER, otherwise blocked by the inert bridged-bounded *CO [18]. Moreover, the two types of bonds are preferentially formed in alkaline pH. Interestingly, its Raman contribution was higher at the beginning of the reaction and then it slowly decreased, following the same trend displayed by the acetic acid during the test of the catalytic activity. Hence, it can be hypothesised that the coexistence of different factors such as (i) the prevalence of cuprite species at low applied potentials, (ii) the presence of *CO species adsorbed on the surface with active bounds, and (iii) an alkaline local pH, confirmed by the presence of CO_3^{2-}, likely promote the C-C coupling and thus favour the formation of CH_3COOH instead of formic acid. On the opposite, during the course of the reaction, the catalytic layer underwent a change in the chemical composition, which decreased the active sites suitable for the C-C coupling in favour of species which prefer the C_1 pathway. Hence, considering these experimental evidences, the formation of formic and acetic acid seems to follow two different competing

reaction pathways which are favoured by different catalytic active sites and the hypothesis of the formation of acetic acid derived from the earlier formic acid production can be excluded.

A final *operando* study was performed upon application of 0 V *vs* RHE (Figure 5.11), at which the catalytic activities displayed a selectivity towards acetic acid for the whole reaction time as formic acid always remained as a secondary product. This latest test was not only aimed to corroborate the idea of the two reaction routes but also to verify if the products even at very low cathodic potentials were the same as those detected at -0.4 V *vs* RHE, or they came from another reaction route independent from the application of a specific potential [36].

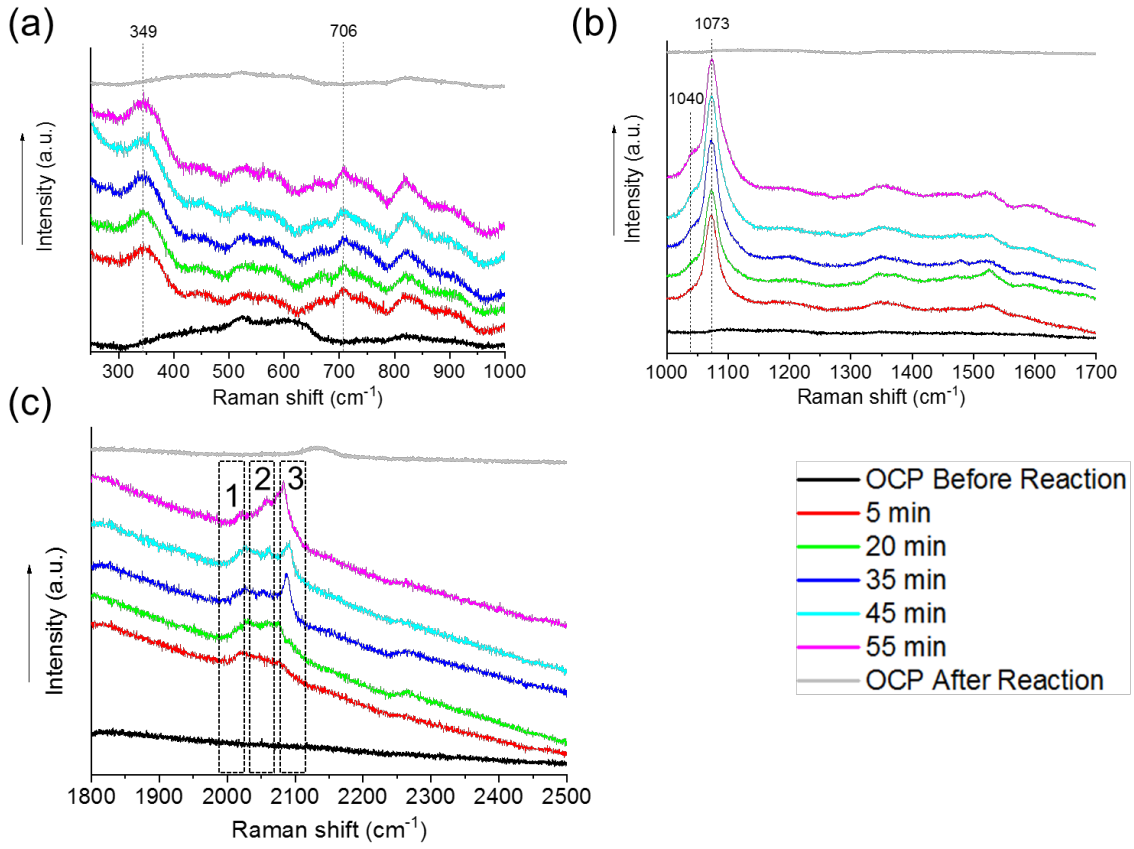

Figure 5.11. *Operando* Surface Enhance Raman spectra recorded on the CuMgAl LDH/Au during CO_2ER at 0 V *vs* RHE, 1h reaction

Figure 5.11a displays the spectra recorded between 250 and 1000 cm^{-1}. The OCP spectrum evidences the presence of the Cu_2O species (black line); the intensity of this broad group of peaks decreased as time passed and, at the same time, an increase of a peak at 349 cm^{-1} was pointed out. Such a peak was not evident in the preliminary study reported in Figure 5.9; however, it is not easy to identify its nature. Several studies have reported different interpretations. Chernyshova *et al.* [53] investigated and confirmed the presence of carboxylate species ($*CO_2^-$) adsorbed on the surface of a Cu electrode during the CO_2ER by SERS analyses, on the basis of the peak at ~350 cm^{-1} which was assigned to the vibrational fingerprints of η^2(C, O)-CO_2^-. However, such a peak was coupled with a shift at 1540 cm^{-1} which is not evident from our spectra recorded at 0 V. Further studies attributed this peak to the vibrational stretching of Cu-CO [54–56], which is, however, present when the operative potential is more cathodic potentials. On the opposite, Zhan *et al.* [16] carried out systematic studies in order to assign the peak around 350-360 cm^{-1} excluding indeed the possibility that it can be attributed to the Cu-CO stretching. In fact, they found out its independence from the CO_2 dissolved in the electrolyte and assigned the peak to the presence of surface Cu carbonate species formed during the reduction of copper oxide in the presence of $KHCO_3$. Moreover, they observed the simultaneous presence of the peak around 706 cm^{-1}, when the potential window was from +0.3 V to 0 V *vs* RHE, which was assigned to hydroxyl species adsorbed at the copper surface (Cu-OH) [57]. However, assigning the last cited peak when the catalyst is a LDH containing Cu can be difficult due to the nature of the material itself since it consists in abundant hydroxyl species coordinated to the cations that could be somehow more evident once the potential is applied. For these reasons, further investigations will be necessary to clearly define the real nature of both peaks (349 and 706 cm^{-1}). No peak around 525 cm^{-1} was recorded, thus confirming that in order to form $CuO_x/Cu(OH)_y$ species a reaction time long enough and a sufficiently cathodic

potential were needed. Therefore, it could be assumed that the cuprite species remained stable upon application of 0 V *vs* RHE for the entire duration of the reaction.

Another interesting point is the peak related to the carbonate species at 1073 cm^{-1} (Figure 5.11b). Contrarily to the spectra recorded at -0.4 V, the intensity of this peak was high as soon as 0 V was applied. However, in this case, it was possible to observe a shoulder at around 1040 cm^{-1},which increases in intensity over time and it can be referred to a different carbonate adsorption site which is generally formed at a less cathodic potential [26]. Since this shoulder was not present at -0.4 V, it can be hypothesised that at that potential the adsorbed carbonate species can be somehow activated and directly participate to the CO_2 reduction processes. This theory led to assume that the productivity of acetic and formic acid at -0.4 V was not only related to the presence of *CO but also CO_3^{2-} could likely play an important role. Contrarily, when the applied potential was 0 V, the adsorbed carbonates species showed much more intense absorptions, and this result could suggest that they are not directly involved in the reaction as occurred at -0.4 V.

Indeed, moving to higher Raman shifts, the recorded spectra revealed the coexistence of *CO (Figure 5.11c), together with CO_3^{2-}. Contrarily to the previous study (Figure 5.10c), the signal related to the carbon monoxide adsorbed on the electrocatalyst surface fell in the range from 2000 to 2100 cm^{-1} and it included different peaks. The presence of *CO species at 0 V *vs* RHE was also reported by the group of Prof. Cuenya [16]. In particular, three regions can be distinguished and they have been assigned in a previous study [42]. On the one hand, the broad peak in position 1 recorded near 1900-2000 cm^{-1} is consistent with the presence of bridged *CO species, while, on the other hand, both peaks between 2000 and 2100 cm^{-1} belonged to the atop site *CO species, both formed in alkaline conditions, as stated before [18]. Moreover, if adsorbed over nanostructured Cu catalysts, the peak of the atop site *CO species splits into a high-frequency band (HFB) and low frequency band (LFB) [43].

However, the presence of bridged or atop site *CO species at a very low cathodic potential is unusual, and thus it is not possible to determine which of the three species (bridged, atop HFB, and atop LFB *CO species) is the most active towards the CO_2 reduction reaction. Nevertheless, *CO species adsorbed on the surface along with the cuprite species that remained stable during the entire reaction, is consistent with the predominance of acetic acid production, and in line with the results achieved by the *operando* studies at -0.4 V *vs* RHE.

Therefore, by comparing the results achieved from the *operando* studies and from the catalytic tests carried out at constant potential, it can be hypothesised that the formation of acetic acid was favoured until the cuprite species (Cu^+) was predominant on the surface of the catalyst. Moreover, it preferentially derived from *CO at 0 V *vs* RHE and from both $*CO_3^{2-}$ and *CO while applying -0.4 V *vs* RHE. Indeed, a possible activation of the carbonate species can be attributed to the low Raman intensity recorded as a function of the applied cathodically increasing potential. Although this hypothesis is in contrast with the generally accepted idea that HCO_3^- and CO_3^{2-} are not suitable reactants for CO_2ER [58], the data here provided suggested their probable contribution at more cathodic potentials. However, since the amount of active carbon species, *i.e.,* *CO and $*CO_3^{2-}$, was supposed to be higher at -0.4 V, a higher production of the C_2 compound would have been expected. In fact, a decrease of the acetic acid production was observed with time. Such a trend was mainly attributed to the growth of the peak at 525 cm^{-1}, which was previously demonstrated to be consistent with the selectivity towards formic acid.

Interestingly, no Raman peak confirming the possible involvement of Mg or Al was detected, thus suggesting their inert nature to the electrocatalytic process.

Later, with the aim of better evaluating the role of the Au support and carbonates in the CO_2 reduction process, several reactions at different applied potentials were performed and compared with the aforementioned achieved results.

5.3.4 The Role of the Substrate

The electrochemical CO_2 reduction reactions were carried out inside the H-type cell, likewise the other tests on the catalytic performances, using bare gold electrodes immersed into a blank solution consisting in 0.3 M KNO_3 under Ar bubbling or a standard solution employing 0.3 M $KHCO_3$ and CO_2. Potentials screening from 0 to -1.2 V *vs* RHE was performed, applying each potential for 10 min, consecutively.

In the absence of any Cu-containing catalyst, no liquid products were detected during the blank reaction, while the formation of formic acid was observed upon application of a potential equal to -0.8 V or more cathodic. Therefore, if the support is made of gold none of C_2 products are obtained.

These experimental evidences revealed that the acetic acid among the CO_2 reduction outcomes is strictly dependent on the CuMgAl LDH catalyst that is capable not only to promote the C-C coupling but also to induce the C_1 pathway at lower cathodic applied potentials, as evidenced by the formic acid production.

5.3.5 Electrocatalytic Tests with Different Carbon Sources

Finally, a preliminary estimation of the carbon species involved in the CO_2 electroreduction process was carried out with the aim of understanding the role of both carbonates species and LDH structure. In particular, the dependence of the quantity of reduction products on the presence of a CO_2 flux was initially investigated. A blank reaction was carried out with no direct carbon sources and with the nitrate as the LDH interlayer anion, and another reaction

was performed with the same electrocatalyst, but in presence of a CO_2 flux. Similarly to the previous tests, a screening of potentials was carried out in the range from 0 to -1.2 V *vs* RHE, applying each potential (0.2 V increment) for 10 min.

The catalytic performances are displayed in Figure 5.12.

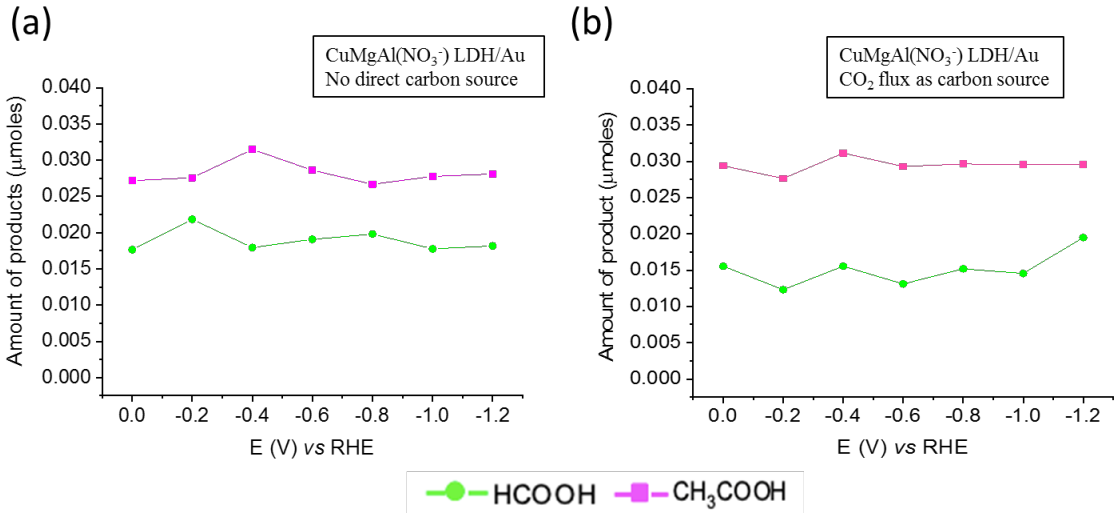

Figure 5.12. CO_2ER performances employing CuMgAl(NO_3^-) LDH/Au in 0.3 M KNO_3 with (a) no direct carbon sources – Ar flux and (b) gaseous carbon source – CO_2 flux

The achieved results by employing the two experimental conditions were unusual and did not follow the trend displayed by the reaction performed in standard conditions (Figure 5.7). In particular, acetic acid remained the main product regardless of the applied potential. To this regard, it can be hypothesised that the different electrolyte, which could not act as buffer, led to a tremendous increase of the local pH at the electrolyte-electrode interface, which likely favoured the production of C_2 products, as already mentioned. Moreover, a different pH might cause different species to form upon application of a specific potential, but no *operando* studies were carried out to validate this hypothesis. Besides, it is worth noting that, even in absence of a direct carbon source, it was possible to detect the usual reduction products in quantities comparable to those achieved with a CO_2 flux. Indeed, since no carbon sources had been introduced inside the cell, no products containing carbon were expected.

The only way carbon could have been in contact with the electrocatalyst was thanks to the affinity of the LDH for CO_2. To verify this idea, X-ray diffraction analysis was performed on the LDH just synthesised and after the reaction in KNO_3 under Ar, in order to investigate if the atmospheric carbon dioxide had entered the structure of the hydrotalcite.

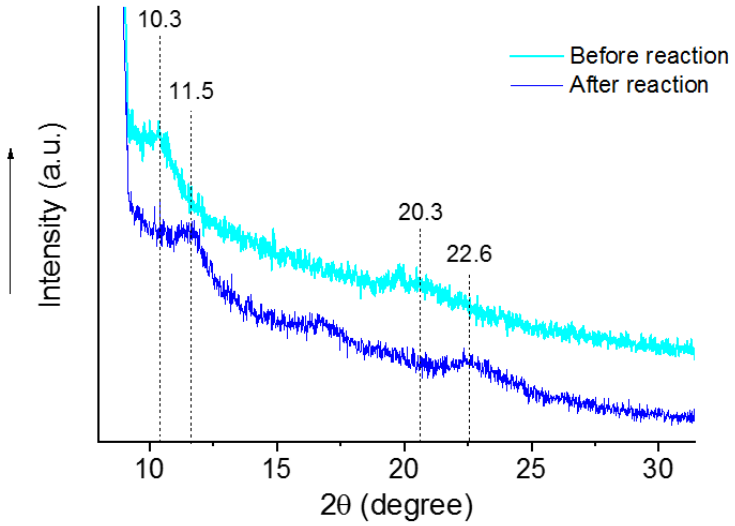

Figure 5.13. X-ray diffraction patterns of CuMgAl LDH/Au before and after CO_2ER in 0.3 M KNO_3 with Ar bubbling

Surprisingly, after the reaction with no carbon sources, a shift in the diffraction pattern concerning the LDH structure was observed (Figure 5.13). In particular, the reflections at 10.3° and 20.3° (2θ) indexed as (003) and (006) reflections, respectively, typical of the intercalated nitrate anions [29,35], shifted towards higher angles, assuming the values ascribable to the carbonate anions [33]. This experimental evidence demonstrated that the LDH structure already contained carbonates species before the reduction reaction, and such anions have promoted the production of the target liquid products. Hence, the presence of a CO_2 flux did not affect significantly the reaction outcome in terms of productivity, thus suggesting that, for 1h reaction at least, the carbonates species adsorbed by the LDH mainly promoted the formation of acetic and formic acids, regardless of the continuous feed of CO_2.

Moreover, assuming that the carbonates species adsorbed on the electrocatalyst, two more CO_2 reduction reactions were carried out starting from the Cu-containing LDH catalysts where CO_3^{2-} have been intercalated inside the layered structure prior the reaction. To this aim two pristine CuMgAl (NO_3^-) LDH/Au were immersed for 2h in 0.3 M $KHCO_3$ and K_2CO_3 solutions, respectively, and the effective intercalation of carbonates species was investigated through X-ray diffraction analyses (Figure 5.14).

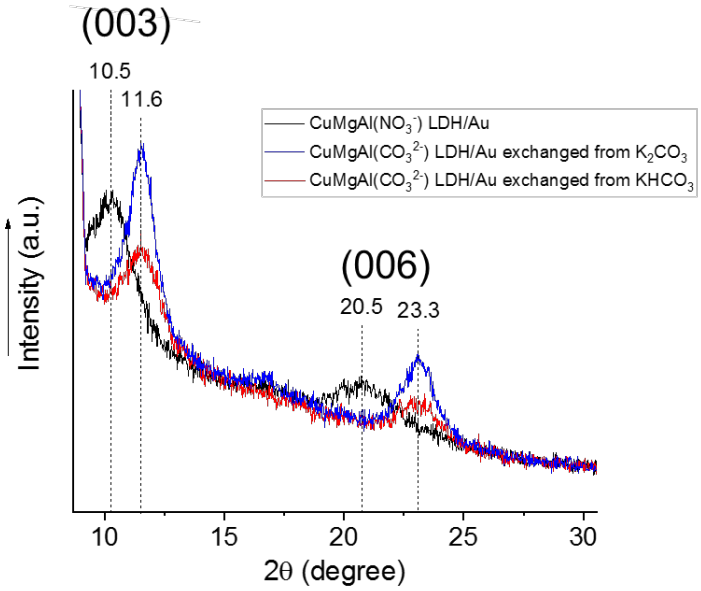

Figure 5.14. X-ray diffraction patterns of CuMgAl(NO_3^-) LDH/Au (black line), CuMgAl(CO_3^{2-}) LDH/Au kept in K_2CO_3 solution (blue line) and CuMgAl(CO_3^{2-}) LDH/Au kept in $KHCO_3$ solution (red line)

In both cases, the reflections attributable to the LDH structure display the typical angles of the carbonates-based hydrotalcites. Moreover, the efficient exchange of nitrate with carbonate was confirmed by the shifts of the d-spacing obtained from the reflection (003), moving from 8.5 to 7.6 $\dot{A}$ [33]. The catalytic performances were evaluated following the same experimental conditions previously employed, avoiding the presence of carbonates inside the electrolyte.

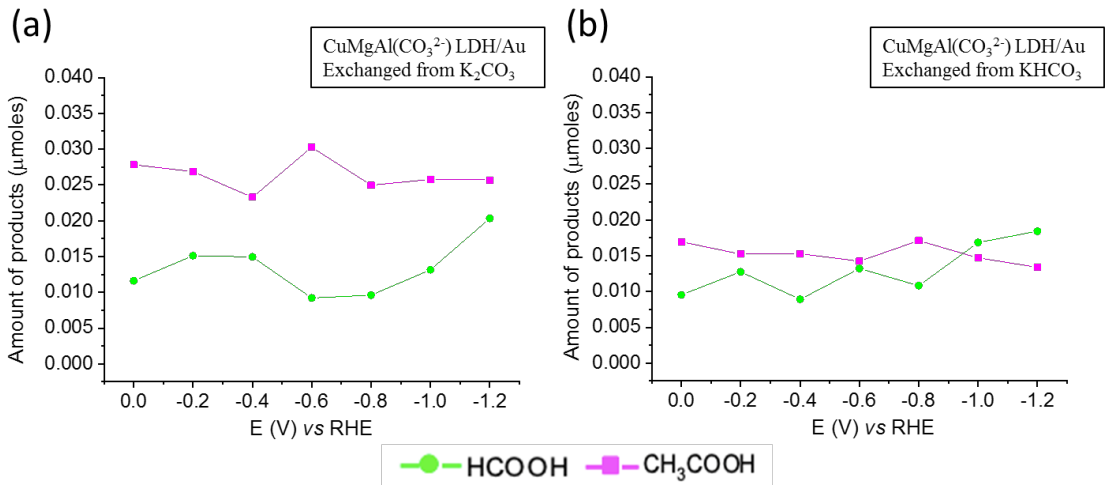

Figure 5.15. Catalytic performances at different applied potentials referred to (a) CuMgAl(CO_3^{2-}) LDH/Au exchanged from K_2CO_3 and (b) CuMgAl(CO_3^{2-}) LDH/Au exchanged from $KHCO_3$

Figures 5.15a and b display the catalytic performances of the LDHs where nitrate anions have been exchanged with carbonate and bicarbonate, respectively. The performances are higher in the presence of carbonate. Such a result suggests that higher is the amount of exchanged carbonates, the more favoured the production of acetic acid is. In fact, it is reasonable to think that performing the exchange in $KHCO_3$, an equilibrium between HCO_3^- and CO_3^{2-} may establish due to the basic nature of the LDH, but the conversion to carbonates is not total. Unfortunately, it was not possible to detect additional carbonaceous species absorbed on the LDH surface (*e.g.*, CO species) that could act as active species together with carbonates, as assumed during the *operando* analyses.

For this reason, further investigations are necessary to clearly define the carbonaceous species that take an active part in the reduction process.

5.4 Conclusions

In this work a preliminary investigation of the possible reaction mechanism involved in the electrochemical CO_2 reduction performed on CuMgAl 2: 1: 1 LDH/Au electrocatalysts was carried out by means of *in situ* and *operando* techniques. Initially, the possibility to electrochemically synthesise ternary CuMgAl LDHs on gold supports was successfully demonstrated, with the same chemical composition as those electrodeposited on the carbonaceous membrane. Indeed, by adapting the potentiodynamic method to the different experimental condition *i.e.,* different support and reference electrodes, X-ray diffraction and SEM-EDS analyses, along with electrochemical studies, revealed the presence of a ternary LDH with additional copper species whose morphological structure was not clearly defined. The optimised electrocatalyst was tested during CO_2ER in liquid phase, performing both potentials screening and kinetic studies at fixed potentials. As a result, the *in situ* H^1-NMR analyses performed on the electrolyte-electrode interface revealed the presence of acetic and formic acid in substantial amount. In particular, acetic acid was the majority product upon application of low cathodic potentials, while the production of formic acid started to increase at potentials more cathodic than -0.8 V *vs* RHE. Moreover, kinetic studies revealed that at 0 and -0.8 V the selectivity towards acetic and formic acid, respectively, was constant during 1h reaction, while at -0.4 V the selectivity changed after 50 min. The reasons why the selectivity underwent those changes was investigated by *Operando* Surface Enhance Raman Spectroscopy. On one hand, it was observed that upon application of a low cathodic potential, *i.e.*, 0 V, the catalytic layer showed the presence of cuprite species along with adsorbed *CO in several configurations. Thanks to the high local pH attributable to the intense carbonates peak, it can be assumed that the *CO species, present in higher amount, represented the active intermediate towards the formation of C-C coupling, thus resulting in a higher production of acetic acid.

Moreover, such a product was preferentially formed in the presence of Cu^{+}/Cu^{0} species. On the other hand, when -0.4 V was chosen as fixed potential, the selectivity changed during the reaction occurrence from acetic to formic acid, that was consistent with the growth of a specific peak likely due to the formation of $CuO_x/Cu(OH)_2$ species. Hence, while the acetic acid was favoured at low cathodic potential and in the presence of *CO and cuprite species, formic acid was preferentially formed with the activation of carbonates and *CO in the presence of the new cathodically produced species, $CuO_x/Cu(OH)_y$. However, the presence of formic acid detected at low cathodic potentials confirmed that in order to obtain a higher selectivity towards C_2 products, a specific species of copper has to outpace the others, *e.g.*, cuprite species over $CuO_x/Cu(OH)_y$.

Due to their non-redox active nature, it was confirmed that Mg and Al cations do not participate in the activation, as well as in further reduction processes, since no effects due to their presence were observed during the *operando* analyses. Moreover, it has been preliminarily demonstrated that the carbonates may have a major role in the formation of the reduction products, even in absence of a direct carbon source. This experimental evidence, together with the *operando* analyses, suggested the high potential of the electrochemically synthesised CuMgAl LDHs to be used as natural CO_2 absorbers capable to promote its reduction by means of copper species, once the carbon dioxide has been incorporated inside the structure.

5.5 References

(1) Adarsh, K. S.; Chandrasekaran, N.; Chakrapani, V. In-Situ Spectroscopic Techniques as Critical Evaluation Tools for Electrochemical Carbon Dioxide Reduction: A Mini Review. *Front. Chem.* **2020**, *8*, 1–9.

(2) Yang, Y.; Xiong, Y.; Zeng, R.; Lu, X.; Krumov, M.; Huang, X.; Xu, W.; Wang, H.; DiSalvo, F. J.; Brock, J. D.; Muller, D. A.; Abruña, H. D. Operando Methods in Electrocatalysis. *ACS Catal.* **2021**, *11* (3), 1136–1178.

(3) Popović, S.; Smiljanić, M.; Jovanovič, P.; Vavra, J.; Buonsanti, R.; Hodnik, N. Stability and Degradation Mechanisms of Copper-Based Catalysts for Electrochemical CO_2 Reduction. *Angew. Chemie Int. Ed.* **2020**, *59* (35), 14736–14746.

(4) Zhu, S.; Li, T.; Cai, W.-B.; Shao, M. CO_2 Electrochemical Reduction As Probed through Infrared Spectroscopy. *ACS Energy Lett.* **2019**, *4* (3), 682–689.

(5) Kim, D.; Kley, C. S.; Li, Y.; Yang, P. Copper Nanoparticle Ensembles for Selective Electroreduction of CO_2 to C_2–C_3 Products. *Proc. Natl. Acad. Sci.* **2017**, *114* (40), 10560–10565.

(6) Dattila, F.; García-Muelas, R.; López, N. Active and Selective Ensembles in Oxide-Derived Copper Catalysts for CO_2 Reduction. *ACS Energy Lett.* **2020**, *5* (10), 3176–3184.

(7) Yang, Y.; Roh, I.; Louisia, S.; Chen, C.; Jin, J.; Yu, S.; Salmeron, M. B.; Wang, C.; Yang, P. Operando Resonant Soft X-Ray Scattering Studies of Chemical Environment and Interparticle Dynamics of Cu Nanocatalysts for CO_2 Electroreduction. *J. Am. Chem. Soc.* **2022**, *144* (20), 8927–8931.

(8) Bernal, M.; Bagger, A.; Scholten, F.; Sinev, I.; Bergmann, A.; Ahmadi, M.; Rossmeisl, J.; Cuenya, B. R. CO_2 Electroreduction on Copper-Cobalt Nanoparticles: Size and Composition Effect. *Nano Energy* **2018**, *53*, 27–36.

(9) Gao, J.; Zhang, H.; Guo, X.; Luo, J.; Zakeeruddin, S. M.; Ren, D.; Grätzel, M. Selective C–C Coupling in Carbon Dioxide Electroreduction via Efficient Spillover of Intermediates As Supported by Operando Raman Spectroscopy. *J. Am. Chem. Soc.* **2019**, *141* (47), 18704–18714.

(10) Quan, W.; Lin, Y.; Luo, Y.; Huang, Y. Electrochemical CO_2 Reduction on Cu: Synthesis-Controlled Structure Preference and Selectivity. *Adv. Sci.* **2021**, *8* (23), 1–22.

(11) Yang, K. D.; Lee, C. W.; Jin, K.; Im, S. W.; Nam, K. T. Current Status and Bioinspired Perspective of Electrochemical Conversion of CO_2 to a Long-Chain Hydrocarbon. *J. Phys. Chem. Lett.* **2017**, *8* (2), 538–545.

(12) Luo, W.; Nie, X.; Janik, M. J.; Asthagiri, A. Facet Dependence of CO_2 Reduction Paths on Cu Electrodes. *ACS Catal.* **2016**, *6* (1), 219–229.

(13) Pérez-Gallent, E.; Figueiredo, M. C.; Calle-Vallejo, F.; Koper, M. T. M. Spectroscopic Observation of a Hydrogenated CO Dimer Intermediate During CO Reduction on Cu(100) Electrodes. *Angew. Chemie Int. Ed.* **2017**, *56* (13), 3621–3624.

(14) Gunathunge, C. M.; Li, X.; Li, J.; Hicks, R. P.; Ovalle, V. J.; Waegele, M. M. Spectroscopic Observation of Reversible Surface Reconstruction of Copper Electrodes under CO_2 Reduction. *J. Phys. Chem. C* **2017**, *121* (22), 12337–12344.

(15) Nitopi, S.; Bertheussen, E.; Scott, S. B.; Liu, X.; Engstfeld, A. K.; Horch, S.; Seger, B.; Stephens, I. E. L.; Chan, K.; Hahn, C.; Nørskov, J. K.; Jaramillo, T. F.; Chorkendorff, I. Progress and Perspectives of Electrochemical CO_2 Reduction on Copper in Aqueous Electrolyte. *Chem. Rev.* **2019**, *119* (12), 7610–7672.

(16) Zhan, C.; Dattila, F.; Rettenmaier, C.; Bergmann, A.; Kühl, S.; García-Muelas, R.; López, N.; Cuenya, B. R. Revealing the CO Coverage-Driven C–C Coupling Mechanism for Electrochemical CO_2 Reduction on Cu_2O Nanocubes via Operando Raman Spectroscopy. *ACS Catal.* **2021**, *11* (13), 7694–7701.

(17) Moradzaman, M.; Mul, G. Optimizing CO Coverage on Rough Copper Electrodes: Effect of the Partial Pressure of CO and Electrolyte Anions (pH) on Selectivity toward Ethylene. *J. Phys. Chem. C* **2021**, *125* (12), 6546–6554.

(18) Gunathunge, C. M.; Ovalle, V. J.; Li, Y.; Janik, M. J.; Waegele, M. M. Existence of an Electrochemically Inert CO Population on Cu Electrodes in Alkaline pH. *ACS Catal.* **2018**, *8* (8), 7507–7516.

(19) Morrison, A. R. T.; Ramdin, M.; van der Broeke, L. J. P.; de Jong, W.; Vlugt, T. J. H.; Kortlever, R. Surface Coverage as an Important Parameter for Predicting Selectivity Trends in Electrochemical CO_2 Reduction. *J. Phys. Chem. C* **2022**, *126* (29), 11927–11936.

(20) Mistry, H.; Varela, A. S.; Bonifacio, C. S.; Zegkinoglou, I.; Sinev, I.; Choi, Y.-W.; Kisslinger, K.; Stach, E. A.; Yang, J. C.; Strasser, P.; Cuenya, B. R. Highly Selective Plasma-Activated Copper Catalysts for Carbon Dioxide Reduction to Ethylene. *Nat. Commun.* **2016**, *7* (1), 1–9.

(21) Eilert, A.; Cavalca, F.; Roberts, F. S.; Osterwalder, J.; Liu, C.; Favaro, M.; Crumlin, E. J.; Ogasawara, H.; Friebel, D.; Pettersson, L. G. M.; Nilsson, A. Subsurface Oxygen in Oxide-Derived Copper Electrocatalysts for Carbon Dioxide Reduction. *J. Phys. Chem. Lett.* **2017**, *8* (1), 285–290.

(22) Ren, D.; Wong, N. T.; Handoko, A. D.; Huang, Y.; Yeo, B. S. Mechanistic Insights into the Enhanced Activity and Stability of Agglomerated Cu Nanocrystals for the Electrochemical Reduction of Carbon Dioxide to n -Propanol. *J. Phys. Chem. Lett.* **2016**, *7* (1), 20–24.

(23) Kwon, Y.; Lum, Y.; Clark, E. L.; Ager, J. W.; Bell, A. T. CO_2 Electroreduction with Enhanced Ethylene and Ethanol Selectivity by Nanostructuring Polycrystalline Copper. *ChemElectroChem* **2016**, *3* (6), 1012–1019.

(24) Luo, R.; Popp, J.; Bocklitz, T. Deep Learning for Raman Spectroscopy: A Review. *Analytica* **2022**, *3* (3), 287–301.

(25) Flores, E.; Novák, P.; Berg, E. J. In Situ and Operando Raman Spectroscopy of Layered Transition Metal Oxides for Li-Ion Battery Cathodes. *Front. Energy Res.* **2018**, *6*, 1–6.

(26) Jiang, S.; Klingan, K.; Pasquini, C.; Dau, H. New Aspects of Operando Raman Spectroscopy Applied to Electrochemical CO_2 Reduction on Cu Foams. *J. Chem. Phys.* **2019**, *150* (4), 1–12.

(27) Lai, S. C. S.; Kleyn, S. E. F.; Rosca, V.; Koper, M. T. M. Mechanism of the Dissociation and Electrooxidation of Ethanol and Acetaldehyde on Platinum As Studied by SERS. *J. Phys. Chem. C* **2008**, *112* (48), 19080–19087.

(28) Gualandi, I.; Vlamidis, Y.; Mazzei, L.; Musella, E.; Giorgetti, M.; Christian, M.; Morandi, V.; Scavetta, E.; Tonelli, D. Ni/Al Layered Double Hydroxide and Carbon Nanomaterial Composites for Glucose Sensing. *ACS Appl. Nano Mater.* **2019**, *2* (1), 143–155.

(29) Musella, E.; Gualandi, I.; Scavetta, E.; Rivalta, A.; Venuti, E.; Christian, M.; Morandi, V.; Mullaliu, A.; Giorgetti, M.; Tonelli, D. Newly Developed Electrochemical Synthesis of Co-Based Layered Double Hydroxides: Toward Noble Metal-Free Electro-Catalysis. *J. Mater. Chem. A* **2019**, *7* (18), 11241–11249.

(30) Musella, E.; Gualandi, I.; Giorgetti, M.; Scavetta, E.; Basile, F.; Rivalta, A.; Venuti, E.; Corticelli, F.; Christian, M.; Morandi, V.; Tonelli, D. Electrosynthesis and Characterization of Layered Double Hydroxides on Different Supports. *Appl. Clay Sci.* **2021**, *202*, 1–12.

(31) Białostocka, A. M.; Klekotka, U.; Kalska-Szostko, B. The Effect of a Substrate Material on Composition Gradients of Fe-Ni Films Obtained by Electrodeposition. *Sci. Rep.* **2020**, *10* (1), 1–8.

(32) Giri, S. D.; Sarkar, A. Electrochemical Study of Bulk and Monolayer Copper in Alkaline Solution. *J. Electrochem. Soc.* **2016**, *163* (3), H252–H259.

(33) Cavani, F.; Trifirò, F.; Vaccari, A. Hydrotalcite-Type Anionic Clays: Preparation, Properties and Applications. *Catal. Today* **1991**, *11* (2), 173–301.

(34) Couderc, J. J.; Garingue, G.; Lafourcade, L.; Nguyen, Q. T. Standard X-Ray Diffraction Powder Patterns. *Zeitschrift fur Met.* **1959**, *50*, 708–716.

(35) Musella, E.; Gualandi, I.; Scavetta, E.; Gazzano, M.; Rivalta, A.; Venuti, E.; Christian, M.; Morandi, V.; Tonelli, D. Electrochemical Approach for the Production of Layered Double Hydroxides with a Well-Defined Co/Me^{III} Ratio. *Chem. – A Eur. J.* **2019**, *25* (71), 16301–16310.

(36) Birdja, Y. Y.; Koper, M. T. M. The Importance of Cannizzaro-Type Reactions during Electrocatalytic Reduction of Carbon Dioxide. *J. Am. Chem. Soc.* **2017**, *139* (5), 2030–2034.

(37) Schouten, K. J. P.; Kwon, Y.; van der Ham, C. J. M.; Qin, Z.; Koper, M. T. M. A New Mechanism for the Selectivity to C_1 and C_2 Species in the Electrochemical Reduction of Carbon Dioxide on Copper Electrodes. *Chem. Sci.* **2011**, *2* (10), 1902–1909.

(38) Handoko, A. D.; Wei, F.; Jenndy; Yeo, B. S.; Seh, Z. W. Understanding Heterogeneous Electrocatalytic Carbon Dioxide Reduction through Operando Techniques. *Nat. Catal.* **2018**, *1* (12), 922–934.

(39) Kloprogge, J. T.; Wharton, D.; Hickey, L.; Frost, R. L. Infrared and Raman Study of Interlayer Anions CO_3^{2-} , NO_3^- , SO_4^{2-} and ClO_4^- in Mg/Al-Hydrotalcite. *Am. Mineral.* **2002**, *87* (5–6), 623–629.

(40) Deng, Y.; Handoko, A. D.; Du, Y.; Xi, S.; Yeo, B. S. In Situ Raman Spectroscopy of Copper and Copper Oxide Surfaces during Electrochemical Oxygen Evolution Reaction: Identification of Cu^{III} Oxides as Catalytically Active Species. *ACS Catal.* **2016**, *6* (4), 2473–2481.

(41) Mora, M.; Jiménez-Sanchidrián, C.; Rafael Ruiz, J. Raman Spectroscopy Study of Layered-Double Hydroxides Containing Magnesium and Trivalent Metals. *Mater. Lett.* **2014**, *120*, 193–195.

(42) Li, H.; Wei, P.; Gao, D.; Wang, G. In Situ Raman Spectroscopy Studies for Electrochemical CO_2 Reduction over Cu Catalysts. *Curr. Opin. Green Sustain. Chem.* **2022**, *34*, 1–8.

(43) An, H.; Wu, L.; Mandemaker, L. D. B.; Yang, S.; Ruiter, J.; Wijten, J. H. J.; Janssens, J. C. L.; Hartman, T.; Stam, W.; Weckhuysen, B. M. Sub-Second Time-Resolved Surface-Enhanced Raman Spectroscopy Reveals Dynamic CO Intermediates during Electrochemical CO_2 Reduction on Copper. *Angew. Chemie Int. Ed.* **2021**, *60* (30), 16576–16584.

(44) Rudolph, W. W.; Irmer, G.; Königsberger, E. Speciation Studies in Aqueous HCO_3^- – CO_3^{2-} Solutions. A Combined Raman Spectroscopic and Thermodynamic Study. *Dalt. Trans.* **2008**, No. 7, 900–908.

(45) Zhu, Z.; Liu, X.; Bao, C.; Zhang, K.; Song, C.; Xuan, Y. How Efficient Could Photocatalytic CO_2 Reduction with H_2O into Solar Fuels Be? *Energy Convers. Manag.* **2020**, *222*, 1–8.

(46) Cosano, D.; Esquivel, D.; Romero-Salguero, F. J.; Jiménez-Sanchidrián, C.; Ruiz, J. R. Use of Raman Spectroscopy to Assess Nitrate Uptake by Calcined LDH Phases. *Colloids Surfaces A Physicochem. Eng. Asp.* **2020**, *602*, 1–6.

(47) Mao, Y.; He, J.; Sun, X.; Li, W.; Lu, X.; Gan, J.; Liu, Z.; Gong, L.; Chen, J.; Liu, P.; Tong, Y. Electrochemical Synthesis of Hierarchical Cu_2O Stars with Enhanced Photoelectrochemical Properties. *Electrochim. Acta* **2012**, *62*, 1–7.

(48) Zhao, Y.; Chang, X.; Malkani, A. S.; Yang, X.; Thompson, L.; Jiao, F.; Xu, B. Speciation of Cu Surfaces During the Electrochemical CO Reduction Reaction. *J. Am. Chem. Soc.* **2020**, 9735–9743.

(49) Smith, B. D.; Irish, D. E.; Kedzierzawski, P.; Augustynski, J. A Surface Enhanced Roman Scattering Study of the Intermediate and Poisoning Species Formed during the Electrochemical Reduction of CO_2 on Copper. *J. Electrochem. Soc.* **1997**, *144* (12), 4288–4296.

(50) Raciti, D.; Mao, M.; Park, J. H.; Wang, C. Local pH Effect in the CO_2 Reduction Reaction on High-Surface-Area Copper Electrocatalysts. *J. Electrochem. Soc.* **2018**, *165* (10), F799–F804.

(51) Calle-Vallejo, F.; Koper, M. T. M. Theoretical Considerations on the Electroreduction of CO to C_2 Species on Cu(100) Electrodes. *Angew. Chemie Int. Ed.* **2013**, *52* (28), 7282–7285.

(52) Kong, X.; Zhao, J.; Ke, J.; Wang, C.; Li, S.; Si, R.; Liu, B.; Zeng, J.; Geng, Z. Understanding the Effect of *CO Coverage on C–C Coupling toward CO_2 Electroreduction. *Nano Lett.* **2022**, *22* (9), 3801–3808.

(53) Chernyshova, I. V.; Somasundaran, P.; Ponnurangam, S. On the Origin of the Elusive First Intermediate of CO_2 Electroreduction. *Proc. Natl. Acad. Sci.* **2018**, *115* (40), E9261–E9270.

(54) Ren, D.; Gao, J.; Pan, L.; Wang, Z.; Luo, J.; Zakeeruddin, S. M.; Hagfeldt, A.; Grätzel, M. Atomic Layer Deposition of ZnO on CuO Enables Selective and Efficient Electroreduction of Carbon Dioxide to Liquid Fuels. *Angew. Chemie* **2019**, *131* (42), 15178–15182.

(55) Zhong, D.; Zhao, Z.; Zhao, Q.; Cheng, D.; Liu, B.; Zhang, G.; Deng, W.; Dong, H.; Zhang, L.; Li, J.; Li, J.; Gong, J. Coupling of Cu(100) and (110) Facets Promotes Carbon Dioxide Conversion to Hydrocarbons and Alcohols. *Angew. Chemie Int. Ed.* **2021**, *60* (9), 4879–4885.

(56) Moradzaman, M.; Mul, G. In Situ Raman Study of Potential-Dependent Surface Adsorbed Carbonate, CO, OH, and C Species on Cu Electrodes During Electrochemical Reduction of CO_2. *ChemElectroChem* **2021**, *8* (8), 1478–1485.

(57) He, M.; Li, C.; Zhang, H.; Chang, X.; Chen, J. G.; Goddard, W. A.; Cheng, M.; Xu, B.; Lu, Q. Oxygen Induced Promotion of Electrochemical Reduction of CO_2 via Co-Electrolysis. *Nat. Commun.* **2020**, *11* (1), 1–10.

(58) Gupta, N.; Gattrell, M.; MacDougall, B. Calculation for the Cathode Surface Concentrations in the Electrochemical Reduction of CO_2 in $KHCO_3$ Solutions. *J. Appl. Electrochem.* **2006**, *36* (2), 161–172.

CHAPTER 6

Final Conclusions

In 1985, the pioneering Hori's studies on the electrochemical CO_2 conversion revealed that Cu has the unique ability to catalyse the CO_2ER in aqueous electrolytes towards hydrocarbons and C_{2+} products in great amount. Indeed, differently from the other metals, Cu has been empirically demonstrated to be able to promote the adsorption of the target intermediates, *i.e.,* *CO, *COOH, and *OCHO so that to make interactions possible in order to promote the C-C coupling formation. Since the CO_2ER reaction displays several drawbacks, like the competitive hydrogen evolution reaction (HER), the required large overpotential, and the low selectivity, the scientific community has brought many innovations in the design of proper Cu-based electrocatalysts. Studies on the effects of the morphology, structure and chemical composition of the electrocatalyst, along with the experimental set-up, allowed to improve the efficiency of the CO_2ER in terms of selectivity and activity.

To this purpose, the potential of micro- and nano-structured materials loaded on eco-friendly supports has been widely demonstrated, which offers the possibility to form lightweight, low-cost and low-power consuming electrochemical platforms in view of their applications inside the artificial photosynthesis-oriented systems, namely the *artificial leaf*. In this scenario, the porous and 3D structure of gas diffusion membranes have shown improvements on the mass fixation of CO_2 at the surface of the electrode, providing a solid-liquid-gas microenvironment not only in gaseous configurations but also when the reaction is performed in a liquid phase experimental set-up.

The studies described in this thesis aim to develop novel Cu-based electrocatalysts, employed as cathodes modifiers and loaded on 4 cm^2-sized carbonaceous gas diffusion layers, which are capable to promote the CO_2ER, preferentially towards C_2 products.

The synthesised materials were chosen on the basis of future applications as eco-friendly electrodes which are suitable for the aforementioned solar-driven CO_2ER set-ups and able to work both in liquid and gaseous conditions.

All the Cu-based electrocatalysts were achieved through one-step and low-cost electrochemical processes, followed by further chemical or electrochemical transformations meant to investigate specific properties. Their catalytic performances were studied in a typical H-cell configuration, using aqueous $KHCO_3$ solutions to promote the sustainability of the process. Differently from the state of the art, the whole experimental set-up was designed to facilitate next future transition to catholyte-less conditions. Hence, the reference electrode was separated from the working electrode, inevitably accepting the higher resistance of the whole electrochemical system.

Several nanostructured $Cu^{0\text{-}I/II}$-based films (crystallites dimension < 40 nm) have been deposited by a potentiostatic method on a carbon fiber-made membrane, followed by further chemical and electrochemical oxidative processes. Through a potential screening, it was possible to find out a potential value selective towards the formation of acetic acid, whose production through the direct hydrogenation of CO_2 is considered of great interest. Indeed, its main industrial production typically involves a high-temperature, multi-step process from methane-derived syngas (MeOH) and successive carbonylation (CH_3COOH), carried out with Rh or Ir based catalysts. In the electrochemical approach optimised in this research work, upon application of -0.4 V *vs* RHE, a substantial productivity (0.31 $mmol_{CH3COOH}\ g_{cat}^{-1}\ h^{-1}$) was observed using the electrocatalyst, containing the Cu^0/Cu^+ active redox couple, that also displayed the highest surface area available for the interaction with the gaseous reactant.
On the opposite, upon application of a more cathodic potential (-1.1 V *vs* RHE), the selectivity was lost and other CO_2 reduction products such as CO and HCOOH were detected, while the

production of acetic acid significantly decreased. These results highlighted the outstanding potential of the Cu^0/Cu^+ active couple in favouring the C-C coupling.

Therefore, with the aim of enhancing the affinity between the electrode surface and CO_2, which has acidic nature, and thus improving the catalytic performances of the nanostructured Cu-based electrocatalysts towards acetic acid, a novel electrocatalyst based on a layered double hydroxide (LDH) was optimised. A CuMgAl LDH was electrochemically achieved on the carbonaceous membrane by means of a potentiodynamic method and it was initially employed as precursor for the formation of a more stable and well-dispersed Cu^+/Cu^0 active phase spread over an alkaline metal oxides support. Indeed, the pristine LDH was subjected to further calcination, reduction, and electrochemical oxidation processes to produce a final material referred as Cu_2O/Cu^0 – MgAl LDO or LDH, depending on the chosen route for the reduction step (H_2 or KNO_2). All the LDH-derived electrocatalysts displayed higher productivity in CH_3COOH at -0.4 V compared to the previous Cu-based films, highlighting the importance of the chemical composition of the electrocatalyst in favouring the interaction with the reactant. Surprisingly, an unprecedent result was obtained by employing the pristine CuMgAl LDH which outpaced the previous production by 5 times (1.5 *vs* 0.31 $mmol_{CH3COOH}\ g_{cat}^{-1}\ h^{-1}$), highlighting the possibility to use the layered double hydroxides as catalysts for electrochemical reduction processes, unlike their usual application for oxidation reactions.

Hence, on the basis of these results, further investigations were performed on the morphology of the ternary CuMgAl LDH, since, from the experimental evidences, the presence of the Cu^0/Cu^+ active redox couple was hypothesised even in the pristine LDH film. As a result, SEM-FEG and EDS analyses revealed the presence of a layered structure containing the three cations in intimate contact with Cu^0/Cu^+ particles of different dimensions and shape.

Moreover, further investigations to optimise the catalytic activity in terms of cations molar ratio and amount of electrocatalyst loaded on the carbonaceous support were performed, and the production of acetic acid at -0.4 V was employed as a reference parameter for comparing the different materials. The CuMgAl LDH with molar ratio of 2: 1: 1, obtained by applying 2 cycles of deposition, displayed the highest productivity equal to 2.0 $mmol_{CH3COOH}\ g_{cat}^{-1}\ h^{-1}$, along with the highest crystallinity detected through the X-ray diffraction analysis, and the highest current density recorded during the reaction. Moreover, the cations molar ratio of 2: 1: 1 investigated for the solid deposit displayed a good match with the molar ratio of the three cations present in the starting electrolytic bath, thus suggesting a high control over the deposition process.

Finally, with the aim of investigating the possible effects of the chemical composition on the selectivity of the reaction carried out with the CuMgAl LDH, *operando* and *in situ* studies were performed. Surface enhanced Raman spectroscopic studies carried out during the reaction revealed that the selectivity towards acetic acid was maintained constant as long as the cuprite species and *CO species were detected on the surface (*e.g.*, at 0 V *vs* RHE). Then, at more cathodic potentials (*e.g.*, at -0.8 V) or during the course of the reaction at -0.4 V, the selectivity shifted towards formic acid in correspondence with the formation of Cu oxides/hydroxides species.

In conclusion, the possibility to obtain nanostructured materials over high surface area carbonaceous 3D membranes with substantial catalytic activity towards the liquid phase CO_2ER has been demonstrated. Furthermore, all the materials investigated as electrocatalysts were achieved by fast and low-cost electrochemical methods, starting from easily available raw-materials. All the electrodes displayed a selectivity of almost 100% towards acetic acid at a low cathodic potential (-0.4 V), as long as the Cu^0/Cu^+ active redox couple was present on

the electrode surface, with a high current density recorded during the reaction. Then, upon the use of more reductive conditions, the selectivity shifted towards formic acid, along with the greater evolution of hydrogen and an initial production of CO. Ranging from the first studied Cu-based films to the eco-friendly and non-hazardous Cu-containing LDHs, the productivity towards CH_3COOH was enhanced of almost 6.5 times thanks to the increased affinity between CO_2 and the LDH. Moreover, the low amount of catalytic layer electrochemically loaded on the carbonaceous gas diffusion membrane (1.1 mg) contributes to make such materials promising electrocatalysts in view of a sustainable decarbonisation process.

In light of these results, such materials will have great potential also for future implementations in gaseous CO_2ER configurations that will pave the way for a possible application inside the artificial photosynthesis-oriented systems. In addition, since the evolution of hydrogen is competitive with acetic acid production in liquid phase, the reaction setups optimised in this thesis might be used also for the production of ethanol.

As future perspectives, in order to enhance the productivity towards acetic acid, electrocatalytic tests, using new cell designs, could be carried out. Based on H-type cell, the use of a sandwich-type cell, for instance, could be a promising strategy to reduce the system resistance, thus favouring the H^+ diffusion towards the active material and increasing the reaction rate (J). The latter parameter is also limited by the use of a batch cell. Indeed, the use of a flow cell would likely avoid the limitation of the CO_2 solubility, resulting in higher current densities.

Finally, as far as the active materials are concerned, further investigations could be carried out in order to study the stability of Cu species during the CO_2ER, employing additional analytical techniques since it was not possible to discuss the topic further by means of the data obtained in this thesis.

Indeed, X-ray photoelectron spectroscopy will help to determine the oxidation state of all the species before and after the reaction, as well as to provide their evolution under working conditions using *operando* investigations. Moreover, additional studies could be performed using Operando Surface Enhanced Raman Spectroscopy on the Layered Double Hydroxides, in particular using $^{13}CO_2$, in order to investigate the source of the carbon contained in the final products.

ACKNOWLEDGMENTS

I would like to express my thank to my PhD supervisor and co-supervisor, professors Francesco Basile and Domenica Tonelli, respectively, who assisted and guided me throughout this project, giving fruitful advices and continuous support. Their ideas and expertise have always stimulated me to give my best, reaching important goals.

I would like to thank professor Erika Scavetta for believing in my abilities from the very beginning and for always being positive and helpful.

I would like to express my sincere thanks to professor Marc T.M. Koper for welcoming me in his group. His immense knowledge and expertise have encouraged me to learn something new every day. In the CASC group I met very talented people who helped me during my journey far from home and with whom I spent unforgettable moments.

A special thank goes to Doctor Federica Mariani with whom I shared "joys and sorrows" during my entire PhD experience. Her advices and patience were fundamental to "survive" in a lot of situations.

I am also grateful to Doctor Andrea Fasolini who was always available to help me whenever I needed and he never stopped encouraging me.

I am extremely grateful to all the members of the group of Analytical Chemistry, working days have never been boring with you guys!

I would like to thank also the group of Catalysis and, in particular, Ms Eleonora Tosi Brandi for helping me both experimentally and morally.

I would like to thank the technicians, Doctors Alessandra Petroli and Fabrizio Tarterini, who helped me to carry on the research.

Finally, I would like to acknowledge support of the Emilia-Romagna region (IT).